MONOLAYER PROTECTED CLUSTERS: SYNTHESIS, ELECTROCHEMISTRY, LIGAND EXCHANGE KIENTICS AND OPTICAL PROPERTIES

Rui Guo

A dissertation submitted to the faculty of the University of North Carolina at Chapel Hill in partial fulfillment of the requirements for the degree of Doctor of Philosophy in the Department of Chemistry (Analytical Chemistry).

Chapel Hill
2006

Approved by
Advisor: Royce W. Murray
Reader: R. Mark Wightman
Reader: H. Holden Thorp

ABSTRACT

Rui Guo: Monolayer Protected Clusters: Synthesis, Electrochemistry, Ligand Exchange Kinetics and Optical Properties

(Under the Direction of Dr. Royce W. Murray)

Chapter One is an introduction to fundamental properties of Monolayer- Protected Gold Clusters (Gold MPCs) including their synthesis, composition and structure, electrochemistry, ligand exchange mechanism and optical properties.

Chapter Two investigates medium effects (supporting electrolyte concentration, type and solvents) on the quantized double layer (QDL) charging capacitance of hexanethiolate coated gold cluster $Au_{140}(SC6)_{53}$. The dependence of ΔV (e/C_{MPC}) on the concentration of supporting electrolyte (from 1 to 100 mM), measured using square wave voltammetry, is shown to be caused, primarily, by changes in the diffuse double layer component ($C_{DIFFUSE}$) of C_{MPC}. A numerical simulation was used to calculate $C_{DIFFUSE}$ successfully. Additionally, significant changes in the magnitude of the compact double-layer component ($C_{COMPACT}$) of C_{MPC} were induced by adding hydrophobic solvent components such as hexane or dodecane or by introducing hydrophobic electrolyte ions (tetrabutyl-, tetrahexyl-, and tetra-octylammonium, perchlorate and tetra-phenylborate).

Chapter Three describes the effects of supporting electrolyte concentration, temperature and solvent environment on the capacitance of molecule-like phenylethanethiolate coated gold clusters $Au_{38}(SC2Ph)_{24}$ at +1 core charge state with square

wave voltammetry (SWV), differential pulse voltammetry (DPV). The effects are interpreted with both the classical double layer theory treating the two continuous oxidation peaks as quantized double layer (QDL) charging peaks of a monolayer protected gold cluster (MPC) and the concept of "molecular capacitance" treating them as a succession of oxidization peaks of a molecule.

Chapter Four compares the kinetics of exchanges of phenylethanethiolate ligands (PhC2S-) on the monolayer-protected clusters (MPCs) $Au_{38}(SC2Ph)_{24}$ and $Au_{140}(SC2Ph)_{53}$ with *p*-substituted arylthiols (*p*-X-PhSH), where X = NO_2, Br, CH_3, OCH_3, and OH at 293 K. It was found that second-order rate constants for ligand exchange on $Au_{38}(SC2Ph)_{24}$ are very close to those of similar exchange reactions on the larger nanoparticle $Au_{140}(SC2Ph)_{53}$ MPCs indicating vertex site reactivity of these two nanoparticles are ca. the same. However, their ligand exchange extent is different. The reverse exchange reaction was also studied for Au_{38}(*p*-X-arylthiolate)$_{24}$ MPCs (X = NO_2, Br, and CH_3), where the in-coming ligand is phenylethanethiol.

Chapter Five investigates a molecule-like substituent effect on redox formal potentials in the nanoparticle series $Au_{38}(SPhX)_{24}$. Electron-withdrawing "X" substituents energetically favor reduction and disfavor oxidation, and give formal potentials that correlate with Hammett substituent constants. The ligand monolayer of the nanoparticles is shown thereby to play a strong role in determining electronic energies of the nanoparticle core, and is more than simply a protecting or capping layer. The substituent effect does not, however, detectably change the homo-lumo gap energy.

Chapter Six investigates the ligand dependent optical properties of $Au_{38}(SC2Ph)_{24}$ upon ligand exchange with different in-coming thiols in THF. It was found that the

luminescence of $Au_{38}(SC2Ph)_{24}$ was enhanced more when more polar thiolate ligands were exchanged. What is more, the luminescence is linearly correlated with the number of incoming ligands exchanged onto the gold core indicating possible existence of localized chemical states of the gold core. Solvent effects on the second order rate constants of ligand exchange reaction were also observed.

Chapter Seven describes the synthesis and characterization of ligand exchange product of $Au_{55}(PPh_3)_{12}Cl_6$ with pentafluorobenzenethiol. The exchange product was characterized by electrochemistry, TGA, TEM, HPLC, UV-vis, Fluorescence, ^{1}H and ^{19}F NMR spectroscopy.

ACKNOWLEDGEMENTS

I would like to thank my research advisor, Dr. Royce W. Murray, for guiding me through my graduate study at the University of North Carolina at Chapel Hill. His broad knowledge, solid technical excellence and great passion for science are truly admirable. I learned from him how to think, solve the problems and what characteristics that a true scientist should have. I am very grateful for his invaluable support and great patience to me. He has been an inspiration to me during my PhD study and will continue in the future.

I would like to thank my fellow Murray group members. I learned a lot and got a lot of help from them. I really enjoyed working in such an innovative and friendly environment these years. And I need to thank Dr. Feldberg as well for his great help and nice discussion.

I also need to thank my parents and other family members. Without their support, I am unable to finish my PhD study in a place so far away from my hometown.

TABLE OF CONTENTS

LIST OF TABLES

LIST OF FIGURES

LIST OF ABBREVIATIONS AND SYMBOLS

2-D	Two-Dimensional
3-D	Three-Dimensional
A	Absorbance
	Amperes
	Electrode area
abbr.	abbreviation
$\mathbf{A_{CLU}}$	MPC surface area
Ag	Silver
AgQRE	Silver quasi-reference electrode
$\mathbf{Ag/Ag^+}$	Silver-silver ion non-aqueous reference electrode
Au	Gold
$\mathbf{AuCl_4^-}$	Tetrachloroaurate
Au(I)-SR	Au(I) thiolate
a	Atto-
aF	AttoFarad
BAS	Bioanalytical Systems
$\mathbf{BH_4^-}$	Borohydride
$\mathbf{Bu_4NClO_4}$	Tetrabutylammonium perchlorate
$\mathbf{Bu_4NPF_6}$	Tetrabutylammonium hexafluorophosphate
C	Carbon
	Concentration
	Coulombs
$\mathbf{^{13}C\ NMR}$	^{13}C Nuclear Magnetic Resonance Spectroscopy
C6	Hexanethiol
C8	Octanethiol
C12	Dodecanethiol
C6OH	6-Mercaptohexanol
°C	Degrees Celsius
$\mathbf{CCl_4}$	Carbon tetrachloride

C_{MPC}	MPC double-layer capacitance
CD_2Cl_2	Deuterated methylene chloride
$C_{COMPACT}$	Compact layer double-layer capacitance
$C_{DIFFUSE}$	Diffuse layer double-layer capacitance
CE	Capillary electrophoresis
CH_2	Methylene group
CH_2Cl_2	Methylene chloride (or dichloromethane)
CH_3	Methyl group
CH_3CN	Acetonitrile
Cn	Alkanethiol with n carbon atoms
COOH	Carboxylic acid group
CV	Cyclic voltammetry
ca.	About
cm	Centimeter
D	Diffusion coefficient
D_{MPC}	MPC diffusion coefficient
DCM	Methylene chloride
DL	Double-layer
DPV	Differential Pulse Voltammetry
D_R	Diffusion coefficient of reduced species
d	Diameter
	Length of MPC monolayer
E	Potential
D**E**	Potential difference
	Potential step
	Pulse amplitude
E^o	Formal potential
$E^o_{Z,Z-1}$	Formal potential of the Z/(Z-1) charge state couple
$E_{1/2}$	Electrochemical half-wave potential
ECLC	Liquid chromatography with electrochemical detector
E_{PZC}	Potential-of-zero charge

EQCM	Electrochemical Quartz Crystal Microbalance
e	Electronic charge
e^-	Electron
equiv	Equivalent
eV	Electron volts
exp	Exponential
F	Farad
	Faraday constant
mF	MicroFarad
Fc	ferrocene
FT-IR	Fourier Transform Infrared Spectroscopy
fd	Fast delivery
g	Gram
H	Hydrogen
^{1}H NMR	Proton Nuclear Magnetic Resonance Spectroscopy
H_2O	Water
H_2SO_4	Sulfuric acid
$HAuCl_4 \cdot xH_2O$	Tetrachloroauric acid hydrate
HO	Alcohol group
HOOC	Carboxylic acid group
HOMO	Highest occupied molecular orbital
HSC6OH	6-mercapto-1-hexanol thiol
HPLC	High performance liquid chromatography
HRTEM	High-Resolution Transmission Electron Microscopy
Hz	Hertz
h	Hour
I	Intercept
I_2	Iodine
IEC	Ion exchange chromatography
IR	Infrared
i	Current

Di	Current difference
i_{LIM}	Limiting current
i.e.	That is
J	Joule
K	Degrees Kelvin
KBr	Potassium bromide
k	Kilo-
k_B	Boltzmann constant
kD	Kilodaltons
keV	Kiloelectron volts
LUMO	Lowest unoccupied molecular orbital
log	Logarithm
LDI-MS	Laser desorption/ionization mass spectrometry
M	Metal
	Molar
mM	Micromolar
MHz	MegaHertz
MPC	Monolayer-protected cluster
$MPC^{As\text{-}prep}$	as-prepared MPC
m	Meter
	Milli-
mg	Milligram
min	Minute
mL	Milliliter
mM	Millimolar
mol	Mole
mV	Millivolt
N	Newtons
	Nitrogen
N_2	Nitrogen gas
N_A	Avogadro's number

$NaBH_4$	Sodium borohydride
NaCl	Sodium chloride
NMR	Nuclear magnetic resonance
n	Number of electrons transferred
nA	NanoAmperes
n_{DL}	Number of double-layer electrons
nm	Nanometer
O	Oxygen
$^{-}$OOC	Deprotonated carboxylic acid group
Oct_4NBr	Tetraoctylammonium bromide
OSWV	Osteryoung Square Wave Voltammetry
PDA	Photo diode array
PE	Place exchange
PhC2S	Phenolethanethiolate
PhC2 MPCs	Phenylethanethiolate monolayer protected clusters
***p*-X-PhSH**	Para-substituted aryl thiol
Pt	Platinum
PZC	Potential-of-zero charge
pH	$-\log [H^+]$
QDL	Quantized double-layer
Q_{DL}	Double-layer charge
RS	Alkanethiolate
RSH	Alkanethiol
r	Radius
rpm	Rotations per minute
S	Slope
	Sulfur
S/N	Signal-to-noise ratio
SAM	Self-assembled monolayer
SCE	Saturated Calomel Electrode
SEC	Size exclusion chromatography

SET	Single electron transfer
SP	Surface plasmon
SSCE	Sodium-Saturated Calomel Electrode
STM	Scanning tunneling microscopy
s	Second?
T	Temperature
TEM	Transmission electron microscopy
TGA	Thermogravimetric analysis
THF	Tetrahydrofuran
UV-visible	Ultraviolet-visible
V	Volt
D**V**	Potential difference
v	Volume
vs	Versus
vv	Vice versa
$\mathbf{W_{1/2}}$	Voltammetric peak-width at half-height
X	Times
XPS	X-ray photoelectron spectroscopy
Z	Charge state
d	Chemical shift
e	Dielectric constant
	Molar absorbance coefficient
e_o	Permittivity of free space
f	quantum efficiency
h	Viscosity
l	Wavelength
m	Micro-
n	Scan rate
p	Pi
w	Omega functional group

=	Equals to
	Double bond
+	Positive
–	Negative
—	Single bond
<	Less than
>	More than
´	Multiplied by
µ	Proportional to

Chapter I

AN INTRODUCTION TO MONOLAYER-PROTECTED CLUSTERS

Recently there has been extensive interest in the fundamental properties and applications of nanosized materials and nanoscale devices. The nano-scale materials, such as metal nanoparticles and semiconductor quantum dots, are at the transition state between molecules and bulk materials, which can result in unique, size-dependent optical, chemical and physical properties[1]. Monolayer-protected metal clusters (MPCs) are nanoparticles coated with dense monolayers of organothiolate[2], organophosphine[3], or organoamine[4] ligands; thiolate ligands are used widely for MPCs with Au cores. The dense monolayer of ligands protects MPCs against aggregation even when solvent is removed, enabling their isolation, purification, derivatization and further characterization[2(a)]. In this chapter, the preparation, chemical and optical properties of gold nanoparticles will be discussed.

1.1 MPC Synthesis: Brust-Schiffrin Synthesis

In early 1994, Brust, Schiffrin and coworkers[2(c)] reported a two-phase synthetic route for MPCs that is now a most popular way to make thermally and air stable gold nanoparticles of relatively controlled core size (typically 1-5 nm core diameter). These nanoparticles can be repeatedly isolated and redissolved in organic solvents without irreversible aggregation or decomposition and can be easily handled and functionalized as stable organic compounds. This so-called “Brust-Schiffrin” synthesis is commonly believed to be a nucleation and

growth process although the detailed mechanism is not fully understood. Briefly, in this two phase synthesis, a phase transfer reagent, tetraoctylammonium bromide (TOABr), is used to transfer $AuCl_4^-$ from water to an organic phase such as toluene. The aqueous phase becomes colorless and the organic phase turns into golden color. Then, a desired amount of thiol is added to the isolated, vigorously-stirred organic phase and the organic solution becomes colorless in ca. one hour indicating formation of colorless Au(I) thiolate polymer. The organic solution is maintained at a certain temperature, say 0°C, for ca. half an hour then an aqueous solution of sodium borohydride ($NaBH_4$) is quickly added. The organic phase immediately turns into black color which indicates the Au(I) thiolate is reduced to Au^0. Au^0 atoms nucleate to form gold cores while thiolates in the solution bind to and passivate the core surface, and the gold nanoparticles form. The organic phase is separated from water and solvent is removed by rotary evaporation. Some polar solvent, such as acetonitrile or methanol, is added to the product to precipitate the MPCs and wash off impurities as well.

A variety of organic soluble MPCs with hydrophobic monolayers can be prepared by employing various non-polar thiols following Brust synthesis[2(a), 5]. Our lab subsequently described the synthesis of water soluble tiopronin MPCs (tiopronin is N- (2-mercaptopropionyl) glycine)[6] and TMA MPCs (TMA is N,N,N-trimethyl(mercaptoundecyl)ammonium)[7] . In addition to gold, other metals, such as Ag[7,8] , Cu[9], Pd[7, 10], Pt[11] or even alloys[12] have been explored as the core material.

The Brust synthesis usually results in MPCs with a core size distribution. By adjusting the initial feed ratio of in-coming thiol/gold core and the reduction temperature, the core size distribution can be roughly tuned. Larger feed ratio, and/or lower temperature (for example, -70 °C) leads to larger portions of smaller (< 2 nm) size MPCs[13]. Etching procedures,

described by Whetten and coworkers[14], have been successful in decreasing MPC core sizes. Annealing reaction[15] has been used to improve monodispersity of Au_{140} clusters bearing hexanethiolate monolayer and decreasing MPC core sizes. Recently, Hutchison and co-workers[16] prepared alkanethiolate-protected Au_{11} by replacing the triphenylphosphine ligands of a preformed Au_{11} core. Alkanethiolate protected Au_{75} MPCs[17] are also obtained by reacting so called "$Au_{55}(PPh_3)_{12}Cl_6$" with different alkane thiols.

1.2 MPC Poly-dispersity and Separation MPCs produced following the Brust-Schiffrin synthesis are usually polydisperse. Their degree of monodispersity and core size distributions are sensitive to the details of the synthesis procedure.[18] Since MPCs' chemical and physical properties are quite size-dependent, producing monodisperse MPCs with controlled core size has become an important issue in current research. Two strategies have been attempted. One focuses on the modifications of synthetic procedures such as heating,[19] etching[14] and annealing,[15] vapor treatment,[20] etc. Although important improvements have been made, the detailed mechanism is not clear, and the processes are either hard to control or repeat as well. The other approach focuses on the separation and isolation of more monodisperse MPCs including solubility fraction,[21] gel electrophoresis[22, 23], capillary electrophoresis[24, 25], size exclusion chromatography (SEC)[26], ion-exchange chromatography (IEC)[27], ion-pair[28] and reversed-phase chromatography[29], and even ultracentrifugation and molecular imprinting[30]. Solubility fractionation, originally introduced by the Whetten group, is of great importance in isolating larger quanties of monodisperse hexanethiolate-coated Au_{140} cluster, $Au_{140}(SC6)_{53}$[15(a)] and phenylethanethiolate- coated Au_{38} cluster, $Au_{38}(SC2Ph)_{24}$[5(c)] . However, it is time-consuming and it is not always possible to find a suitable solvent to do a good fractionation. Gel electrophoresis and capillary electrophoresis are usually used to separate

water soluble MPCs, such as Tiopronin MPCs[6] and Glutathione-protected MPCs[22, 23]. Fractionated MPCs can then be subjected to mass spectrometry and optical measurement to gain better understanding of their core size and electronic properties. Chromatographic separations have advantages but also disadvantages, including irreversible adsorption by SEC column packing materials, and the inapplicability of IEC and ion pair chromatography to neutral nanoparticles. SEC is good for separation of larger nanoparticles but reversed phase HPLC is better for 1-2 nm nanoparticles due to its high resolving power. However, the separation of MPCs by reversed phased HPLC is affected by lots of factors such as core size, core charge state, type of ligands and ligand heterogeneity, etc; thus it is very complicated.

1.3 Electrochemistry of Gold Nanoparticles

1.3.1 Quantized Double Layer Charging of Hexanethiolate-coated Au_{140} cluster

$Au_{140}(SC6)_{53}$ Properties of small nanoparticles (1-10 nm) show a dependence on the particle size and nature of the protecting ligand shell.[31] "Coulomb Staircase" behavior[32] is the first quantum size effect observed on MPCs, which was the single-electron transition between a STM tip and single MPCs. The theory behind this phenomenon is that: when a nanoparticle is small enough and its capacitance becomes so small that the energy required to remove one electron, $E = e^2/2C$ (C is capacitance of MPC), is greater than the thermal disturbance, $E_T = k_b T$ (k_b is the Boltzman constant, 1.38×10^{-23} J/K, and T is the absolute temperature), observation of single-electron transition becomes possible at the temperature studied.

An analogous single-electron transfer behavior[15,33] was soon observed in the traditional electrochemical domain where voltammograms of alkanethiolate coated MPCs show redox-like, continuous charging peaks corresponding to sequential single electron transfer event in the charging of MPCs' electrical double layer, see Figure 1.1. It is termed "Quantized double

layer charging". The gold core of MPC is surrounded by a dielectric medium (thiolate monolayer), thus can be viewed as a spherical capacitor in structural concern, see Figure 1.2. The capacitance of MPC in a solution with high electrolyte concentration (diffuse layer capacitance contribution to total capacitance is negligible) can be expressed as:[33(c)]

$$C_{MPC} = e / \Delta V \cong 4pee_{o}\frac{r}{d}(r+d)$$

where C_{MPC} is MPC capacitance in F/nanoparticle, ε is the dielectric constant of the monolayer, ε_0 is the permittivity of free space, r is the core radius, and d is the monolayer chain length. For hexanethiolate-coated Au_{140} cluster $Au_{140}(SC6)_{53}$, its capacitance is ca. 0.6 aF thus the corresponding potential change ΔV when one electron is taken out or injected to the gold core is ca. 260 mV, much greater than room temperature thermal disturbance (~ 25 mV). As a result, sequential single electron transfers between the working electrode and MPCs diffusing to it can be resolved on the potential axis of cyclic voltammogram. The continuous QDL charging peaks are smeared out when the MPC core size is too large[34] or is polydisperse.[35] Thus reasonable monodispersity of MPCs is a critical requirement of observing QDL charging phenomenon. At lower electrolyte concentration, where the diffuse layer capacitance of MPCs cannot be neglected, the total capacitance can then be taken as two serial capacitors ($C_{COMPACT}$, $C_{DIFFUSE}$). Supporting electrolyte concentration[36] dependent of C_{MPC} was also investigated and further confirmed the charging of MPCs is due to double layer charging. Other than electrolyte concentration, the QDL charging capacitance C_{MPC} is also dependent on electrolyte type, solvent type, temperature[37], etc. QDL charging phenomenon was first observed for freely diffusing MPCs in an electrolyte solution[33], later it was also seen for MPCs attached to an electrode as a film.[38] Not only hexanethiolate coated Au_{140} cluster, but also other organic soluble thiolate coated Au_{140} can display QDL charging

Figure 1.1 Cyclic voltammogram (CV) of 0.08 mM $Au_{140}(SC6)_{53}$ in CH_2Cl_2 with 0.1 M Bu_4NClO_4 at 283 K.

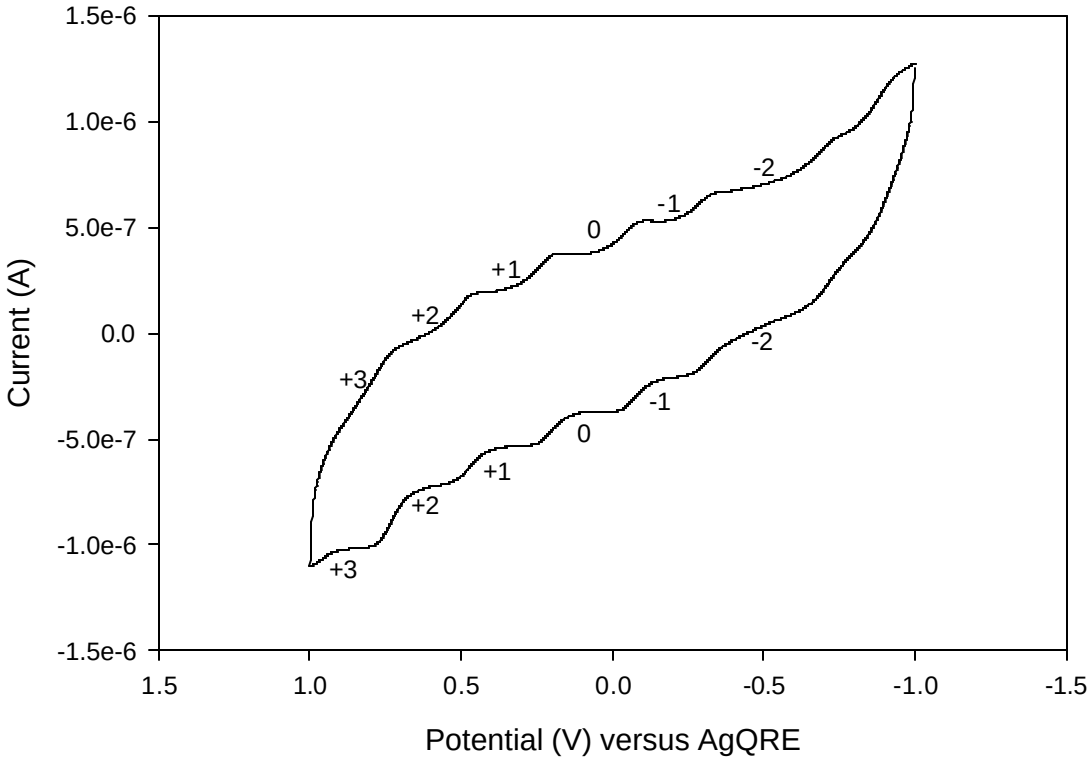
1.5e-6
1.0e-6
5.0e-7
0.0
-5.0e-7
-1.0e-6
-1.5e-6
Current (A)
1.5
1.0
0.5
0.0
-0.5
-1.0
-1.5
Potential (V) versus AgQRE
+3
+2
+1
0
-1
-2
+3
+2
+1
0
-1
-2

Figure 1.2 Spherical capacitor model of monolayer-protected gold nanoparticles.

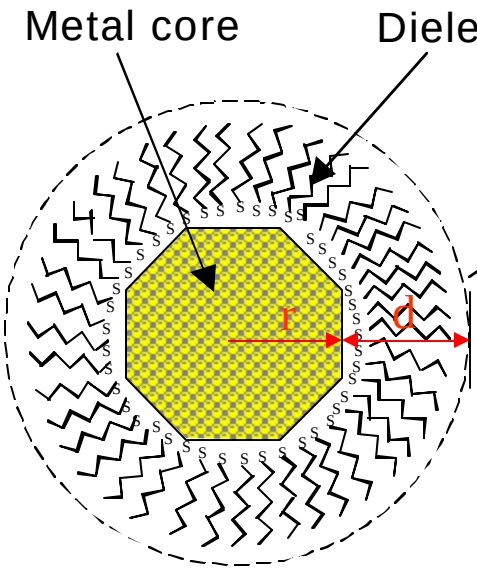

$$C_{MPC} = e/\Delta V \cong 4\pi\varepsilon_{MONO}\,\varepsilon_0 \frac{r}{d}(r+d)$$

(@ high supporting electrolyte concentration)

as long as the MPCs are made monodisperse enough. A newly synthesized modestly monodisperse hexanethiolate coated Au_{225} cluster for example displays QDL charging peaks.[39]

1.3.2 Electrochemistry of Molecule-like Phenylethanethiolate Coated $Au_{38}(SC2Ph)_{24}$ and Hexanethiolate Coated $Au_{75}(SC6)_{40}$ clusters Molecule-like charging behavior has been observed for very small MPCs. A size-dependent opening of a HOMO-LUMO (the highest occupied and lowest unoccupied molecular orbitals) energy gap, representing the bulk-to-molecule transition, was demonstrated from voltammetric studies of alkanethiolate-coated gold MPCs with core mass from 8 to 38 kDa.[33(b)] In particular, phenylethanethiolate coated $Au_{38}(SC2Ph)_{24}$ [5(c),40] synthesized by our lab displayed irregular charging peaks in the cyclic voltammogram with an electrochemical gap of ~ 1.6 V between first oxidation and first reduction which reflects a molecule-like HOMO-LUMO electronic energy structure. Another molecule-like MPC synthesized in our lab is hexanethiolate coated $Au_{75}(SC6)_{40}$ cluster[17] which bears a similar voltammogram pattern but with a smaller electrochemical gap ~ 0.75V. Other monolayer protected Au_{38} clusters can be obtained by ligand exchange reactions with $Au_{38}(SC2Ph)_{24}$ and also display similar pattern in their voltammograms.[41] Yang and Chen[42] obtained Au_{11} nanoparticle following Hutchison's procedure[16] and investigated its electrochemical and optical properties. The electrochemical gap increased from 1.4 to 1.8 eV when initial triphenylphosphine ligands are replaced with dodecanethiolate ligands indicating ligand effects on the electronic structure of the gold core.

1.4 Optical Properties of Gold Nanoparticles Gold MPCs display size and ligand dependent optical properties such as UV-vis absorbance and luminescence. At a fundamental level, optical absorption spectra provide information on the electronic structure of small

metallic particles. Solutions of larger colloidal gold nanoparticles (~ 100 nm) show a deep red color due to the surface plasmon absorption originating from the coherent oscillation of the conduction electrons in response to the incident light. For the gold MPCs synthesized in our lab, surface plasmon resonance at ca.520 nm is observed for MPCs with core size greater than 2 nm in the UV-vis spectrum[18]. However, when the core size is decreased to ~ 1.6 nm, such as $Au_{140}(SC6)_{53}$, the surface plasmon absorption is absent and its UV-vis spectrum shows an exponential and basically featureless decay[18]. When the core size is even smaller, say for $Au_{38}(SC2Ph)_{24}$[5(c),40] with 1.1 nm core diameter, a step-like fine structure characteristic of molecule-like behavior is observed. Other smaller MPCs also shows step-like fine structure in their UV-vis spectra such as dodecanethiolate-coated Au_{11} MPCs prepared by Chen et al.[42], glutathione-protected gold clusters Au_{10}, Au_{15}, Au_{18}, Au_{22}, Au_{25}, Au_{29}, Au_{33}, Au_{39} isolated by Tsukuda et al.[23, 43], and glutathione-protected $Au_{28}(SG)_{16}$ obtained by Whetten et. al.[22(a), 44], etc.

Luminescence usually occurs when there is an energy band gap in the substance. After an electron is excited from the ground state to an excited state (molecular model) or from the valence band to the conduction band (solid-state model), there are several ways for the excited electron to lose extra energy such as by nonradiative decay, or by luminescence. Luminescence is normally not favorable for metals because metals do not have an energy band gap. Thus the nonradiative decay dissipates all the energy through the continuous energy states to the ground state. However, when the dimension of bulk metals decreases to a certain extent, the density of electronic states becomes discrete and a HOMO-LUMO energy gap emerges thus luminescence occurs such as the alkanethiolate coated Au_{11}[42], Au_{38}[40], Au_{75}[17] MPCs, glutathione-protected magic-numbered gold clusters mentioned above[44].

Poly(amidoamine) dendrimers (PAMAM) encapsulated Au_5, Au_8, Au_{13}, Au_{23}, Au_{31} clusters are investigated by Dickson et al.[45]; they found that the emission energy and quantum efficiency are higher for smaller size (less number of atoms) gold clusters.

However, an energy gap is not required to observe luminescence since luminescence from MPCs not only depends on the size, but also depends on surface characteristics. Tiopronin coated MPCs, with an average core diameter 1.8 nm, show a broad emission peak[46] from 650 nm to 1250 nm and it does not have a HOMO-LUMO band gap. Whetten and coworkers[47] have also observed photoluminescence emission at similar energies from Au_{145} MPC passivated by dodecanethiolates. But its quantum efficiency is two orders magnitude smaller than that of tiopronin coated MPCs. Luminescence for gold MPCs without an obvious energy gap is likely due to the sp to sp-like transition analogous to the intraband transition in bulk gold.

1.5 Ligand Exchange Reactions of Gold Nanoparticles One vital aspect of MPCs is that their chemical properties can be manipulated by varying the monolayer with ligand place-exchange reactions [2(a), 17, 34(b), 41, 42, 48]. Ligand exchange reaction was first utilized by our group and has been proven to be a very powerful tool to prepare functionalized gold MPCs. By reacting the MPC with a solution of a new in-coming thiol ligand, the originate thiolate ligand can be either partially or sometimes fully replaced[17, 41, 42] by the new in-coming thiol. The exchange reaction can be generally expressed as:

$$Au_x(SR)_y + m\ (HSR') \longrightarrow Au_x(SR)_{y-m}(SR')_m + m\ (HSR)$$

It was found[34(b), 48(a)] that a) the exchange reactions follow a 1:1 stoichiometry, releasing one out-going ligand as a thiol from the MPC monolayer for every newly bound in-coming thiolate, in a second order process, b) disulfides or oxidized sulfur species are not involved,

c) the exchange rate is accelerated if the core is made electron-deficient (as by oxidative charging) and d) the exchange rate is initially rapid but then slows dramatically. Based on a recent study[49] of a Au(I) thiolate complex produced by oxidizing MPC cores, an improved mechanistic exchange model has newly been proposed: two parallel kinetic routes exist in exchange reactions – associative exchange route (main reaction under N_2, controlled by various surface sites) and dissociative exchange route (catalyzed by the Au(I)SR complex produced either by positive electrochemical core charge or by chemical oxidation via oxygen).

According to theoretical calculations, the gold core surface is heterogeneous[50, 51] and has different Au-S binding sites, such as vertex, edge and terrace sites. Vertex and edge sites are analogous to defect sites of 2D-SAMs and have much higher reactivity than terrace sites. Thus ligand exchange occurs first at vertex and edge sites and then terrace sites, that is the exchange reaction is expected to be fast at the beginning and then slow down. MPCs of different core size have different percentages of surface defect sites[50]. Smaller MPCs have higher surface to volume ratio and higher percentage of surface defect sites. Core size dependent ligand exchange kinetics[48(c)] was investigated and it was found that the reactivity of vertex /edge sites does not vary much for different core size MPCs, however, the exchange extent varies a lot, for smaller MPCs, its exchange extent is much higher than bigger MPCs.

1.6 Theoretical Calculation of Gold MPCs

A series of gold clusters spanning the size range from Au_6 through Au_{147} (with diameter from 0.7 to 1.7 nm) in icosahedral, octahedral, and cuboctahedral structure has been theoretically investigated by Rösch et al.[50] in order to analyze the convergence of cluster properties toward the corresponding bulk metal values. They found that gold 4f core level

binding energy shifts for the surface sites are all positive and distinguish among the corner, edge and face-centered sites which provides theoretical evidence of heterogeneous gold core surface. Some other theoretical calculations have been focused on the structural evolution of smaller gold nanocrystals[52], the capacitance and charge transfer between the passivated clusters[53] and the impact of surface passivation on the clusters[54]. The atomistic structure and morphology of different sized clusters have been resolved and the electronic structure is proposed. In particular, energetics, electronic structure, charging and capacitive properties of bare and methanethiolate passivated Au_{38} clusters[51] were investigated via density-functional theory. Although the simplest thiol (methanethiolate) is used as a model ligand, the density of energy states and surface morphology are found to change by passivation. In another theoretical study of interactions between thiol molecular linkers and Au_{13} core[55], methanethiol and benzenethiol have been used to calculate the impact of thiolate bonding on the gold surface. Gold-gold bond length, for those gold atoms bonded to sulfur, elongate differently with different thiolate. Furthermore, the charge transfer from the metal to the molecule layer (S atom) has been observed for both Au_{38} [51] and Au_{13} [55] clusters.

1.7 References

1 (a) Fendler, J. H.; Meldrum, F. C. The colloidal Chemical Approach to Nanostructured Materials. *Adv. Mater*. **1995**, *7*, 697. (b) Brus, L. E. *J. Chem. Phys*. **1984**, *80*, 4403.

2 (a) Templeton, A. C.; Wuelfing, W. P.; Murray, R. W. *Acc. Chem. Res.* **2000, *33*, 27**. (b) Whetten, R. L.; Shafigullin, M. N.; Khoury, J. T.; Schaaff, T. G.; Vezmar, I.; Alvarez, M. M.; Wilkinson, A. *Acc. Chem. Res.* **1999**, *32*, 397. (c) Brust, M.; Walker, M.; Bethell, D.; Schiffrin, D. J.; Whyman, R. J.; *Chem. Soc. Chem. Commun.* **1994**, *801*. (d) Brown, L. O.; Hutchison, J. E. *J. Am. Chem. Soc.* **1997**, *119*, 12384.

3 (a) Schmid, G. *Chem. Rev*. **1992**, *92*, 1709. (b) Weare, W. W.; Reed, S. M.; Warner, M. G.; Hutchison, J.E. *J. Am. Chem. Soc.* **2000**, *122*, 12890. (c) Petroski, J.; Chou, M. H.; Creutz, C. *Inorg. Chem.* **2004**, *43*, 1597.

4 Brown, L. O.; Hutchison, J. E. *J. Am. Chem. Soc.* **1999**, *121*, 882.

5 (a) Hostetler, M. J.; Murray, R. W. *Curr. Opin. Colloid Interface Sci.* **1997**, *2*, 42. (b) Porter, L. A., Jr.; Ji, D.; Westcott, S. L.; Graupe, M.; Czernuszewicz, R. S.; Halas, N. J.; Lee, T. R. *Langmuir*, **1998**, *14*, 7378. (c) Donkers, R. L.; Lee, D.; Murray, R. W. *Langmuir* **2004**, *20(5)*, 1945. (d) Wuelfing, W. P.; Gross, S. M.; Miles, D. T.; Murray, R. W. *J. Am. Chem. Soc.* **1998**, *120*, 12696.

6 Templeton, A.C.; Chen, S.; Gross, S.M.; Murray, R.W. *Langmuir* **1999**, *15*, 66.

7 Cliffel, D. E.; Zamborini, F. P.; Gross, S. M.; Murray, R. W. *Langmuir*, **2000**, *16*, 9699.

8 Collier, C. P.; Saykally, R. J.; Shiang, J. J.; Henrichs, S. E.; Heath, J. R., *Science* **1997**, *277*, 1978.

9 Chen, S.; Sommers, J. M. *J. Phys. Chem. B* **2001**, *105*, 5397.

10 (a) Zamborini, F. P.; Gross, S. M.; Murray, R. W. *Langmuir* **2001**, *17*, 481. (b) Yee, C. K.; Jordan, R.; Ulman, A.; White, H.; King, A.; Rafailovich, M.; Sokolov, J. *Langmuir* **1999**, *15*, 3486.

11 (a) Ahmadi, T. S.; Wang, Z. L.; Hengelein, A.; El-Sayed, M. A. *Chem. Mater.* **1996**, *8*, 1161. (b) Ahmadi, T. S.; Wang, Z. L.; Green, T. C.; Hengelein, A.; El-Sayed, M. A. *Science* **1996**, *272*, 1924.

12 (a) Hostetler, M. J.; Zhong, C-J.; Yen, B.K.H.; Anderegg, J.; Gross, S. M.; Evans, N. D.; Porter, M.; Murray, R. W. *J. Am. Chem. Soc.* **1998**, *120*, 9396; (b) Shon, Y.-S.; Dawson, G. B.; Porter, M.; Murray, R. W. *Langmuir* **2002**, *18(10)*, 3880.

13 Jimenez, V. L.; Georganopoulou, D. G.; White, R. J.; Harper, A. S.; Mills, A. J.; Lee, D.; Murray, R. W. *Langmuir*, **2004**, *20*, 6864.

14 Schaaff, T. G.; Whetten, R. L. *J. Phys. Chem. B* **1999**, *103*, 9394.

15 (a) Hicks, J. F.; Miles, D. T.; Murray, R. W. *J. Am. Chem. Soc.* **2002**, *124*, 13322. (b) Quinn, B. M.; Liljeroth, P.; Ruiz, V.; Laaksonen, T.; Kontturi, K. *J. Am. Chem. Soc*. **2003**, *125*, 6644.

16 Woehrle, G. H.; Warner, M. G.; Hutchison, J. E. *J. Phys. Chem. B* **2002**, *106*, 9979.

17 Balasubramanian, R; Guo, R; Mills, A.J.; Murray, R. W. *J. Am. Chem. Soc.* **2005,** *127(22)*, 8126-8132.

18 Hostetler, M. J.; Wingate, J. E.; Zhong, C. J.; Harris, J. E.; Vachet, R. W.; Clark, M. R.; Londono, J. D.; Green, S. J.; Stokes, J. J., Wignall, G. D.; Glish, G. L.; Murray, R. W. *Langmuir* **1998**, *14*, 17.

19 Devenish, R. W.; Goulding, T.; Heaton, B. T.; Whyman, R. *J. Chem. Soc., Dalton Trans*. **1996**, *5*, 673-679.

20 a) Maye, M. M.; Zheng, W.; Leibowitz, F. L.; Ly, N. K.; Zhong, C. J. *Langmuir* **2000**, *16*, 490. b) Zhong, C. J.; Zhang, W. X.; Leibowitz, F. L.; Eichelberger, H. H. *Chem. Commun.* **1999**, *13*, 1211.

21 Whetten, R. L.; Khoury, J. T.; Alvarez, M. M.; Murthy, S.; Vezmar, I.; Wang, Z. L.; Stephens, P. W.; Cleveland, C. L.; Luedtke, W. D.; Landman, U. *Adv. Mater.* **1996**, *8*, 428.

22 (a) Schaaff, T.G.; Knight, G.; Shafigullin, M.N.; Borkman, R.F. and Whetten,R.L. *J. Phys. Chem.B* **1998,** *102*, 10643. (b) Schaaff, T. G.; Whetten, R.L . *J. Phys. Chem. B* **2000,** *104*, 2630.

23 Negishi, U.; Nobusada, K.; Tsukuda, T. *J. Am. Chem. Soc.* **2005,** *127*, 5261.

24 Templeton, A. C., Cliffel, D. E.; Murray, R. W. *J. Am. Chem. Soc.* **1999,** *121*, 7081.

25 (a) Schnabel, U.; Fishcher, C.; Kenndler, E. *J. Microcolumn Sep.* **1997**, *9*, 529. (b) Rodriguez, M. A.; Armstrong, D. W. *J. Chromatogr. B* **2004**, *800*, 7. (c) Liu, F.-K.; Lin, Y.-Y.; Wu, C.-H. *Anal. Chim. Acta* **2005**, *528*, 249.

26 (a) Wei, G. T.; Liu, F. *J. Chromatogr., A* **1999**, *836*, 253. (b) Wei, G.; Liu, F.; Wang, C. R. C. *Anal. Chem.* **1999**, *71*, 2085. (c) Wilcoxon, J. P.; Martin, J. E.; Provencio, P. *Langmuir* **2000**, *16*, 9912. (d) Wilcoxon, J. P.; Martin, J. E.; Provencio, P. *J. Chem. Phys.* **2001**, *115*, 998. (e) Siebrands, T.; Giersig, M.; Mulvaney, P.; Fischer, C. –H. *Langmuir* **1993**, *9*, 2297. (f) Fischer, C.-H.; Weller, H.; Katsikas, L.; Henglein, A. *Langmuir* **1989**, *5*, 429.

27 Bos, W.; Steggerda, J. J.; Yan, S.; Casalnuovo, J. A.; Mueting, A. M.; Pignolet, L. H. *Inorg. Chem.* **1988**, *27*, 948.

28 Choi, M. M. F.; Douglas, A. D.; Murray, R. W. *Anal. Chem* .**2006** *ASAP article.*

29 (a) Jimenez, V. L.; Leopold, M. C.; Mazzitelli, C.; Jorgenson, J. W.; Murray, R. W. *Anal. Chem*. **2003**, *75*, 199. (b) Song, Y.; Jimenez, V. L.; Mckinney, C.; Donkers, R. L.; Murray, R. W. *Anal. Chem*. **2003**, *75*, 5088. (c) Song, Y.; Heien, M. LAV; Jimenez, V.; Wightman, R. M.; Murray, R. W. *Anal. Chem* .**2004,** *76*, 4911.

30 (a) Calabrette, M.; Jamison, J. A.; Falkner, J. C.; Liu, Y.; Yuhas, B. D.; Matthews, K. S.; Colvin, V. L. *Nano. Lett*. **2005,** *5*, 963. (b) Koenig, S.; Chechik, V. *Chem. Commun.* **2005**, 4110.

31 Brust, M.; Kiely, C. J. *Colloids Surf. A: Physicochem. Eng. Asp*. **2002**, *202*, 175.

32 (a) Guo, L.; Leobandung, E.; Chou, S. Y. *Science* **1997,** *275*, 649. (b) Hartmann, E.; Marquardt, P.; Ditterich, J.; Radojkovic, P.; Steinberger, H. *Appl. Surf. Sci.* **1996,** *107*, 197. (c) Sato, T. and Ahmed, H. *Appl. Phys. Lett.* **1997**, *70*, 2759. (d) Amman, M.; Wilkins, R.; Ben-Jacob, B.; Maker, P. D.; Jaklevic, R. C. *Phys. Rev. B* **1991**, *43*, 1146.

33 (a) Ingram, R. S.; Hostetler, M. J.; Murray, R. W.; Schaaf, T. G.; Khoury, J. T.; Whetten, R. L.; Bigioni, T. P.; Guthrie, D. K.; First, P. N. *J. Am. Chem. Soc.* **1997,** *119*, 9279. (b) Chen, S.; Ingram, R. S.; Hostetler, M. J.; Pietron, J. J.; Murray, R. W.; Schaaff, T. G.; Khoury, J. T.; Alvarez, M. M.; Whetten, R. L. *Science*, **1998**, *280*, 2098. (c) Hicks, J. F.; Templeton, A. C.; Chen, S.; Sheran, K. M.; Jasti, R.; Murray, R. W.; Debord, J.; Schaaf, T. G.; Whetten, R. L. *Anal. Chem.* **1999**, *71*, 3703.

34 (a) Ingram, R. S.; Hostetler, M. J.; Templeton, A. C.; Murray, R. W. *J. Am. Chem. Soc.* **1997**, *119*, 9175. (b) Hostetler, M. J.; Templeton, A. C.; Murray, R. W. *Langmuir* **1999**, *15*, 3782. (c) Ingram, R. S.; Murray, R. W. *Langmuir* **1998**, *14*, 4115.

35 Miles, D. T.; Leopold, M. C.; Hicks, J. F.; Murray, R. W. *J. Electroanalytical Chem.* **2003**, *554-555*, 87.

36 Guo, R.; Georganopoulou, D; Feldberg, S. W.; Donkers, R. L.; Murray, R. W. *Anal. Chem.* **2005**, *77(8)*, 2662-2669.

37 Miles, D. T.; Murray, R. W. *Anal. Chem.* **2003**, *75*, 1251.

38 Hicks, J. F.; Zamborini, F. P.; Osisek, A. J.; Murray, R. W. *J. Am. Chem. Soc.* **2001**, *123(29),* 7048.

39 Wolfe, R. L.; Murray, R. W. *Anal. Chem.* **2006**, *78*, 1167.

40 Lee, D.; Donkers, R. L.; Wang, G.; Harper, A. S.; Murray, R. W. *J. Am. Chem. Soc.* **2004**, *126*, 6193.

41 Guo, R.; Murray, R. W. *J Am. Chem. Soc.* **2005**, *127(34),* 12140.

42 Yang, Y.; Chen, S. *Nano Lett*. **2003**, *3*, 75.

43 (a) Shichibu, Y.; Negishi, Y.; Tsukuda, T.; Teranishi, T. *J. Am. Chem. Soc.* **2005**; *127*(39); 13464-13465. (b) Negishi, Y.; Takasugi, Y.; Sato, S.; Yao, H.; Kimura, K.; Tsukuda, T. *J. Am. Chem. Soc.* **2004**; *126*(21); 6518-6519.

44 Link, S.; Beeby, A.; FitzGerald, S.; El-Sayed, M. A.; Schaaff, T. G.; Whetten, R. L. *J. Phys. Chem. B,* **2002**, *106*, 3410.

45 Zheng, J; Zhang, C.; Dickson, R. M. *Phys. Rev*. *Lett*. **2004**, *93(7)*, 077402.

46 Huang, T.; Murray, R.W. *J. Phy. Chem.B* **2001,** *105(50),* 1249.

47 Bigioni, T. P. Whetten, R. L.; Dag, ö. *J. Phys. Chem. B* **2000**, *104*, 6983.

48 (a) Song, Y.; Murray, R. W. *J. Am. Chem. Soc.* **2002**, *124*, 7096. (b) Donkers, R. L.; Song Y.; Murray, R. W. *Langmuir* **2004,** *20,* 4703-4707. (c) Guo, R.; Song, Y.; Wang G.; Murray, R. W. *J. Amer. Chem. Soc.* **2005**, *127*, 2752-2757.

49 Song, Y.; Huang, T.; Murray, R. W. *J. Am. Chem. Soc.* **2003**, *125*, 11694.

50 Häberlen, O. D.; Chung, S.; Stener, M.; Rösch, N. *J. Chem. Phys*. **1997**, *106*, 5189.

51 Häkkinen, H.; Barnett, R. N. and Landman, U. *Phys. Rev. Lett*. **1999**, *82*, 3264.

52 Cleveland, C. L.; Landman, U.; Schaaff, T. G.; Shafigullin, M. N.; Stephens, P. W.; Whetten, R. L. *Phys. Rev*. *Lett*. **1997**, *79*, 1873.

53 Reimers, J.; Hush, N. S. *J. Phys. Chem. B* **2001**, *105*, 8979.

54 Barnett, R. N.; Cleveland, C. L.; Häkkinen, H.;Luedtke, W. D.; Yannouleas, C.; Landman, U. *Eur. Phys. J. D* **1999**, *9*, 95.

55 Larsson, J. A.; Nolan, M. and Greer, J. C. *J. Phys. Chem. B* **2002**, 106, 5931.

Chapter II

SUPPORTING ELECTROLYTE AND SOLVENT EFFECTS ON SINGLE ELECTRON DOUBLE LAYER CAPACITANCE CHARGING OF HEXANETHIOLATE-COATED Au_{140} NANOPARTICLES

2.1 INTRODUCTION

The chemically vital aspect of nanometer-scale gold particles coated with a dense, protecting monolayer of thiolate ligands—known as monolayer-protected gold clusters (MPCs)—is the stability afforded by the monolayer protection of the core and the ensuing ability to design and manipulate the monolayer's functionality.[1] Further, the small (sub-attofarad) double-layer capacitance[2,3] (C_{MPC}) of alkanethiolate-protected MPCs with 1.6 nm diameter cores allows single-electron charging events to be seen in their electrochemistry at room temperature. That is, the voltage intervals ΔV (= e/C_{MPC}) between successive one-electron charging steps[2-4] of the MPC cores are significantly larger than k_BT/e, leading to observations like the square wave voltammetry of a $Au_{140}(SC6)_{53}$ MPC solution shown in Figure 2.1 (discussed further later). This phenomenon, termed[2-4] quantized double-layer charging (QDL), is also observed, with approximately unchanged capacitance values, for Au_{140} MPCs attached to electrodes as monolayers[5] or multilayers.[6] Observing QDL charging requires that the MPC sample be reasonably monodisperse (or has a dominant population in core size).

Figure 2.1 Osteryoung square wave voltammograms (OSWV) of 0.08 mM $Au_{140}(SC6)_{53}$ (SC6 stands for hexanethiolate) in CH_2Cl_2 at 283K with Bu_4NClO_4 concentrations (A) 0.74 mM, (B) 1.02 mM, (C) 100 mM at 283K. The voltammograms have been adjusted to a common E_{PZC} potential vs AgQRE; E_{PZC} is about -0.2V[5c] with respect to Ag/AgCl. OSWVs for Bu_4NClO_4 concentrations in between 1.02 mM and 100 mM are not shown in this figure. The mono-dispersity of the $Au_{140}(SC6)_{53}$ sample employed is estimated to be ~ 43% of the overall MPCs, based on using $(i_{peak+1/0} - i_{valley+1})/i_{peak+1/0}$ values in 100 mM electrolyte. OSWV peak currents at low electrolyte concentrations are depressed because the cell time constants ($R_{UNC}C_{DL}$ ~ 17 msec at 1 mM electrolyte) are comparable to the potential step duration (33 msec), so that full potential control is not attained. (This does not materially affect current peak positions.)

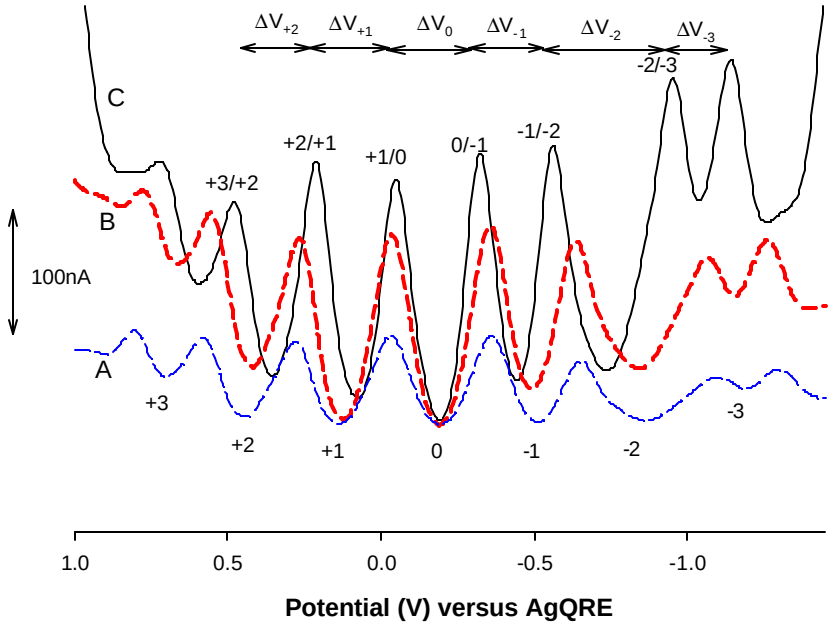
ΔV+2
ΔV+1
ΔV0
ΔV-1
ΔV-2
ΔV-3
-2/-3
C
+2/+1
+1/0
0/-1
-1/-2
+3/+2
B
100nA
A
+3
+2
+1
0
-1
-2
-3
1.0
0.5
0.0
-0.5
-1.0
Potential (V) versus AgQRE

The present investigation is aimed at furthering our understanding of experimental values of C_{MPC} for nanoparticles like $Au_{140}(SC6)_{53}$. The double layer capacitance of a metal/electrolyte solution interface is classically represented by a series equivalent circuit comprising the "compact layer" ($C_{COMPACT}$) and "diffuse layer" ($C_{DIFFUSE}$) capacitances,[7a]

$$1/C_{MPC} = 1/C_{COMPACT} + 1/C_{DIFFUSE} \quad (1)$$

In this chapter, C_{MPC}, $C_{COMPACT}$, and $C_{DIFFUSE}$ are expressed as F/nanoparticle rather than the more common area-normalized dimension.

In the context of planar surfaces, compact layer capacitances tend to be significantly smaller than diffuse layer capacitances, and thus dominate values of double layer capacitances, especially at high electrolyte concentrations and at potentials much more positive or negative than the potential of zero charge (E_{PZC}).[7b] Our earliest analyses[4,8a] of C_{MPC} values, in solutions with high (typically 100 mM) electrolyte concentration, assumed that $C_{MPC} \simeq C_{COMPACT}$ and were based on a concentric sphere capacitor model of $C_{COMPACT}$:

$$C_{MPC} \approx 4\pi\varepsilon_{MONO}\varepsilon_o r_{CORE}\,(r_{CORE}+d)/d \quad (2)$$

where ε_{MONO} and d are the static dielectric constant and thickness, respectively, of the MPC monolayer (for hexanethiolate-coated MPCs, $\varepsilon_{MONO} \sim 3$[4,8]), ε_o is the permittivity of free space, and r_{CORE} is the radius of the gold core. Implicitly the outer surface of the monolayer shell, whose radius is $r_{CORE} + d$, is taken as equivalent to the surface of closest approach of electrolyte ions to the MPC (outer Helmholtz plane). Equation (2), while a remarkably good first approximation of experimental behavior,[4] remains an admittedly crude model.

The present study further explores the quantized double layer capacitance interpretation[8a] by asking if experimental values of C_{MPC} are measurably influenced by the "diffuse layer" (ionic space charge) capacitance $C_{DIFFUSE}$. The value of $C_{DIFFUSE}$ is computed

using the spherical diffuse-layer model discussed by Quinn, *et al.*[9] Since $C_{DIFFUSE}$ is expected to be a minor component of C_{MPC} (eqn 1), the difference between using the spherical and planar (i.e., the classical Gouy Chapman expression) models to compute $C_{DIFFUSE}$ is subtle and requires a thorough analysis. The classical Gouy Chapman relation[7c] for $C_{DIFFUSE}$ is

$$C_{DIFFUSE} = \left(2e_{SOLV}e_o z^2 e^2 n^\circ / k_B T\right)^{1/2} \cosh\left(zef_2 / 2k_B T\right) 4p\,(r_{CORE} + d)^2 \qquad (3)$$

where e_{SOLV} is the solvent static dielectric constant, z and n° are electrolyte ion charge and number concentration, respectively, of ions in a z:z electrolyte ($n^\circ = 10^{-3}\ C^* \times N_A$, where C^* is electrolyte concentration (M) and N_A is Avogadro's number), k_B is the Boltzmann constant, and f_2 is the potential at distance r_{CORE} + d from the MPC center with respect to the bulk solution. In Equation 3, the MPC area is that at the monolayer/solution interface ($4\pi(r_{CORE}+d)^2$).

The spherical model[9] offers discernible improvement over Eqn. 3 for representing $C_{DIFFUSE}$. Very early numerical computations of $C_{DIFFUSE}$ for spherical colloidal particles[10] showed that the diffuse double layer thickness around the MPC is compressed relative to a planar surface. We will show that this effect is enhanced with increasingly smaller r_{CORE} and/or lower concentrations of supporting electrolyte (see later Figure 2.6 and Supporting Information Figure 2S-4).

Effects of some of the parameters important in the overall value of C_{MPC} have been studied. The temperature dependency[11] of C_{MPC} for CH_2Cl_2 solutions of $Au_{140}(SC6)_{53}$ appears to reflect that expected from Eqn. 3, but the temperature dependencies of the dielectric constants of the hexanethiolate monolayer and of the solvent are also significant. An increase[4] in alkanethiolate monolayer chainlength decreases the C_{MPC} values of

$Au_{140}(SC6)_{53}$ in CH_2Cl_2 solutions in rough agreement (±10%) with Eqn. 2. C_{MPC} changes with different organic solvents were mostly within ±10%. More profound changes—attributed to ion association—were seen when the water-insoluble alkanethiolate-coated MPCs were attached to electrode surfaces contacted by aqueous electrolyte.[12]

The classical way[7b] to detect diffuse layer capacitance is, however, with lowered electrolyte concentration, where $C_{DIFFUSE}$ is manifested by a dip in overall capacitance centered at E_{PZC}. Becka, *et al*.[13] used this approach in a study of a dodecanethiolate self-assembled monolayer on a planar Au electrode; a *ca*. 700 mV wide minimum in capacitance was seen at mM and lower concentrations of aqueous CF_3CO_2Na electrolyte. A minimum in the capacitance was seen[5c] in the ac impedance of surface-attached MPC monolayers in 50mM Hx_4NClO_4 in 2:1 toluene:acetonitrile. We previously mentioned[11] preliminary results at low electrolyte concentrations in which MPC solutions displayed an apparent capacitance minimum near E_{PZC}. In a study of Au_{147} MPCs dissolved in 10 mM electrolyte in CH_2Cl_2, Quinn, *et al*.[9] observed an apparent ?V maximum near the E_{PZC}.

Here, we undertake a more detailed analysis of the diffuse double layer component of C_{MPC}. Using Osteryoung square wave voltammetry (OSWV), ?V values were determined for $Au_{140}(C6)_{53}$ MPCs at electrolyte concentrations from =1 to 100 mM Bu_4NClO_4 electrolyte in CH_2Cl_2 solutions and at slightly reduced temperatures. Unlike previous investigations[4,8a] where *average* values of C_{MPC} were obtained from slopes of plots of $E^o_{Z,Z-1}$ *vs*. MPC electronic charge state, individual variations in peak-to-peak spacings (? V) between adjacent single electron steps are scrutinized, emphasizing the peaks near E_{PZC}, where effect(s) of diffuse layer charging should be most pronounced.[7b]

It is important to note that the analysis used here makes no assumptions about the nature of the energies of the Au core electronic states. The work required to insert an electron (or hole) into the core will be a function not only of the work required to cross the charged interfacial capacitance but also of the energies of the states (which may not be identical), the number of states, and electron pairing energies. The values of what we refer to as $C_{COMPACT}$ below will be a manifestation of such phenomena as well as the apparent chemical effects uncovered. To the extent that there are a large number of degenerate or nearly degenerate states in the Au_{140} core, their effects may be subtle – leaving the spacing of the square-wave peaks relatively uniform even at the low charge states that we analyze in capacitance terms.

Careful measurements of ? V also reveal that varying the hydrophobicity of electrolyte ions and of the solvent also provokes capacitance changes for $Au_{140}(SC6)_{53}$ MPCs. These effects suggest that hydrophobic associations between MPC and hydrophobic solvent and/or ionic constituents can change $C_{COMPACT}$ by changing the dielectric constant and/or the thickness of the dielectric shell surrounding the Au core. For brevity we will refer to these phenomena collectively as solvation/penetration phenomena.

2.2 EXPERIMENTAL SECTION

2.2.1 Chemicals. $HAuCl_4 \bullet 3H_2O$ was synthesized according to literature procedures.[14] Hexanethiol (C6SH, Sigma), sodium borohydride and tetrahydrofuran (THF, ACROS), dichloromethane, acetonitrile, hexane, dodecane, toluene, and acetone (Fisher), absolute ethanol (AAPER), tetra-butylammonium, tetra-hexylammonium and tetra-octylammonium perchlorates (Bu_4NClO_4, Hx_4NClO_4, and Oct_4NClO_4, Fluka), tetra-octylammonium bromide and tetra-butylammonium tetra-phenylborate (Bu_4NBPh_4, Aldrich) were used as received.

Water was purified with a Barnstead NANOpure system.

2.2.2 Synthesis of Ethanol-Soluble C6 MPC. Hexanethiolate-coated MPCs were prepared using the Brust reaction[15,16] at a thiol:$AuCl_4^-$ mole ratio of 3:1 in toluene, adding the $NaBH_4$ reducing agent at 0? and maintaining this temperature with an ice water bath for 30 min. The toluene solvent of the MPC-containing organic layer was removed under vacuum in a rotary evaporator with no added heat, and the crude product extracted with absolute ethanol for 4 hours. The ethanol-soluble fraction was isolated by filtration through a medium-porosity frit and the filtrate rotovaped to dryness. The solid was suspended in 300 ml acetonitrile overnight, filtered, and rinsed with an additional 100 ml of acetonitrile. This ethanol-soluble hexanethiolate-coated product (C6 MPC) has an *average* composition of $Au_{140}(SC6)_{53}$ based on previous analyses[15] of similarly prepared MPCs, with a gold core diameter ($2r_{CORE}$) of 1.6 nm and C6 chain length (d) about 0.8 nm.

2.2.3 Electrochemical Measurements. Cyclic voltammetry (see example in supporting information, Fig.S-1) and Osteryoung square wave voltammetry (OSWV) were performed using a Bioanalytical Systems (BAS) Model 100B. The 1.6 mm dia. Pt working electrode was polished, rinsed and sonicated in NANOpure water, rinsed with absolute ethanol and acetone, and cleaned by potential-cycling in 0.5 M H_2SO_4 for 15 min. A Pt coil counter electrode and Ag wire quasi-reference electrode were used. The OSWV voltammetry was taken at slightly reduced temperature, which enhances[11] the QDL peak definition. OSWV scans are faster and offer somewhat improved sensitivity over differential pulse voltammetry (DPV),[7d] which we have used extensively in the past. The OSWV results (such as in Figure 2.1) are adjusted to a common E_{PZC} potential in 100 mM electrolyte, to eliminate spurious effects of changes in the Ag quasi-reference electrode potential with electrolyte

concentration. The OSWV voltammograms were taken on freshly prepared solutions and were recorded with both positive and negative-going potential scans, and values of peak potentials from the two scans were averaged to eliminate iR_{UNC} effects. Uneven variation of the Au_{140} MPC diffusion coefficients would have some minor effects on ΔV values, but prior work[17] shows that diffusion coefficients evaluated for different core charge states (Z_{MPC}) are relatively constant.

A previous paper[18] has noted the effects of ion-pairing of electrolyte ions on electrolyte concentration and consequently diffuse capacitance, but used much higher concentrations (up to 1.5M) and a cation (Li^+) much more charge-dense than the Bu_4N^+ cation used here. We believe ion-pairing of Bu_4N^+ with ClO_4^- to be minor if present at all in the solutions employed.

2.3 RESULTS AND DISCUSSION

2.3.1 Effect of Bu_4NClO_4 electrolyte concentration on MPC capacitance near E_{PZC}.

Figure 2.1 shows Osteryoung square wave voltammograms (OSWV) of 0.08 mM $Au_{140}(SC6)_{53}$ solutions in CH_2Cl_2 at low (0.74 and 1.0 mM, Curves A and B) and high (100 mM, Curve C) Bu_4NClO_4 concentrations. The current minima in Figure 2.1 correspond to MPCs of different integral charge states (indicated below the minima) being in equilibrium with the working electrode. (Background currents in voltammetry on naked Pt electrodes and in MPC-free electrolyte solution are smaller than those at the current minima in Figure 2.1. The continuum of current flow below the current minima is due to the imperfect mono-disperse sizes of MPCs in the Au_{140} sample, as previously discussed.[19]) The current peaks lie at the formal potentials[8a] of the MPC charge state couples (indicated above the peaks). The peak-to-peak ΔV values are more reliably measured, and are used to obtain the one-

electron d(charge)/d(voltage) differential capacitances (i.e., $C_{MPC} = e/\Delta V$). (That C_{MPC} is a differential not an integral capacitance is discussed in Supporting Information.) The notation for ΔV is shown at the top of the figure; for example ΔV_{+1} and the corresponding capacitance C_{MPC+1} are taken from ΔV of the formal potentials of the $Au_{140}^{+2/+1}$ and $Au_{140}^{+1/0}$ couples. We will focus on the behavior of the ΔV_{+1}, ΔV_0, and ΔV_{-1} results at varied electrolyte concentration.

Qualitatively, Figure 2.1 shows that ΔV becomes larger (i.e., C_{MPC} becomes smaller) at lower electrolyte concentrations. Figure 2.2 shows that this electrolyte concentration-induced decrease in C_{MPC} is greatest at the potential of zero charge (E_{PZC}). As noted above, a dip in capacitance is classically expected[7e] from the potential dependence (ϕ_2) of the diffuse layer capacitance; $C_{DIFFUSE}$ is smallest at E_{PZC} and larger at more positive and negative potentials. We take note of several additional aspects of Figure 2.2: *a*) The capacitance dip seems to persist at higher electrolyte concentrations, where diffuse capacitance contributions are normally thought[7b] to dwindle, *b*) the dip is asymmetrical (ΔV_{+1} and C_{MPC+1} differ from ΔV_{-1} and C_{MPC-1}), and *c*) ΔV_{+2} is less dependent on electrolyte concentration. These effects and others appearing in Figure 2.1 will be examined within the overall analysis of the experimental results.

A numerical simulation of the spherical diffuse layer, following the approach used by Quinn, *et al.*,[9] was used to obtain a plot (Figure 2.3) of the dependence of ϕ_2 (potential at the monolayer/electrolyte interface) on the charge on the MPC core, Z_{MPC}. $C_{DIFFUSE}$ at different integral values of Z_{MPC} was obtained (from the simulation) in a manner equivalent to the slopes[7c] of Figure 2.3, i.e.,

$$C_{DIFFUSE} = e\, dZ_{MPC}/d\phi_2 \qquad (4)$$

Table 2.1 Calculated ϕ_2 values of 0.08 mM $Au_{140}(SC6)_{53}$ in CH_2Cl_2 at different Bu_4NClO_4 concentrations and core charge states at 283K, taken from radial simulation results (such as Figure 2.7). Parameters[4] for $Au_{140}(SC6)_{53}$: radius r ~ 0.8 nm, hexanethiolate monolayer thickness d ~ 0.8 nm; dielectric constant of CH_2Cl_2 at 283 K ca. 9.0.

Core charge / ϕ_2 (mV) / Bu_4NClO_4 (mM)	±4	±3	±2	±1	0
1.02	± 155	± 136	± 108	± 62.5	0
3.07	± 130	± 112	± 87.3	± 50.0	0
7.51	± 110	± 93.8	± 71.4	± 40.1	0
25.2	± 83.2	± 68.8	± 50.5	± 27.3	0
50.2	± 69.0	± 56.0	± 40.2	± 21.3	0
100	± 55.8	± 44.4	± 31.2	± 16.2	0

Figure 2.2 MPC capacitances, derived from ΔV results in Figure 2.1, versus MPC core charge state Z_{MPC}. 0.08 mM $Au_{140}(SC6)_{53}$ MPCs in CH_2Cl_2 with indicated Bu_4NClO_4 concentrations at 283K. In taking the capacitances from OSWV data, peak potentials taken in forward and reverse potential scans are averaged in order to cancel residual IR_{UNC} distortion of the peak position, which is important at low Bu_4NClO_4 concentrations. The upper curve is results for $C_{COMPACT}$ from Table 2.2, with associated error bars. (Results at more negative potentials are given in Figure 2S-2 and Table 2S-1).

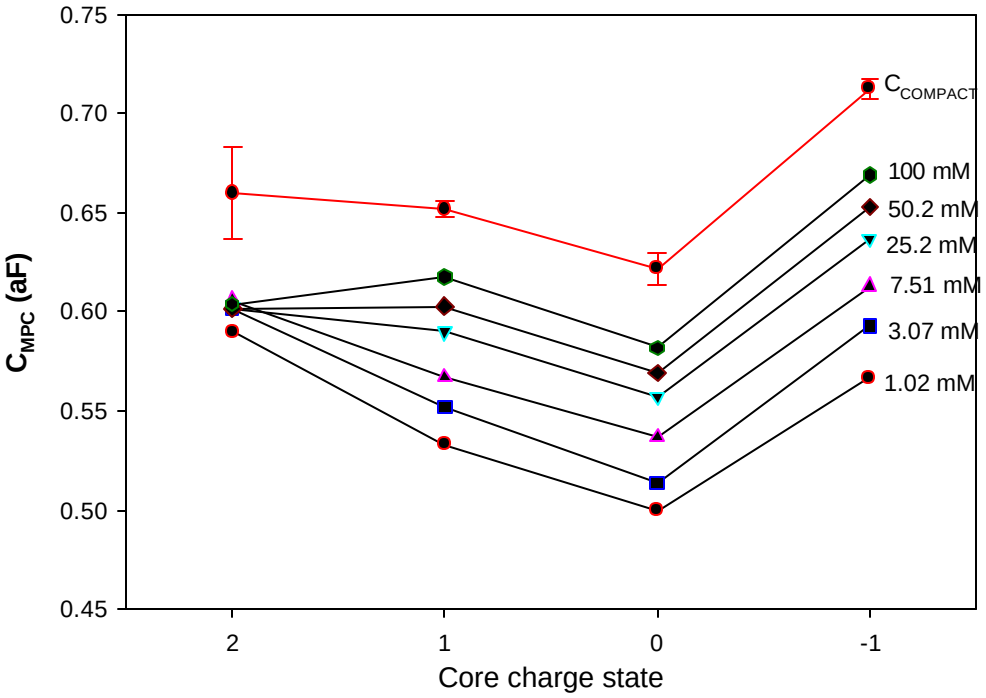
0.75
0.70
0.65
0.60
0.55
0.50
0.45
C_{MPC} (aF)
2
1
0
-1
Core charge state
$C_{COMPACT}$
100 mM
50.2 mM
25.2 mM
7.51 mM
3.07 mM
1.02 mM

where Z_{MPC} is the number of charges on the core. Figure 2.3 is the simulation result for the specific case of 0.08 mM $Au_{140}(SC6)_{53}$ in CH_2Cl_2 with 1.02 mM Bu_4NClO_4 electrolyte. Data for ϕ_2 and $C_{DIFFUSE}$ are given in Tables 2.1 and 2.2, respectively, for other electrolyte concentrations at the same temperature.

The results for $C_{DIFFUSE}$ in Table 2.2 are *predicted* values. Using Eqn. 1, they are combined in Table 2.2 with experimental C_{MPC} values (Figure 2.2) at each MPC charge state to produce values of $C_{COMPACT}$. The results in Table 2.2 show that $C_{COMPACT}$ remains constant at constant Z_{MPC}, especially for +1, 0, and -1, and also that the theoretical simulation of the radially distributed diffuse layer is quite good. Figure 2.4 presents this analysis in an alternative way, in terms of a plot of Equation 1, showing the Equation to accurately represent the capacitance behavior. $C_{COMPACT}$ at Z_{MPC} = +2 is also independent of electrolyte concentration, at < 10 mM, but drifts downward at high electrolyte concentration, causing the poor fit to Equation 1 in Figure 2.4. Table 2.2 further shows that $C_{COMPACT}$ varies with charge state, being *a*) smallest nearest E_{PZC} and *b*) different for the +1 and –1 charge states (asymmetric property).

The preceding analysis clearly shows that a diffuse double layer contribution exists within the overall double layer capacitance values of the MPC nanoparticles, and that it can be quantitatively modeled near E_{PZC}. This important result is a central conclusion of this study in that it supports the general premise[8a] that the experimentally observed dependence of ΔV values on the concentration of supporting electrolyte is primarily due to changes in the diffuse layer capacitance, $C_{DIFFUSE}$.

Consider next several nuances of the Figure 2.2/Table 2.2 results. Firstly, it is generally expected that at potentials farther from E_{PZC}, $C_{DIFFUSE}$ becomes insignificant relative to

Table 2.2 Experimental values[a] of C_{MPC} (from Figure 2.2), simulated values of $C_{DIFFUSE}$ (taking the radial distribution of the diffuse layer into account) and values of $C_{COMPACT}$ (aF per MPC) calculated using Equation 1, at different core charge states Z_{MPC} and different Bu_4NClO_4 concentrations, in CH_2Cl_2 solvent, at 283K. C_{MPC} values are from a single batch of nanoparticles (see Table 2S-1 for effective capacitance $C_{MPC-2,-3}$).

Bu_4NClO_4 (mM)	$C_{DIFFUSE+2}$ (aF)	$C_{COMPCT+2}$ (aF)	C_{MPC+2} (aF)	$C_{DIFFUSE\pm1}$ (aF)	$C_{COMPCT+1}$ (aF)	C_{MPC+1} (aF)	$C_{DIFFUSE0}$ (aF)	$C_{COMPCT0}$ (aF)	C_{MPC0} (aF)	$C_{COMPCT-1}$ (aF)	C_{MPC-1} (aF)
1.02	4.48	**0.68**	0.59	2.88	**0.65**	0.53	2.45	**0.63**	0.50	**0.72**	0.57
3.07	5.25	**0.68**	0.60	3.58	**0.65**	0.55	3.07	**0.61**	0.51	**0.71**	0.59
7.51	6.13	**0.68**	0.61	4.46	**0.65**	0.57	3.86	**0.63**	0.54	**0.71**	0.61
25.2	7.71	**0.65**	0.60	6.27	**0.65**	0.59	5.78	**0.62**	0.56	**0.71**	0.64
50.2	9.36	**0.64**	0.60	7.80	**0.65**	0.60	7.47	**0.62**	0.57	**0.71**	0.65
100	11.3	**0.64**	0.61	10.0	**0.66**	0.62	9.90	**0.63**	0.59	**0.72**	0.67

a. Labeling of capacitance follows that of Figure 2.1, so that for example $\Delta V_{+1}/e = 1/C_{MPC+1} = 1/C_{COMPACT+1} + 1/C_{DIFFUSE+1}$ where ΔV_{+1} is measured between the MPC +2/+1 and +1/0 formal potentials. Experimental reproducibility of ΔV is *ca*. 10mV, which translates to *ca*. 0.01 to 0.02 aF in C_{MPC}.

Figure 2.3 Z_{MPC} versus ϕ_2 plot from diffuse layer simulations (see Figure 2.7), using parameters appropriate to 0.08 mM $Au_{140}(SC6)_{53}$ in CH_2Cl_2 with 1.02 mM Bu_4NClO_4 at 283 K. Parameters for $Au_{140}(SC6)_{53}$ are radius r_{CORE} ~ 0.8 nm, hexanethiolate monolayer thickness d ~ 0.8 nm, dielectric constant of CH_2Cl_2 at 283 K ca. 9.0. Solid curve is a polynomial fit.

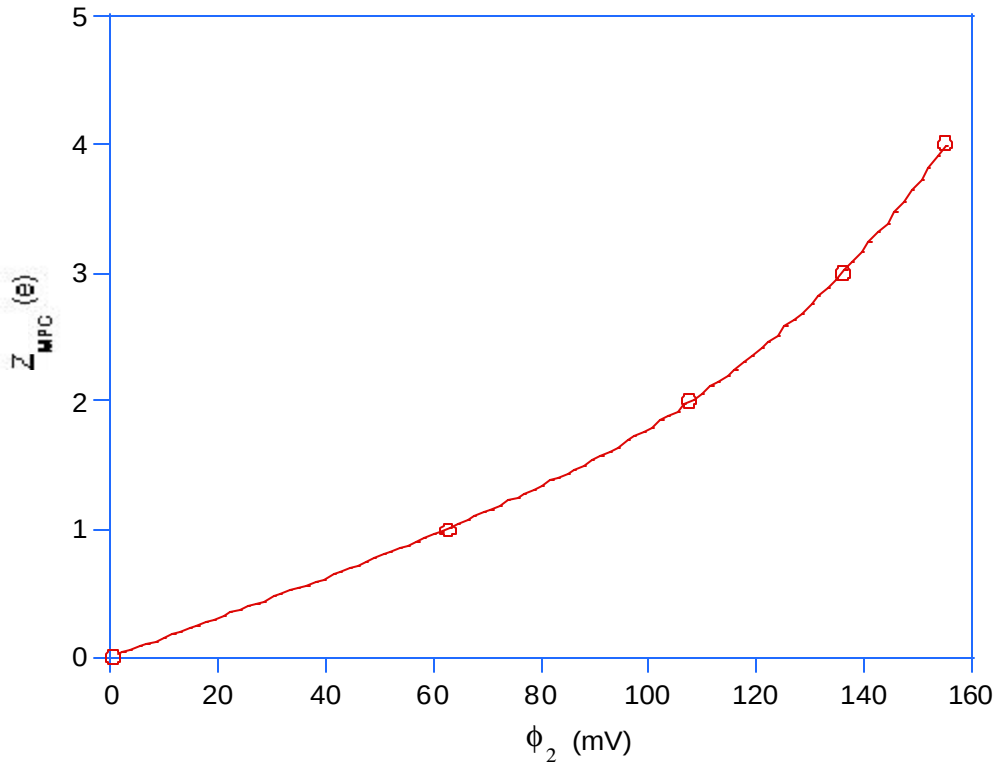
5
4
3
2
1
0
Z_{MPC} (e)
0
20
40
60
80
100
120
140
160
ϕ_2 (mV)

Figure 2.4 Plot of Equation 1, according to experimental C_{MPC} data and $C_{DIFFUSE}$ calculations from the spherical model (values listed in Table 2.2). Slopes are 0.257 (+2 charge state),1.06 (+1 charge state), 0.99 (0 charge state), and 1.05 (-1 charge state). An analogous plot is given as Figure 2S-5 showing that $C_{DIFFUSE}$ calculated from the Gouy Chapman theory fails in a comparison to Equation 1.

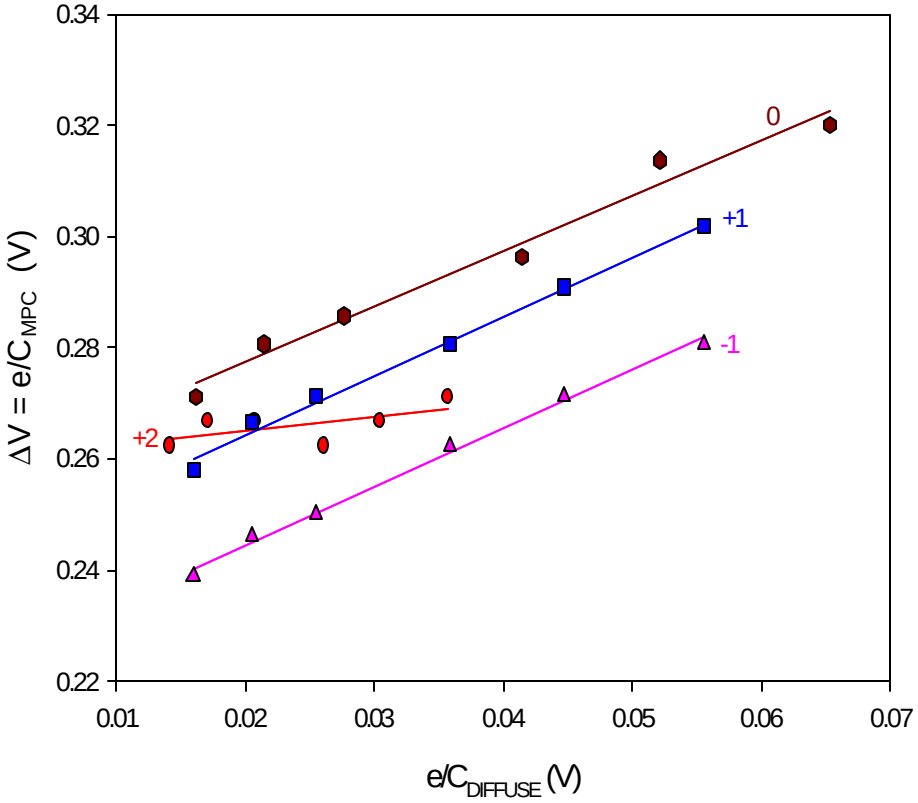
0.34
0.32
0.30
0.28
0.26
0.24
0.22
0.01
0.02
0.03
0.04
0.05
0.06
0.07
ΔV = e/C_MPC (V)
e/C_DIFFUSE (V)
0
+1
-1
+2

$C_{COMPACT}$, blurring any dip in C_{MPC} at E_{PZC}. This is indeed seen in Figure 2.2 at the +2 core charge state (and -2, -3 core charge states as well, see Figure 2S-2), where the effect of electrolyte concentration vanishes. Secondly, the dip in C_{MPC} at E_{PZC} can now be explained as a manifestation of minima in *both* $C_{DIFFUSE}$ and $C_{COMPACT}$ at the E_{PZC} (see upper curve, Figure 2.2). Further, the asymmetry of the $C_{COMPACT}$ results in Table 2.2, at positive versus negative charges, also accounts for the corresponding asymmetry in the C_{MPC} results (Figure 2.2). In short, although $C_{DIFFUSE}$ contributes measurably at low electrolyte concentrations, in the main the behavior of C_{MPC} is rooted in that of $C_{COMPACT}$. Finally, the apparent electrolyte concentration independence of C_{MPC} at Z_{MPC} = +2 (Figure 2.2) arises in part because the higher charge density compresses the diffuse layer and thus increases the value of $C_{DIFFUSE}$, and in part because of opposing dependencies of $C_{COMPACT}$ and $C_{DIFFUSE}$ with electrolyte concentration (Table 2.2).

Equation 2 has been used to describe $C_{COMPACT}$, as noted above, and indicates that increasing the thickness of the monolayer, *d*, and/or diminishing the monolayer dielectric constant (ε_{MONO}) should decrease C_{MPC}. We propose that variations in one or both of these parameters cause both the dip in $C_{COMPACT}$ at E_{PZC} and lead to the asymmetry of values on opposite sides of E_{PZC}, and that these variations are most probably rooted in the strong surface curvature of MPCs. Planar surface alkanethiolate SAMs are known[20] to be well-organized and dense, and penetration of electrolyte ions and solvent into them is regarded as minor except for shorter (6-8 carbons) alkanethiolate chains.[8b] The MPC hexanethiolate monolayers used in these studies are both short and, because of the small r_{CORE}, considerably less dense at their outer boundaries. Some penetration by electrolyte ions and solvent is thus unsurprising and indeed Taylor dispersion measurements[21] of hydrodynamic radii are

consistent with solvent penetration into at least the outer portion of the MPC monolayer. Thus, as suggested in the Figure 2.5 cartoon, non-hydrophobic electrolyte ions simply form an ionic space charge around a charged MPC, but those with hydrophobic chain exteriors may also permeate the monolayer to some extent. Alkane solvent constituents added to the CH_2Cl_2 solvent bath that are considerably less polar than CH_2Cl_2, would also be expected to permeate the monolayer. Considering the relatively non-polar (ε_{MONO}) alkanethiolate MPC monolayer, a relatively minor degree of solvent or ion penetration could provoke significant changes in $C_{COMPACT}$. We refer to these phenomena collectively as solvation/penetration.

The experiments reported in Tables 2.3 and 2.4 test the solvation/penetration ideas. Figure 2.6 and Table 2.3 show the effects of adding different volume fractions of hexane and dodecane to the CH_2Cl_2 solvent. For Z_{MPC} = +1, 0 and –1, ΔV progressively increases, and C_{MPC} correspondingly decreases, for more or longer-chain added hydrocarbons. These capacitance changes can be ascribed to displacement of CH_2Cl_2 solvation/penetration of the MPC monolayer by that of the hydrocarbon, effectively *a*) thickening the MPC monolayer (increasing d, Eqn. 2), and/or *b*) depressing the MPC monolayer dielectric constant (hexane $\varepsilon \sim 2$; CH_2Cl_2 $\varepsilon \sim 9$), and/or *c*) lessening any electrolyte ion penetration. The change in C_{MPC} is substantial, being as much as 20% at E_{PZC}.

Further results, using different electrolyte ions in CH_2Cl_2, are shown in Table 2.4. For all tested, the value of C_{MPC} is smallest at E_{PZC} and increases more sharply at negative potentials versus positive ones. C_{MPC} decreases for Z_{MPC} = +1, 0 and –1 at increasing quaternary salt chain-lengths (Bu_4N^+ to Hx_4N^+ or Oct_4N^+), which is consistent with increased solvation/penetration by the longer-chain quaternary ammonium cations. That C_{MPC} is lowered by hydrophobic cations even for the cationic MPC^{+1} must reflect the importance of

Figure 2.5 Cartoons of the distribution of counter ions comprising the compact layer around MPC surface in CH_2Cl_2 for (a) core charge state +1, (b) core charge state -1. The counter ion Bu_4N^+ at -1 core charge state shows a closer approach than the counter ion ClO_4^- at +1 core charge state due to solvation/penetration of the MPC hexanethiolate monolayer by Bu_4N^+.

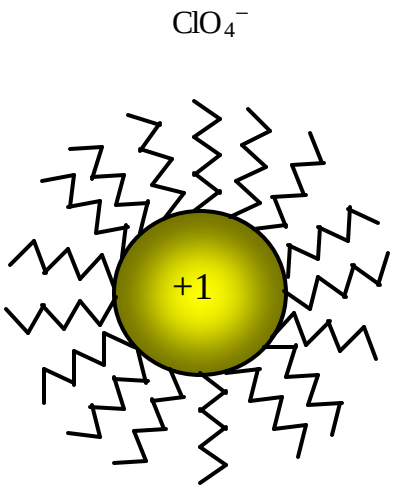

(a)

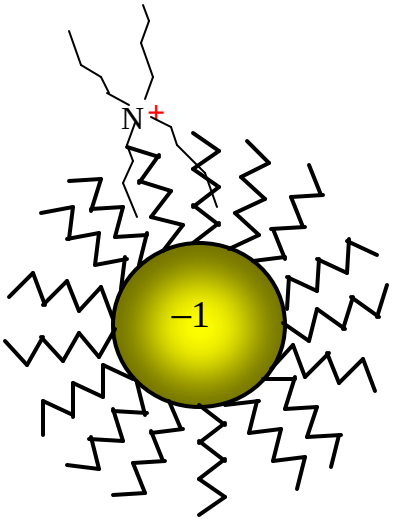

(b)

Table 2.3 C_{MPC} results for 0.04 mM $Au_{140}(SC6)_{53}$ MPCs at different core charge states in different solvent mixtures, at 283K with Bu_4NClO_4 (0.1 M) as the supporting electrolyte.

Core Charge State / Capacitance (aF) / Solvent Component	+3	+2	+1	0	-1
100% CH_2Cl_2	0.78 ± 0.01	0.61 ± 0.01	0.63 ± 0.01	0.60 ± 0.01	0.68 ± 0.01
80% CH_2Cl_2 + 20% hexane	0.82 ± 0.01	0.67 ± 0.01	0.61 ± 0.01	0.57 ± 0.01	0.65 ± 0.01
60% CH_2Cl_2 + 40% hexane	0.80 ± 0.01	0.77 ± 0.01	0.55 ± 0.01	0.48 ± 0.01	0.59 ± 0.01
80% CH_2Cl_2 + 20% dodecane	0.80 ± 0.01	0.64 ± 0.01	0.59 ± 0.01	0.55 ± 0.01	0.65 ± 0.01
65% CH_2Cl_2 + 35% dodecane	0.78 ± 0.01	0.72 ± 0.01	0.53 ± 0.01	0.48 ± 0.01	0.60 ± 0.01

Table 2.4 C_{MPC} results for 0.06 mM $Au_{140}(SC6)_{53}$ at different core charge states in CH_2Cl_2 with different supporting electrolytes (0.1 M), at 283K

Core Charge State / Capacitance (aF) / Electrolyte (0.10M)	+2	+1	0	-1
Bu_4NClO_4	0.61 ± 0.01	0.63 ± 0.01	0.60 ± 0.01	0.68 ±0.01
Hx_4NClO_4	0.59 ± 0.01	0.60 ± 0.01	0.57 ± 0.01	0.65 ± 0.01
Oct_4NClO_4	0.60 ± 0.01	0.58 ± 0.01	0.57 ± 0.01	0.64 ± 0.01
$Bu_4N\phi_4B$	0.56± 0.01	0.59 ± 0.01	0.56 ± 0.01	0.65 ± 0.01

hydrophobic effects in solvation/penetration of the alkanethiolate monolayer. Table 2.4 also shows that Bu_4NPh_4B electrolyte lowers C_{MPC}, in comparison to Bu_4NClO_4, at all charge states, further illustrating the strong hydrophobic solvation/penetration effect.

The Z_{MPC} = +2 and +3 results in Table 2.3 are not as straightforwardly understood as those above, since C_{MPC} no longer decreases with increasing hydrocarbon solvent content. C_{MPC} instead increases with hydrocarbon content at Z_{MPC} = +2, and becomes relatively invariant at Z_{MPC} = +3. This behavior indicates the presence of two (at least) opposing influences on $C_{COMPACT}$. For example, the preceding arguments ignore the changes in solvation of the ClO_4^- electrolyte ion in a more hydrocarbon-like solvent; the consequently less well-solvated anion might associate more strongly with a strongly (+2, +3) cationic MPC (than in CH_2Cl_2 alone) in spite of its alkanethiolate monolayer. The importance of competitive solvation/penetration of the MPC by solvent and electrolyte ion solvation is also found in results in THF solvent, where for example (Supporting Information Fig.S-3), $C_{MPC-1} < C_{MPC+1}$, which is opposite to that in Table 2.3 for CH_2Cl_2.

The present study, of necessity, lead us into an examination of the radial distribution of the diffuse double layer around small charged objects like MPCs. An early[10] computational study showed that the diffuse double layer thickness around a small colloidal particle should be compressed (i.e., $C_{DIFFUSE}$ increases), relative to the diffuse double layer at a planar surface. Our calculations are summarized in Figure 2.7 for a normalized charge (Z_{NORM}) value appropriate to the present MPCs (see Figure 2S-4 for other Z_{NORM} values). The vertical axis in the figure is proportional to ϕ_2 and the horizontal axis to (log) electrolyte concentration and overall particle radius ($r_0 = r_{CORE} + d$). The vertical bars encompass the boundaries of the electrolyte concentrations employed here. The two curves shown in

Figure 2.6 Osteryoung square wave voltammograms (OSWV) of 0.04 mM $Au_{140}(SC6)_{53}$ with 0.1 M Bu_4NClO_4 as the supporting electrolyte at 283 K in (A) 100% CH_2Cl_2, (B) 40% hexane + 60% CH_2Cl_2.

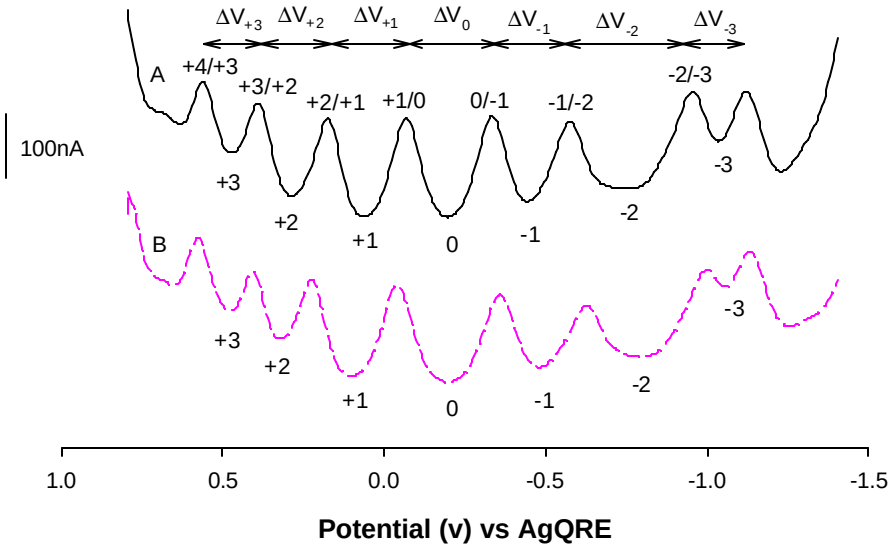
ΔV+3
ΔV+2
ΔV+1
ΔV0
ΔV-1
ΔV-2
ΔV-3
A
+4/+3
+3/+2
+2/+1
+1/0
0/-1
-1/-2
-2/-3
100nA
+3
+2
+1
0
-1
-2
-3
B
+3
+2
+1
0
-1
-2
-3
1.0
0.5
0.0
-0.5
-1.0
-1.5
Potential (v) vs AgQRE

Figure 2.7 U_{dl} versus $\log_{10}(\kappa r_0)$ plot based on numerical simulation of spherical diffuse layer. $U_{dl} = Z_{SE}\, e\, \phi_2/k_BT$, $\kappa = (2n_{SE}Z_{SE}^2e^2/\varepsilon\varepsilon_0k_BT)^{1/2}$, $Z_{NORM} = Z_{SE}Z_{MPC}e^2/(4\pi r_0\varepsilon\varepsilon_0k_BT)$, r_0 is the summation of the Au_{140} MPC core radius and the hexanethiolate monolayer thickness (i.e., $r_{CORE}+d$). Z_{SE} is the charge of the supporting electrolyte ions, which is 1 for Bu_4NClO_4, n_{SE} is the number concentration of Bu_4NClO_4, Z_{MPC} is the MPC core charge state, and the other symbols have their usual meaning. U_{dl}(SIM) is the spherical simulation result, while U_{dl}(GC) is the result based on Gouy-Chapman theory (planar electrode SAM). Z_{NORM} = 4.1 when Z_{MPC} = 1, Z_{SE} =1, T = 283K. $\text{Log}_{10}(\kappa r_0)$ falls in between -0.293 and 0.703 (see vertical lines) when Bu_4NClO_4 concentration varies from 1.02 mM to 100 mM at 283K.

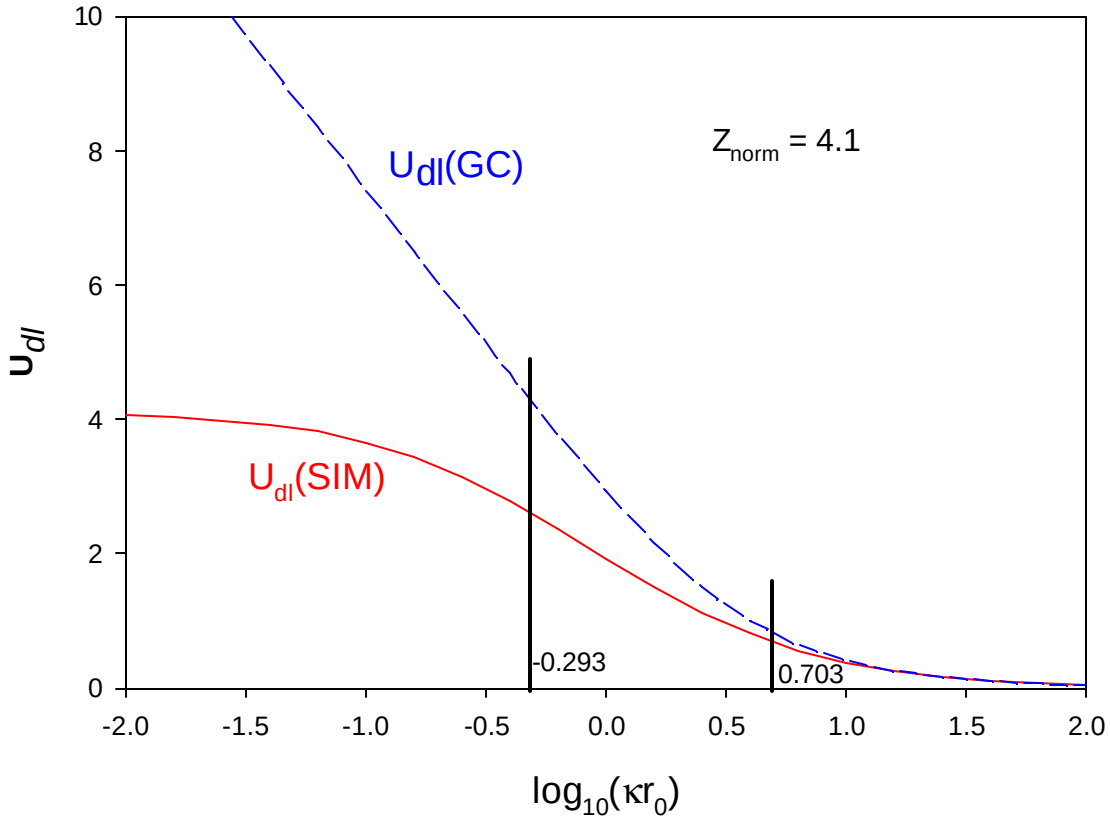
10
8
6
4
2
0
-2.0
-1.5
-1.0
-0.5
0.0
0.5
1.0
1.5
2.0
U_dl
log10(κr0)
U_dl(GC)
U_dl(SIM)
Z_norm = 4.1
-0.293
0.703

Figure 2.7 are for a planar SAM (upper curve, based on the classical Gouy-Chapman relation) and for a spherical model of the SAM (lower curve) analogous to that by Quinn.[9] It is evident that the radial calculation produces a smaller value of ϕ_2 for a given electrolyte concentration, and thus a thinner diffuse layer with a larger value of $C_{DIFFUSE}$. That is, $C_{DIFFUSE}$ has a larger value, *relative* to $C_{COMPACT}$, than is the case at a planar SAM surface, and is thus a less significant term in determining the overall value of C_{MPC}. Qualitatively, the smaller value of ϕ_2 is readily understood by considering that the area of the spherical MPC monolayer/solution interface is larger than that of the core/monolayer interface, so that the charge density at the MPC monolayer/solution interface is smaller (for $Au_{140}(SC6)_{53}$ MPC, about 4-fold) than that at the core/monolayer interface. At a planar SAM, the two charge densities would be the same. Figure 2S-5 shows further, that application of $C_{DIFFUSE}$ data calculated from the Gouy Chapman theory to Equation 1 fails, by poor linearity and non-unity slopes.)

Finally, it is evident in Figure 2.1 that at MPC charge states more positive or more negative than 2/-2, the peak-to-peak spacing between single-electron charge state changes becomes quite irregular. At negative potentials, relative to values at E_{PZC}, the apparent C_{MPC} becomes first smaller, then larger, and then smaller again at the potential limit of the observation. Up-and-down-and-up-again changes in C_{MPC} are very difficult to rationalize in terms of strictly double layer phenomena. The double layer capacitance model used above relies on the assumption that the electronic states within the Au MPC core are degenerate. If instead, the electronic state energies are uniformly incremented, e.g., ε, $\varepsilon+\Delta\varepsilon$, $\varepsilon+2\Delta\varepsilon$,…… $\varepsilon+n\Delta\varepsilon$, then the increment $\Delta\varepsilon$ could masquerade as a component of C_{MPC}. It is important to note that our analysis focuses on changes in C_{MPC} being induced by changes in the

electrolyte concentration, and does not include any non-degeneracy of the energy levels near E_{PZC}. We have speculated[17] that the peak-to-peak spacing irregularities at higher and lower core charging energies (more negative and positive potentials) may reflect an insufficient density of electronic states there. This would not be surprising given the proximity of the Au_{140} core size to sizes showing obvious molecule-like behaviors[22] such as exhibition of homo-lumo gaps in electronic levels. The present work supports the double layer picture at energies near E_{PZC} but does not provide any further evidence regarding this speculation.

2.4 References

1 Templeton, A. C.; Wuelfing, W. P.; Murray, R. W. *Acc. Chem. Res.* **2000**, *33*, 27-36.

2 Ingram, R. S.; Hostetler, M. J.; Pietron, J. J.; Murray, R. W., et al *J. Am Chem. Soc.* **1997**, *119*, 9279.

3 Chen, S.; Ingram, R. S.; Hostetler, M. J.; Pietron, J. J.; Murray, R. W.; Schaaff, T. G.; Khoury, J. T.; Alvarez, M. M.; Whetten, R. L. *Science* **1998**, *280*, 2098.

4 Hicks, J. F.; Templeton, A. C.; Chen, S.; Murray, R. W.; Debord, J; Schaaff, T. G.; Whetten, R. L. *Anal. Chem*. **1999**, *71*, 3703.

5 (a) Chen, S. *J. Phys. Chem. B* **2000**, *104*, 663-667. (b) Hicks, J. F.; Zamborini, F. P.; Murray, R. W. *J. Phys. Chem. B* **2002**, *106*, 7751-7757. (c) Chen, S. and Murray, R. W. *J. Phys. Chem. B* **1999**, *103*, 9996-10000.

6 Zamborini, F. P.; Hicks, J. F.; Murray, R. W. *J. Am Chem. Soc.* **2000**, *122*, 4515.

7 Bard, A. J.; Faulker, L. R. *Electrochemical Methods*; Wiley: New York, 2nd Ed., **2001**, (a) page 553, equation (13.3.30); (b) page 553, Fig.13.3.7; (c) page 550, equation (13.3.21a); (d) page 295, 298; (e) page 550, Fig. 13.3.5.

8 (a) Chen, S. and Murray, R. W.; Feldberg, S.W. *J. Phys. Chem. B* **1998**, *102*, 9898-9907. (b) Porter, M. D.; Bright, T. B.; Allara, D. L. and Chidsey, C. E. D. *J. Am Chem. Soc.* **1987**, *109*, 3559-3568.

9 Quinn, B. M.; Liljeroth, P.; Ruiz, V.; Laaksonen, T. and Kontturi. K. *J. Am. Chem. Soc*. **2003**, *125*, 6644-6645.

10 Leob, A. L.; Overbeek, J. T.; Wiersema, P. H. *The Electrical Double Layer Around a Spherical Colloid Particle*, MIT press, 1961.

11 Miles, D. T. and Murray, R. W. *Anal. Chem.*, **2003**, *75*, 1251-1257.

12 Chen,S. *J. Am Chem. Soc.* **2000**, *122*, 7420-7421.

13 Becka, A. M. and Miller, C. J. *J. Phys. Chem.***1993**, *97*, 6233-6239.

14 *Handbook of Preparative Inorganic Chemistry*, Brauer, G., Ed.; Academic Press: New York, **1965**; p 1054.

15 Hostetler, M. J.; Wingate, J. E.; Zhong, C.; Harris, J. E.; Vachet, R. W.; Clark, M. R.; Londono, J. D.; Green, S. J.; Stokes, J. J.; Wignall, G. D.; Glish, G. L.; Porter, M. D.; Evans, N. D. and Murray, R. W. *Langmuir* **1998**, *14*, 17-30.

16 (a) Brust, M.; Walker, M.; Bethell, D.; Schiffrin, D. J.; Whyman, R. *J. Chem. Soc., Chem. Commun.* **1994**, 801-802. (b) Terrill, R. H.; Postlethwaite, T. A.; Chen, C.; Poon, C.; Terzis, A.; Chen, A.; Hutchison, J. E.; Clark, M. R.; Wignall, G.; Londono, J. D.; Superfine, R.; Falvo, M.; Johnson Jr., C. S.; Samulski, E. T. and Murray, R. W. *J. Am Chem. Soc.* 1995, 117, 12537.

17 Hicks, J. F.; Miles, D. T.; Murray, R. W. *J. Am Chem. Soc*. **2002**, *124*, 13322-13328.

18 Drogowska, M. A.; Fawcett, W. R. *J. Electroanalyt. Chem.* **1987**, *222*, 293-303.

19 Miles, D. T.; Leopold, M. C.; Hicks, J. F.; Murray, R. W. *J. Electroanalyt. Chem.* **2003**, *554*, 87-97.

20 (a) Dubois, L. H.; Nuzzo, R. G. Annu. Rev. Phys. Chem. **1992**, *43*, 437-463. (b) Ulman, A. *An Introduction to Ultrathin Organic Films*, Academic Press, New York, **1991**. (c) Bain, C. D.; Whitesides, G. M. *Angew. Chem., Int. Ed. Engl.* **1989**, *28*, 506-512. (d) Ulman, A. *Chem. Rev.* **1996**, *96*, 1533-1554.

21 Wuelfing, W. P.; Templeton, A. C.; Hicks, J. F. and Murray, R. W. *Anal. Chem.* **1999**, *71*, 4069-4070.

22 Lee, D.; Donkers, R. L.; Wang, G.; Harper, A. S.; Murray, R. W. *J. Am. Chem. Soc.* **2004**, *126*, 6193.

APPENDIX OF CHAPTER II

e/D V is a differential not an integral capacitance.

A key premise of this paper is that over the region of interest, essentially the potential spacings between the peaks of interest, we can write:

$$\frac{\Delta V}{\Delta q} \cong \frac{1}{C_d} \qquad \text{2S-1}$$

where C_d is the differential capacitance, ΔV is a finite change in potential and Δq is a finite change in charge. For the charging of a mono-disperse collection of MPCs, Chen et al (Ref. 8a) showed that the standard potential, $E^0_{z+1/z}$, obtains when the number of MPCs with charge n_{z+1} equals the number with charge n_z; similarly, the standard potential , $E^0_{z/z-1}$, obtains when the number of MPCs with charge n_z equals the number with charge n_{z-1}.

The difference in these two standard potentials, $E^0_{z+1/z,c_{SE}} - E^0_{z/z-1,c_{SE}}$ defines the change in potential required to convert the system from the condition where $n_{z+1} = n_z$ to the condition where $n_z = n_{z-1}$ - a transition that requires the transfer of a single unit of charge per MPC if we assume that virtually all of the charge resides essentially in two forms at the standard potential. Thus Equation S-1 can be expressed as:

$$E^0_{z+1/z,c_{SE}} - E^0_{z/z-1,c_{SE}} \cong \frac{e}{C_{MPC,z}} \qquad \text{2S-2}$$

where $C_{MPC,z}$ is differential capacitance approximately at the point where the MPC has *z* charges. This equation is valid for a given value of the concentration of supporting

electrolyte, c_{SE}. We can express $C_{MPC,z}$ in terms of its compact and diffuse differential capacitive components:

$$\frac{1}{C_{MPC,z}} = \frac{1}{C_{COMPACT,z}} + \frac{1}{C_{DIFFUSE,z,c_{SE}}} \qquad \text{2S-3}$$

Combining Equations S-1 and S-2 gives

$$E^0_{z+1/z,c_{SE}} - E^0_{z/z-1,c_{SE}} \cong \frac{e}{C_{MPC,z}} = e\left(\frac{1}{C_{COMPACT,z}} + \frac{1}{C_{DIFFUSE,z,c_{SE}}}\right) \qquad \text{2S-4}$$

We assume that only $C_{DIFFUSE,z,c_{SE}}$ is a function of c_{SE}. The value of $E^0_{z+1/z,c_{SE}} - E^0_{z/z-1,c_{SE}}$ is experimentally determined and the values of $C_{DIFFUSE,z,c_{SE}}$ can be theoretically computed using the spherical diffuse layer simulation. A plot of $E^0_{z+1/z,c_{SE}} - E^0_{z/z-1,c_{SE}}$ vs $e/C_{DIFFUSE,z,c_{SE}}$ for a given *z* and different values of c_{SE} should have a slope of unity and an intercept of $e/C_{COMPACT,z}$. A slope of unity along with a sensible intercept (likely different for different values of *z*) confirms the validity of the analysis, as is shown in Figure 2.4 The analogous plot of Gouy Chapman $C_{DIFFUSE}$ calculations according to Equation 1, shown as Figure 2S-5, shows that the flat-surface model is a poor approximation for nanoparticles.

Figure 2S-1. Cyclic voltammogram (CV) of 0.08 mM $Au_{140}(SC6)_{53}$ in CH_2Cl_2 with 0.1 M Bu_4NClO_4 at 283 K.

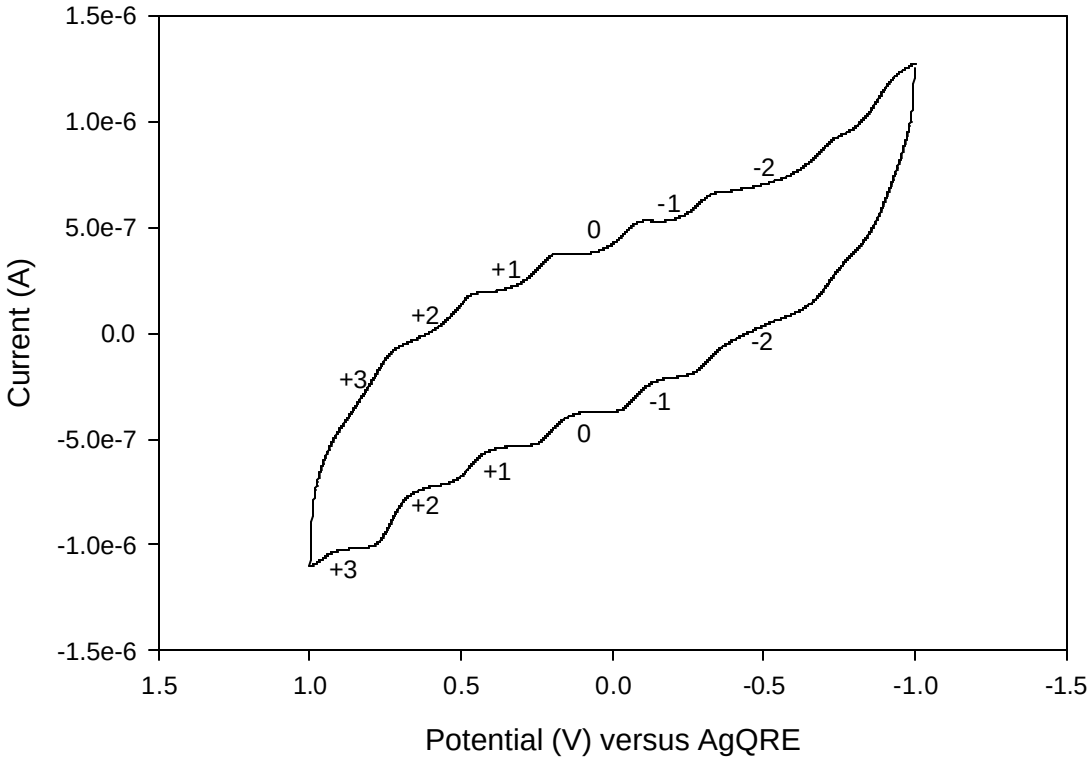
1.5e-6
1.0e-6
5.0e-7
0.0
-5.0e-7
-1.0e-6
-1.5e-6
Current (A)
1.5
1.0
0.5
0.0
-0.5
-1.0
-1.5
Potential (V) versus AgQRE
+3
+2
+1
0
-1
-2
+3
+2
+1
0
-1
-2

Figure 2S-2. Capacitance versus MPC core charge state plot of 0.08 mM $Au_{140}(SC6)_{53}$ in CH_2Cl_2 with different Bu_4NClO_4 concentrations at 283 K. At core charge states +2, +1, 0, -1, -2, -3. In taking the capacitances from OSWV data, peak potentials taken in forward and reverse potential scans are averaged in order to cancel the residual IR_{UNC} distortion of the peak position, which is important at low Bu_4NClO_4 concentrations.

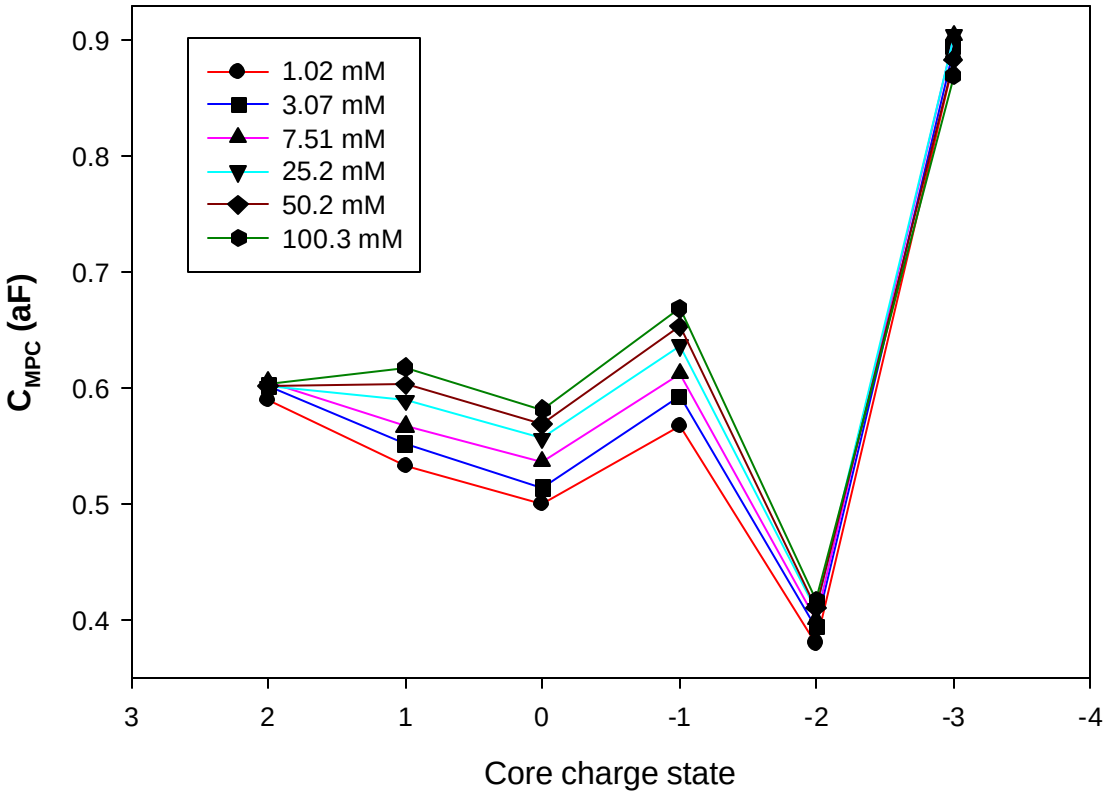
1.02 mM
3.07 mM
7.51 mM
25.2 mM
50.2 mM
100.3 mM
C_{MPC} (aF)
0.9
0.8
0.7
0.6
0.5
0.4
3
2
1
0
-1
-2
-3
-4
Core charge state

Figure 2S-3. Osteryoung square wave voltammogram (OSWV) of 0.05 mM $Au_{140}(SC6)_{53}$ in THF with Bu_4NClO_4 (0.1 M) as the supporting electrolyte at 283 K.

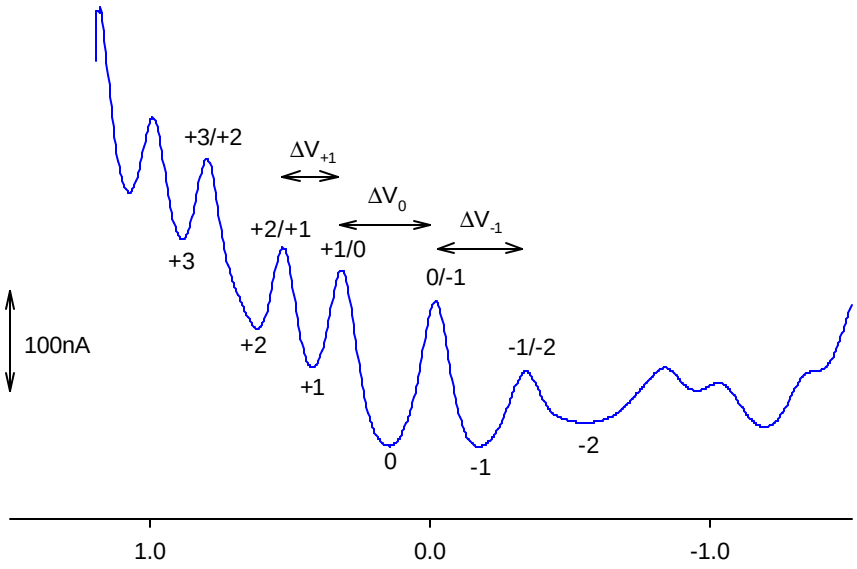
+3/+2
ΔV+1
ΔV0
ΔV-1
+2/+1
+1/0
0/-1
+3
+2
+1
0
-1
-1/-2
-2
100nA
1.0
0.0
-1.0
Potential (V) versus AgQRE

Figure 2S-4. U_{dl} versus $\log_{10}(\kappa r_0)$ plot based on numerical simulation of spherical diffuse layer. $U_{dl} = Z_{SE}\, e\, \phi_2/k_BT$, $\kappa = (2n_{SE}Z_{SE}^2e^2/\varepsilon\varepsilon_0k_BT)^{1/2}$, $Z_{norm} = Z_{SE}Z_{MPC}e^2/(4\pi r_0\varepsilon\varepsilon_0k_BT)$, r_0 is the summation of the Au_{140} MPC core radius and the hexanethiolate monolayer thickness (i.e., r_{CORE} + d). Z_{SE} is the charge of the supporting electrolyte ions, which is 1 for Bu_4NClO_4, n_{SE} is the number concentration of Bu_4NClO_4, Z_{MPC} is the MPC core charge state, and the rest symbols have their usual meaning. U_{dl}(SIM) is the spherical simulation result, while U_{dl}(GC) is the result based on Gouy-Chapman theory (planar electrode SAM). $\text{Log}_{10}(\kappa r_0)$ falls in between -0.293 and 0.703 (see vertical lines) when Bu_4NClO_4 concentration varies from 1.02 mM to 100.3 mM at 283K. (a) Z_{NORM} = 8.2, when Z_{MPC} = 2, Z_{SE} =1, T = 283K. (b) Z_{NORM} = 20.5, when Z_{MPC} = 5, Z_{SE} =1, T = 283K. It is obvious that when Z_{MPC} becomes larger, U_{dl}(GC) is getting closer to U_{dl} (SIM) results.

(a)

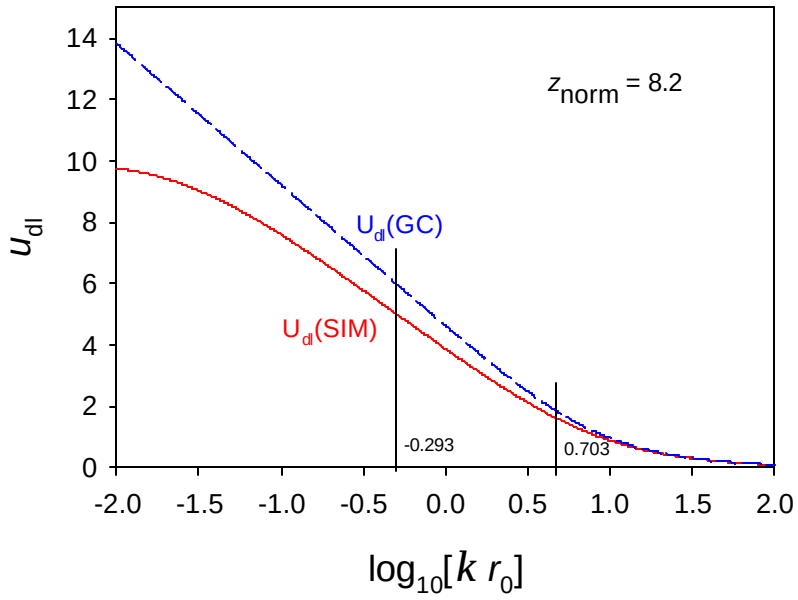
z_{norm} = 8.2
U_{dl}(GC)
U_{dl}(SIM)
-0.293
0.703
u_{dl}
$\log_{10}[k\ r_0]$

(b)

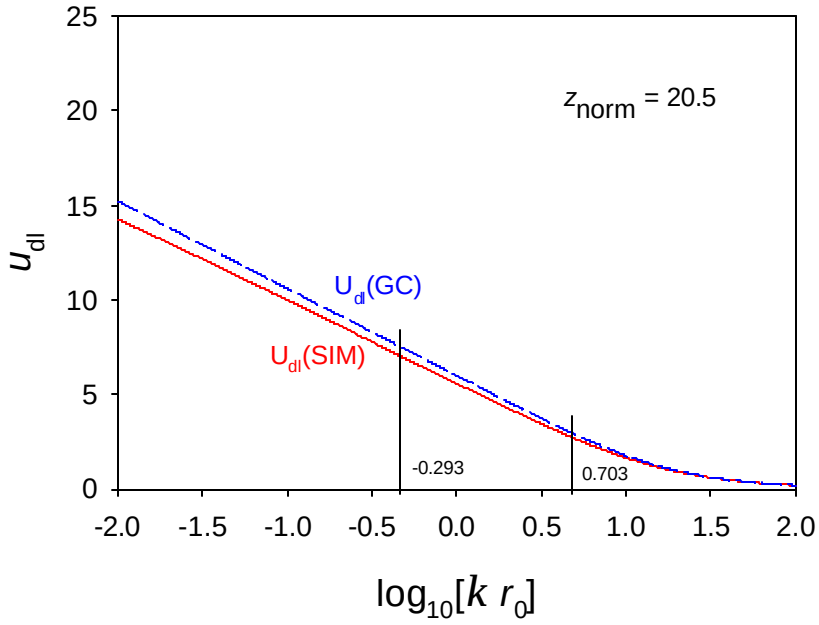
z_{norm} = 20.5
U_{dl}(GC)
U_{dl}(SIM)
-0.293
0.703
u_{dl}
$\log_{10}[k\ r_0]$

Figure 2S-5. Plot of Equation 1, according to experimental C_{MPC} data and $C_{DIFFUSE}$ calculations from Gouy-Chapman theory (Ref. 7a). Slopes are 0.45 (+2 charge state), 1.21 (+1 charge state), 0.40 (0 charge state), and 1.20 (-1 charge state).

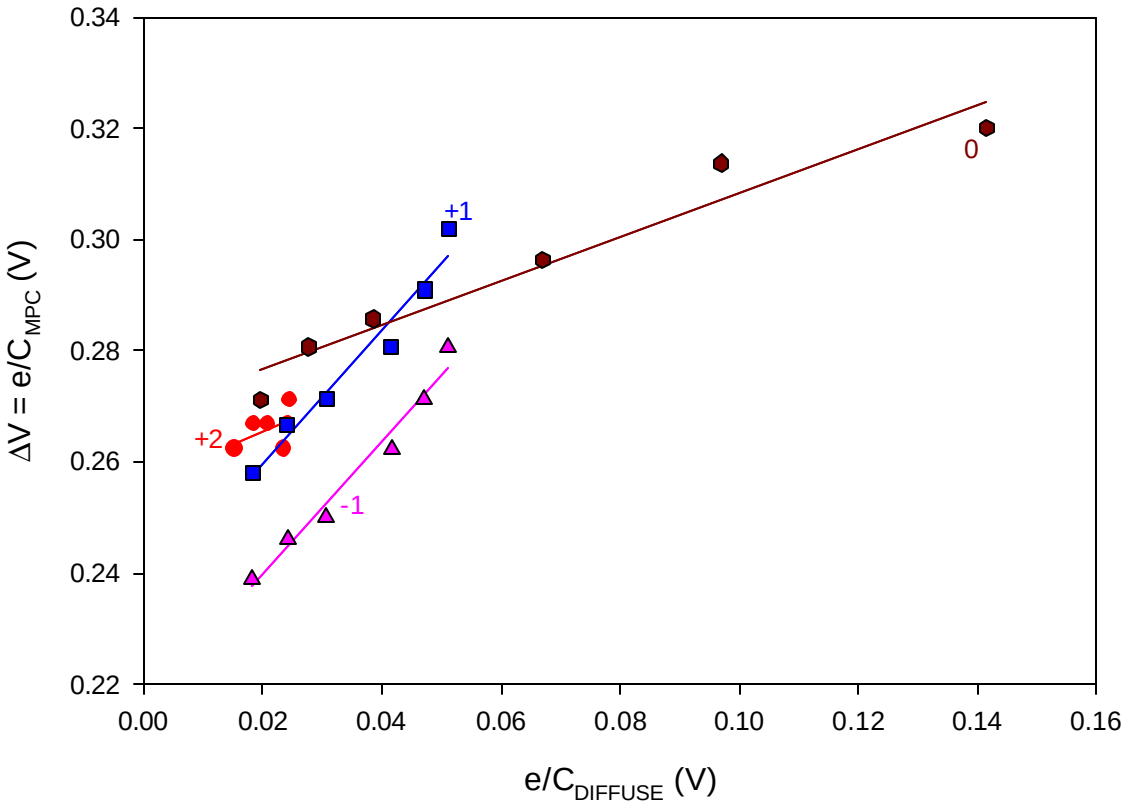
0.34
0.32
0.30
0.28
0.26
0.24
0.22
0.00
0.02
0.04
0.06
0.08
0.10
0.12
0.14
0.16
ΔV = e/C_MPC (V)
e/C_DIFFUSE (V)
0
+1
+2
-1

Table 2S-1. Capacitance of 0.08 mM $Au_{140}(SC6)_{53}$ at different core charge states in CH_2Cl_2 with different Bu_4NClO_4 concentrations at 283 K (calculated from e/ΔV, where ΔV is the average peak to peak spacing of forward and reverse scans of OSWV in Figure 2.1). C_{MPC-2} and C_{MPC-3} are the effective capacitances.

Bu_4NClO_4 (mM)	C_{MPC+2} (aF)	C_{MPC+1} (aF)	C_{MPC0} (aF)	C_{MPC-1} (aF)	C_{MPC-2} (aF)	C_{MPC-3} (aF)
1.02	0.59	0.53	0.50	0.57	0.38	0.88
3.07	0.60	0.55	0.51	0.59	0.39	0.89
7.51	0.61	0.57	0.54	0.61	0.40	0.90
25.2	0.60	0.59	0.56	0.64	0.41	0.90
50.2	0.60	0.60	0.57	0.65	0.41	0.88
100.3	0.61	0.62	0.59	0.67	0.42	0.87

Chapter III

SUPPORTING ELECTROLYTE, TEMPERATURE AND SOLVENT EFFECTS ON THE CAPACITANCE OF MOLECULE-LIKE PHENYLETHANETHIOLATE - COATED GOLD CULSTERS $Au_{38}(SC2Ph)_{24}$

3.1 INTRODUCTION

Gold nanoparticles have evoked much research interest in recent years due to their unique optical, electronic and chemical properties.[1] Among them, nanoparticles containing less than 200 down to a few tens of gold atoms are of particular interest because they represent the bulk-to-molecule transition region from varieties of spectral and electrochemical observations[2] where the continuum of electronic band structure of bulk gold yields to quantum confinement effects and discrete electronic states emerge. The voltammetry of alkanethiolate-coated monolayer-protected gold clusters (MPCs) with core mass of 8 – 38 kDa has been reported[2d] and the core-size dependent optical and electrochemical band gap representing molecular behavior was also observed.[2c,d,5,6,18]

Phosphine-stablized undecagold derivatives have been synthesized and widely used as biological labeling tags in electron microscopy.[3] However, they are generally not stable under ambient conditions. Recently, Hutchison *et al*.[4] employed an exchange-reaction route to replace the triphenylphosphine protecting shell with alkanethiols and obtained stable Au_{11} nanoparticles which are the smallest thiolate stabilized gold nanoparticles isolated to date.

Chen *et al.*,[5] using a slightly modified procedure, synthesized Au_{11} particles, which were found to exhibit semiconductor electronic characteristics with a band gap of ~ 1.8 eV, as evaluated from voltammetric and spectroscopic measurements. In our laboratory, hexanethiolate monolayer protected gold clusters $Au_{38}(SC6)_{24}$ were synthesized using modified Brust synthesis at a -78 °C reduction temperature; a ~ 1.6 eV electrochemical energy gap and ~ 1.3 eV optical HOMO-LUMO energy absorbance edge are observed.[6(a)] A recently synthesized and analytically characterized small gold nanoparticle with a composition of $Au_{38}(SC2Ph)_{24}$[6(b)] was place-exchanged with thiolated polyethylene glycol (PEG) ligands to produce a nanoparticle with an estimated composition of $Au_{38}(SC2Ph)_5(PEG)_{19}$. The mixed monolayer gave this MPC sufficient melt-like properties to study its voltammetry and electron-transfer dynamics in a semisolid, ionically conductive phase.[7]

In dichloromethane (CH_2Cl_2) with 0.1 M Bu_4NClO_4 as the supporting electrolyte, Osteryoung square wave voltammograms (OSWV) or differential pulse voltammograms (DPV) of $Au_{38}(SC2Ph)_{24}$ clearly show features consistent with an electrochemical band gap of about 1.67ev as indicated in Figure 3.1(a) which suggests a molecular behavior, compared to bulk gold. However, the peak spacing of the two neighboring oxidation peaks beside the band gap is about 300 mV which is similar to that of quantized double layer (QDL) charging peaks observed for $Au_{140}(SC6)_{53}$.[8] This peak spacing is affected by the supporting electrolyte concentration, temperature and solvent environment in a manner similar to what we observed for $Au_{140}(SC6)_{53}$[9,11] where classical double layer theory was used to interpret the phenomena. The QDL capacitance is expressed by a series combination of compact layer and diffuse layer capacitance[10a]:

$$1/C_{MPC} = 1/C_{COMPACT} + 1/C_{DIFFUSE} \quad (1)$$

or[9,11]

$$\frac{1}{C_{MPC}} = \frac{d}{4\pi e_{MONO} e_0 r(r+d)} + \frac{1}{\left(2e_{SOLV} e_o z^2 e^2 n^\circ / k_B T\right)^{1/2} \cosh\left(ze f_2 / 2k_B T\right) 4\pi (r+d)^2} \quad (2)$$

where ε_{MONO} is the dielectric constant of monolayer, ε_0 the permittivity of free space, r the gold core radius, d the monolayer thickness (which we take as equivalent to the plane of closest approach of electrolyte ions to the MPC surface), ε_{SOLV} is the static dielectric constant of the solvent surrounding the nanoparticle, *z* the electrolyte ion charge, n° the number concentration of ions in a *z:z* electrolyte ($n^\circ = C^* \times N_A$, where C^* is electrolyte concentration and N_A is Avogadro's number), k_B the Boltzmann constant (1.38×10^{-23} J/K), and f_2 the potential at distance r+d from the MPC center with respect to the bulk solution. The far right hand term is the classical expression of diffuse layer capacitance for a planar electrode surface,[10b] and has been converted to an area-dependent value by including the *outer sphere* area of the MPC, to semi-quantitatively represent the MPC diffuse layer capacitance $C_{DIFFUSE}$. That to the left of it represents the compact layer capacitance, $C_{COMPACT}$ (aF/nanoparticle), and is derived from a concentric sphere relation used previously[12] to represent the MPC capacitance at large supporting electrolyte concentration. Equation (2) is analogous to early computations of double layer diffuse capacitance phenomenon for spherical colloidal particles.[13] However, the Debye length (compact plus diffuse double layer thickness) around the MPC, given its extremely small 0.55 nm core radius is expected to be somewhat compressed. Note that equation (2) contains electrolyte concentration dependent term n°, f_2, temperature dependent terms ε_{MONO}, ε_{SOLV}, T, f_2 and solvent dependent term ε_{SOLV}.

Weaver *et al.*[14] studied the sequential electron-transfer energetics for solution-phase metallic clusters such as fullerenes, Pt carbonyl clusters with simple electrostatic treatment and provided a useful expression for the potential spacing between successive one-electron transfers:

$$\Delta V = (e/4\pi\varepsilon_0 \varepsilon_{SOLV} r)[1+ (r/d_s)]^{-1} \quad (3)$$

where ΔV is the peak (potential) spacing, e is the electron charge, ε_0, ε_{SOLV} have the same meaning as above, r is the cluster core radius and d_s is the Debye screening length which denotes the distance over which the charge on the central (cluster) ion is screened by the surrounding electrolyte ions. Equation (3) can be rewritten as

$$\Delta V = (14.4 \text{ V}/\varepsilon_{SOLV} r)[1+ (r/d_s)]^{-1} \quad (4)$$

where r and d_s are given in angstroms. Weaver coined the term "molecular capacitance" and provided the expression:

$$C_s = 4p\varepsilon_0 \varepsilon_{SOLV} r/d_s (r + d_s) \quad (5)$$

where C_s is the "molecular capacitance", the rest of the symbols have the same meaning as above. Equation (5) can be directly deduced from equation (3) using $e/\Delta V$.

The metal clusters they studied[14] are similar to our $Au_{38}(SC2Ph)_{24}$ nanoparticles except that the nanoparticles have a phenylethanethiolate monolayer in between the gold core and the solvent. In order to account for the combined dielectric contributions from the PhC2S-monolayer and the solvent in our study, an effective dielectric constant, $\varepsilon_{effective}$, is used and equation (4) and (5) are then expressed as:

$$\Delta V = (14.4 \text{ V}/\varepsilon_{effective} r)[1+ (r/d_s)]^{-1} \quad (6)$$

$$C_{effective} = 4p\varepsilon_0 \varepsilon_{effective} r/d_s (r + d_s) \quad (7)$$

respectively, where $C_{effective}$ is the "effective molecular capacitance". Both $\varepsilon_{effective}$ and d_s are electrolyte concentration, temperature and solvent dependent.

Both classical double layer theory and the concept of "molecular capacitance" can qualitatively account for the observed electrolyte concentration, temperature and solvent dependent behavior of the potential spacing, i.e., the capacitance (calculated by $e/\Delta V$) between the two continuous peaks beside the band gap of $Au_{38}(SC2Ph)_{24}$. In this chapter, we seek better understanding of this phenomena using the above two theories. Finally, the diffusion coefficient of $Au_{38}(SC2Ph)_{24}$ in CH_2Cl_2 was measured with different electrochemical methods.

3.2 EXPERIMENTAL SECTION

3.2.1 Chemicals. $HAuCl_4 \bullet 3H_2O$ was synthesized according to literature procedures. Tetraoctylammonium bromide (Aldrich), 1,2-dichloroethane (Aldrich), phenylethanethiol (PhC2SH, Sigma), sodium borohydride (ACROS), tetrahydrofuran (THF, ACROS), n-butylbenzene (ACROS), dichloromethane (Fisher), acetonitrile (Fisher), hexane (Fisher), toluene (Fisher), acetone (Fisher), absolute ethanol (AAPER), tetrabutylammonium perchlorate (Bu_4NClO_4, Fluka) were used as received. Water was purified with a Barnstead NANOpure system.

3.2.2 Synthesis of $Au_{38}(SC2Ph)_{24}$. Phenylethanethiolate-coated MPCs were prepared according to the Brust reaction, [15] using a thiol:$AuCl_4^-$ mole ratio of 3:1 in toluene, adding the $NaBH_4$ reducing agent at 0°C and maintaining this temperature with an ice water bath and stirring for 20 hours. The MPC-containing organic layer was placed in a rotary evaporator and the toluene solvent was removed under vacuum with no added heat. The crude MPC products were then covered with absolute ethanol overnight. This mixture was

poured through a medium-porosity glass frit and the products on the frit were collected and washed with excess ethanol. The acetonitrile soluble portion of these products was then isolated and purified by dissolving in a minimal amount of dichloromethane and then precipitated with ethanol. The final product had an estimated composition of $Au_{38}(SC2Ph)_{24}$ based on elemental analysis and thermogravimetric analysis. The core diameter of $Au_{38}(SC2Ph)_{24}$, measured using TEM is about 1.1 nm and the PhC2S- chain length is about 0.68 nm.[12b]

3.2.3 Electrochemical Measurements. Osteryoung square wave voltammetry (OSWV), differential pulse voltammetry (DPV), microelectrode voltammetry, rotating disk electrode voltammetry (RDE) were performed using a Bioanalytical Systems (BAS) 100B electrochemical analyzers. The 1.6 mm Pt working electrode was polished, rinsed and sonicated in NANOpure water, rinsed with absolute ethanol and acetone, cleaned by potential-cycling in 0.5 M H_2SO_4 for 15 min and used in OSWV and DPV measurements. A 9 μm-diameter Pt microelectrode was polished and then sonicated in NANOpure water and used in microelectrode voltammetry mearurements. A 3-mm diameter Au working electrode coated with a mercaptoundecanoic acid (MUA) self-assembled monolayer (SAM) was used in the RDE and OSWV measurements of the diffusion coefficient of $Au_{38}(SC2Ph)_{24}$ in CH_2Cl_2 at 283 K. The MUA layer is used to depress the background currents. A Pt coil counter electrode and Ag wire quasi-reference electrode were used in the experiments. Reduced temperature experiments were performed using cold acetone/dry ice bath.

3.3 RESULTS AND DISCUSSION

3.3.1 Effect of Supporting Electrolyte (Bu_4NClO_4) Concentration on the Capacitance at +1/0 to +2/+1 Core Charge State Change of $Au_{38}(SC2Ph)_{24}$. Figure 3.1(a) shows the

Osteryoung square wave voltammogram (OSWV) of 0.14 mM $Au_{38}(SC2Ph)_{24}$ in CH_2Cl_2 with 0.1 M Bu_4NClO_4 at 283 K. The electrochemical band gap of ~ 1.67 V in the negative potential window corresponds to a HOMO-LUMO band gap plus charging energy which represents the molecular behavior of the Au_{38} core.[2d, 6, 16,18] To the left of the band gap, there is a doublet of oxidation peaks (core charge states are indicated in the figure) and the peak spacing between the +1/0 and +2/+1 core charge states is ~ 300 mV. At more positive potentials, there is another gap of ~ 0.75 V in between +2 and +3 core charge states which is due to a decrease in the density of electronic states (DOS) distribution. It is evident that the discretization and spacing of electronic levels of the Au_{38} core are qualitatively different from those of Au_{140} nanoparticles.[2d] Influences of HOMO-LUMO gap, electronic coupling and ligand-metal or metal-metal interactions[17] result in the uneven voltage spacing of redox state changes for $Au_{38}(SC2Ph)_{24}$ and other multivalent redox molecules.

The focus of this study is the 300 mV peak spacing between +1/0 and +2/+1 core charge states. These two pronounced peaks are electrochemically reversible. Table 3.1 shows the peak spacing ΔV_{+1} and corresponding capacitance of 0.072 mM $Au_{38}(SC2Ph)_{24}$ in CH_2Cl_2 at 283 K with different supporting electrolyte Bu_4NClO_4 concentrations (the electrochemical band gap did not change significantly with Bu_4NClO_4 concentrations). With increase of Bu_4NClO_4 concentration from 0.8 mM to 100.3 mM, the peak spacing ΔV_{+1} decreased from 375 mV to 310 mV corresponding to a capacitance C_{MPC+1} (calculated from $e/\Delta V_{+1}$) increase from 0.427 aF to 0.516 aF, a 21% increase. At 100.3 mM electrolyte concentration, for $C_{MPC+1} \approx C_{compact+1} = 4\pi\varepsilon_{PhC2S}\varepsilon_0 r(r+d)/d$ based on concentric sphere model[18], where r is the Au_{38} core radius 0.55 nm, d is the PhC2S- chain

Figure 3.1. Osteryoung square wave voltammogram (OSWV) of 0.14 mM $Au_{38}(SC2Ph)_{24}$ in CH_2Cl_2 with 0.1 M Bu_4NClO_4 at (a) 283 K; (b) 241K.

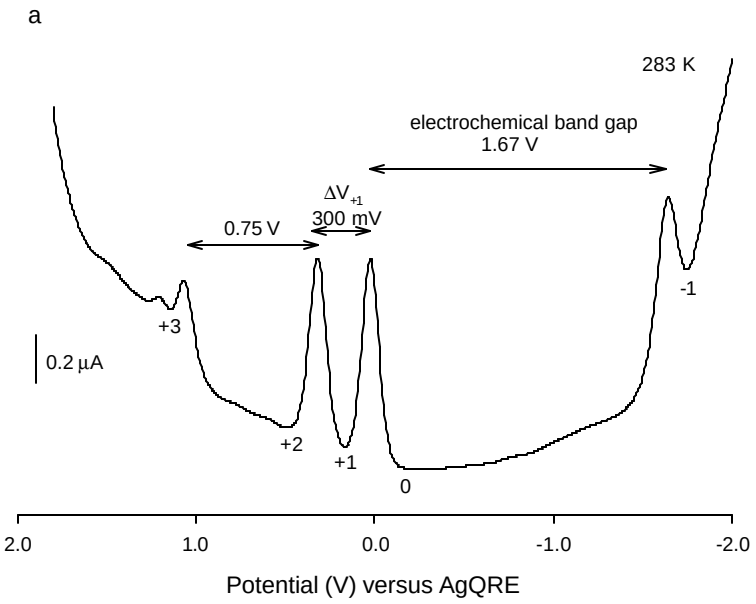
a
283 K
electrochemical band gap
1.67 V
ΔV+1
300 mV
0.75 V
+3
-1
0.2 μA
+2
+1
0
2.0
1.0
0.0
-1.0
-2.0
Potential (V) versus AgQRE

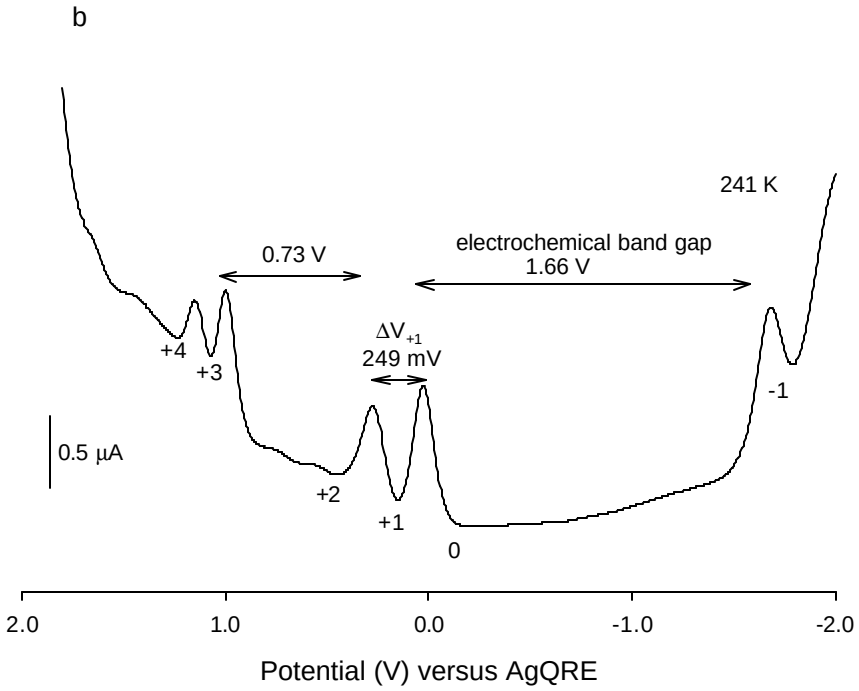
b
241 K
0.73 V
electrochemical band gap
1.66 V
ΔV+1
249 mV
+4
+3
-1
0.5 μA
+2
+1
0
2.0
1.0
0.0
-1.0
-2.0
Potential (V) versus AgQRE

Table 3.1 Peak spacing ΔV_{+1} and corresponding capacitance C_{MPC+1} at +1 core charge state of 0.072 mM $Au_{38}(SC2Ph)_{24}$ in CH_2Cl_2 at 283 K with different supporting electrolyte Bu_4NClO_4 concentrations.

Bu_4NClO_4 (mM)	0.8	3.2	7.0	10.8	25.7	50.4	100.3
Peak spacing ΔV_{+1} (mV)[a]	375	360	346	338	326	318	310
Capacitance C_{MPC+1} (aF)[b]	0.427	0.444	0.462	0.474	0.491	0.503	0.516

[a] Average peak spacing of forward and reverse OSWV scan. [b] Calculated from $e/\Delta V_{+1}$.

length (0.68 nm, equivalent to the plane of closest approach of electrolyte ions to the MPC surface), and ε_{PhC2S-} is the dielectric constant of PhC2S- monolayer, the calculated ε_{PhC2S-} is about 4.7. Chen *et al.*[12b] used 4.0 as the dielectric constant in a PhC2SAu QDL capacitance calculation where the gold core radius was 1.1 nm—twice as large as the Au_{38} core radius here. Considering the smaller gold core and larger core polarity, it is reasonable that a larger dielectric constant for PhC2S- monolayer is obtained.

Classical double layer theory, equation (2), predicts an increase of capacitance with an increase of supporting electrolyte concentration at a constant temperature, owing to the diffuse layer component. Following a similar numerical simulation method to that applied for $Au_{140}(SC6)_{53}$[9], we obtained the Z_{MPC} versus ϕ_2 plot, Figure 3.2, where ϕ_2 in Table 3.2 is the potential at the edge of the monolayer (outer Helmoltz plane) with respect to the bulk solution when the core is at +1 charge state. The differential diffuse layer capacitance $C_{DIFFUSE}$ can be expressed as[10(f)]:

$$C_{DIFFUSE}\ (F/m^2) = d\sigma/d\phi_2 \qquad (8)$$

Where σ is the charge density of the outersphere of the nanoparticle and equal to $Z_{MPC}/4\pi(r+d)^2$, and ϕ_2 has its usual meaning. The total diffuse layer capacitance of the nanoparticle $C_{DIFFUSE}$ (F/MPC) is then equal to $C_{DIFFUSE}\ (F/m^2) \times 4\pi(r+d)^2$, thus equal to $dZ_{MPC}/d\phi_2$. Figure 3.2 shows the Z_{MPC} versus ϕ_2 plot of 0.072 mM $Au_{38}(SC2Ph)_{24}$ in CH_2Cl_2 with 3.2 mM Bu_4NClO_4 at 283K. From this plot, we can obtain the MPC diffuse layer capacitance from the slope of the tangent line at +1 core charge state. Values of $C_{DIFFUSE+1}$ thus calculated for different electrolyte concentrations are given in Table 3.2. These predicted values (Table 3.2) are combined with experimental C_{MPC+1} values

Figure 3.2. Calculated Z_{MPC} versus ϕ_2 plot of 0.14 mM $Au_{38}(SC2Ph)_{24}$ in 5 ml CH_2Cl_2 with 3.2 mM Bu_4NClO_4 at 283 K.

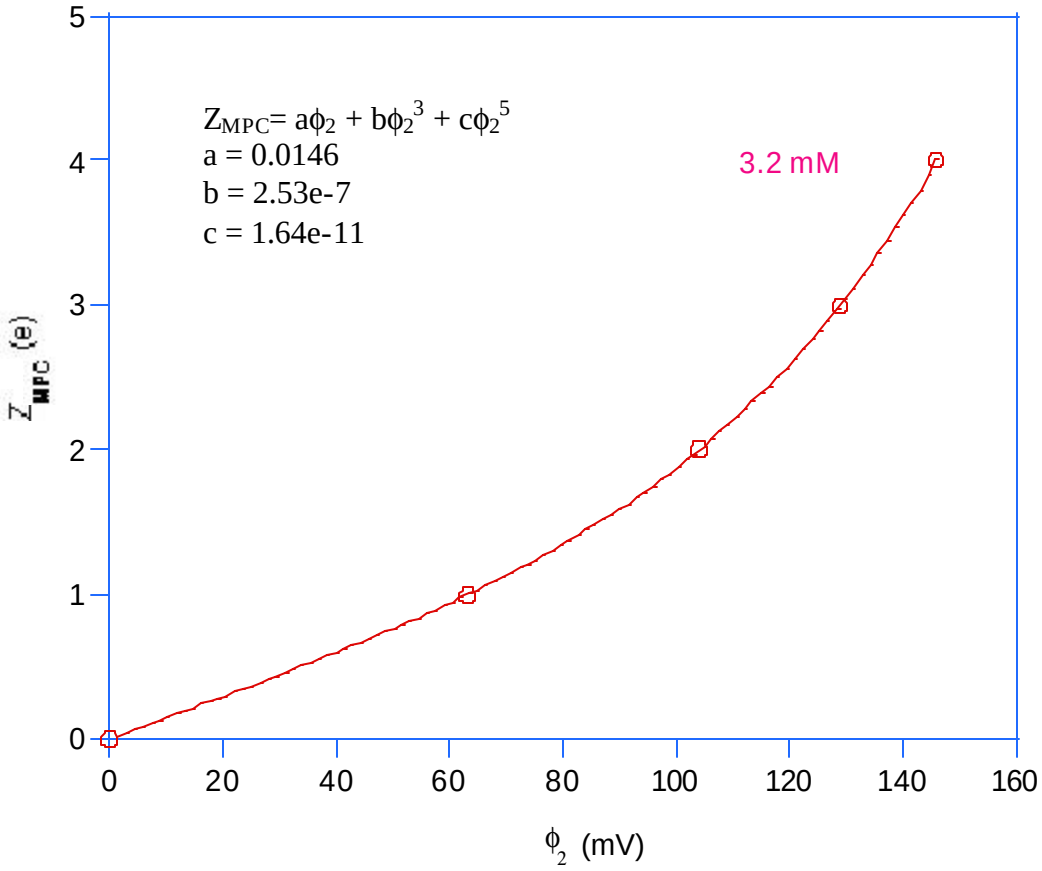
$Z_{MPC}= a\phi_2 + b\phi_2^3 + c\phi_2^5$
a = 0.0146
b = 2.53e-7
c = 1.64e-11
3.2 mM
Z_{MPC} (e)
ϕ_2 (mV)
0
1
2
3
4
5
0
20
40
60
80
100
120
140
160

Table 3.2 Calculated ϕ_2, $C_{DIFFUSE+1}$, $C_{COMPACT+1}$ of 0.072 mM $Au_{38}(SC2Ph)_{24}$ at +1 core charge state in CH_2Cl_2 at 283 K with different Bu_4NClO_4 concentrations.

Bu_4NClO_4 (mM)	ϕ_2 (mV)	ΔV_{+1} (mV)	C_{MPC+1} (aF)	$C_{DIFFUSE+1}$ (aF)	$C_{COMPACT+1}$ (aF)
0.8	88.6	375	0.427	2.186	**0.53**
3.2	69.7	360	0.444	2.784	**0.53**
7.0	58.6	346	0.462	3.248	**0.54**
10.8	52.9	338	0.473	3.552	**0.55**
25.7	41.3	326	0.491	4.368	**0.55**
50.4	33.0	318	0.503	5.248	**0.56**
100.3	25.7	310	0.516	6.752	**0.56**

(Table 3.1) to produce (Eqn. 1) values of $C_{COMPACT+1}$ given in Table 3.2. $C_{COMPACT+1}$ does not change much, varying from 0.53 aF (0.8 mM Bu_4NClO_4) to 0.56 aF (100.3 mM), a 2% difference for the overall concentration range of Bu_4NClO_4, indicating the combination of classical double layer treatment with numerical simulation for the particular +1 core charge state is quite satisfactory.

Based on simple electrostatic treatment, equation (6) and (7) also predict the electrolyte concentration dependent peak spacing and "effective molecular capacitance" at +1 core charge state. Table 3.3 shows the diffuse layer thickness $1/\kappa$, Debye length d_s, peak spacing ΔV_{+1}, $\varepsilon_{effective}$ and $C_{effective}$ values of 0.072 mM $Au_{38}(SC2Ph)_{24}$ at +1 core charge state in CH_2Cl_2 with different supporting electrolyte Bu_4NClO_4 concentrations at 283 K. The diffuse layer thickness is estimated using the equation $1/\kappa = (\varepsilon_{CH2Cl2}\varepsilon_0 kT/2n^0Z^2e^2)^{1/2}$ [10c] which is for planar electrode surface. The Debye length d_s is taken as the summation of PhC2S- monolayer thickness and diffuse layer thickness. Peak spacing ΔV_{+1} values are measured experimentally, $\varepsilon_{effective}$ values are calculated from equation (6) and $C_{effective}$ is calculated either from equation (7) or e/?V_{+1}. The increase of Bu_4NClO_4 concentration from 0.8 mM to 100.3 mM results in a decrease of the estimated diffuse layer thickness $1/\kappa$ from 35.1 Å to 3.2 Å and the Debye length d_s decreases from 41.9 Å to 10.0 Å. The calculated $\varepsilon_{effective}$ values from equation (6) decreased from 6.2 to 5.4. $C_{effective}$ actually has the same values as C_{MPC+1} because they are both equal to e/?V_{+1}.

$\varepsilon_{effective}$ is used to account for the dielectric contribution from both the PhC2S- monolayer (ε_{PhC2S-} ~ 4.7 at 283K) and CH_2Cl_2 (ε_{CH2Cl2} ~ 9.3 at 283K). As expected, all the

Table 3.3 Diffuse layer thickness $1/\kappa$, Debye length d_s, peak spacing , ΔV_{+1}, effective dielectric constant $\varepsilon_{effective}$ and effective molecular capacitance $C_{effective}$ at +1 core charge state of 0.072 mM $Au_{38}(SC2Ph)_{24}$ in CH_2Cl_2 with different supporting electrolyte Bu_4NClO_4 concentrations at 283 K. d_{SC2Ph} = 6.8 Å , core radius r = 5.5 Å.

Bu_4NClO_4 (mM)	0.8	3.2	7.0	10.8	25.7	50.4	100.3
$1/\kappa$ (Å)	35.1	17.8	12.0	9.7	6.3	4.5	3.2
d_s (Å) [b]	41.9	24.6	18.8	16.5	13.1	11.3	10.0
Peak spacing ΔV_{+1} (V) [c]	0.375	0.360	0.346	0.338	0.326	0.318	0.310
$\varepsilon_{effective}$ [d]	6.2	5.9	5.9	5.8	5.7	5.5	5.4
$C_{effective}$ (aF) [e]	0.43	0.44	0.46	0.47	0.49	0.50	0.52

[a] Calculated from $1/\kappa = (\varepsilon_{CH2Cl2}\varepsilon_0 kT/2n^0Z^2e^2)^{1/2}$ [10c]. [b] Taken as the summation of monolayer thickness and diffuse layer thickness. [c] Average peak spacing of forward and OSWV scan. [d] Calculated from equation (6). [e] Calculated either from equation (7) or $e/\Delta V_{+1}$.

$\varepsilon_{effective}$ values fall in between ε_{PhC2S-} and ε_{CH2Cl2}. At high Bu_4NClO_4 concentration (100.3 mM), $\varepsilon_{effective}$ = 5.4 is close to ε_{PhC2S-} suggesting that $\varepsilon_{effective}$ mainly comes from the dielectric contribution of PhC2S- monolayer. With the decrease of Bu_4NClO_4 concentration from 100.3 mM to 0.8 mM, the $\varepsilon_{effective}$ value increased from 5.4 to 6.2 suggesting an increased dielectric contribution from the solvent (CH_2Cl_2), however, the PhC2S- monolayer still contributed more than that of the solvent. The change of $\varepsilon_{effective}$ values with Bu_4NClO_4 concentration is further illustrated in Figure 3.3 which shows that $\varepsilon_{effective}$ does not change linearly with the Bu_4NClO_4 concentration, but increases more sharply at low electrolyte concentrations than at high electrolyte concentrations. In the context of equation 2, this is because the increase of diffuse layer thickness is more pronounced at low electrolyte concentrations thus making the dielectric contribution of the solvent more pronounced.

The above discussions show that by picking suitable $\varepsilon_{effective}$ and d_s values, equation (6), based on a simple electrostatic treatment, can also be used to interpret the electrolyte concentration dependent behavior of the peak spacing at +1 core charge state. The accuracy of $\varepsilon_{effective}$ values is determined by the reliability of d_s values. The "effective molecular capacitance" $C_{effective}$ is equal to the QDL capacitance at +1 core charge state C_{MPC+1}. The form of "effective molecular capacitance" shown in equation (7) is analogous to the MPC's compact layer capacitance $C_{compact}$ --- the only difference is that it uses $\varepsilon_{effective}$ and d_s instead of ε_{PhC2S-} and d_{PhC2S-} to account for the capacitance contribution from the combined compact (PhC2S- monolayer) and diffuse layer components.

3.3.2 Effect of Solvent Temperature on the Capacitance at +1 Core Charge State of $Au_{38}(SC2Ph)_{24}$. Figure 3.1(b) shows the OSWV of 0.14 mM $Au_{38}(SC2Ph)_{24}$ in CH_2Cl_2 with

Figure 3.3 $e_{effective}$ versus [Bu_4NClO_4] plot of 0.072 mM $Au_{38}(SC2Ph)_{24}$ in CH_2Cl_2 at 283K. [Bu_4NClO_4] is Bu_4NClO_4 concentration in mM. $e_{effective}$ is calculated from equation (6).

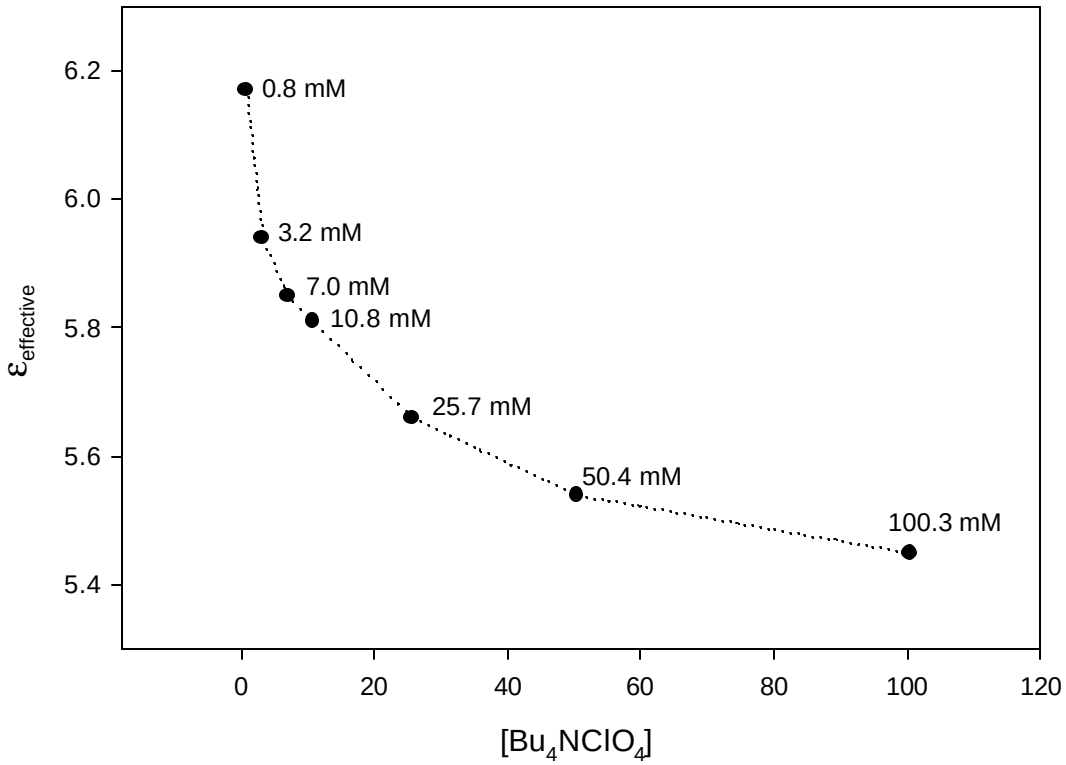
6.2
6.0
5.8
5.6
5.4
$\varepsilon_{effective}$
0.8 mM
3.2 mM
7.0 mM
10.8 mM
25.7 mM
50.4 mM
100.3 mM
0
20
40
60
80
100
120
[Bu_4NClO_4]

0.1 M Bu_4NClO_4 at 241 K. Compared to Figure 3.1(a), ΔV_{+1} decreased from 300 mV to 249 mV while the electrochemical band gap[18] and the left ~ 730 mV "gap" did not change significantly with temperature. The peaks of +3 and +4 oxidation states are better defined than those at 283 K due to better background current suppression at lower temperature and possibly greater chemical stability. Table 3.4 shows the peak spacing ΔV_{+1} and corresponding capacitance C_{MPC+1} (calculated from $e/\Delta V_{+1}$) at the +1 core charge state of 0.043 mM $Au_{38}(SC2Ph)_{24}$ in CH_2Cl_2 at different temperatures with (I) 5.2 mM and (II) 100.3 mM Bu_4NClO_4 present respectively. The decrease of solvent temperature from 278 K to 228 K results in the peak spacing decrease from 352 mV (303 mV) to 262 mV (232 mV), a decrease of ~ 26% (23%). The corresponding capacitance increased from 0.455 aF (0.528 aF) to 0.611 aF (0.690 aF), an increase of ~ 34% (31%).

Equation (2) based on classical double layer theory predicts a capacitance increase with decreasing solvent temperature. The diffuse layer capacitance term in equation (2) contains an explicit $T^{1/2}$ term, predicting an increase of MPC capacitance with lowered temperature. Concurrent with this is an increase in ε_{MONO} and e_{SOLV} when the temperature decreases. Changes in the $\cosh(Ze\phi_2/2KT)$ term with temperature are very small due to the offset by the temperature dependent ϕ_2 term. Figure 3.4 shows the $1/C_{MPC+1}$ versus $(T/e_{CH2Cl2})^{1/2}$ plot of 0.043 mM $Au_{38}(SC2Ph)_{24}$ in CH_2Cl_2 at different temperatures from 278 K to 228 K with 5.2 mM and 100.3 mM Bu_4NClO_4 present respectively. Linear regressions of these two sets of data points gave slopes of 0.574 and 0.458 respectively. Examining the diffuse layer capacitance term in equation (2), the predicted slope ratio of plot (I)/(II) is determined by the ratio of $1/[n_0^{1/2}\cosh(Ze\phi_2/2KT)]$ for 5.2 mM and 100.3 mM Bu_4NClO_4, respectively. The calculated $\cosh(Ze\phi_2/2KT)$ values are 3.06 and 1.20 for 5.2 mM and 100.3 mM Bu_4NClO_4,

Figure 3.4 $1/C_{MPC+1}$ versus $(T/e_{CH2Cl2})^{1/2}$ plot of 0.043 mM $Au_{38}(SC2Ph)_{24}$ in CH_2Cl_2 at different temperatures from 278 K down to 228 K with 5.2 mM and 100.3 mM Bu_4NClO_4 respectively. The data points are fitted with linear regression and the coefficients are indicated in the figure. The temperature-dependent e_{CH2Cl2} values are estimated from temperature-dependent, high pressure data (ref19(a), atmospheric pressure data are not available), following ref19(b) by extrapolating the 300-400 K results to lower temperatures according to the equation $e_{CH2Cl2} = 31\exp(-0.0041T)$, empirically fitted to a plot of the e_{CH2Cl2} data versus temperature.

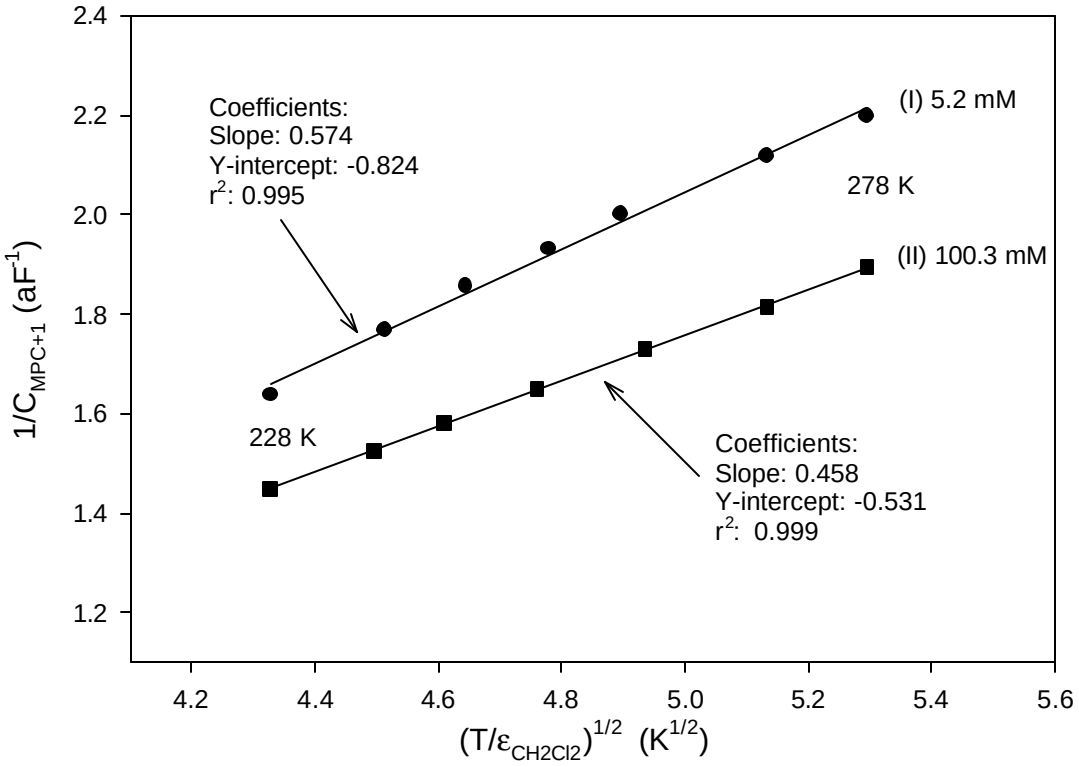
Coefficients:
Slope: 0.574
Y-intercept: -0.824
r2: 0.995
(I) 5.2 mM
278 K
(II) 100.3 mM
228 K
Coefficients:
Slope: 0.458
Y-intercept: -0.531
r2: 0.999
1/CMPC+1 (aF-1)
(T/εCH2Cl2)1/2 (K1/2)
2.4
2.2
2.0
1.8
1.6
1.4
1.2
4.2
4.4
4.6
4.8
5.0
5.2
5.4
5.6

Table 3.4 Peak spacing ΔV_{+1} and corresponding capacitance C_{MPC+1} at +1 core charge state of 0.043 mM $Au_{38}(SC2Ph)_{24}$ in CH_2Cl_2 at different temperatures with Bu_4NClO_4 concentration (I) 5.2 mM, and (II) 100.3 mM.

(I) 5.2 mM Bu_4NClO_4

T (K)	228	238	245	252	258	270	278
Peak spacing ΔV_{+1} (mV)[a]	262	283	297	309	320	339	352
Capacitance C_{MPC+1} (aF)[b]	0.611	0.565	0.539	0.518	0.500	0.472	0.455

(II) 100.3 mM Bu_4NClO_4

T (K)	228	237	243	251	260	270	278
Peak spacing ΔV_{+1} (mV)[a]	232	244	253	264	277	289	303
Capacitance C_{MPC+1} (aF)[b]	0.690	0.656	0.632	0.606	0.578	0.554	0.528

[a] Average peak spacing of forward and reverse OSWV scan. [b] Calculated from $e/\Delta V_{+1}$.

respectively, (the cosh($Ze\phi_2/2KT$) term does not change significantly with temperature as mentioned above). The predicted slope ratio of plot (I)/(II)is 1.72 ($[(100)^{1/2} \times 1.2] / (5.2)^{1/2} \times 3.06]$) which is close to the experimental slope ratio of plot (I)/(II) = 0.574/0.458 = 1.25. This result suggests the effectiveness of equation (2) as a semi-quantitative expression for MPC capacitance. If we carefully examine the data collected in 5.2 mM Bu_4NClO_4 or plot (I), we can see a small curvature especially at lower temperatures which is caused by the temperature dependent e_{PhC2S-} and thus $C_{COMPACT}$ value. This suggests the Y-intercept in this plot is not exactly equal to 1/ $C_{COMPACT}$ because it varies with temperature. Ideally, larger curvature in data points of 100.3 mM Bu_4NClO_4 case or plot (II) should be observed because, at large electrolyte concentration, the temperature dependent 1/ $C_{COMPACT}$ value should have larger effect on the curvature of plot (II). However its linear coefficient 0.999 is very close to unity which is because n^0, the fully dissociated electrolyte ion concentration, decreases when the temperature decreases thus effectively linearizes the line. Indeed, at temperatures lower than 228K, the solvent became turbid because of the precipitated Bu_4NClO_4.

Equation (6) or (7) also shows that ?V or $C_{effective}$ is temperature dependent. Because both ε_{CH2Cl2} and ε_{PhC2S-} will increase with decreasing temperature, changes of $1/\kappa$ (estimated from $1/\kappa = (\varepsilon_{CH2Cl2}\varepsilon_0 kT/2n^0Z^2e^2)^{1/2}$) with temperature are offset by the temperature dependent ε_{CH2Cl2}, thus d_s does not change significantly with temperature. However, $e_{effective}$ can vary with temperature considerably. Table 3.5 shows the peak spacing ΔV_{+1}, effective dielectric constant $\varepsilon_{effective}$ and effective molecular capacitance $C_{effective}$ at +1 core charge state of 0.043 mM $Au_{38}(SC2Ph)_{24}$ in CH_2Cl_2 at different temperatures with Bu_4NClO_4 concentration (I) 5.2 mM , and (II) 100.3 mM. At 5.2 mM (100.3 mM) Bu_4NClO_4 , the

Table 3.5 Peak spacing ΔV_{+1}, effective dielectric constant $\varepsilon_{effective}$ and effective molecular capacitance $C_{effective}$ at +1 core charge state of 0.043 mM $Au_{38}(SC2Ph)_{24}$ in CH_2Cl_2 at different temperatures with Bu_4NClO_4 concentration (I) 5.2 mM , (II) 100.3 mM.

(I) 5.2 mM Bu_4NClO_4 : $1/\kappa = 14.5$ Å, $d_s = d_{PhC2S}+1/\kappa = 6.8+14.5 = 21.3$ Å

T (K)	228	238	245	252	258	270	278
Peak spacing ΔV_{+1} (V)[a]	0.262	0.283	0.297	0.309	0.320	0.339	0.352
$\varepsilon_{effective}$[b]	7.9	7.4	7.0	6.7	6.5	6.1	5.9
$C_{effective}$ (aF)[c]	0.61	0.57	0.54	0.52	0.50	0.47	0.46

(II) 100.3 mM Bu_4NClO_4 : $1/\kappa = 3.3$ Å, $d_s = d_{PhC2S}+1/\kappa = 6.8+3.3 = 10.1$ Å

T (K)	228	237	243	251	260	270	278
Peak spacing ΔV_{+1} (V)[a]	0.232	0.244	0.253	0.264	0.277	0.289	0.303
$\varepsilon_{effective}$[b]	7.3	6.9	6.7	6.4	6.1	5.9	5.6
$C_{effective}$ (aF)[c]	0.69	0.66	0.63	0.61	0.58	0.55	0.53

[a] Average peak spacing of forward and reverse OSWV scan. [b] Calculated from equation (6). [c] Calculated from equation (7) or $e/\Delta V_{+1}$.

$e_{effective}$ value increased from 5.9 (5.6) to 7.9 (7.3) when the temperature decreased from 278 K to 228 K, an increase of ~ 34% (31%). For CH_2Cl_2, the estimated e_{CH2Cl2} increased from 9.9 to 12.2 (estimated by $e_{CH2Cl2}=31\exp(-0.0041T)$[19]) when the temperature decreased from 278 K to 228 K, an increase of ~ 23%. The change of e_{PhC2S-} with temperature is unknown. Using the data in Table 3.5, plots of $\ln(e_{effective})$ versus solvent temperature were made as indicated in Figure 3.5 and the data points are fitted with a linear regression. The slopes are -0.0058 and -0.0053 for plot (I) and (II) respectively. Because $C_{effective} = C_{MPC+1} = e/?V_{+1}$, for (II) 100.3 mM Bu_4NClO_4 case, from equation (7), we have:

$$\frac{d\ln(C_{MPC+1})}{dT} = \frac{d\ln(C_{effective})}{dT} = \frac{d\ln(e_{effective})}{dT} = Slope(II) = -0.0053\ K^{-1}.$$

The temperature dependence of the capacitance of alkanethiolate monolayers on planar Au surfaces[20] was reported to be $d\ln(C_{SAM})/dT \sim -0.001\ K^{-1}$ at large electrolyte concentration. Miles *et al.*[11] studied the temperature dependent QDL capacitance of $Au_{140}(SC6)_{53}$ and found $d\ln(C_{MPC})/dT \sim -0.0025\ K^{-1}$ in 0.1M Bu_4NClO_4/CH_2Cl_2. The difference between our value -0.0053 K^{-1} and former ones might be due to (i) the dielectric constants of phenylethanethiolate and alkanethiolate monolayer are different and their extent of temperature dependence may be different too; (ii) even for the same monolayer, its dielectric constant may vary when it is coated on Au surfaces of different curvature such as planar surface, Au_{140} core or the Au_{38} core because of their different polarity; (iii) the larger the curvature, the larger contribution from the diffuse layer at the same electrolyte concentration thus the larger temperature effect on the MPC capacitance. All these effects may lead to the larger $d\ln(C_{MPC})/dT$ value for $Au_{38}(SC2Ph)_{24}$.

Finally, the temperature dependence of the width of the DPV charging peaks was

Figure 3.5 $\ln(e_{effective})$ versus solvent temperature plots of 0.043 mM $Au_{38}(SC2Ph)_{24}$ in CH_2Cl_2 at different temperatures from 278 K down to 228 K at (I) 5.2 mM, (II) 100.3 mM Bu_4NClO_4 respectively. The data points are fitted with linear regression and the coefficients are indicated in the figure. $e_{effective}$ values are taken from Table 3.5. Regression line equations are $e_{effective}$= 29.3 exp(-0.0058T) for plot (I) and $e_{effective}$= 24.2 exp(-0.0053T) for plot (II) respectively.

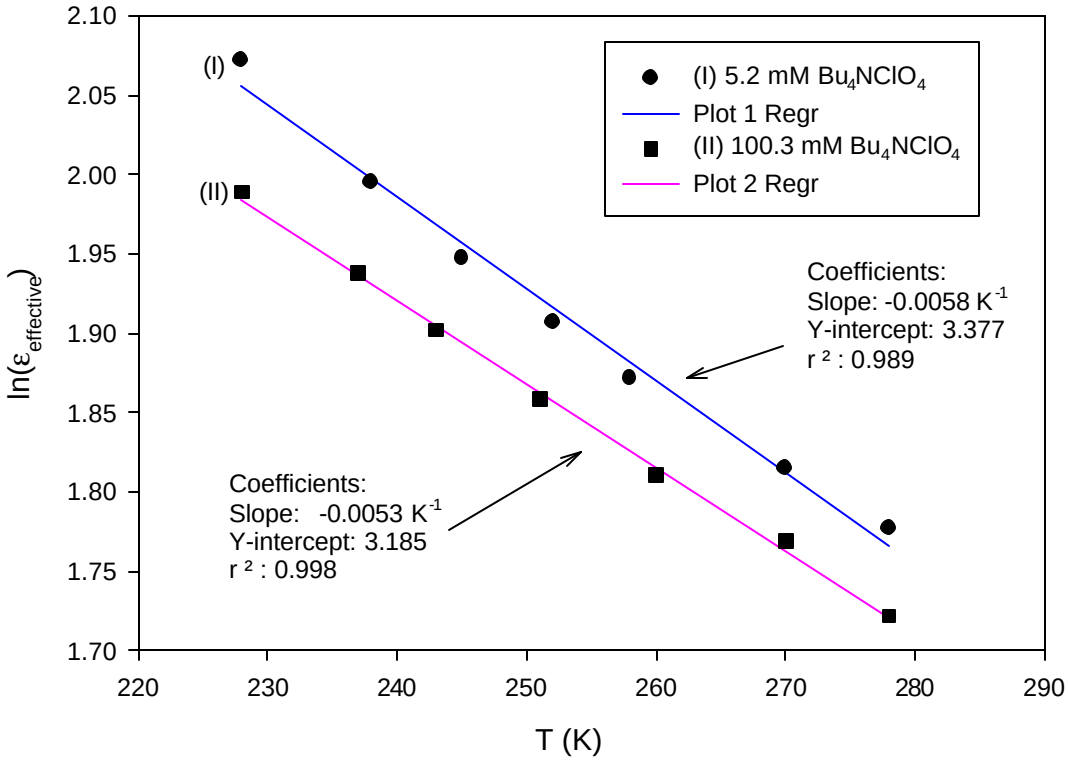
2.10
2.05
2.00
1.95
1.90
1.85
1.80
1.75
1.70
220
230
240
250
260
270
280
290
T (K)
ln(ε effective)
(I)
(II)
(I) 5.2 mM Bu4NClO4
Plot 1 Regr
(II) 100.3 mM Bu4NClO4
Plot 2 Regr
Coefficients:
Slope: -0.0058 K-1
Y-intercept: 3.377
r ² : 0.989
Coefficients:
Slope: -0.0053 K-1
Y-intercept: 3.185
r ² : 0.998

studied. Their full-width at one-half maximum, $W_{1/2}$, should decrease with temperature according to

$$W_{1/2} = 3.52\ RT/F \qquad (8)$$

where R is the gas constant and F the Faraday constant. The broadening is essentially a Boltzmann energy effect. The limiting values (pulse amplitude of DPV is 0 mV) of $W_{1/2}$ is 83, 77, 72, 68 and 63 mV at 275, 253, 238, 223, 209 K respectively. The pulse amplitude used in these experiments is 20 mV thus the measured $W_{1/2}$ values are all 10-13 mV larger than the limiting values. Figure 3.6 shows the plot of $W_{1/2}$ of the first oxidation peak in DPV versus temperature of 0.062 mM $Au_{38}(SC2Ph)_{24}$ in CH_2Cl_2 with 0.1 M Bu_4NClO_4 (the second oxidation peak is asymmetric and was not measured). The data points were then fit with linear regression. Theoretically, this line should pass origin and the Y-intercept is 11.27 mV, close to the theoretical value. The slope is 0.293 mV/K which is remarkably close to the theoretical value 0.303 mV/K (3.52 R/F).

3.3.3 Effect of the Addition of A Second Hydrophobic Solvent to CH_2Cl_2 on the Capacitance at +1 Core Charge State of $Au_{38}(SC2Ph)_{24}$. We have studied the effect of addition of hexane or dodecane to CH_2Cl_2 on the QDL capacitance of $Au_{140}(SC6)_{53}$ at 283 K with large electrolyte concentration.[9] It was observed that the individual peak spacing near the potential of zero charge (E_{PZC}) was greatly enlarged, thus decreasing the individual QDL capacitance (calculated by $e/\Delta V$) considerably. For $Au_{38}(SC2Ph)_{24}$, the same effect was observed. When hexane or n-butylbenzene was added to CH_2Cl_2 (hexane or n-butylbenzene: CH_2Cl_2 = 40%:60% in volume) at 283 K with 0.1 M Bu_4NClO_4, the peak spacing at +1 core charge state increased from 303 mV to ~ 370 mV, an increase of ~23%,

Figure 3.6 Plot of $W_{1/2}$ of the first oxidation peak in DPV versus temperature of 0.062 mM $Au_{38}(SC2Ph)_{24}$ in CH_2Cl_2 with 0.1 M Bu_4NClO_4. The second oxidation peak is asymmetric and was not measured. The pulse amplitude of DPV was 20 mV.

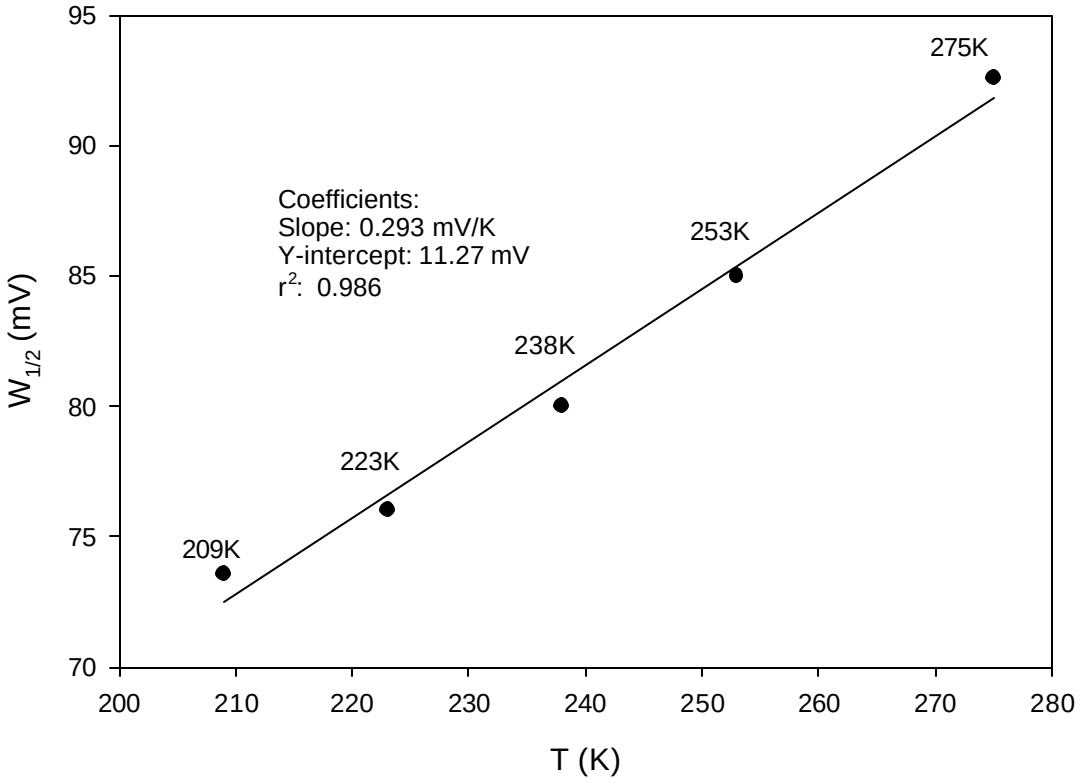
95
90
85
80
75
70
200
210
220
230
240
250
260
270
280
W1/2 (mV)
T (K)
275K
253K
238K
223K
209K
Coefficients:
Slope: 0.293 mV/K
Y-intercept: 11.27 mV
r2: 0.986

see Figure 3.7, while the electrochemical band gap basically remained unchanged with solvent environment[18].

From the point of view of classical double layer theory, at 0.1 M Bu_4NClO_4 concentration, the diffuse layer capacitance can be neglected. Thus the MPC capacitance is governed by the compact layer capacitance. $C_{MPC+1} \approx C_{COMPACT+1} = 4\pi\varepsilon_{PhC2S}\varepsilon_0 r(r+d)/d$[18], where d is compact layer thickness and estimated to be the PhC2S-monolayer length in CH_2Cl_2. When hexane or n-butylbenzene is added to CH_2Cl_2, a hydrophobic layer is created outside MPC's PhC2S-monolayer because these solvents tend to preferentially solvate the MPC's PhC2S-monolayer relative to CH_2Cl_2. This effect should force the ClO_4^- anions (counter ions for +1 core charge state) farther away from the positively charged Au_{38} core making the effective compact layer thickness larger than the PhC2S-monolayer length. This leads to a smaller $C_{compact+1}$ (C_{MPC+1}) and larger peak spacing at +1 core charge state ΔV_{+1}. ε_{PhC2S-} may also be partly affected by the solvent environment. Because ε_{hexane} is about 1.9 at 298 K ($\varepsilon_{n\text{-}butylbenzene}$ ~ 2.4 at 298 K), which is much smaller than ε_{CH2Cl2} (about 8.9 at 298 K), the addition of hexane or n-butylbenzene may reduce the ε_{PhC2S-} value; this also decreases the C_{MPC+1} and thus a larger peak spacing, ΔV_{+1}, was observed.

Equation (6), based on simple electrostatic treatment, also predicts a peak spacing increase with the addition of a second hydrophobic solvent. d_s is increased because a hydrophobic layer is created outside MPC's PhC2S-monolayer. As mentioned above, $\varepsilon_{effective}$ should account for the dielectric contribution from both the PhC2S-monolayer and the solvent although it is mainly determined by ε_{PhC2S-}. The solvent mixture's dielectric constant is less than ε_{CH2Cl2} after the addition of hexane or n-butylbenzene to CH_2Cl_2 which will make $\varepsilon_{effective}$ slightly smaller. Both increased d_s and decreased $\varepsilon_{effective}$ lead to larger peak spacing

Figure 3.7 Osteryoung square wave voltammograms (OSWV) of 0.10 mM $Au_{38}(SC2Ph)_{24}$ with 0.1 M Bu_4NClO_4 at 283 K (a) 100% CH_2Cl_2; (b) 40% hexane + 60 % CH_2Cl_2. The small peak labeled with * near first oxidation peak is due to unknown impurities; the bump at around -0.1 V is due to residual oxygen in the solution.

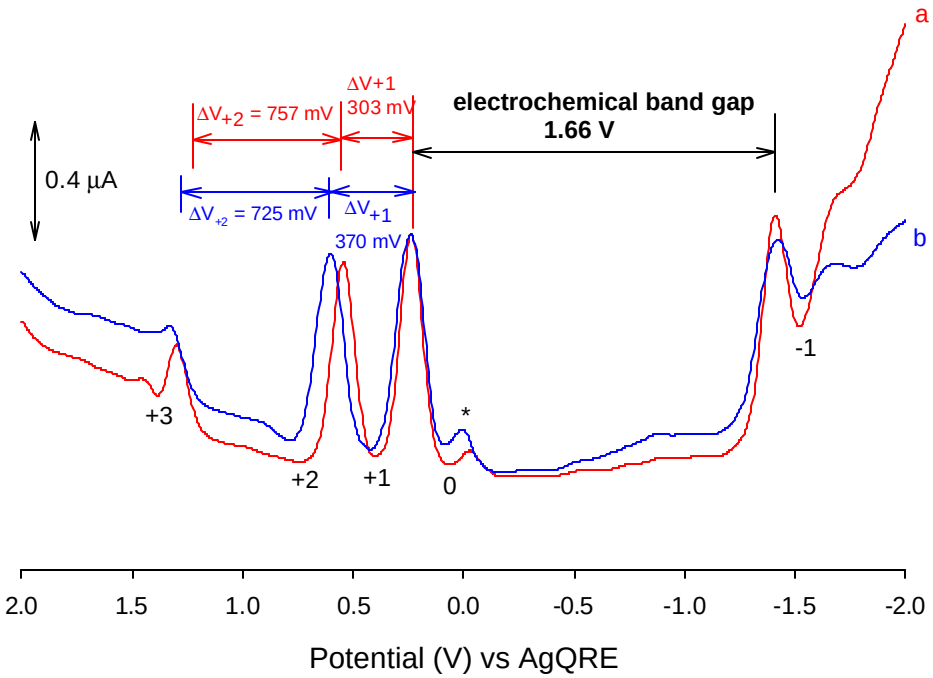
a
b
ΔV+1
303 mV
ΔV+2 = 757 mV
electrochemical band gap
1.66 V
0.4 µA
ΔV+2 = 725 mV
ΔV+1
370 mV
+3
+2
+1
0
*
-1
2.0
1.5
1.0
0.5
0.0
-0.5
-1.0
-1.5
-2.0
Potential (V) vs AgQRE

ΔV_{+1} and smaller $C_{effective}$ value (from equation (7) or $e/\Delta V_{+1}$).

The peak spacing ΔV_{+1} and C_{MPC+1} values in different solvents are summarized in Table 3.6. Tetrahydrofuran (THF, ε_{THF} ~ 7.4 at 298 K) and 1,2-dichloroethane (ε ~ 10.1 at 298 K) were also used as solvents with 0.1 M Bu_4NClO_4 as the supporting electrolyte. In THF, a peak spacing of ~ 360 mV at +1 core charge state was observed and in 1,2-dichloroethane, a peak spacing of ~ 260 mV was observed in contrast to the ~ 303 mV peak spacing observed in CH_2Cl_2 at the same temperature. Because the change of dielectric constant is small (within 1.5 with respect to CH_2Cl_2) among these three solvents, the change of d_s at 0.1 M electrolyte concentration should be very small too. $\varepsilon_{effective}$ is mainly determined by the dielectric contribution from the PhC2S-monolayer and the solvent, thus, the solvent dielectric constant plays a significant role in C_{MPC+1}. Qualitatively, the $\varepsilon_{effective}$ trend in these solvents is $\varepsilon_{effective}$ (THF) < $\varepsilon_{effective}$ (CH_2Cl_2) < $\varepsilon_{effective}$ (CH_2ClCH_2Cl). Examining equation (6), for the same small extent change of d_s and $\varepsilon_{effective}$, the $\varepsilon_{effective}$ change will have more effect on the peak spacing. This may be the main reason that such a large peak spacing change is observed among these three solvents, that is ΔV_{+1} (THF) > ΔV_{+1} (CH_2Cl_2) > ΔV_{+1} (CH_2ClCH_2Cl).

3.3.4 Measurements of the Diffusion Coefficient of $Au_{38}(SC2Ph)_{24}$ in CH_2Cl_2 at 283K.

Microelctrode Voltammetry. The doublet of oxidation peaks of $Au_{38}(SC2Ph)_{24}$ beside the band gap appear in the microelectrode voltammetry as a succession of sigmoidal waves. Figure 3.8 shows the result of 0.072 mM $Au_{38}(SC2Ph)_{24}$ in CH_2Cl_2 with 0.1 M Bu_4NClO_4 electrolyte at 283 K on a 9-μm diameter Pt working electrode. Each wave corresponds to a one-electron reaction between the nanoparticle and the electrode surface. The diffusion coefficient (D) of $Au_{38}(SC2Ph)_{24}$ can be calculated from the average of the two limiting

Table 3.6 Peak spacing ΔV_{+1} and corresponding capacitance C_{MPC+1} at +1 core charge state of 0.043 mM $Au_{38}(SC2Ph)_{24}$ in different solvent environment with 0.1 M Bu_4NClO_4 concentration at 283 K.

Solvent	Dielectric constant (298 K)	Peak spacing ΔV_{+1} (mV)[a]	Capacitance C_{MPC+1} (aF)[b]
100% CH_2Cl_2	8.9	303	0.528
60% CH_2Cl_2 + 40% hexane	< 8.9	370	0.432
60% CH_2Cl_2 + 40% n-butylbenzene	< 8.9	370	0.432
Tetrahydrofuran (THF)	7.4	360	0.444
1,2-dichloroethane	10.1	260	0.615

[a] Average peak spacing of forward and reverse OSWV scan. [b] Calculated from $e/\Delta V_{+1}$.

currents, indicated in the figure, using

$$i_{LIM} = 4nrFDC_{MPC} \quad (9)$$

where r is the electrode radius 4.5 μm, C_{MPC} is the $Au_{38}(SC2Ph)_{24}$ concentration 0.072 mM, n is the number of electron transfer and F the Faraday constant. The average of i_{LIM1} and i_{LIM2}, n = 1 were used and we obtained $D = (3.5 \pm 0.3) \times 10^{-6}$ cm^2/s at 283 K. The D value will be slightly smaller if measured at 278 K according to the Stokes-Einstein equation:

$$D = \frac{k_B T}{2p\,\eta d_H} \quad (10)$$

where η is the viscosity of CH_2Cl_2, d_H is the MPC hydrodynamic diameter. Because η increases with the decrease of temperature, D value is calculated to be 3.18×10^{-6} cm^2/s at 278 K due to smaller T/η value. This D value of $Au_{38}(SC2Ph)_{24}$ is still about 4 times larger than that of $Au_{140}(SC6)_{53}$ measured at 278 K.[11] The reason is mostly likely due to the smaller diameter of $Au_{38}(SC2Ph)_2$ (~ 2.5 nm) than that of $Au_{140}(SC6)_{53}$ (~3.2 nm), thus its d_H is also smaller leading to larger D value. In fact, d_H is calculated to be 3.6 nm for $Au_{38}(SCPh)_{24}$ in CH_2Cl_2 at 278 K while 13.5 nm for $Au_{140}(SC6)_{53}$ in the same solvent and temperature using the D values obtained above and from literature.[11]

Rotating Disk Electrode Voltammetry (RDE.) Rotating disk electrode voltammetry of 0.026 mM $Au_{38}(SC2Ph)_{24}$ in CH_2Cl_2 with 0.1 M Bu_4NClO_4 electrolyte at 283 K (Figure 3.9) displays a pair of sigmoidal oxidation waves, similar to the microelectrode voltammetry response. The inset of Figure 3.9 (Levich plot) demonstrates that the limiting currents for the +1/+2 charge state are proportional to the square root of the RDE angular velocity ($\omega^{1/2}$). Similar behavior is observed for the 0/+1 charge state. According to the Levich equation, this linearity indicates that the observed currents are entirely mass-transport controlled.[10d]

Figure 3.8 Microelectrode voltammetry of 0.072 mM $Au_{38}(SC2Ph)_{24}$ in CH_2Cl_2 with 0.1 M Bu_4NClO_4 at 283K on a 9-μm-diameter Pt working electrode, Pt coil counter electrode and Ag wire quasi-reference electrode. Potential scan rate = 10 mV/s.

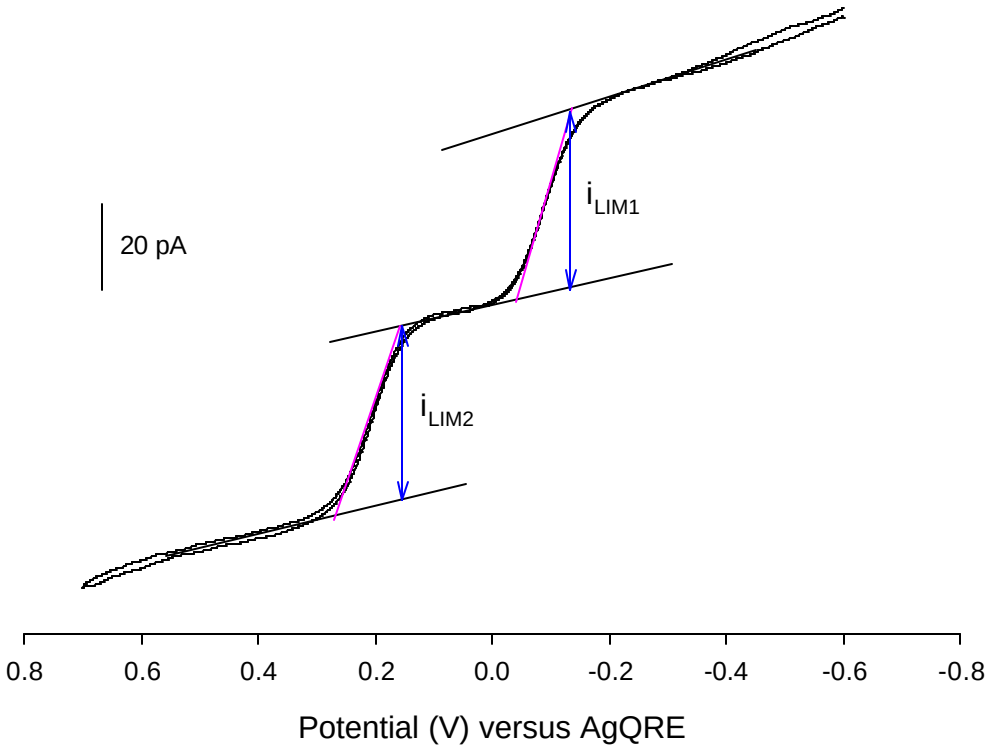
20 pA
i_{LIM1}
i_{LIM2}
0.8
0.6
0.4
0.2
0.0
-0.2
-0.4
-0.6
-0.8
Potential (V) versus AgQRE

The diffusion coefficient of $Au_{38}(SCPh)_{24}$ can be calculated from the Levich plot presented in Figure 3.9. The Levich equation describes the relationship of the limiting current to the rotation rate under conditions of total mass-transfer-limitation and is defined as[10e]:

$$i_{lim} = 0.62nFAD^{2/3}\omega^{1/2}\nu^{-1/6}C_{MPC} \quad (11)$$

where ω is the RDE angular velocity, ν is the kinematic viscosity of the solvent (0.00374 cm^2s^{-1} for CH_2Cl_2 at 283 K)[21], C_{MPC} is the concentration of the $Au_{38}(SC2Ph)_{24}$ solution, n, F and A have their usual meaning. The average value of D calculated using the Levich plots for the 1st (0/+1) and 2nd (+1/+2) oxidations is $(3.3 \pm 0.3) \times 10^{-6}$ cm^2 s^{-1} at 283 K which is pretty close to the microelectrode voltammetry result.

Square Wave Voltammetry. This technique, invented by Ramaley and Krause[22], has been developed extensively by the Osteryoungs and their coworkers[23]. Compared to differential pulse voltammetry (DPV), Osteryoung square wave voltammetry (OSWV) takes much less time for a simple potential scan and has slightly higher sensitivity. The peak spacing given by OSWV is the same as DPV while its peak current can be used to calculate the diffusion coefficient applying

$$\Delta i_p = \frac{nFAD^{1/2}C_{MPC}}{p^{1/2}t_p^{1/2}}\Delta\Psi_p \quad (11)$$

where Δi_p is the peak current, A is the disk electrode area, D is the diffusion coefficient, n and F have their usual meaning, C_{MPC} the concentration of $Au_{38}(SC2Ph)_{24}$, t_p the pulse width, $\Delta\Psi_p$ the dimensionless peak current which is 0.5649 with pulse height ΔE_p = 25 mV, step height ΔE_s = 5 mV. A mercaptoundecanoic acid (MUA) self-assembled monolayer (SAM) coated Au electrode was used to measure the background current (blank experiment) and the peak currents of the first two oxidation peaks at 283 K. Δi_p is then taken as the difference of

Figure 3.9 Rotating disk electrode voltammetry (RDE) of 0.026 mM $Au_{38}(SC2Ph)_{24}$ in CH_2Cl_2 with 0.1 M Bu_4NClO_4 electrolyte at 283 K utilizing a 3-mm diameter Au working electrode coated with a mercaptoundecanoic acid (MUA) self-assembled monolayer (SAM). Voltammograms are at electrode rotation rates of 250, 400, 700, 1000, 1250, 1500, and 2000 rpm; potentials are versus Ag wire quasi-reference, Pt wire counter electrode. Inset, Levich equation plot for the MPC charge state $+1 \rightarrow +2$.

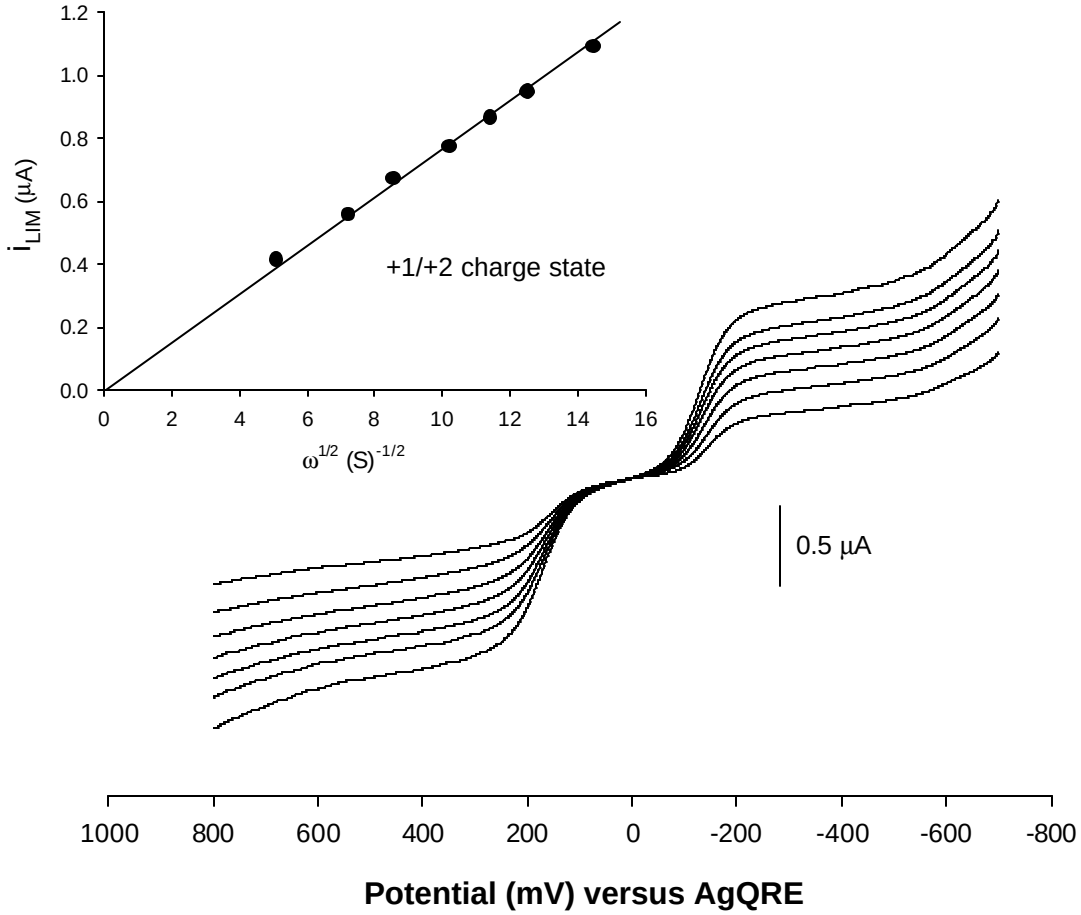
1.2
1.0
0.8
0.6
0.4
0.2
0.0
i_{LIM} (μA)
+1/+2 charge state
0
2
4
6
8
10
12
14
16
$\omega^{1/2}$ (S)$^{-1/2}$
0.5 μA
1000
800
600
400
200
0
-200
-400
-600
-800
Potential (mV) versus AgQRE

the average peak current and the background current. The calculated D value is about (2.6 ± 0.3) $\times 10^{-6}$ cm^2/s at 283 K which is in good agreement with the results of microelectrode and RDE voltammetry.

3.4 References

1 (a) Schmid, G., Ed. *Clusters and Colloids*; VCH: Weinheim, **1994**. (b) Hayat, M. A., Ed. Colloidal Gold: Principles, Methods, and Applications; Academic Press: San Diego, **1991**.

2 (a) Brown, L. O.; Hutchison, J. E. *J. Am. Chem. Soc.* **1997**, *119*, 12384. (b) Schmid, G. *Inorg. Synth.* **1990**, *27*, 214. (c) Schaaff, T. G.; Shafigullin, M. N.; Khoury, J. T.; Vezmar, I.; Whetten, R. L.; Cullen, W. G.; First, P. N.; Gutierrez-Wing, C.; Ascensio, J.; Jose-Yacaman, M. J. *J. Phys. Chem. B* **1997**, *10*1, 7885. (d) Chen, S.; Ingram, R. S.; Hostetler, M. J.; Pietron, J. J.; Murray, R. W.; Schaaff, T. G.; Khoury, J. T.; Alvarez, M. M.; Whetten, R.L., *Science* **1998**, *280*, 2098.

3 (a) Wall, J. S.; Hainfeld, J. F.; Bartlett, P. A.; Singer, S. J. *Ultramicroscopy*, **1982**, *8*, 397. (b) Hainfeld, J. F. *Science* **1987**, *236*, 450. (c) Jahn, W. Z. *Naturforsch., B: Chem. Sci.* **1989**, *44*, 1313.

4 Woehrle, G.H.; Warner, M. G.; Hutchison, J. E. *J. Phys. Chem. B* **2002**, *106*, 9979-9981.

5 Yang, Y; Chen, S. *Nano Letters*, **2003**, *3(1)*, 75-79.

6 (a) Jimenez, V. L.; Georganopoulou, D. G.; White, R. J.; Harper, A. S.; Mills, A. J.; Lee, D; Murray, R. W. *Langmuir*, **2004**, *20(16)*, 6864-6870. (b) Donkers, R. L.; Lee, D.; Murray, R. W. *Langmuir*, **2004**, *20(5)*, 1945-1952.

7 Lee, D.; Donkers, R. L.; DeSimone, J. M.; Murray, R. W. *J. Am. Chem. Soc.* **2003**, *125*, 1182-1183.

8 (a) Hicks, J. F.; Miles, D. L.; Murray, R. W. *J. Am. Chem. Soc.* **2002**, *124*, 13322-13328. (b) Quinn, B. M.; Liljeroth, P.; Ruiz, V.; Laaksonen, T.; Kontturi, K. *J. Am. Chem. Soc.* **2003**, *125*, 6644-6645.

9 Guo, R.; Georganopoulou, D; Feldberg, S. W.; Donkers, R. L.; Murray, R. W. *Anal. Chem.* **2005**, *77(8)*, 2662-2669.

10 Bard, A. J.; Faulker, L. R. *Electrochemical Methods*; Wiley: New York, 2nd Ed., 2001, (a) page 553, equation (13.3.30); (b) page 553, equation (13.3.29); (c) page 548, equation (13.3.15a); (d) page 341; (e) page 339, equation (9.3.22); (f) page 550, equation (13.3.21a)

11 Miles, D. T.; Murray, R. W. *Anal. Chem.* **2003**, *75*, 1251-1257.

12 (a)Hicks, J. F.; Templeton, A. C.; Chen, S.; Sheran, K. M.; Jasti, R.; Murray, R. W.; Debord, J.; Schaaff, T. G.; Wheten, R. L. *Anal. Chem.* **1999,** *71*, 3703-3711. (b) Chen, S.; Murray, R. W.; Feldberg, S.W. *J. Phys. Chem. B* **1998,** *102*, 9898-9907.

13 Leob, A. L.; Overbeek, J. T.; Wiersema, P. H. *The Electrical Double Layer Around a Spherical Colloid Particle*, MIT press, **1961**.

14 Weaver, M. J.; Gao, X. *J. Phys. Chem.* **1993**, *97*, 332-338.

15 (a) Hostetler, M. J.; Wingate, J. E.; Zhong, C.; Harris, J. E.; Vachet, R. W.; Clark, M. R.; London, J. D., Green, S. J.; Stokes, J. J.; Wignall, G. D., Glish, G. L.; Porter, M. D.; Evans, N. D. and Murray, R. W. *Langmuir* **1998**, *14*, 17-30. (b) Brust, M.; Walker, M.; Bethell, D.; Schiffrin, D. J.; Whyman, R. *J. Chem. Soc., Chem. Commun.* **1994**, *801-802*. (c) Terrill, R. H.; Postlethwaite, T. A.; Chen, C.; Poon, C.; Terzis, A.; Chen A.; Hutchison J. E.; Clark M. R.; Wignall, G.; Londono, J. D., Superfine, R.; Falvo, M.; Johnson Jr., C. S.; Samulski, E. T. and Murray, R. W. *J. Am Chem. Soc.* **1995**, *117*, 12537.

16 (a) Schaaff, T. G.; Whetten, R. L. *J. Phys. Chem. B* **2000**, *104*, 2630-2641. (b) Hakkinen, H.; Barnett, R. N.; Landman, U. *Physical Review Letters* **1999**, *82(16)*, 3264. (c) Bigioni, T. P.; Whetten, R. L. *J. Phys. Chem. B* **2000**, *104*, 6983-6986.

17 Ward, M. D. *Chem. Soc. Rev*. **1995**, *24*, 121.

18 Lee, D.; Donkers, R. L.; Wang, G.; DeSimone, J. M.; Murray, R. W. *J. Amer. Chem. Soc*, **2004**, *126*, 6193-6199.

19 (a) Diguet, R.; Deul, R.; Franck, E. U. *Ber. Bunsen Ges. Phys. Chem.* **1985**, *89*, 800-804. (b) Malmberg, C. G.; Maryott, A. A. *J. Res. Natl. Bur. Stds.* **1956**, *56*, 1.

20 Smalley, J. F.; Feldberg, S. W. Personal communication, Oct. 2002.

21 Riddick, J. A.; Bunger, W. B.; Sakano, T. K. *Organic Solvents: Physical Properties and Methods of Purification*, 4th Ed., Wiley, New York, **1986.**

22 Ramaley, L.; Krause Jr., M. S. *Anal. Chem.* **1969**, *41*, 1362.

23 (a) Osteryoung, R. A.; Osteryoung, J. *Phil. Trans. Roy. Soc. London, Ser.* A. **1981**, *302*, 315.(b) Osteryoung, J.; O'Dea, J. J. *Electroanal. Chem.* **1986**, *14*, 209. (c) Osteryoung, J. *Accts. Chem. Res.* **1993**, *26*, 77.

Chapter IV

CORE SIZE DEPENDENT LIGAND EXCHANGE KINETICS OF MONOLAYER PROTECTED GOLD CLUSTERS

4.1 Introduction

Monolayer-protected metal clusters (MPCs) are nanoparticles coated with dense, protecting monolayers of organothiolate,[1-4] organophosphine,[5-7] or organoamine ligands.[8] Thiolate ligands are used widely for MPCs with Au cores. One vital aspect of MPCs is that their chemical properties can be manipulated by varying the monolayer with ligand place-exchange reactions,[4, 8-22] as we showed for thiolate ligands on Au nanoparticles some time ago.[23]

The electrochemical properties of MPCs are known[24-28] to be core-size dependent, but whether their ligands exhibit size-dependent *chemical* reactivity has not been established. An important aspect of Au nanoparticle surface chemistry is that their surfaces are not uniform, but nanocrystalline, and accordingly contain a diversity of ligand binding sites—vertexes, edges, and terraces. These different locations on the nanoparticle surface can have different electron densities[29, 33] and steric accessibilities that potentially lead to equilibrium binding thermodynamics and ligand exchange kinetics that vary for different core sites. This mix of chemical properties depends on the MPC core size; for smaller cores the fraction

of atoms that lie on vertex and edges sites increases relative to terrace sites. The vertex and edge sites are called “defect sites” in the context of self-assembled monolayers (2D SAMs) on flat Au surfaces.[30] Studies of ligand place exchange reactions on macroscopically flat self-assembled monolayers show a large diversity of exchange reactivity of surface sites, some being readily reactive (presumably terrace edges, steps and other defect sites) while otheres (Au(111) terraces) displaying very slow exchange.

The ligand exchange kinetics of alkanethiolate-coated Au MPCs with average core diameters 1.6 and 2.2 nm, and corresponding average compositions $Au_{140}(ligand)_{53}$ and $Au_{314}(ligand)_{91}$ have been investigated[9,10] using ^{1}H NMR, finding that: a) the exchange reactions follow a 1:1 stoichiometry, releasing one out-going ligand as a thiol from the MPC monolayer for every newly bound in-coming thiolate, in a second order associative process, b) disulfides or oxidized sulfur species are not involved, c) the exchange rate is accelerated if the core is made electron-deficient (as by oxidative charging), and d) the exchange rate is initially rapid but then slows dramatically. The rate profile was interpreted [9,10] as reflecting high kinetic reactivity of vertex and edge sites relative to low kinetic reactivity of terrace-like core surface sites. The last point was supported by more recent exchange dynamics results[31] for $Au_{140}(SC2Ph)_{53}$ (1.6 nm core dia.) MPCs, where after the initial (5-8) ligand exchanges (again in a second order process), there was a gradual and then near-cessation of the reaction rate (over days) at <50% exchange of the original ligands. Besides reflecting very large differences in reactivity of defect versus terrace-like sites for ligand exchange, these results require that ligand surface migration between different kinds of sites is quite slow.

The present study was prompted by an interest in the extent to which ligand exchange dynamics depend on the MPC core size. The previous ligand exchange investigations were

not designed with an eye to effects of core size. $Au_{140}(SC2Ph)_{53}$ and $Au_{38}(SC2Ph)_{24}$ MPCs are anticipated from theoretical studies[29] to have truncated octahedral nanocrystalline shapes, in which the nanocrystals have 96 and 32 surface atoms, respectively. The number of vertex atom sites is the same on the two cores, but their proportion is far greater for the Au_{38} core. The electronic properties also differ; the Au_{140} core is metal-like, no homo-lumo gap has been detected, and its electrochemical properties in electrolyte solutions are dominated by charging effects called "quantized double layer" (QDL) charging.[25] The Au_{38} core, in contrast, is molecule-like, displaying a homo-lumo gap[26] of about 1.3 eV. The former has a more-or-less uniform (although perhaps thin) continuum of electronic states, while electron density in the latter has collapsed to definable molecular orbitals. Are these differences in electronic structure reflected in ligand reactivity differences, even if the reaction occurs at the same kind of core surface site? We will show here that at least for the ligand exchange dynamics of the early-exchanging, presumably vertex sites, the exchange rates for Au_{38} and Au_{140} cores are very close to each other.

Another result of the present study is that the different proportions of defect versus terrace sites for Au_{38} versus Au_{140} cores leads to different ligand exchange reaction profiles for the later-exchanging ligands. The Au_{38} exchange rate continues with a modest diminution in rate; that for Au_{140} shows a drastic slowing . Additionally, the nearly 100% exchange that can be accomplished for $Au_{38}(SC2Ph)_{24}$ MPCs allows isolation of $Au_{38}(SPhX)_{24}$ exchange products, and subsequent inspection of the rate of the *reverse* exchange reaction. The reverse exchange displays a nearly identical substituent effect and allows estimation of the (initial) ligand exchange equilibrium constant.

Previous ligand exchanges[9,10] followed by batch reaction/quenching procedures were replaced by a continuous ^{1}H NMR method in the most recent study.[31] An analogous method was also used here since it allows collection of more detailed kinetic data. Besides ^{1}H NMR, EPR spectroscopy has also been used to follow ligand exchange reaction of nanoparticles protected by phosphines or short chain thiols with disulfides functionalized with a spin label.[34-36] Certain peaks of the EPR spectrum originate from spin-spin interactions between the adjacent spin labels in unbound disulfide, those peaks gradually disappear as cleavage of the S-S disulfide bond occurs during the exchange reaction. In particular, Chechik[36] observed ligand exchange kinetics with spin-labeled disulfides slowed down when the 2.6 nm gold nanoparticle was aged in solution for a certain period of time--- as long as 146h.

4.2 Experimental Section

4.2.1 Chemicals. 4-Nitrothiophenol (ACROS, 95%), *p*-toluenethiol (ACROS, 98%), 4-methoxybenzenethiol (ACROS, 98%), phenylethylthiol (PhC2SH, Aldrich, 98%), 4-bromothiophenol (Aldrich, 95%), 4-mercaptophenol (Aldrich, 90%), tetra-*n*-octylammonium bromide (Oct_4NBr, Fluka, 98%), sodium borohydride (Aldrich, 99%), toluene (Fisher) and d_2-methylene chloride (Cambridge Isotope Laboratories, Inc.) were all used as received. Hydrogen tetrachloroaurate trihydrate (from 99.999% pure gold) was prepared by a literature procedure[37] and stored in a freezer at –20^o C. Millipore Nanopure water purification system was used to obtain low conductivity water.

4.2.2 Synthesis of *p*-X-PhSD thiols. *p*-X-PhSD thiols were synthesized as previously described.[31] In the general procedure for X = NO_2, Br, CH_3 and OCH_3**,** 3mL of deuterium oxide was added to *ca*. 100 mg of the thiol in 3 mL deuterated methylene chloride, the two phase solution mixture was vigorously stirred for 24h. The organic layer (bottom) was then

separated and dried over sodium sulfate, filtered and rotary evaporated. Complete loss of the SH signal in the ^{1}H NMR spectrum in dry CD_2Cl_2 indicated complete D/H exchange. The deuterated thiols were used immediately after being characterized.

4.2.3 Synthesis of $Au_{38}(SC2Ph)_{24}$. $Au_{38}(SC2Ph)_{24}$ was synthesized as described before.[38] Briefly, in a two-phase Brust[3] synthesis, hydrogen tetrachloroaurate (3.1g, 11.1 mmole) was phase-transferred into toluene with Oct_4NBr, followed by addition of a 3-fold molar excess (relative to Au) of phenylethylthiol, forming a gold(I)-thiol polymer. This was reduced by rapidly adding a 10-fold excess of aqueous $NaBH_4$ at 0^{o}C, vigorously stirring the solution at 0^{o}C for 20 hours. Removing the bottom aqueous layer, the toluene was rotary-evaporated at room temperature and the $Au_{38}(SC2Ph)_{24}$ extracted from the crude product with acetonitrile. The dried product was washed copiously with methanol until mostly cleaned of Oct_4N^+ cation (one gold core associated with approximately one Oct_4N^+ cation in average or ca. 5.3% in weight percent), according to ^{1}H NMR. The product was characterized by ^{1}H NMR (Figure 4S-1) and UV-Vis spectra as previously.[38]

4.2.4 Ligand Exchange Kinetics by ^{1}H NMR Spectroscopy. ^{1}H NMR spectra of solution mixtures of $Au_{38}(SC2Ph)_{24}$ (6.0 mg/2.0 mL after mixing) and *p*-X-PhSH ligands (amounts varied based upon desired reactant ratios) in CD_2Cl_2 were collected with a Bruker AC500 spectrometer at 293 K. Ferrocene (sublimed, typically 0.6 mg/2.0 mL after mixing) served as an internal standard. Briefly, after acquiring a ^{1}H NMR spectrum of the initial solution (1mL) of ferrocene and *p*-X-PhSH, it is rapidly mixed with the MPC solution (6.0 mg/1mL) and placed in the pre-shimmed spectrometer for repetitive collection of 1-9 ppm (vs. TMS) spectra, using a 17 second acquisition time per spectrum and a time interval between spectra of 2 minutes. T_1 was set at 1s instead of 0s as was done in the $Au_{140}(SC2Ph)_{53}$ case.[31] The

ca. 2.8 ppm quartet resonance originates exclusively from the liberated phenylethanethiol (HS-***CH*****$_2$**-CH_2Ph), which was used to monitor the extent of the exchange reaction; its (integrated)growth, relative to the ferrocene standard, illustrated in Figure 4.1. The % exchanged PhC2S- from the $Au_{38}(SC2Ph)_{24}$ nanoparticle is the percentage of liberated phenylethanethiol versus the initial 24 phenylethanethiolate ligands of the nanoparticle. The rates of previously[31] reported ligand exchange for $Au_{140}(SC2Ph)_{53}$ were re-measured using the above procedure at the same temperature 293K, for consistency of method and for a more rigorous comparison with the $Au_{38}(SC2Ph)_{24}$ data. Judging from the rest potential measurements, both $Au_{38}(SC2Ph)_{24}$ and $Au_{140}(SC2Ph)_{53}$ MPCs were very close to neutral charge state, and the core charge state remained approximately the same after ligand exchange within the time scale (less than 3 hours) we studied. In measurements of the reverse exchange reaction, the singlet from liberated ***H***S-Ph-X was monitored to follow the extent of exchange. MPC solutions used for NMR meaurements in the present work are not deoxygenated.

4.3 Results and Discussion

4.3.1 Ligand Exchange Kinetics. The previous[31]NMR approach to ligand exchange dynamics of $Au_{140}(SC2Ph)_{53}$ (using $T_1 = 0$ relaxation delay pulse to effectively suppress signals from Au_{140} MPC-bound thiolate ligands) failed in the present case because the sharper resonances for Au_{38} ligands were not similarly suppressed. The ligand exchange was instead followed using the α-CH_2 *ca*. 2.8 ppm quartet resonance of phenylethanethiol liberated from the $Au_{38}(SC2Ph)_{24}$ monolayer by exchange with *p*-X-PhSH thiols. Figure 4.1 illustrates the monitoring scheme; although the quartet signal is initially small, it is well resolved from resonances from Au_{38}-bound phenylethanethiolate ligands at *ca*. 2.9 ppm

Figure 4.1 ^{1}H NMR spectrum for the exchange of phenylethanethiolate (PhC2S-) by 4-nitrothiophenol (4-NO_2-PhSH) onto $Au_{38}(SC2Ph)_{24}$ at 293 K Inset: (a) at t = 3 min; (b) at t = 37 min. Ferrocene serves as internal standard. Quartet at *ca*. 2.8 ppm is α-CH_2 on liberated phenylethanethiol (HS-***CH_2***-CH_2-Ph) and is used for the kinetic measurement. The α-CH_2 resonance on bound phenylethanethiolate, a broad peak at *ca*. 3.35 ppm (Figure 4S-1), is somewhat suppressed in this spectrum. The *ca*. 2.9 ppm peak is from β-CH_2 on bound phenylethanethiolate (-S-CH_2-***CH_2***-Ph) and on liberated phenylethanethiol (HS-CH_2-***CH_2***-Ph); the ca.3.1 ppm triplet is from a-proton of (Oct_4)NBr salt impurity (ca. one gold core associated with one Oct_4^+ cation based on calculation from ferrocene internal standerd thus its influence on ligand exchange rate should be small).

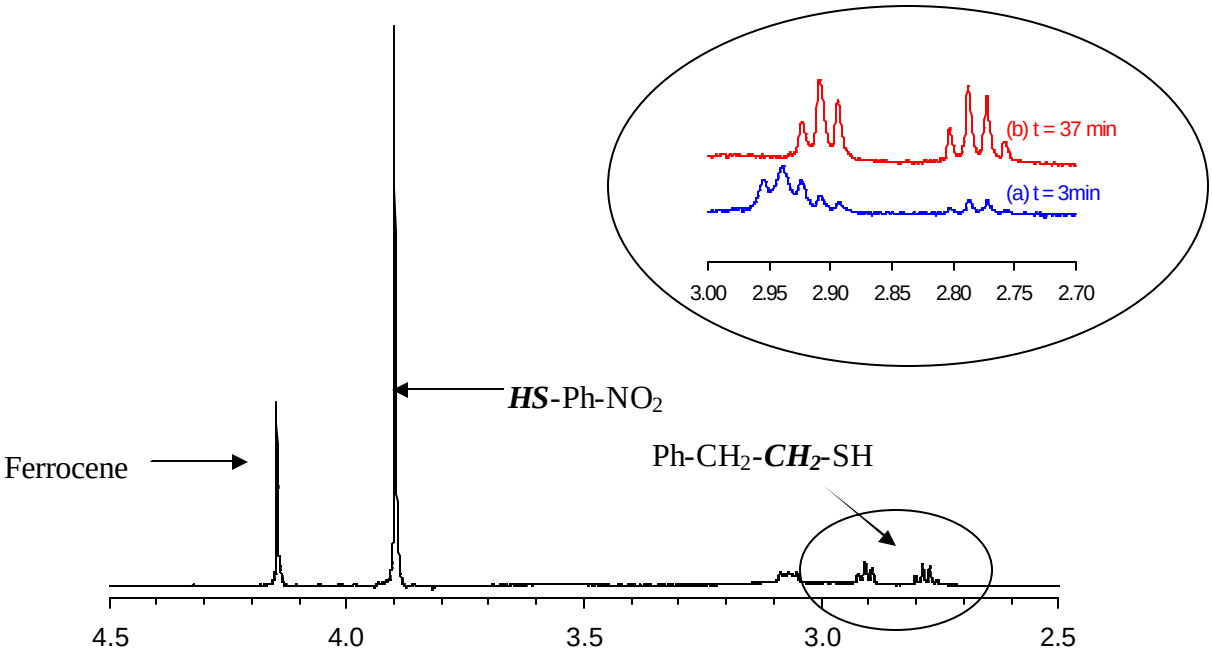
(b) t = 37 min
(a) t = 3min
3.00
2.95
2.90
2.85
2.80
2.75
2.70
HS-Ph-NO2
Ferrocene
Ph-CH2-CH2-SH
4.5
4.0
3.5
3.0
2.5

(triplet) and at 3.35 ppm (broad, see Figure 4S-1). No signals suggestive of disulfides or other oxidized forms of organic sulfur were observed, as was the case previously.[9, 10, 31]

Kinetic results for exchange with in-coming ligand *p*-NO_2-PhSH are shown in Figure 4.2 for $Au_{38}(SC2Ph)_{24}$ (curvea) and $Au_{140}(SC2Ph)_{53}$ (curve b), converting the NMR peak integrals percentages and numbers of original phenylethanethiolate ligands exchanged as explained in Experimental. The kinetic profile for the $Au_{140}(SC2Ph)_{53}$ MPC is very similar to the previous report;[31] the initially rapid reaction slows down dramatically and comes to an apparent near-halt after 40-50% of PhC2S- monolayer is replaced. In contrast, the $Au_{38}(SC2Ph)_{24}$ MPC exchange reaction continues within the time-frame of Figure 4.2a to replace 75% of the monolayer. (Figure 4S-2 shows kinetic profile with Y-axis both in %PhC2S-exchanged and number of ligands exchanged.)

Figure 4.3 shows a first order rate analysis of the kinetic profiles of Figure 4.2. Due to the near unity linear coefficient and time scale (typically less than 3 hours) of ligand exchange we studied in this work, we did not observe obvious aging effect of the nanoparticles as was observed by Chechik.[36] Both reactions are roughly biphasic—a more rapid first order process transitioning to a slower first order process. This signals serial first order reactions in which the second, slower (Phase II) reaction becomes dominant when the participants in the faster first reaction (Phase I) are exhausted. We use the designation of Phase I to represent exchange of the first *ca*. 25% of the PhC2S- ligands by *p*-NO_2-PhSH, and Phase II to represent[32] the ensuing *ca*. 40%. For $Au_{38}(SC2Ph)_{24}$ MPCs, the Phase II rate constants are only *ca*. 20% smaller than those in Phase I, whereas for $Au_{140}(SC2Ph)_{53}$ the Phase II rates are 4 to 5-fold smaller. This pattern of differences in Phase I *vs*. Phase II rates for the two MPCs was observed for the kinetics of all three *p*-substituted arylthiols (X = NO_2, Br, and

Figure 4.2 Reaction profile for exchange of phenylethanethiolate (PhC2S-) by *p*-nitrothiophenol (NO_2PhSH) onto (a) $Au_{38}(SC2Ph)_{24}$ and (b) $Au_{140}(SC2Ph)_{53}$ at mole ratios of NO_2PhSH/ PhC2S- = 4.2 :1 and 1.3 :1, respectively. MPC concentration is 2.8×10^{-4} M in both cases and at the same temperatue 293 K. Judging from rest potential measurements, both MPCs are close to neutral charge state.

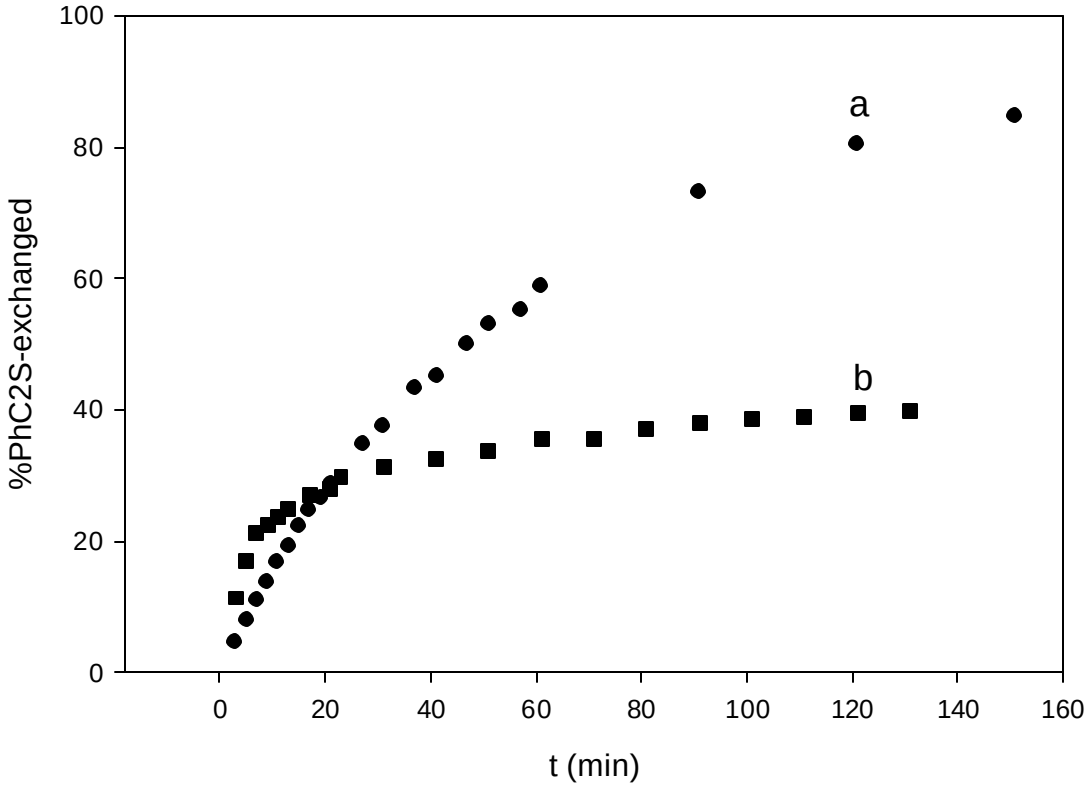
100
80
60
40
20
0
%PhC2S-exchanged
0
20
40
60
80
100
120
140
160
t (min)
a
b

Figure 4.3 (a) Pseudo-first-order rate plots for exchange of phenylethanethiolate (PhC2S-) by *p*-nitrothiophenol (NO_2PhSH) onto (Panel a) $Au_{38}(SC2Ph)_{24}$ and (Panel b) $Au_{140}(SC2Ph)_{53}$, at mole ratios of NO_2PhSH/ PhC2S- = 4.2 :1 and 1.3 :1, respectively. In the plots, Phase I corresponds to exchange of the initial *ca*. 25% of the PhC2S-monolayer and Phase II to *ca*. 40% of the PhC2S-monolayer.

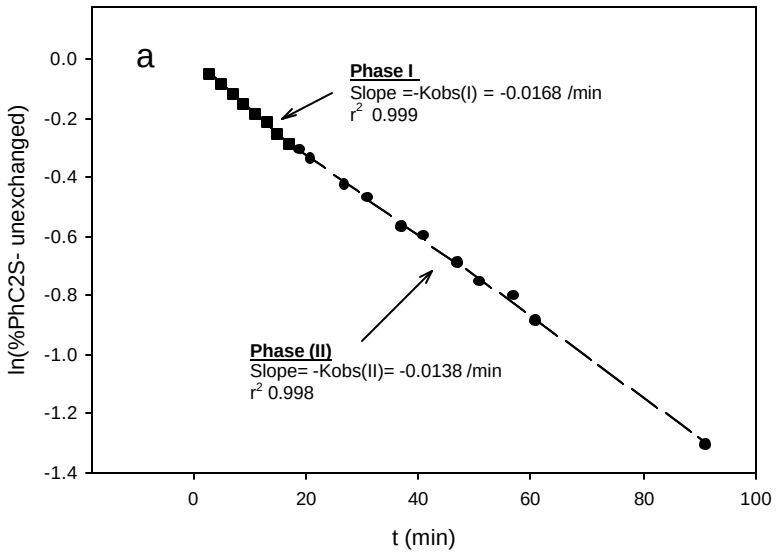
a
Phase I
Slope =-Kobs(I) = -0.0168 /min
r2 0.999
Phase (II)
Slope= -Kobs(II)= -0.0138 /min
r2 0.998
ln(%PhC2S- unexchanged)
t (min)
0.0
-0.2
-0.4
-0.6
-0.8
-1.0
-1.2
-1.4
0
20
40
60
80
100

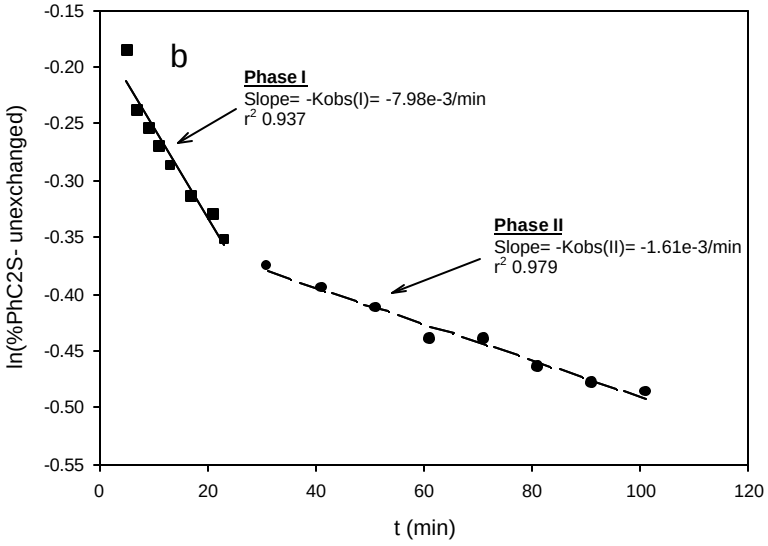
b
Phase I
Slope= -Kobs(I)= -7.98e-3/min
r2 0.937
Phase II
Slope= -Kobs(II)= -1.61e-3/min
r2 0.979
ln(%PhC2S- unexchanged)
t (min)
-0.15
-0.20
-0.25
-0.30
-0.35
-0.40
-0.45
-0.50
-0.55
0
20
40
60
80
100
120

CH_3), even though their rates for both MPCs decreased concurrently by *ca*. 4 to 6-fold through the series of in-coming ligands. Interpretation of these observations is deferred to below.

The $Au_{38}(SC2Ph)_{24}$ ligand exchange by *p*-substituted arylthiols was also first order for X = Br, CH_3, OCH_3, and OH, and Phase I and Phase II behavior was again seen (Supporting Information Figures 4S-3, 4S-4). Further, first order behavior was established for X = NO_2, Br, CH_3 and OCH_3 for different in-coming thiol concentrations (Table 4.1); plots of the Phase I results are shown in Figure 4.4. Figure 4.4 demonstrates an overall second order behavior; the plots are linear with intercepts within *ca*. ± 0.00002 s^{-1} of the origin. (The non-zero intercept seen[31] for X = NO_2 in the previous $Au_{140}(SC2Ph)_{53}$ study was not encountered for $Au_{38}(SC2Ph)_{24}$.) The second order rate constants ($K_{PE(I)}$) taken from the slopes of Figure 4.4 (Phase I of the reaction) are summarized in Table 4.2. The Phase II first order rate constants were also established to vary linearly with in-coming ligand concentration for the case of X = NO_2 (Figure 4S-5); the $K_{PE(II)}$ results given in Table 4.2 for the other *p*-substituted arylthiols assume their corresponding second order behavior.

The first interpretation that can be given the $K_{PE(I)}$ data in Table 4.2 is that the second order reaction—first order each in MPC (due to MPC solubility and instrument sensitivity issue, we only tested that K_{obs} varied linearly with nanoparticle amount from 3-10 mg in 1 mL CD_2Cl_2 at a constant in-coming ligand concentration) and in-coming ligand—supports the associative ligand exchange mechanism proposed previously[9, 10, 31] for larger core Au_{314} and Au_{140} MPCs. That is, the second order associative process seems to be preserved over a range of Au core dimensions, at least for the early, faster Phase I stage of the ligand exchange. Secondly, the rate of phenylethanethiolate ligand exchange by thiolates of *p*-X-

Figure 4.4 Second-order rate plot for reaction of 2.8×10^{-4} M $Au_{38}(SC2Ph)_{24}$ with in-coming ligands (ð) $HSPhNO_2$, (o) HSPhBr, (Δ) $HSPhCH_3$, and (∇) $HSPhOCH_3$. Y-intercepts are zero within experimental error.

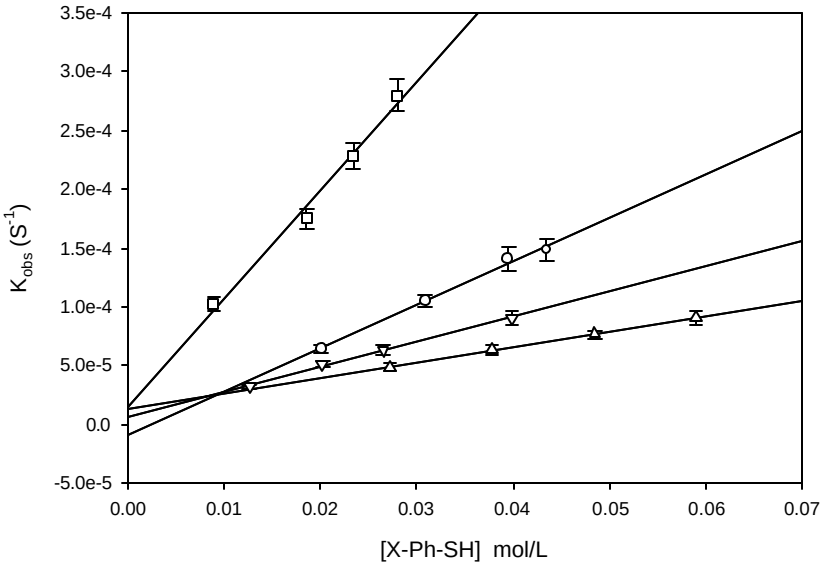
3.5e-4
3.0e-4
2.5e-4
2.0e-4
1.5e-4
1.0e-4
5.0e-5
0.0
-5.0e-5
K_{obs} (S^{-1})
0.00
0.01
0.02
0.03
0.04
0.05
0.06
0.07
[X-Ph-SH] mol/L

Table 4.1 Summary of pseudo-first-order rate constants for ligand exchange reactions of different para-substituted arylthiols with 2.8×10^{-4} M $Au_{38}(SC2Ph)_{24}$ MPCs.

$[NO_2PhSH]^a$ (M)	k_{obs} (s^{-1}) $\times 10^{-4}$	$[BrPhSH]^a$ (M)	k_{obs} (s^{-1}) $\times 10^{-4}$	$[CH_3PhSH]^a$ (M)	k_{obs} (s^{-1}) $\times 10^{-4}$	$[OCH_3PhSH]^a$ (M)	k_{obs} (s^{-1}) $\times 10^{-4}$
0.0089	1.02 ± 0.06	0.0201	0.64 ± 0.04	0.0272	0.49 ± 0.03	0.0126	0.32 ± 0.02
0.0185	1.75 ± 0.09	0.0309	1.05 ± 0.05	0.0378	0.64 ± 0.04	0.0202	0.51 ± 0.03
0.0234	2.28 ± 0.11	0.0395	1.41 ± 0.10	0.0485	0.77 ± 0.03	0.0265	0.63 ± 0.04
0.0280	2.80 ± 0.14	0.0435	1.48 ± 0.10	0.0590	0.91 ± 0.06	0.0399	0.91 ± 0.06

[a] The rate constant for deuterothiol, *p*-X-PhSD, at the lowest concentration was identical to that for *p*-X-PhSH within experimental error.

Table 4.2 Second-order rate constants of ligand exchange reaction of gold nanoparticles $Au_{38}(SC2Ph)_{24}$ and $Au_{140}(SC2Ph)_{53}$ with different *p*-substituted arylthiols (*p*-XPhSH).

MPCs	In-coming ligand	Ratio of in-coming ligand/PhC2 [a]	$k_{PE(I)}$[b] (10^{-3} $M^{-1}s^{-1}$)	Ratio of in-coming ligand/PhC2[a]	$k_{PE(II)}$[c] (10^{-3} $M^{-1}s^{-1}$)
$Au_{38}(SC2Ph)_{24}$[d]	NO_2PhSH	(1.3 - 4.2) : 1	10.1 ± 0.6	4.2 : 1	8.5
	BrPhSH	(3.1 - 6.7) : 1	3.4 ± 0.3	6.7 : 1	1.8
	CH_3PhSH	(4.3 - 9.3) : 1	1.6 ± 0.2	4.3 : 1	1.1
	CH_3OPhSH	(1.8 - 6.0) : 1	2.4 ± 0.3	4.0 : 1	1.3
	HOPhSH	7.1 : 1	2.3	7.1 : 1	1.0
$Au_{140}(SC2Ph)_{53}$[d,e]	NO_2PhSH	1.3 : 1	7.8	1.3 : 1	1.7
	BrPhSH	2.2 : 1	2.2	2.2 : 1	0.6
	CH_3PhSH	3.3 : 1	1.8	3.3 : 1	0.6

[a] The relative number of moles of in-coming arylthiols and the original phenylethanethiolate ligands in the monolayers of the $Au_{38}(SC2Ph)_{24}$ and $Au_{140}(SC2Ph)_{53}$ MPCs.

[b] Average second-order rate constants of Phase I (*ca*. 25% of the PhC2S-thiolate is exchanged), for *p*-substituted X = NO_2, Br, CH_3, OCH_3. For X = OH, $k_{PE(I)}$ is taken from a single in-coming ligand concentration and second-order is assumed.

[c] Second-order rate constants of Phase II (exchange of *ca*. 40% of the PhC2S-thiolates) calculated from results at a single in-coming ligand concentration.

[d] The solutions of both MPCs, judging from electrochemical rest potentials, contained roughly equal amounts of Au^0 and Au^{+1} cores.

[e] The previous[31] results for X = NO_2, Br, and CH_3 were $K_{PE(I)}$ = 14, 6.4, and 4.3 $\times 10^{-3}$ $M^{-1}s^{-1}$, respectively. Considering the differences in the NMR procedure and that data were acquired from different batch of Au_{140} samples by different workers, the level of agreement is acceptable.

PhSH varies with the nature of X, i.e., there is a substituent effect on the reaction rate. This was also observed in the Au_{140} study[31] and shows explicitly that the in-coming ligand is involved in the rate-controlling step of the exchange, further supporting an associative process. The third and perhaps most significant observation taken from Table 4.2 is that the rate constants for Phase I ligand exchange are very close for the $Au_{38}(SC2Ph)_{24}$ and $Au_{140}(SC2Ph)_{53}$ MPCs. (In fact, the second order rate constants $k_{PE(I)}$ in Table 4.2 are near the *ca*. $1x10^{-2}$ M^{-1} s^{-1} rate constant determined for Au_{314} MPC[10], although the ligands employed were different.) This leads to the important conclusion that the exchange kinetics of the first population (Phase I) of exchanging ligands *are almost independent of the nanoparticle core dimension.* That is, the (early) ligand exchange is not a size-dependent property, in spite of the facts that a) the $Au_{38}(SC2Ph)_{24}$ MPC is definitely molecule-like and exhibits a substantial homo-lumo gap energy,[26] whereas b) any homo-lumo gap energy for $Au_{140}(SC2Ph)_{53}$ MPCs is less than the one-electron energy increments (0.2-0.3 eV) of quantized double layer charging.[25] Theoretical studies[33] predict that Au 4f binding energies for vertex sites on Au_{38}, while lower than for edge and terrace-like sites, are only about 10% lower than vertex sites on Au_{140}. In this regard, theory and experiment seem consistent.

Our earliest[10] analysis of ligand exchange on Au MPCs assigned the initial, faster stage of the reaction to ligands on vertex sites of the Au nanocrystal (see Scheme 1 of Ref. 10), and later, slower steps to reactions of ligands on edge and then on even slower terrace-like sites. This view has basis in the classical understanding[30] of site reactivity on flat metal surfaces having various kinds of defects; defect sites are more reactive. We propose that the earliest stages of ligand exchange on $Au_{38}(SC2Ph)_{24}$ MPCs also involves ligands on vertex sites. Further, as noted in the introduction, the fraction of the surface atom population on Au_{38} *vs.*

Au_{140} nanocrystals corresponding to defect (vertex plus edge) sites is far larger on the former nanoparticle. Au_{38} surface can be analogous to monolayers of short alkanethiols on flat gold surface which are substantially disordered and hence the *entire* surface can act as defect sites enabling adsorbed, but disordered alkanethiols to be rapidly and completely exchanged.[30(a, e, f)] The ensuing expectation is that ligand binding dynamics on a Au_{38} core should be much less dispersive (i.e., less varied); this expectation is fully consistent with the serial-reaction, Phase I *vs*. Phase II behavior described above. Phase I rate constants for Au_{38} and Au_{140} are pretty close to each other; the reactions occur on the same (vertex) kind of core site. Phase II reactions are slower for Au_{140}, being for ligands on edge and terrace-like sites, than on Au_{38} cores where the remaining ligand sites are on or neighbors of vertex atoms.

The Phase I second order rate constants in Table 4.2 show a definite substituent effect for both $Au_{38}(SC2Ph)_{24}$ and $Au_{140}(SC2Ph)_{53}$ MPCs. It is most noticeable that the polar, electron-withdrawing NO_2 substituent provokes a substantially faster ligand exchange. Results for $Au_{140}(SC2Ph)_{53}$ MPCs gave a well-formed Hammett substituent plot as shown previously.[31] The data for $Au_{38}(SC2Ph)_{24}$ MPCs are presented as a Hammett plot in Figure 4.5a, using standard σ substituent values.[39] The $Au_{38}(SC2Ph)_{24}$ plot is not as organized as the previous[31] $Au_{140}(SC2Ph)_{53}$ data, but the rate constants that we most carefully assessed, X = NO_2, Br, and CH_3, give a linear segment with slope of 0.86. The comparable Hammett slope for $Au_{140}(SC2Ph)_{53}$ MPCs was[31] also positive 0.44. We will return to a further consideration of the substituent effect below.

4.3.2 The Reverse Ligand Exchange Reaction. The nearly complete ligand exchanges accomplished for $Au_{38}(SC2Ph)_{24}$ MPCs yield Au_{38} core MPCs with different monolayers: according to the NMR analysis, $Au_{38}(SPhNO_2)_{24}$, $Au_{38}(SPhBr)_{22}(SC2Ph)_2$, and

$Au_{38}(SPhCH_3)_{22}(SC2Ph)_2$. (See Supporting Information Fig. S-6 for ^1H NMR spectrum of $Au_{38}(SPh\text{-}NO_2)_{24}$). The new MPCS were isolated from large-scale exchange reactions. That the Au_{38} core is preserved after exchange is supported by preservation of the pattern of electrochemical reactions and associated energy gap seen[26] for the $Au_{38}(SC2Ph)_{24}$ MPC, as will be reported elsewhere.[40]

The fully exchanged MPCs opened the door to study the reverse ligand exchange reaction, where $Au_{38}(SPhX)_{24}$ MPCs are reacted with phenylethanethiol:

$$Au_{38}(SPhX)_{24} + mPhC2SH \rightarrow Au_{38}(SC2Ph)_m(SPhX)_{24-m} + mHSPhX \quad (1)$$

The reaction was followed by monitoring the growth of the S-*H* resonance of the *p*-substituted arylthiol, HSPhX, liberated from $Au_{38}(SPhX)_{24}$. The early part of the reverse reaction is again first order; Table 4.3 gives the associated second order rate constants for X= NO_2, Br, and CH_3. There is, again, an obvious substituent effect on the exchange dynamics; the rate constants are $k_{PE(NO2)} > k_{PE(Br)} > k_{PE(CH3)}$. The Hammett plot of these results in Figure 4.5b has remarkably, a slope, 0.82, that is nearly identical to that for the same substituents in Figure 4.5a (0.86). That the same substituent effect appears in both the forward and reverse exchange reactions makes conclusive our argument that the reaction is an associative process. Additionally, in discussion of the substituent effect in the ligand exchange[31] for $Au_{140}(SC2Ph)_{53}$ MPCs, we noted that, classically, it is an indicator of how electronic effects of substituents affect charge distribution in the transition state. Lowering of the reaction's activation barrier for electron-withdrawing substituents (e.g., $-NO_2$) implies stabilizing of a buildup of negative charge taking place on the sulfur atom (or positive charge on the Au atom to which it is bonded) in the rate-determining step. Observation of the same substituent effect in both directions of the exchange reaction, i.e., Figures 4.5a and b, further

Figure 4.5 Panel a. Hammett plot of $k_{PE(I)}$ rate constants for ligand place exchange reactions of $Au_{38}(SC2Ph)_{24}$ against standard substituent parameters, σ, for $–NO_2$; -Br; $-CH_3$; $-OCH_3$; -OH. Panel b. Hammett plot for the reverse ligand exchange reaction.

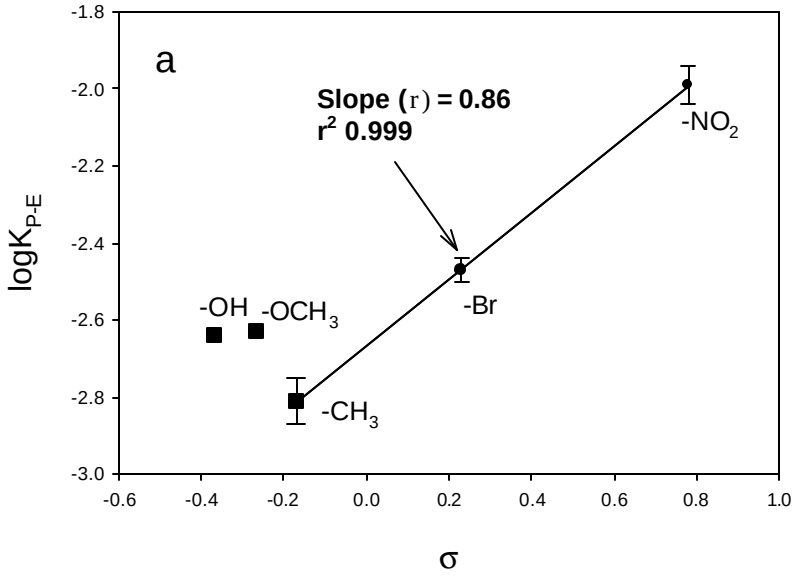
a
Slope (r) = 0.86
r2 0.999
-NO2
-Br
-OH
-OCH3
-CH3
logKP-E
σ

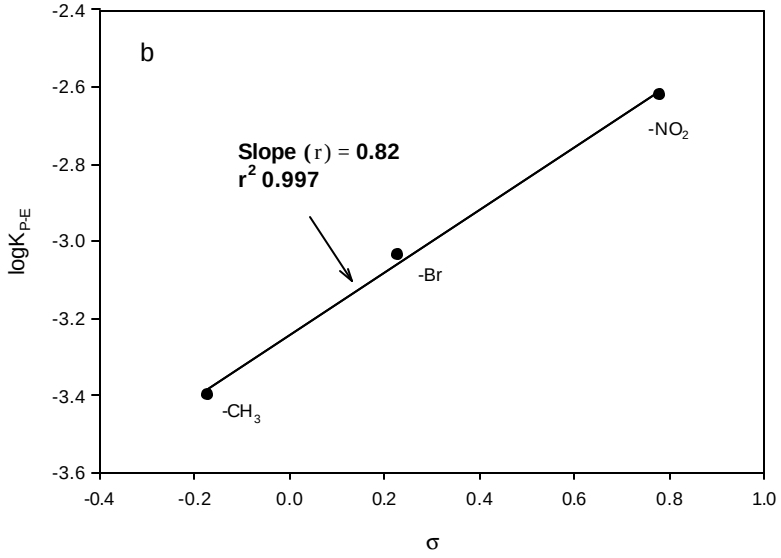
b
Slope (r) = 0.82
r2 0.997
-NO2
-Br
-CH3
logKP-E
σ

Table 4.3 Second-order rate constants of the reverse ligand exchange reaction: $Au_{38}(SPh\text{-}X)_{24}$ + mPhC2SH → $Au_{38}(SC2Ph)_m(SPh\text{-}X)_{24\text{-}m}$ + mHS-Ph-X

MPCs	PhC2SH/SPh-X [a]	$k_{PE(I)}$ (10^{-3} $M^{-1}s^{-1}$)	$K_{EQ,PE}$ [b]
$Au_{38}(SPhNO_2)_{24}$	2.2 : 1	2.4	4.2
$Au_{38}(SPhBr)_{22}(SC2Ph)_2$	6.0 : 1	0.92	3.7
$Au_{38}(SPhCH_3)_{22}(SC2Ph)_2$	7.3 : 1	0.40	4.0

[a] The relative number of moles of in-coming phenylethanethiol and the original thiolates in the monolayers of $Au_{38}(SPhX)_{24}$ MPCs.

[b] Ratio of $k_{PE(I)\ forward}$ from Table 4.2 versus $k_{PE(I)\ reverse}$ from Table 4.3.

implies a concurrent bonding of both in-coming and leaving ligands to the same Au atom (or a neighbor) in the rate-determining step.

The $k_{PE(I)}$ forward (Table 4.2) and reverse (Table 4.3) ligand exchange reaction rates refer to exchanges of the faster-reacting ligand population—which we postulate is that on the MPC core vertices. The equilibrium constant $K_{EQ,PE}$ for exchanges of phenylethanethiolate ligands with those of the three *p*-substituted arylthiols at those core sites is the ratio[41] of the forward and reverse rate constants, as given in Table 4.3. Remarkably, there is little variation among the $K_{EQ,PE}$ results; the average is 4.0 ± 0.3. That is, $K_{EQ,PE}$ lacks an evident substituent effect, implying that the reaction free energy for replacement of phenylethanethiolate ligands with -SPhX ligands is constant, and that bonding of -SPhX ligands at the vertex sites is more stable than phenylethanethiolate bonding by *ca*. 3.4 kJ/mol (or 0.035 eV/ MPC). That there is a thermodynamic stabilization of MPC bonding of a Au-SPhX moiety relative to that of Au-$S(CH_2)_2Ph$, that is more or less independent of "X", further implies that the difference in the Au-thiolate bonding energies lies in alkyl (i.e., $-SCH_2CH_2Ph$) versus aryl (-SPhX) bonding to the sulfur. A related observation is that the activation energy barrier for ligand exchange on Au_{38} vertices depends on substituents ("X") whereas the bonding strength ($K_{EQ,PE}$) does not. This is consistent with the activation model presented above.

4.4 References

1 Templeton, A. C.; Wuelfing, W. P.; Murray, R. W. *Acc. Chem. Res.* **2000,** *33***, 27**.

2 Whetten, R. L.; Shafigullin, M. N.; Khoury, J. T.; Schaaff, T. G.; Vezmar, I.; Alvarez, M. M.; Wilkinson, A. *Acc. Chem. Res.* **1999**, *32*, 397.

3 Brust, M.; Walker, M.; Bethell, D.; Schiffrin, D. J.; Whyman, R. J.; *Chem. Soc. Chem. Commun.* **1994**, 801.

4 Brown, L. O.; Hutchison, J. E. *J. Am. Chem. Soc.* **1997**, *119*, 12384.

5 Schmid, G. *Chem. Rev.* **1992**, *92*, 1709.

6 Weare, W. W.; Reed, S. M.; Warner, M. G.; Hutchison, J.E. *J. Am. Chem. Soc.* **2000**, *122*, 12890.

7 Petroski, J.; Chou, M. H.; Creutz, C. *Inorg. Chem.* **2004**, *43*, 1597.

8 Brown, L. O.; Hutchison, J. E. *J. Am. Chem. Soc.* **1999**, *121*, 882.

9 Song, Y.; Murray, R. W. *J. Am. Chem. Soc.* **2002**, *124*, 7096.

10 Hostetler, M. J.; Templeton, A. C.; Murray, R. W. *Langmuir* **1999**, *15*, 3782.

11 Kell, A. J.; Stringle, D. L. B.; Workentin, M. S. *Org. Lett.* **2000**, 3381.

12 Han, L.; Daniel, D. R.; Maye, M. M.; Zhong, C.-J. *Anal. Chem.* **2001**, *73*, 4441.

13 Kell, A. J.; Workentin, M. S. *Langmuir* **2001**, *17*, 7355.

14 Wuelfing, W. P.; Zamborini, F. P.; Templeton, A. C.; Wen, W.; Yoon, H.; Murray, R. W. *Chem. Mat.* **2001**, *13*, 87.

15 Ionita, P.; Caragheorgheopol, A. *J. Am. Chem. Soc.* **2002**, *124*, 9048.

16 Lin, S.-Y.; Liu, S.-W.; Lin, C.-M.; Chen, C. *Anal. Chem.* **2002**, *74*, 330.

17 Wuelfing, W. P.; Murray, R. W. *J. Phys. Chem. B.* **2002**, *106*, 3139.

18 Zamborini, F. P.; Leopold, M. C.; Hicks, J. F.; Kulesza, P. J.; Malik, M. A.; Murray, R. W. *J. Am. Chem. Soc.* **2002**, *124*, 8958.

19 Lee, D.; Donkers, R. L.; DeSimone, J. M.; Murray, R. W. *J. Am. Chem. Soc.* **2003**, *125*, 1182.

20 Li, D.; Li, J. *Surf. Sci.* **2003**, *522*, 105.

21 Pengo, P.; Broxterman, Q. B.; Kaptein, B.; Pasquato, L.; Scrimin, P. *Langmuir* **2003**, *19*, 2521.

22 Woehrle, G. H. ; Warner, M. G. ; Hutchison, J. E. *J. Phys. Chem. B* **2002**, *106*, 9979.

23 Hostetler, M. J. ; Green, S. J.; Stokes, J. J. ; Murray, R. W. *J. Am. Chem. Soc* **1996**, *118*, 4212.

24 Chen, S.; Ingram, R. S.; Hostetler, M. J.; Pietron, J. J.; Murray, R. W.; Schaaff, T. G.; Khoury, J. T.; Alvarez, M. M.; Whetten, R. L. *Science* **1998**, *280*, 2098.

25 Hicks, J. F.; Miles, D. T.; Murray, R. W. *J. Am. Chem. Soc.* **2002**, *124*, 13322.

26 Lee, D.; Donkers, R. L.; Wang, G.; Harper, A. S.; Murray, R. W. *J. Am. Chem. Soc.* **2004**, *126*, 6193.

27 Jimenez, V. L.; Georganopoulou, D. G.; White, R. J.; Harper, A. S.; Mills, A. J.; Lee, D.; Murray, R. W. *Langmuir*, **2004**, *20*, 6864.

28 Yang, Y.; Chen. S. *Nano Letters*, **2003**, *3*, 75.

29 Häkkinen, H.; Barnett, R. N.; Landman, U. *Phys. Rev. Lett.* **1999**, *82*, 3264.

30 (a) Collard, D. M.; Fox, M. A. *Langmuir* **1991**, *7*, 1192. (b) Kolega, R. R.; Schlenoff, J. B. *Langmuir* **1998,** 14, 5469. (c) Lin, P. H.; Guyot-Sionnest, P. *Langmuir*, **1999**, 15, 6825. (d) Chidsey, C. E. D.; Bertozzi, C. R.; Putvinski, T. M. and Mujsce, A. M. *J. Am. Chem. Soc.* **1990**, *112*, 4301. (e) Bain, C. D.; Troughton, E. B.; Tao, Y.-T.; Evall, J.; Whitesides, G. M.; Nuzzo, R. G. *J. Am. Chem. Soc.* **1989,** *111*, 321. (f) Hutt, D. A.; Leggett, G. J. *Langmuir* **1997**, *13*, 3055.

31 Donkers, R. L.; Song, Y.; Murray, R. W. *Langmuir*, **2004**, *20*, 4703.

32 For the purpose of comparisons, the 40% segment was dictated by the practical fact that beyond 40%, ligand exchange for $Au_{140}(SC2Ph)_{53}$ exhibits a continued slowing. A plot of Figure 4.3b at even longer times becomes curved and eventually almost flat, signaling a near-cessation of the reaction rate.

33 Häberlen, O. D.; Chung, S.-C.; Stener, M.; Rösch, N. *J. Chem. Phys.* **1997**, *106*, 5189.

34 (a) Ionita, P.; Caragheorgheopol, A.; Gilbert, B. C.; Chechik, V. *J. Am. Chem. Soc.* **2002**, *124*, 9048. (b) Ionita, P.; Caragheorgheopol, A.; Gilbert, B. C. and Chechik, V. *Langmuir* **2004**, *20*, 11536.

35 Chechik, V.; Wellsted, H. J.; Korte, A.; Gilbert, B. C.; Caldararu, H.; Ionita, P.; Caragheorgheopol, A. *Far. Disc.* **2004**, *125*, 279.

36 Chechik, V. *J. Am. Chem. Soc.* **2004**, *126*, 7780.

37 Handbook of Preparative Inorganic Chemistry, Brauer, G., Ed.; Academic Press: New York, **1965**; p 1054.

38 Donkers, R. L.; Lee, D. L.; Murray, R. W. *Langmuir*, **2004**, *20*, 1945.

39 Lowry, T. H.; Richardson, K. S. *Mechanism and Theory in Organic Chemistry*; 3 ed.; Harper & Row: New York, **1987**.

40 Guo, R; Murray, R. W. *J Am. Chem. Soc.* **2005**, *127(34)*, 12140.

41 The values of $k_{PE(I)}$ are initial rate constants and are taken at sufficiently large excesses of in-coming ligand that consideration of back-reaction rates is not necessary.

APPENDIX OF CHAPTER IV

Figure 4S-1. ^{1}H NMR spectrum of $Au_{38}(SC2Ph)_{24}$ in CD_2Cl_2. Triplet at ca. 3.1 ppm is from a- proton of $(Oct_4)NBr$ salt, triplet at ca. 0.9 ppm is from its methyl group, peaks at ca. 1.3 ppm are from its methylene groups.

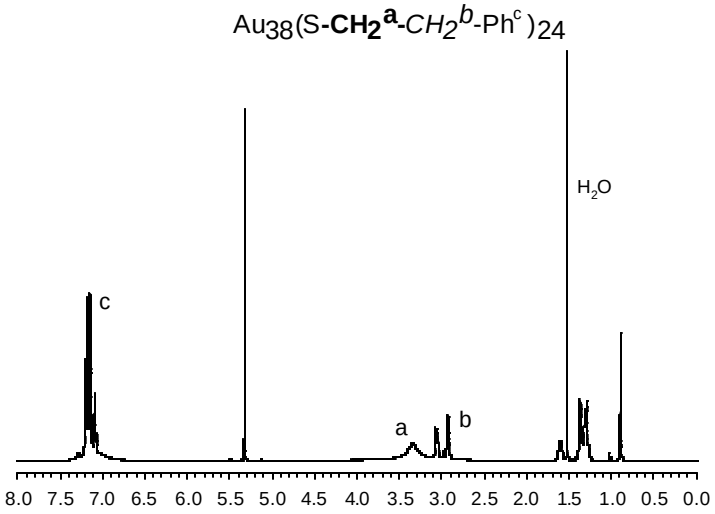
Au38(S-CH2a-CH2b-Phc)24
H2O
c
a
b
8.0 7.5 7.0 6.5 6.0 5.5 5.0 4.5 4.0 3.5 3.0 2.5 2.0 1.5 1.0 0.5 0.0

Figure 4S-2. Reaction profile for exchange of phenylethanethiolate (PhC2S-) by *p*-nitrothiophenol (NO_2PhSH) onto (Panel a) $Au_{38}(SC2Ph)_{24}$ and (Panel b) $Au_{140}(SC2Ph)_{53}$ at mole ratios of NO_2PhSH/ PhC2S- = 4.2 :1 and 1.3 :1, respectively. MPC concentration is 2.8×10^{-4} M in both cases and at the same temperature 293 K. Both %PhC2S-exchanged and number of ligand exchanged are indicated in Y-axis.

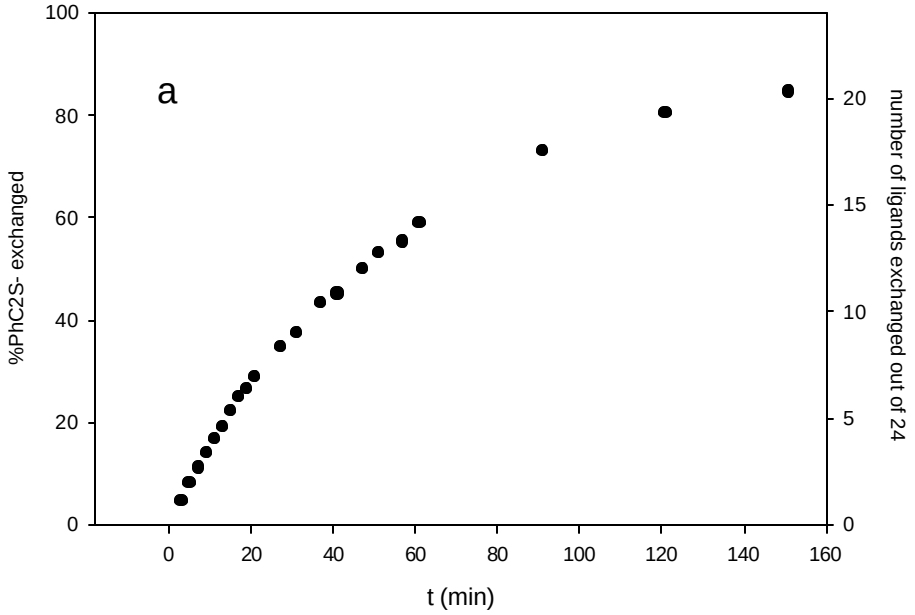
a
%PhC2S- exchanged
number of ligands exchanged out of 24
t (min)
0
20
40
60
80
100
120
140
160
0
5
10
15
20

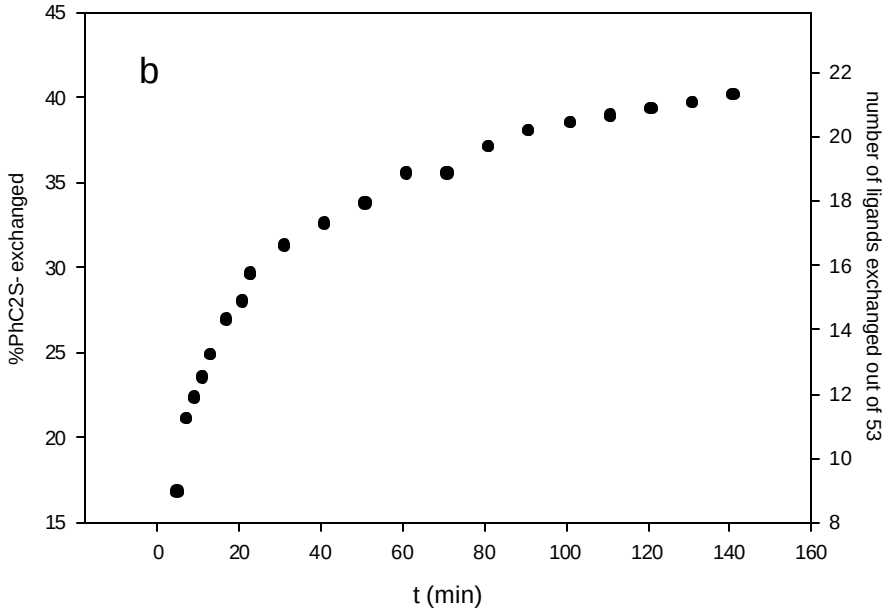
b
%PhC2S- excharged
number of ligands exchanged out of 53
t (min)
15
20
25
30
35
40
45
8
10
12
14
16
18
20
22
0
20
40
60
80
100
120
140
160

Figure 4S-3. Pseudo-first-order rate plots for exchange of phenylethanethiolate (PhC2S-) by 4-Bromothiophenol (4-Br-PhSH) onto (Panel a) $Au_{38}(SC2Ph)_{24}$ and (Panel b) $Au_{140}(SC2Ph)_{53}$ at mole ratio of 4-Br-PhSH/ PhC2S- = 6.7 :1 and 2.2 :1, respectively. MPC concentration is 2.8×10^{-4} M in both cases.

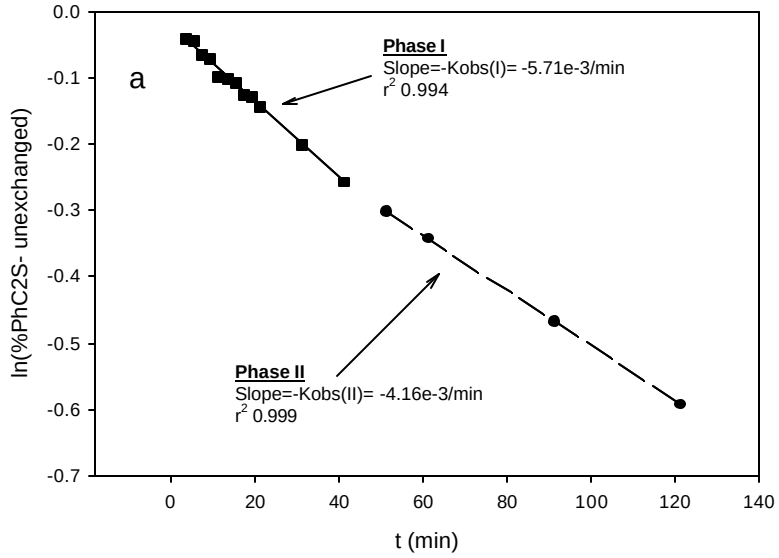
a
Phase I
Slope=-Kobs(I)= -5.71e-3/min
r2 0.994
Phase II
Slope=-Kobs(II)= -4.16e-3/min
r2 0.999
ln(%PhC2S- unexchanged)
t (min)
0.0
-0.1
-0.2
-0.3
-0.4
-0.5
-0.6
-0.7
0
20
40
60
80
100
120
140

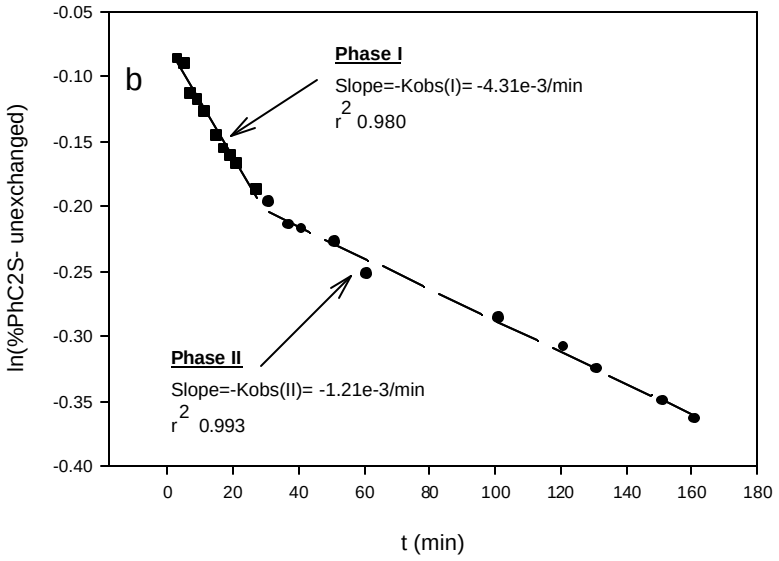
b
Phase I
Slope=-Kobs(I)= -4.31e-3/min
r2 0.980
Phase II
Slope=-Kobs(II)= -1.21e-3/min
r2 0.993
ln(%PhC2S- unexchanged)
t (min)
-0.05
-0.10
-0.15
-0.20
-0.25
-0.30
-0.35
-0.40
0
20
40
60
80
100
120
140
160
180

Figure 4S-4. Pseudo-first-order rate plots for exchange of phenylethanethiolate (PhC2S-) by *p*-toluenethiol (4-CH_3-PhSH) onto (Panel a) $Au_{38}(SC2Ph)_{24}$ and (Panel b) $Au_{140}(SC2Ph)_{53}$ at mole ratio of 4-CH_3-PhSH/ PhC2S- = 4.3 :1 and 3.3 :1, respectively. MPC concentration is 2.8×10^{-4} M in both cases.

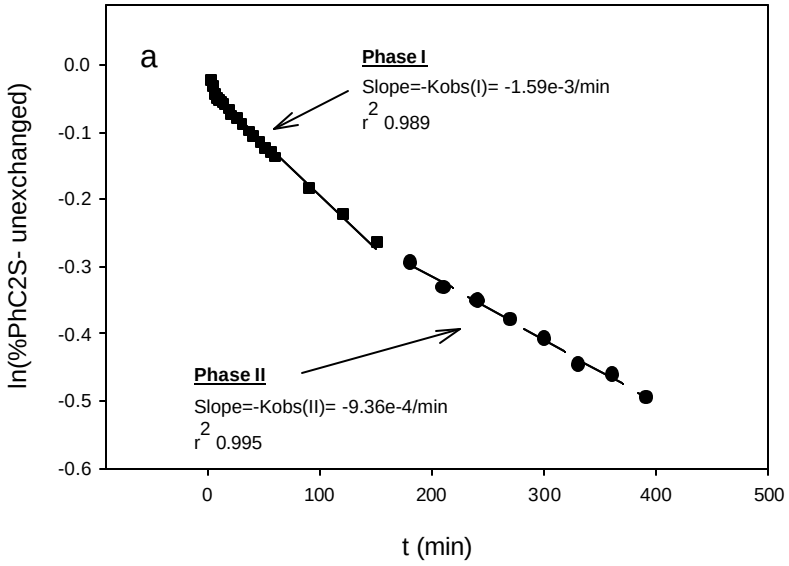
a
Phase I
Slope=-Kobs(I)= -1.59e-3/min
r2 0.989
Phase II
Slope=-Kobs(II)= -9.36e-4/min
r2 0.995
ln(%PhC2S- unexchanged)
t (min)
0.0
-0.1
-0.2
-0.3
-0.4
-0.5
-0.6
0
100
200
300
400
500

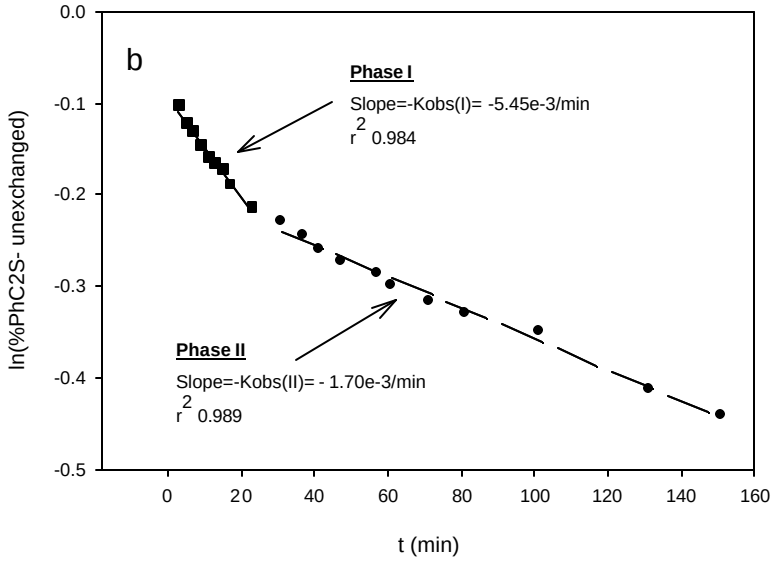
b
Phase I
Slope=-Kobs(I)= -5.45e-3/min
r2 0.984
Phase II
Slope=-Kobs(II)= - 1.70e-3/min
r2 0.989
ln(%PhC2S- unexchanged)
t (min)
0.0
-0.1
-0.2
-0.3
-0.4
-0.5
0
20
40
60
80
100
120
140
160

Figure 4S-5. Second-order rate plot (**Phase II**) of $Au_{38}(SC2Ph)_{24}$ for in-coming ligand HS-Ph-NO_2.

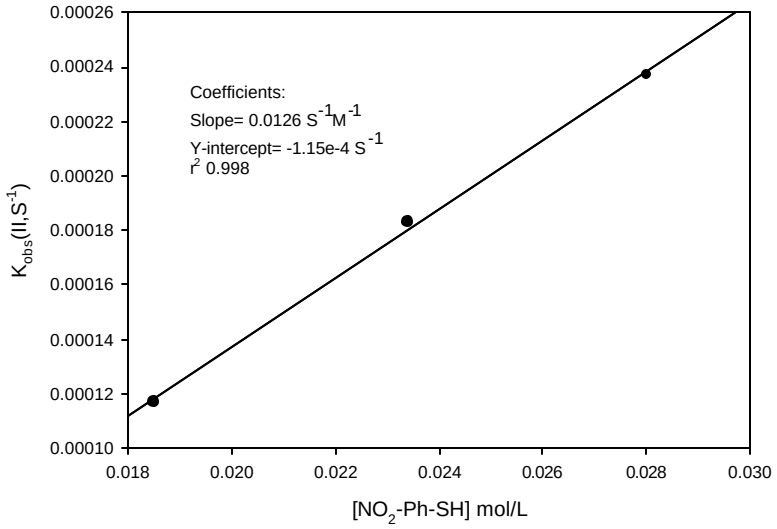
0.00026
0.00024
0.00022
0.00020
0.00018
0.00016
0.00014
0.00012
0.00010
Coefficients:
Slope= 0.0126 S-1M-1
Y-intercept= -1.15e-4 S-1
r2 0.998
Kobs(II,S-1)
0.018
0.020
0.022
0.024
0.026
0.028
0.030
[NO2-Ph-SH] mol/L

Figure 4S-6. ^{1}H NMR spectrum of $Au_{38}(SPh\text{-}NO_2)_{24}$ in CD_2Cl_2. The disappearance of triplet at ca. 2.9 ppm indicates that the PhC2S-thiolate on the nanoparticle is fully replaced by -SPh-NO_2 thiolate.

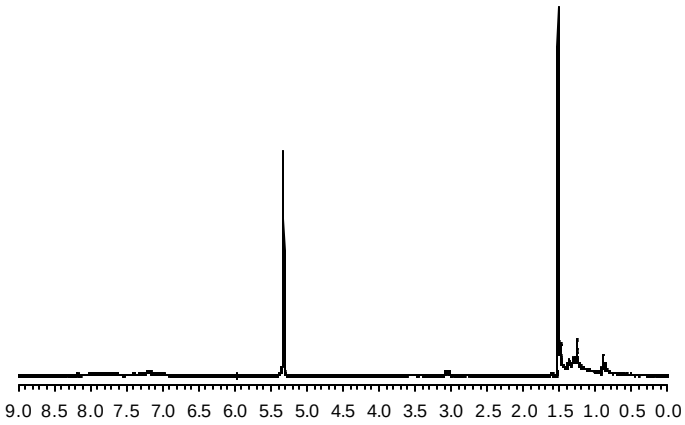
9.0 8.5 8.0 7.5 7.0 6.5 6.0 5.5 5.0 4.5 4.0 3.5 3.0 2.5 2.0 1.5 1.0 0.5 0.0

Chapter V

SUBSTITUENT EFFECTS ON REDOX POTENTIALS AND OPTICAL GAP ENERGIES OF MOLECULE-LIKE $Au_{38}(SPhX)_{24}$ NANOPARTICLES

5.1 Introduction

Unsupported Au nanoparticles with dimensions of a few nanometers and protected by a monolayer of thiolated ligands (MPCs) display interesting properties such as single-electron charging and molecule-like homo-lumo energy gaps, and offer uses in optical and chemical sensing.[1, 2] $Au_{38}(SC2Ph)_{24}$ (SC2Ph = phenylethylthiolate) is an example[3] of a molecule-like nanoparticle, exhibiting a *ca*. 1.33 eV homo-lumo (highest, lowest occupied molecular orbitals) energy gap, as assessed[4] from redox potential and optical absorbance band-edge measurements. Replacing the original protective ligands of such nanoparticles with new ligands is an important way to introduce new chemical functionality for various purposes.[2,5,6] This chapter reports that, in the case of Au_{38} nanoparticles, changes in the ligand monolayer can *also* provoke substantial change in energies for removing or adding electrons to the core; i.e., the monolayer of "monolayer-protected clusters" (MPCs)[2] is more than a merely protective capping shell or source of reactive functionality.

In a recent study[7] of the kinetics of ligand exchanges on $Au_{38}(SC2Ph)_{24}$ MPCs, we found that the original ligands could be exhaustively replaced by *p*-substituted thiophenolate ligands (~100% by ^{1}H NMR), without apparent change in the Au_{38} core. This enabled the

preparation of a new series of nanoparticles, $Au_{38}(SPhX)_{24}$ (where X= NO_2, Br, H, CH_3, OCH_3), and allowed subsequent examination of how the substituent "X" affects the core electronic energies, notably the homo energies and homo-lumo energy gaps of $Au_{38}(SPhX)_{24}$. Substituent effects on reversible redox potentials of small molecules are well-known, as are linear free energy correlations with Hammett σ constants.[8] Structural effects on redox potentials of polyoxometallate nanoparticles are also known.[9] There has been to our knowledge, however, no previous observation of substituent effects on redox properties of metal nanoparticles.

5.2 Experimental Section

5.2.1 Chemicals. 4-Nitrothiophenol (ACROS, 95%), *p*-toluenethiol (ACROS, 98%), 4-methoxybenzenethiol (ACROS, 98%), phenylethylthiol (PhC2SH, Aldrich, 98%), 4-bromothiophenol (Aldrich, 95%), 4-mercaptophenol (Aldrich, 90%), tetra-*n*-octylammonium bromide (Oct_4NBr, Fluka, 98%), tetra-butylammonium perchlorate (Bu_4NClO_4, Fluka, ≥ 99%), sodium borohydride (Aldrich, 99%), toluene (Fisher), methylene chloride (Fisher) and d_2-methylene chloride (Cambridge Isotope Laboratories, Inc.) were all used as received. Water was purified with a Barnstead NANOpure system.

5.2.2 Synthesis of $Au_{38}(SPhX)_{24}$ nanoparticles by ligand exchange reactions of thiophenols HSPhX with $Au_{38}(SC2Ph)_{24}$. Typically, 6 mg $Au_{38}(SC2Ph)_{24}$ MPCs[7] dissolved in 2ml CH_2Cl_2 (not degassed) were reacted with a 4 to 8 molar excess (molar ratio of HSPhX/PhC2S-) of in-coming thiol HSPhX (X= NO_2, Br, H, CH_3, OCH_3) for periods from overnight to 2 days (depending on the X group; $HSPhNO_2$ takes less time to reach complete exchange, $HSPhOCH_3$ takes longer). After the reaction, the solvent is evaporated and the

product washed copiously with MeOH to remove excess thiol. ^{1}H NMR shows no signal from residual bound PhC2S- ligand, indicating close to 100% ligand exchange.

5.2.3 Measurements. Osteryoung square wave voltammetry (OSWV) was performed at 11°C in 0.1M Bu_4NClO_4/CH_2Cl_2 using a Bioanalytical Systems (BAS) Model 100B. (Cyclic voltammograms (not shown) are also routinely taken as a quality check.) The 1.6 mm dia. Pt working electrode was polished, rinsed and sonicated in NANOpure water, rinsed with absolute ethanol and acetone, and cleaned by potential-cycling in 0.5 M H_2SO_4 for 15 min. A Pt coil counter electrode and Ag wire quasi-reference electrode were used. Sublimed ferrocene was added as an internal reference.

^{1}H NMR spectra of $Au_{38}(SPhX)_{24}$ and $Au_{38}(SC2Ph)_{24}$ in d_2-methylene chloride were collected with a Bruker AC400 spectrometer. UV-vis spectra of $Au_{38}(SPhX)_{24}$ and $Au_{38}(SC2Ph)_{24}$ in methylene chloride were taken using a Shimadzu UV-1601 UV-visible spectrophotometer.

5.3 Results and Discussion

The voltammetry of the new series of nanoparticles $Au_{38}(SPhX)_{24}$ follows a pattern of electron transfers similar[4] to that of the parent, $Au_{38}(SC2Ph)_{24}$, as shown in the square wave voltammetric results of Figure 5.1 (Actually the core size is also pretty much maintained, see Figure 5.2). The current peaks for $Au_{38}^{1+/0}$ and $Au_{38}^{2+/1+}$ represent the successive removal of single electrons from the homo level. The peak for $Au^{0/-1}$ represents the first reduction step (lumo). These potentials include charging energies.[10] Notably, the peaks shift to more positive potentials—relative to ferrocene$^{0/1+}$ as internal standard—by as much as 450 mV, as "X" is changed from electron-donating (OCH_3) to electron-withdrawing (NO_2). At the same time, the electrochemical gap ΔV_0 between the first oxidation peak and the first reduction

Figure 5.1 Osteryoung square wave voltammograms (positive-going scan only) of A) $Au_{38}(SPhNO_2)_{24}$, B) $Au_{38}(SPhBr)_{24}$, C) $Au_{38}(SPh)_{24}$, D) $Au_{38}(SPhCH_3)_{24}$, E) $Au_{38}(SPhOCH_3)_{24}$, F) $Au_{38}(SC2Ph)_{24}$ at 11°C in 0.1M Bu_4NClO_4/CH_2Cl_2. The core charge states and spacing between peaks are labeled. The potential scale was calibrated with ferrocene as internal standard (voltammetry not shown).

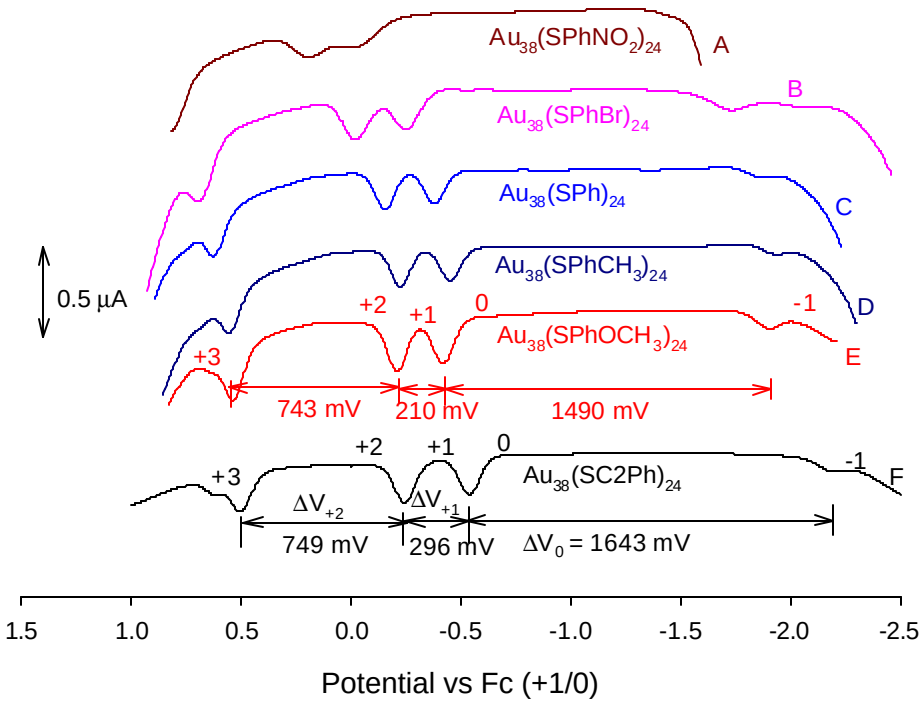
Au38(SPhNO2)24
A
B
Au38(SPhBr)24
Au38(SPh)24
C
Au38(SPhCH3)24
0.5 µA
+2
+1
0
-1
D
Au38(SPhOCH3)24
E
+3
743 mV
210 mV
1490 mV
+2
+1
0
-1
+3
Au38(SC2Ph)24
F
ΔV+2
ΔV+1
749 mV
296 mV
ΔV0 = 1643 mV
1.5
1.0
0.5
0.0
-0.5
-1.0
-1.5
-2.0
-2.5
Potential vs Fc (+1/0)

Figure 5.2 TEM images and associated size histograms of $Au_{38}(SC2Ph)_{24}$ (A) and $Au_{38}(SPhOCH_3)_{24}$ (B). Although some larger size nanoparticles (> 2.5 nm) appear in the TEM image in (B), there remain significant amounts of nanoparticles of the original size, ~ 1.2 nm. No surface plasmon band at 520 nm appears in UV-Vis spectra nor do any extra peaks appear in electrochemistry of the exchange product.

(A) $Au_{38}(SC2Ph)_{24}$: 1.2 ± 0.32 nm

(B) $Au_{38}(SPhOCH_3)_{24}$: 1.35 ± 0.49 nm

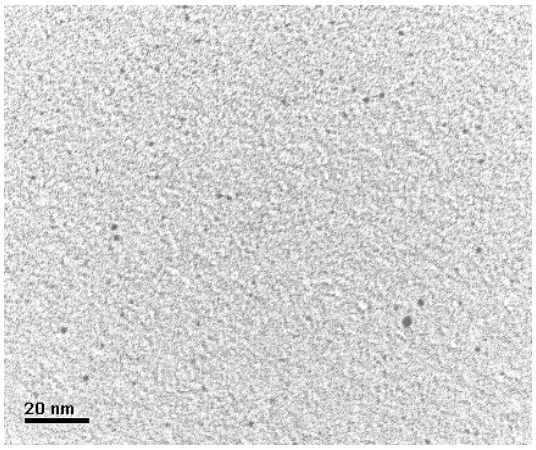

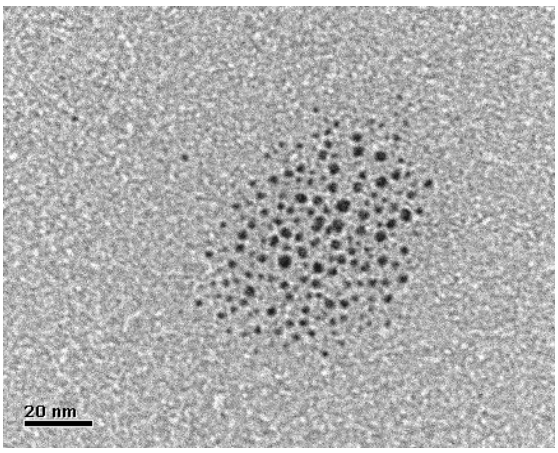

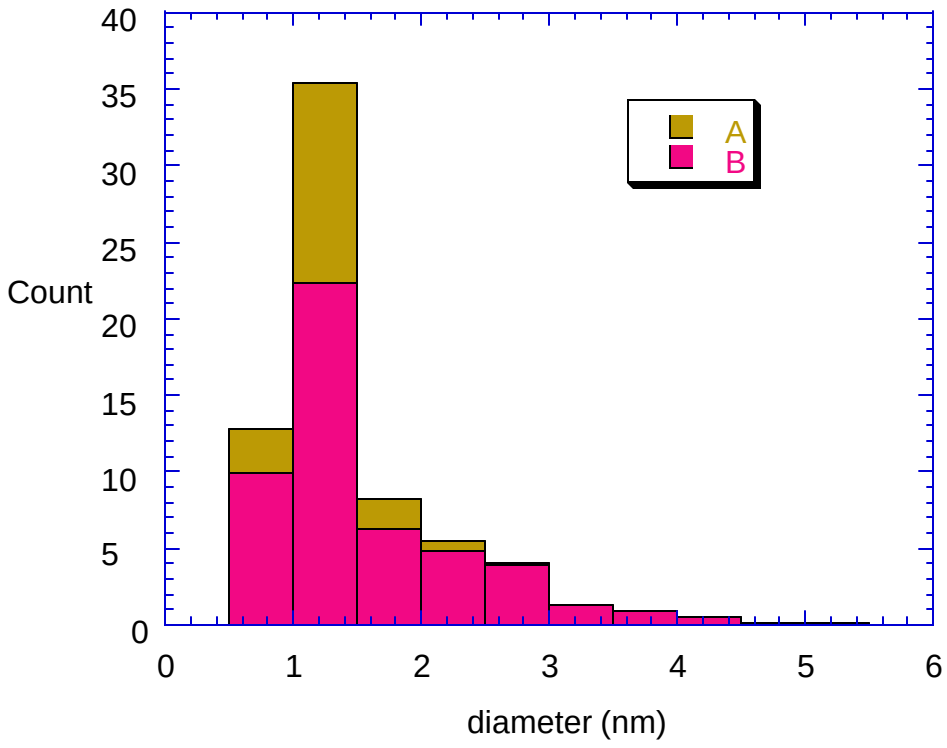

Table 5.1 Osteryoung square wave voltammetry[a] and optical[b] absorbance band-edge results for Au_{38} nanoparticles.

Peak spacing[c] / Au_{38} NPs	ΔV_{+2} (V)	ΔV_{+1} (V)	ΔV_0 electrochemical gap, V	$\Delta V_0 - \Delta V_{+1}$ corrected echem gap,V	optical band-edge, eV
$Au_{38}(SPhNO_2)_{24}$	N/A	0.21_8	N/A	N/A	1.30
$Au_{38}(SPhBr)_{24}$	0.71_3	0.22_6	1.50	1.27	1.30
$Au_{38}(SPh)_{24}$	0.75_7	0.21_0	1.49_4	1.28	1.29
$Au_{38}(SPhCH_3)_{24}$	0.76_1	0.22_6	1.48_5	1.26	1.30
$Au_{38}(SPhOCH_3)_{24}$	0.74_3	0.21_0	1.49	1.28	1.30
$Au_{38}(SC2Ph)_{24}$	0.74_9	0.29_6	1.64_3	1.34_7	1.34[d]

[a] Voltammetry acquired at 11°C in 0.1M Bu_4NClO_4/CH_2Cl_2. Formal potentials in Figure 5.3, and peak spacings in this table, are averages of peak potentials in positive and negative-going potential scans, to cancel out iR_{UNC} distortion. See Supporting Information for the complete data set. [b] in CH_2Cl_2 solutions. [c] See Figure 5.1 for definitions of ΔV parameters. Estimated uncertainties in ΔV and band edges are 0.01-0.02V. [d] Agrees with previous (Ref. 4) data, 1.33 eV, within experimental uncertainty.

peak, *ca*. 1490±10 mV, and ΔV_{+1} between the first and second oxidation peaks, *ca*. 220±10 mV, are nearly constant within the $Au_{38}(SPhX)_{24}$ nanoparticle series (Table 5.1).

The observed shifts of the Au_{38} homo and lumo energies with "X" are consistent with the classical expectation[8] that electron-withdrawing substituents drive the formal potential for oxidation of a molecular electron donor to more positive values. Hammett constants offer one route for analysis of electron inductive effects of molecular substituents (another is outlined below). Figure 5.3 presents Hammett substituent plots of the formal potentials ($E^{o'}$, see Table 5.2) of the two oxidation peaks and the one reduction peak of the MPCs $Au_{38}(SPhX)_{24}$. All three plots are reasonably linear, with similar slopes (0.43 V for the oxidations and 0.35 V for the reduction). While these slopes are similar to the 0.1-0.5 V values[8a] common in classical substituent correlations to electrochemical potentials of benzene derivatives, the Au_{38} system is unique in that there are a large number (24) of substituents. Little is known about the spatial distribution of the homo and lumo molecular orbitals that are measured by the voltammetry of the Au_{38} nanoparticles, or whether, for example, the electron "hole" in Au_{38}^{1+} is delocalized over the entire core surface, or is localized to certain, degenerate kinds of surface sites and undergoes exchange among them. Theory[11] by Landman for methylthiolate-coated Au_{38} casts the homo orbital as a three-fold degenerate state, concentrated around the outermost 24 Au atoms and surrounding 24 sulfur atoms. Experiments indicate a non-uniform chemistry of the Au_{38} core surface, notably variations in ligand exchange kinetics[7] and luminescence results[12] showing the presence of surface electronic states on their cores. (Extrinsic surface states are well-established[13] as sources of mid-gap luminescence of semiconductor quantum dots.) It seems possible, then, that the homo orbital whose associated redox potentials in Figure 5.1 are affected by the

Table 5.2 Formal potentials of Au_{38} nanoparticles, vs. ferrocene$^{1+/0}$. Voltammetry acquired at 11°C in 0.1M Bu_4NClO_4/CH_2Cl_2. Formal potentials are averages of peak potentials in positive and negative-going square wave voltammetry potential scans, in order to cancel out iR_{UNC} distortion.

$E^{o'}$ / Au_{38} NPs	$V_{3+/2+}$ (V)	$V_{2+/1+}$ (V)	$V_{1+/0}$ (V)	$V_{0/-1}$ (V)
$Au_{38}(SPhNO_2)_{24}$	N/A	0.211	-0.007	N/A
$Au_{38}(SPhBr)_{24}$	0.689	-0.024	-0.250	-1.750
$Au_{38}(SPh)_{24}$	0.587	-0.170	-0.380	-1.874
$Au_{38}(SPhCH_3)_{24}$	0.537	-0.224	-0.450	-1.935
$Au_{38}(SPhOCH_3)_{24}$	0.533	-0.210	-0.420	-1.910
$Au_{38}(SC2Ph)_{24}$	0.505	-0.244	-0.540	-2.183

Figure 5.3 Plot of formal potentials of $Au_{38}(SPhX)_{24}$ couples versus standard substituent σ_X constants (ref. 8). (Square wave voltammetry potentials are "half-wave potentials" and differ from true formal potentials E^{o}' by log(ratio of diffusion coefficients of oxidized and reduced forms). This ratio is not expected to vary significantly with "X".)

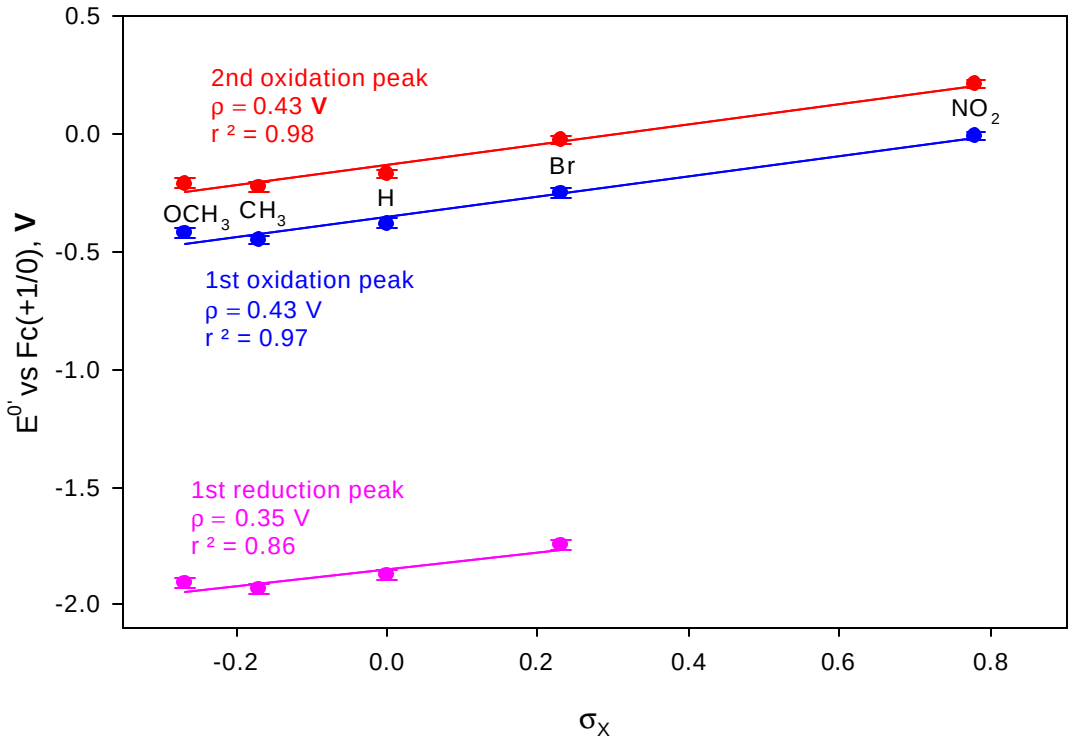
0.5
0.0
-0.5
-1.0
-1.5
-2.0
-0.2
0.0
0.2
0.4
0.6
0.8
E0' vs Fc(+1/0), V
σX
2nd oxidation peak
ρ = 0.43 V
r ² = 0.98
1st oxidation peak
ρ = 0.43 V
r ² = 0.97
1st reduction peak
ρ = 0.35 V
r ² = 0.86
OCH3
CH3
H
Br
NO2

substituents' properties, is not uniformly distributed over the core surface, but has significant amplitude only on a sub-set of the Au-thiolate bonding sites on the nanoparticle surface (such as the vertices). Whether the orbital is delocalized over those sites is unknown. However, the very presence of substituent effects and Hammett correlation of redox potentials for this small nanoparticle serve to emphasize its molecule-like nature.

The homo-lumo gap energies of the $Au_{38}(SPhX)_{24}$ nanoparticles can be estimated from their electrochemical gap energies (ΔV_0) by correcting for charging energy[10] (a factor associated with solvation/ion association of the electron donor and acceptor states). For $Au_{38}(SC2Ph)_{24}$, we estimated[4,14] the charging energy from the potential spacing between the first and second oxidation steps (ΔV_{+1} = 0.30 V), giving a corrected gap energy (Table 5.1) that was in accord with the 1.34 optical band edge result. Similarly, correcting ΔV_0 for the $Au_{38}(SPhX)_{24}$ nanoparticles (Table 5.1, "corrected echem gap") gives a (smaller) homo-lumo gap energy of 1.27±0.01 eV that is *unresponsive* to the substituent X, i.e., the "X" substituent must exert a nearly identical electronic effect on both homo and lumo energies. That the estimated $Au_{38}(SPhX)_{24}$ homo-lumo gaps are smaller than that of $Au_{38}(SC2Ph)_{24}$ is consistent with the similar (to $Au_{38}(SC2Ph)_{24}$) 1.33 eV absorbance band-edge energy result[15] for the related hexanethiolate-protected nanoparticle $Au_{38}(SC6)_{24}$. While the effects of X substituents in the $Au_{38}(SPhX)_{24}$ series are presumably largely inductive, the estimated electrochemical (and optical) homo-lumo gap differences between $Au_{38}(SC2Ph)_{24}$ and $Au_{38}(SPhX)_{24}$ MPCs suggests a possible minor role of resonance stabilization (present for $Au_{38}(SPhX)_{24}$ but not $Au_{38}(SC2Ph)_{24}$) of core electronic energies. Resonance interactions of ligands with nanoparticles is an unexplored topic and study of aromatic thiolated ligands has been initiated.

Optical absorbance band edges are shown in Figure 5.4 for $Au_{38}(SC2Ph)_{24}$ and $Au_{38}(SPhX)_{24}$ MPCs. All spectra show the absorbance shoulder just above the edge associated[4] with homo level occupancy. While the step-like higher energy absorbance features of $Au_{38}(SPhX)_{24}$ do vary modestly with X (Figure 5.4a), the optical band edge energies in the $Au_{38}(SPhX)_{24}$ series are again unresponsive to X (Table 5.1) and, while slightly larger than the electrochemical gap estimates, still show a smaller homo-lumo gap relative to $Au_{38}(SC2Ph)_{24}$.

An alternative analysis of the data in Figure 5.3 can be fashioned. Variations in (inductive) Hammett substituent constants are simply indirect representations of the substituents' effects on the molecular dipole moments of the thiolated ligands. The collective (and ordered, with respect to the nanoparticle core surface) dipole of the 24 $–NO_2$ substituents in $Au_{38}(SPhNO_2)_{24}$ would yield, effectively, an increase in the core work function, corresponding changes in nanoparticle ionization potential and electron affinity, and thus in redox potentials. One can estimate[16] that the 0.45V shift in $Au_{38}^{1+/0}$ redox potential can be accounted for by a not-unreasonable difference of ~1.2 D between the dipole moments of $–SPhCH_3$ and $–SPhNO_2$ ligands. This electrostatic analysis of the redox behavior of $Au_{38}(SPhX)_{24}$ nanoparticles ignores, of course, their molecular character. One is reminded of an analogous, molecular double layer capacitance, representation of electrostatic effects on the potentials of serial electron transfers by Weaver.[17]

It is also noteworthy that the previously reported[7,18] rate constants of ligand exchanges in which -SC2Ph ligands are replaced by–SPhX ligands also display a substituent effect, and Hammett correlation, in which X = NO_2 leads to the fastest exchange rates (*in either direction* of exchange[7]) and X = CH_3 the slowest. Effects of a substituent on a buildup of

Figure 5.4 UV-vis spectra of (a) $Au_{38}(SC2Ph)_{24}$ and $Au_{38}(SPhX)_{24}$ nanoparticles in CH_2Cl_2. (b) Optical band edge of $Au_{38}(SC2Ph)_{24}$ and $Au_{38}(SPhOCH_3)_{24}$.

(a)

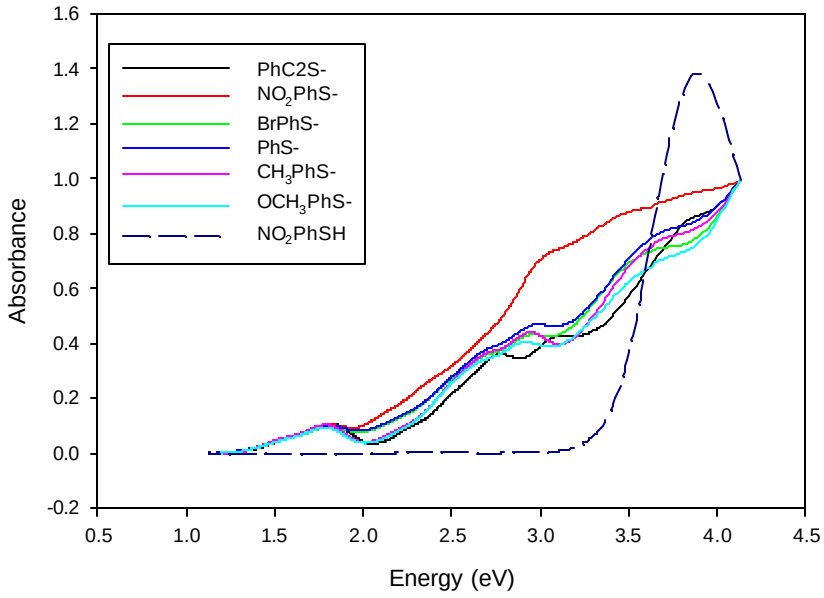
PhC2S-
NO2PhS-
BrPhS-
PhS-
CH3PhS-
OCH3PhS-
NO2PhSH
Absorbance
Energy (eV)

(b)

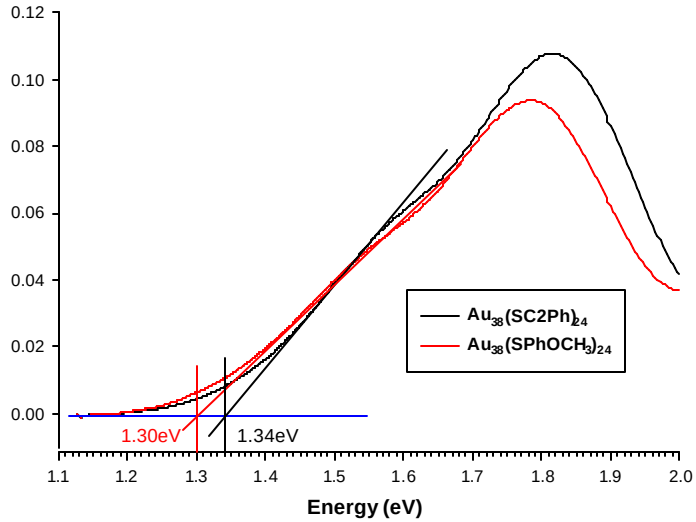
Au38(SC2Ph)24
Au38(SPhOCH3)24
1.30eV
1.34eV
Energy (eV)

charge at the Au-S interface in the rate-determining step of a ligand exchange is obviously consonant with a substituent effect on the energy of loss or gain of electronic charge at that interface.

In summary, this chapter describes a molecule-like substituent effect on the redox formal potentials of the nanoparticle series $Au_{38}(SPhX)_{24}$, in which electron-withdrawing substituents energetically favor reduction and disfavor oxidation. The ligand monolayer of the nanoparticles is shown thereby to play a strong role in determining the electronic energies in the nanoparticle core. The substituent effect does not, however, produce a change in the homo-lumo gap energy, being identical for the homo and lumo levels, which is consistent with a mainly inductive effect of the ligand.

5.4 Notes and references

1 (a) Storhoff, J. J.; Mirkin, C. A. *Chem. Rev.*, **1999**, *99*, 1849. (b) Nam, J. M.; Thaxton, C. S.; Mirkin, C. A. *Science*, **2003**, *301*, 1884. (c) Zanchet, D. M.; Micheel, C. M.; Parak, W. J.; Gerison, D.; Alivisatos, A. P. *NanoLett*., **2001**, *1*, 32. (d) Chen, S.; Ingram, R. S.; Hostetler, M. J.; Pietron, J. J.; Murray, R. W.; Schaaff, T. G.; Khoury, J. T.; Alvarez, M. M.; Whetten, R. L. *Science*, **1998**, *280*, 2098.

2 Templeton, A. C.; Wuelfing, W. P.; Murray, R. W. *Acc. Chem. Res.*, **2000**, *33*, 27.

3 Donkers, R. L.; Lee, D.; Murray, R. W. *Langmuir*, **2004**, *20*, 1945.

4 Lee, D.; Donkers, R. L.; Wang, G.; Harper, A. S.; Murray, R. W. *J. Amer. Chem. Soc.*, **2004**, *126*, 6193.

5 (a) Woehrle, G. H.; Warner M. G.; Hutchison, J. E. *J. Phys. Chem. B*, **2002**, *106*, 9979. (b) Woehrle, G. H.; Brown, L. O.; and Hutchison, J. E. *J. Amer. Chem. Soc.* **2005**, *127*, 2172-2183.

6 Yang, Y.; Chen, S. *NanoLett*., **2003**, *3*, 75.

7 Guo, R.; Song, Y.; Wang G.; Murray, R. W. *J. Amer. Chem. Soc.* **2005**, *127*, 2752-2757.

8 (a) Zuman, P. *Substituent Effects in Organic Polarography*, Plenum, New York, **1967**, Chap. 1, Tables III-1,4. (b) Lin, C.; Fang, M.; Cheng, S. *J. Electroanalyt. Chem.* **2002**, *531*, 155-162. (c) Graff, J. N.; McElhaney, A. E.; Basu, P.; Gruhn, N. E.; Chang, C.; Enemark, J. H. *Inorg. Chem.* **2002**, *41*, 2642-2647. (d) Batterjee, S. M.; Marzouk, M.I.; Aazab, M. E.; EI-hashash, M. A. *Appl. Organometal. Chem.* **2003**, *17*, 291-297. (e) Johnston, R. F.; Borjas, R. E.; Furilla, J. L. *Electrochimica Acta*, **1995**, *40*, 473-477. (f) Hansch, C.; Leo, A.; Taft, R. W. *Chem. Rev.* **1991**, *91*, 165-195.

9 Keita, B.; Mbomekalle, I-M.; Nadjo, L.; Haut, C. *Electrochem. Commun.* **2004**, *6*, 978-983.

10 Franceschetti, A.; Zunger, A. *Phys. Rev. B* **2000**, *62*, 2614.

11 (a) Häkkinen, H.; Barnett, R. N.; Landman, U. *Phys. Rev. Lett.* **1999**, *82*, 3264. (b) Häberlen, O. D.; Chung, S.-C.; Stener, M.; Rösch, N. *J. Chem. Phys.* **1997**, *106*, 5189.

12 Wang, G.; Huang, T.; Murray, R. W. Menard, L; Nuzzo, R. G. *J. Am. Chem. Soc.* **2005** *127*, 812.

13 (a) Shim, M.; Shilov, S. V.; Braiman, M. S.; Guyot-Sionnest, P. J. Phys. Chem. B 2000, 104, 1494-1496. (b) Fu, H.; Zunger, A. Phys. Rev. B 1997, 56, 1496-1508.

(c) Poles, E.; Selmarten, D. C.; Micic, O. I.; Nozik, A. J. Appl. Phys. Lett. 1999, 75, 971-973.

14 The electrochemical gap ΔV_0 contains charging or addition energy terms (Ref. 10) that are estimated from the separation between the $Au_{38}^{+2/0}$ and $Au_{38}^{+1/0}$ formal potentials. That separation ΔV_{+1} is roughly represented by a concentric sphere capacitor model, $\Delta V_{+1} = e/C_{MPC} = ed/4\pi\varepsilon\varepsilon_0 r (r+d)$, where e is electron charge, ε_0 is the permittivity of free space, ε is the static dielectric constant of the monolayer medium around the metal core, r is the radius of the gold core, and d is the thickness of the monolayer medium. The ligand-specific parameters are ε and d. The model is approximate since it ignores solvation effects. The *effective* values of ε calculated from the model are 5.2 (SC2Ph), 6.5 ($SPhNO_2$), 6.2 (SPhBr), 6.3 (SPhH), 6.3 ($SPhCH_3$), and 7.2 ($SPhOCH_3$), based on d = 7.9, 6.5, 6.4, 5.7, 6.5, and 7.5 Å.

15 Jimenez, V. L.; Georganopoulou, D. G.; White, R. J.; Harper, A. S.; Mills, A. J.; Lee, D.; Murray, R. W. *Langmuir*, **2004**, *20*, 6864.

16 (a) This estimate, suggested by a reviewer[b)], draws on studies of substituent effects in self assembled monolayers, and the approximate relation $\Delta V \sim N (\mu_{CH3} - \mu_{NO2})/\varepsilon\varepsilon_o$ where ΔV is redox potential of X = CH_3 vs. X = NO_2, *N* = area density of the thiolate ligand, μ = ligand dipole moment for indicated substituent, ε the static dielectric constant of the ligand shell, and ε_o = free space permittivity. ε is taken as ~ 6.5 for the two ligands from application of a concentric sphere capacitor model[11] to the value of ΔV_{+1}. (b) Campbell, I. H.; Kress, J. D.; Martin, R. L.; Smith, D. L.; Barashkov, N. N.; Ferraris, J. P. *Appl. Phys. Lett.* **1997**, *71*, 3528-3530.

17 Weaver, M. J.; Gao, X. *J. Phys. Chem*. **1993**, 97, 332-338.

18 Donkers, R. L.; Song Y.; Murray, R. W. *Langmuir* **2004,** *20*, 4703-4707.

APPENDIX OF CHAPTER V

Figure 5S-1. NMR spectra of $Au_{38}(SPhNO_2)_{24}$ (A), $Au_{38}(SPhBr)_{24}$ (B), $Au_{38}(SPh)_{24}$ (C), $Au_{38}(SPhCH_3)_{24}$ (D), $Au_{38}(SPhOCH_3)_{24}$ (E), $Au_{38}(SC2Ph)_{24}$ (F) in CD_2Cl_2. Triplet at ca. 3.1 ppm is from α-proton of $(Oct)_4NBr$ salt impurity (ca. one Oct_4N^+ cation per MPC), triplet at ca. 0.9 ppm is from its methyl group, peaks at ca. 1.3 ppm are from its methylene groups.

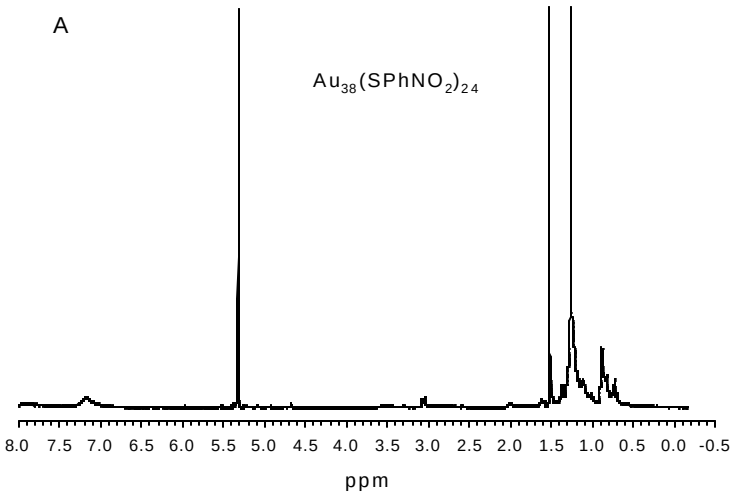
A
$Au_{38}(SPhNO_2)_{24}$
8.0 7.5 7.0 6.5 6.0 5.5 5.0 4.5 4.0 3.5 3.0 2.5 2.0 1.5 1.0 0.5 0.0 -0.5
ppm

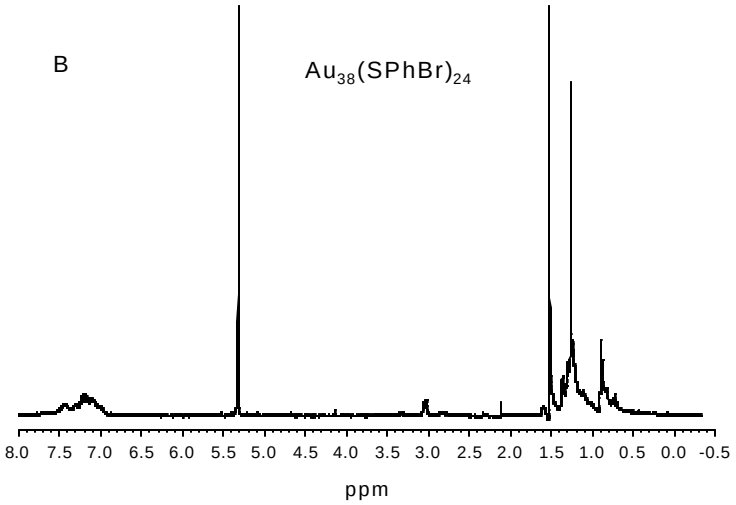
B
$Au_{38}(SPhBr)_{24}$
8.0 7.5 7.0 6.5 6.0 5.5 5.0 4.5 4.0 3.5 3.0 2.5 2.0 1.5 1.0 0.5 0.0 -0.5
ppm

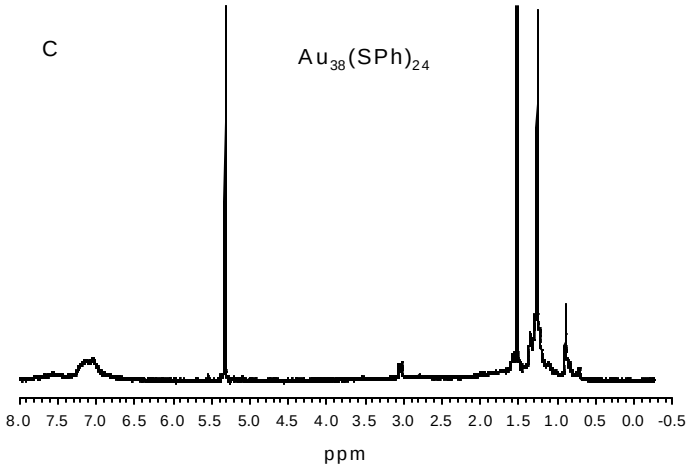
C
$Au_{38}(SPh)_{24}$
8.0 7.5 7.0 6.5 6.0 5.5 5.0 4.5 4.0 3.5 3.0 2.5 2.0 1.5 1.0 0.5 0.0 -0.5
ppm

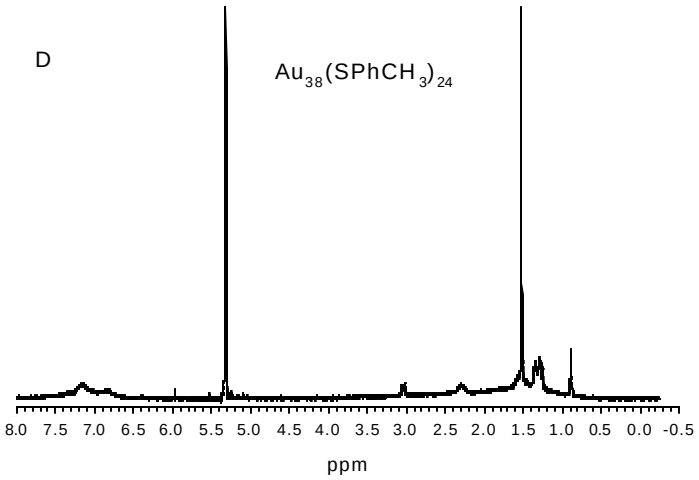
D
$Au_{38}(SPhCH_3)_{24}$
8.0 7.5 7.0 6.5 6.0 5.5 5.0 4.5 4.0 3.5 3.0 2.5 2.0 1.5 1.0 0.5 0.0 -0.5
ppm

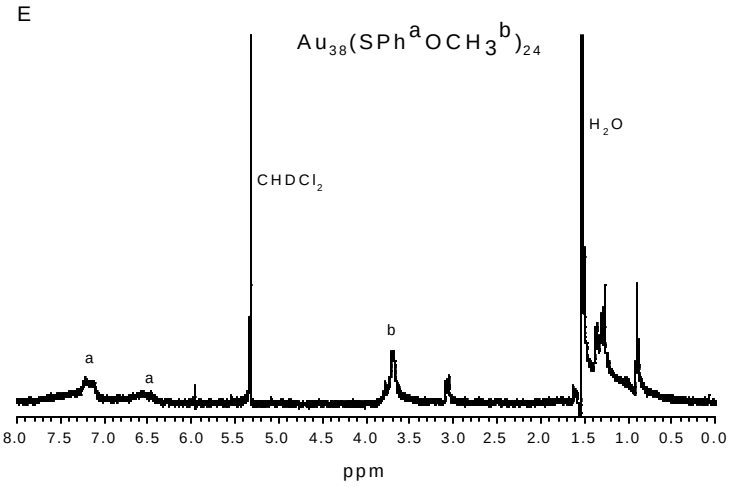
E
$Au_{38}(SPh^{a}OCH_3{}^{b})_{24}$
H_2O
$CHDCl_2$
a
a
b
8.0 7.5 7.0 6.5 6.0 5.5 5.0 4.5 4.0 3.5 3.0 2.5 2.0 1.5 1.0 0.5 0.0
ppm

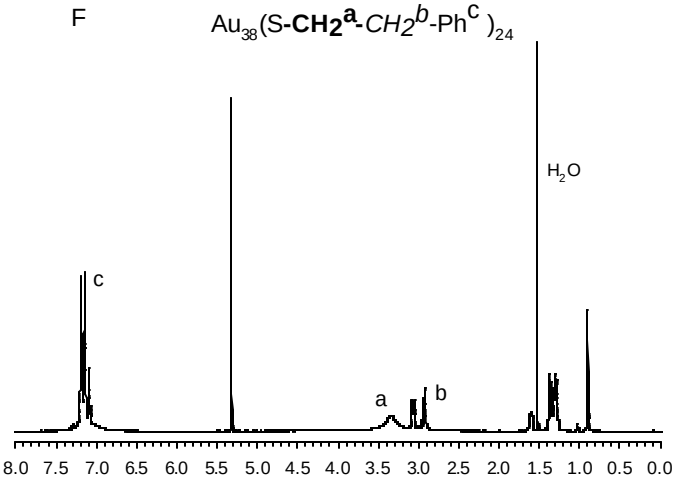
F
$Au_{38}(S\text{-}\mathbf{CH_2^{a}}\text{-}CH_2^{b}\text{-}Ph^{c})_{24}$
H_2O
c
a
b
8.0 7.5 7.0 6.5 6.0 5.5 5.0 4.5 4.0 3.5 3.0 2.5 2.0 1.5 1.0 0.5 0.0

Chapter VI

LIGAND DEPENDENT OPTICAL PROPERTIES OF $Au_{38}(SC2Ph)_{24}$ DURING LIGAND EXCHANGE REACTIONS IN TETRAHYDROFURAN

6.1 INTRODUCTION

Brust synthesis[1] of thiolate monolayer-protected gold clusters (MPCs) has provoked a broad exploration of the chemistry and properties of Au nanoparticles in the < 3 nm size range. An alternative way to obtain very small nanoparticles is by using poly(amidoamine) (PAMAM) dendrimers to sequester small numbers of metal ions, including gold, [2,3] which are then reduced to PAMAM-encapsulated nanoparticles. Interest on MPCs has been focused on several aspects: a) synthetic control of MPC core dimensions,[4-7] b) separation[8-14] and analysis[15,16] of MPC size and composition especially with respect to producing more monodisperse samples, c) chemistry of the alkanethiolate ligands including reactions of appended ligand functionalities,[17,18] ligand exchange reactions, [19-21] dispersity of ligand properties as detected chromatographically[14] and by NMR, [22-24] and the ligand effects on MPC properties especially for <100 atom MPC cores,[24-26] and d) core size dependent properties, such as electrochemical[22] and spectroscopic properties.[23] It was found that core sizes of MPCs produced by the Brust synthesis[1] lie in the transition between bulk and molecular regimes where bulk electron energetics yield first to quantized capacitance-based charging properties[27,28] and then to quantum confinement effects and emergence of discrete

molecule-like electronic states,[26, 29,30] e.g., the metal to molecule transition. The results show that the transition occurs over a remarkably sharp range of dimensions for Au nanoparticles, i.e., HOMO-LUMO energy gaps are undetectable (< ca. 0.1 eV) for 1.6 nm[27] cores (Au_{140}) but are measurable for 1.4 nm diameter Au cores (Au_{75}).[30]

Due to efficient non-radiative decay and the absence of an energy gap, luminescence[31,32] of metals is usually very weak. Quantum confinement effects become important when the dimensions of the metal are sufficiently decreased thus luminescence becomes more likely. Luminescence properties of a variety of < 5 nm Au nanoparticles with capping ligands varying from PAMAM[3] dendrimer to thiolate,[33-36] has been reported. The luminescence energies of PAMAM-encapsulated Au nanoparticles are reported[3] to vary significantly with their size, from 3.2 to 1.4 eV for Au_5 to Au_{31}. In contrast, for thiolate-protected Au nanoparticles, their luminescence energies vary only modestly with size, for example that[35,36] for glutathione-protected MPCs ranging in size from Au_{10} to Au_{39} all lie in the 1.4-1.7 eV range. The broad 1.1-1.3 eV NIR emission[37] in a collection of Au_{13}, Au_{38}, and Au_{140} MPCs having a variety of different thiolate monolayers did not vary much either. Although the extent of size dependent luminescence is different for PAMAM-encapsulated and thiolate-protected gold nanoparticles, the trend is the same: intensities increase with decreasing size, and at the smallest sizes, quite impressive quantum efficiencies are obtained.[3, 37]

As mentioned above, a recent report has described[37] an insensitivity of NIR luminescence wavelengths to the core sizes of Au MPCs with dimensions in the 1-2 nm dia. range. This phenomenon was preliminarily interpreted as reflecting participation of surface electronic states in the emission process. The results also indicated[37] that the NIR

luminescence intensity varied with different thiolate ligands present in the MPC protective monolayer. In this chapter, we reported the ligand dependent optical properties of molecule-like $Au_{38}(SC2Ph)_{24}$ upon ligand exchange with different in-coming ligands and further confirmed that the NIR luminescence intensity is quite sensitive to the chemistry of the MPC thiolate ligands.

6.2 EXPERIMENTAL SECTION

6.2.1 Chemicals. 4-Nitrothiophenol (ACROS, 95%), 4-Chlorothiophenol (ACROS, 98%), *p*-toluenethiol (ACROS, 98%), 4-methoxybenzenethiol (ACROS, 98%), phenylethylthiol (PhC2SH, Aldrich, 98%), 4-bromothiophenol (Aldrich, 95%), 4-Mercaptophenol (Aldrich, 90%), 2-Mercaptoethanol (98%, Aldrich), 3-Mercaptopropionic acid (Aldrich, 99%), Tetrahydrofuran-d_8 (Aldrich, 99.5atom%D), sodium borohydride (Aldrich, 99%), 1-hexanethiol (Fluka, 95%), N-acetyl-L-cysteine (Sigma, 99%), N-(2-mercaptopropionyl)-glycine (Tiopronin, Sigma, 99%), Tetrahydrofuran (Sigma-Aldrich, 99.9%), tetra-*n*-octylammonium bromide (Oct_4NBr, Fluka, 98%), toluene (Fisher), were all used as received. Hydrogen tetrachloroaurate trihydrate (from 99.999% pure gold) was prepared by a literature procedure and stored in a freezer at –20^o C. Millipore Nanopure water purification system was used to obtain low conductivity water.

6.2.2 Synthesis of $Au_{38}(SC2Ph)_{24}$. $Au_{38}(SC2Ph)_{24}$ was synthesized as described before.[38] Briefly, in a two-phase Brust synthesis[1], hydrogen tetrachloroaurate (3.1g, 11.1 mmole) was phase-transferred into toluene with Oct_4NBr, followed by addition of a 3-fold molar excess (relative to Au) of phenylethylthiol, forming a gold(I)-thiol polymer. This was reduced by rapidly adding a 10-fold excess of aqueous $NaBH_4$ at 0^{o}C, vigorously stirring the solution at 0^{o}C for 20 hours. Removing the bottom aqueous layer, the toluene was rotary-evaporated at

room temperature and the $Au_{38}(SC2Ph)_{24}$ extracted from the crude product with acetonitrile. The dried product was washed copiously with methanol until mostly cleaned of Oct_4N^+ cation, according to ^1H NMR. The product was characterized by ^1H NMR and UV-Vis spectra as previously.

6.2.3 Synthesis of Au(I)-SR. Hydrogen tetrachloroaurate (0.31g, 1.11 mmole) was phase-transferred from H_2O into toluene with Oct_4NBr, followed by addition of a 3-fold molar excess (relative to Au) of different thiols, gold(I)-thiol polymers Au(I)-SR were formed and subjected to luminescence and UV-vis measurements.

6.2.4 Ligand Exchange Kinetics by ^1H NMR Spectroscopy. ^1H NMR spectra of solution mixtures of $Au_{38}(SC2Ph)_{24}$ (~ 5.0 mg/2.0 mL after mixing) and different thiol ligands (amounts varied based upon desired reactant ratios) in THF-d_8 (not degassed) were collected with a Bruker AC 500 MHz spectrometer. Ferrocene (sublimed, typically 0.6 mg/2.0 mL after mixing) served as an internal standard. Briefly, after acquiring a ^1H NMR spectrum of the initial solution (1mL) of ferrocene and in-coming thiol, it is rapidly mixed with the MPC solution (~5.0 mg/1mL), part of the solution mixture is placed in the pre-shimmed spectrometer for repetitive collection of 1-10 ppm (vs. TMS) spectra, using a 17 second acquisition time per spectrum and a time interval between spectra of 2 minutes. The rest of solution mixture is used for fluoresence and UV-vis measurements. The *ca*. 2.8 ppm quartet resonance originates exclusively from the liberated phenylethanethiol (HS-***CH_2***-CH_2Ph), which was used to monitor the extent of the exchange reaction as indicated in Figure 6.12.

6.2.5 Fluorescence and UV-vis Measurements. 5.5 μL $Au_{38}(SC2Ph)_{24}$ solution before mixing and 11 μL solution mixture after mixing with in-coming thiols are diluted with 3 mL

THF for optical measurements while ligand exchange kinetics are measured by ^{1}H NMR simultaneously. UV-vis spectra were taken with Shimadzu UV-1601 UV-visible spectrophotometer and luminescence spectra were taken in a 90 degree geometry on a modified ISA Fluorolog FL321 spectrometer, equipped with a 450W Xenon source and Hamamatsu R928 PMT (visible wavelengths) and InGaAs (near IR wavelengths, connected via a T channel) detectors. Dilute solutions (most UV absorbance less than 0.1 at 450 nm) were used to acquire fluorescence spectra in order to minimize the influences of self-absorbance and self-quenching. All luminescence sepctra were excited at 450 nm and the intensity of each spectrum has been normalized with respect to its UV-vis absorbance at 450 nm. Other than 4-nitrothiophenol, no obvious UV-vis absorbance is observed for the rest ligands at 450 nm. No Au(I)-SR (RSH are ligands used in this study) shows luminescence in the range where we studied luminescence from $Au_{38}(SC2Ph)_{24}$ and its exchange product.

6.3 RESULTS AND DISSCUSSION

6.3.1 Linear Dependency of Luminescence Intensity of $Au_{38}(SC2Ph)_{24}$ upon Ligand Exchange with 4-Bromothiophenol.

$Au_{38}(SC2Ph)_{24}$ shows a certain amount of luminescence with peak maximum at ca. 1050 nm. Ligand exchange kinetics are monitored by ^{1}H NMR simultaneously with the luminescence measurements (see Figure 6.12) as before. Figure 6.1 (a) shows the luminescence spectra of $Au_{38}(SC2Ph)_{24}$ in THF upon ligand exchange with 4-bromothiophenol. The luminescence intensity increased steadily as exchange process went on with only a slight blue shift of peak maximum. A small change of step-like structure in the range of 400 – 470 nm (mainly due to ligand effect) was observed in the corresponding UV-vis spectra, shown in Figure 6.1 (b), indicating the core size was basically maintained during ligand exchange reactions.

Figure 6.1 Luminescence spectra (excited at 450 nm) (a), and UV-vis spectra (b) of $Au_{38}(SC2Ph)_{24}$ upon ligand exchange with 4-bromothiophenol in THF. (c) Plot of number of exchanged 4-bromothiophenol ligands and luminescence intensity at 1020 nm versus time respectively. (d) Luminescence intensity at maximum versus number of PhC2S- ligands exchanged for various in-coming thiols: I 4-NO_2-PhSH; II 4-Cl-PhSH; III 4-Br-PhSH; IV 4-CH_3-PhSH; V 4-OCH_3-PhSH.

(a)

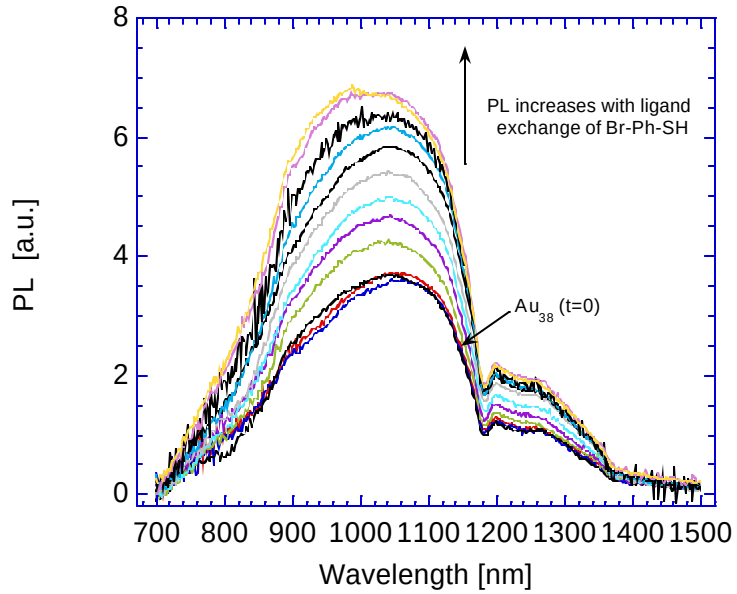
PL increases with ligand exchange of Br-Ph-SH
Au38 (t=0)
PL [a.u.]
Wavelength [nm]
0
2
4
6
8
700
800
900
1000
1100
1200
1300
1400
1500

(b)

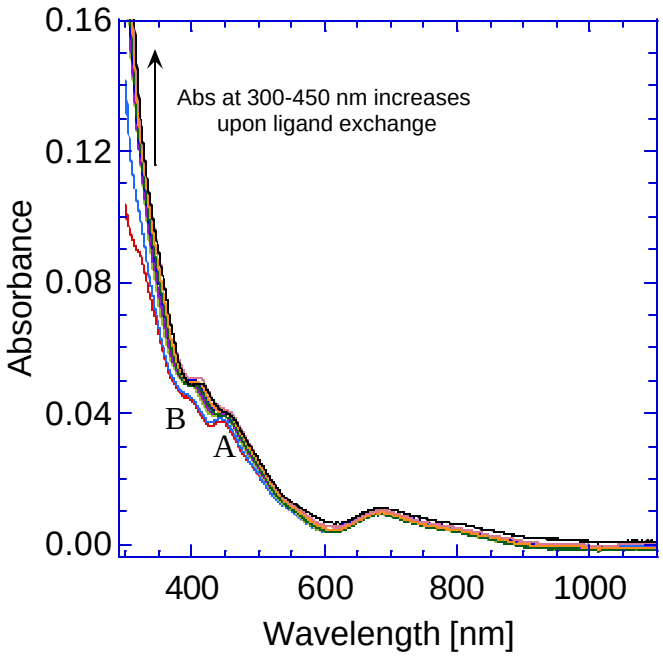
Abs at 300-450 nm increases upon ligand exchange
B
A
Absorbance
Wavelength [nm]
0.00
0.04
0.08
0.12
0.16
400
600
800
1000

(c)

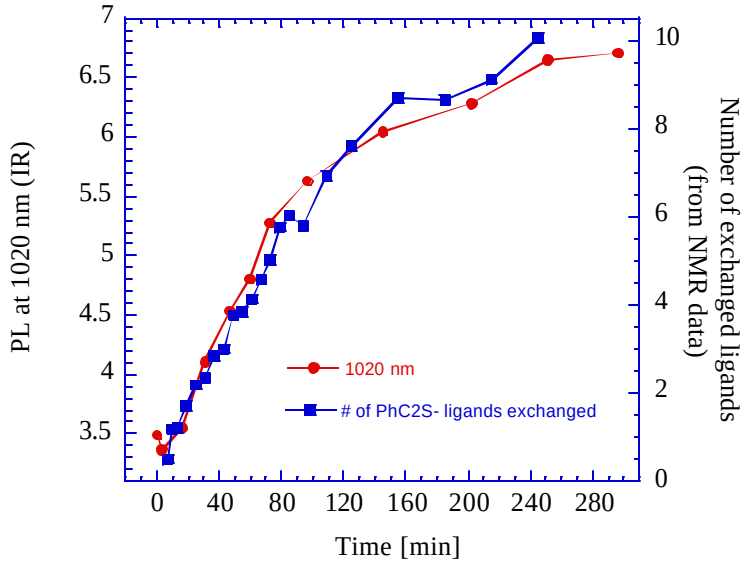
PL at 1020 nm (IR)
Number of exchanged ligands (from NMR data)
Time [min]
1020 nm
# of PhC2S- ligands exchanged
7
6.5
6
5.5
5
4.5
4
3.5
10
8
6
4
2
0
0
40
80
120
160
200
240
280

(d)

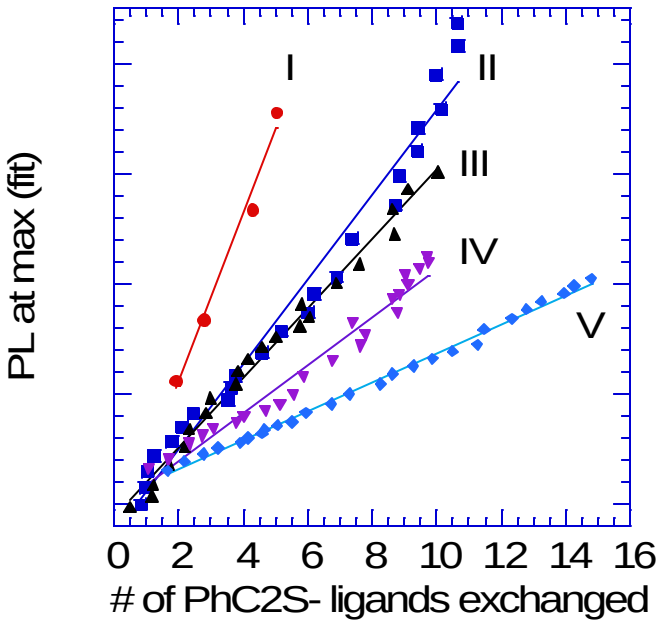
PL at max (fit)
# of PhC2S- ligands exchanged
I
II
III
IV
V
0
2
4
6
8
10
12
14
16

Figure 6.1 (c) shows the plot of number of exchanged 4-bromothiophenol ligands and luminescence intensity at 1020 nm versus time respectively. We can see that these two curves overlap very well. The same behavior was also seen in all the ligands used in this study for at least first 5- 10 exchanged ligands which is really remarkable. Linear correlation is observed between luminescence intensity and number of PhC2S- ligand exchanged by in-coming 4-bromothiophenol, shown in Figure 6.1 (d). An interesting question is then raised--what does this linear correlation tell us? It seems that each of the first 5-10 in-coming 4-Br-PhSH ligands enhanced luminescence of Au_{38} core without interfering each other. Does it indicate the existence of localized chemical state?[37] This will be discussed in greater detail in the following paragraphs.

6.3.2 Optical Properties of $Au_{38}(SC2Ph)_{24}$ during Ligand Exchange. Listed in Table 1 are various ligands used in this study with a large range of polarity. These ligands fall into three categories, the first one is para-substituted arylthiols or *p*-X-Ph-SH, the second is water soluble tiopronin and N-acetyl-L-cysteine ligands, the third is some alkane thiols. Figure 6.2 (a) shows the luminescence spectra of $Au_{38}(SC2Ph)_{24}$ in THF upon ligand exchange with 4-chlorothiophenol. The peak maximum blue shifted from ~ 1050 nm (1.16 eV) to ~ 950 nm (1.31 eV) and intensity increased about twice when ca. eleven 4-chlorothiophenol ligands are exchanged onto the gold core. Similar to 4-bromothiophenol case, only a small change of step-like structure in the range of 400 – 470 nm was observed in the corresponding UV-vis spectra, see Figure 6.2 (b). Curves of number of exchanged 4-chlorothiophenol ligands and luminescence intensity at maximum versus time again overlap very well, shown in Figure 6.2 (c). When the in-coming ligands are 4-CH_3-PhSH and 4-OCH_3-PhSH, luminescence spectra basically remained the same shape with only a small blue shift of the peak maximum, see

Table 6.1 Number of ligands exchanged, photoluminescence enhancement (PL) at the end of experiments, PL per exchanged ligand gain, second order rate constants K_{P-E} of ligand exchange reactions of different ligands with $Au_{38}(SC2Ph)_{24}$ in THF-d_8. K_{P-E} data in CD_2Cl_2 are taken from previous measurements.[41]

Exchanging thiols	# Ligands exchanged (exchange time, min)	Emission Q.E. enhancement[a]	Emission gain per exchanged ligand [a.u.]	K_{P-E} ($10^{-3}\times M^{-1}\bullet S^{-1}$)	
				THF-d_8 (In-coming ligand /PhC2S- ratio	CD_2Cl_2 (In-coming ligand/PhC2S-ratio
NO_2-Ph-SH, **I**	14 (250)	3.6	0.59	74.0 (1.4 : 1)	10.1 (4.2 : 1)
Cl-Ph-SH, **II**	11 (245)	2.3	0.39	10.5 (1.6 : 1)	N/A
Br-Ph-SH, **III**	10 (245)	1.7	0.32	5.5 (1.8 : 1)	3.4 (6.7 : 1)
CH_3-Ph-SH, **IV**	8 (312)	1.5	0.22	6.6 (2.9 : 1)	1.6 (4.3 : 1)
CH_3O-Ph-SH, **V**	15 (374)	1.2	0.13	8.5 (2.0 : 1)	2.4 (4.0 : 1)
Tiopronin	19 (470)	49	1.1	5.6 (3.3 : 1)	N/A
N-acetyl-L-cysteine	10 (200)	3.9	0.24	3.3 (3.2 : 1)	N/A
HO-CH_2CH_2-SH	11 (250)	6.7	0.35	6.8 (2.0 : 1)	N/A
HO_2C-CH_2CH_2SH	7 (310)	2.3	0.15	3.0 (2.0 : 1)	N/A
C_6H_{13}-SH	9 (246)	2.3	0.012	8.3 (3.6 : 1)	N/A
Ph-CH_2CH_2-SH	N/A (273)	1.1	N/A	N/A	N/A

[a] - [(PL at ?max)$_t$ / (Abs at 685nm)$_t$] / [(PL at ?max)$_{t=0}$ / (Abs at 685nm)$_{t=0}$] ~ Q.E.(final) /Q.E (initial)

Figure 6.2 Luminescence spectra (excited at 450 nm) (a), and UV-vis spectra (b) of $Au_{38}(SC2Ph)_{24}$ upon ligand exchange with 4-chlorothiophenol in THF. (c) Plot of number of exchanged 4-chlorothiophenol ligands and luminescence intensity at 960 nm versus time respectively.

(a)

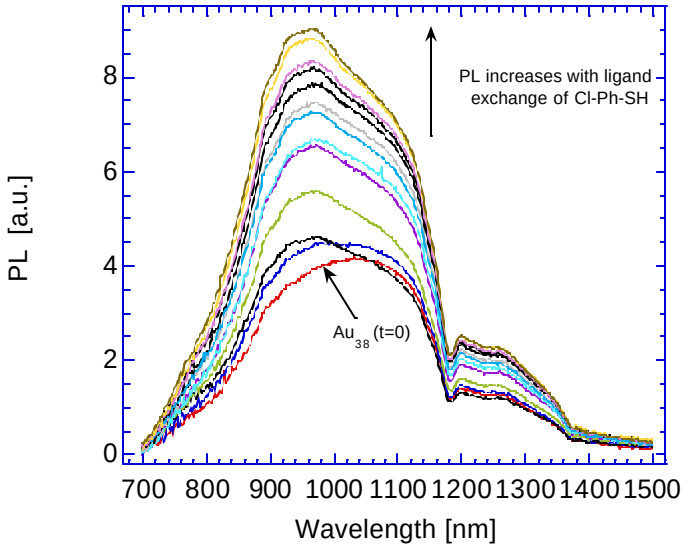
PL increases with ligand exchange of Cl-Ph-SH
Au38 (t=0)
PL [a.u.]
Wavelength [nm]
0
2
4
6
8
700
800
900
1000
1100
1200
1300
1400
1500

(b)

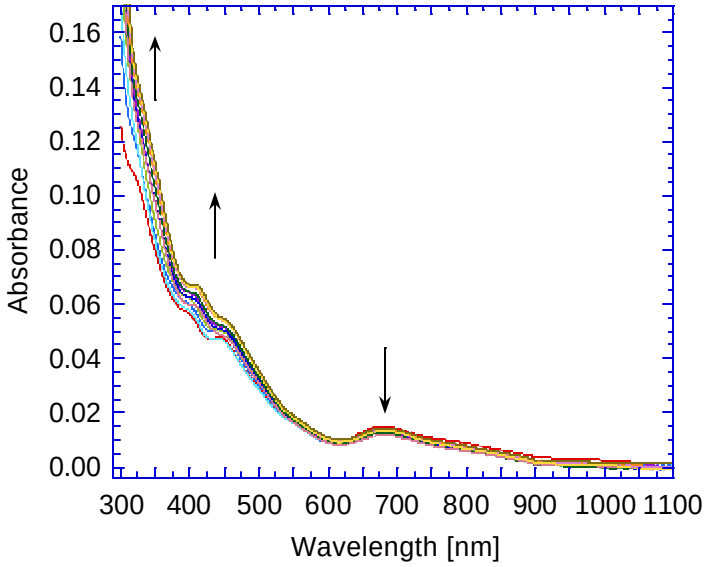
Absorbance
Wavelength [nm]
0.00
0.02
0.04
0.06
0.08
0.10
0.12
0.14
0.16
300
400
500
600
700
800
900
1000
1100

(c)

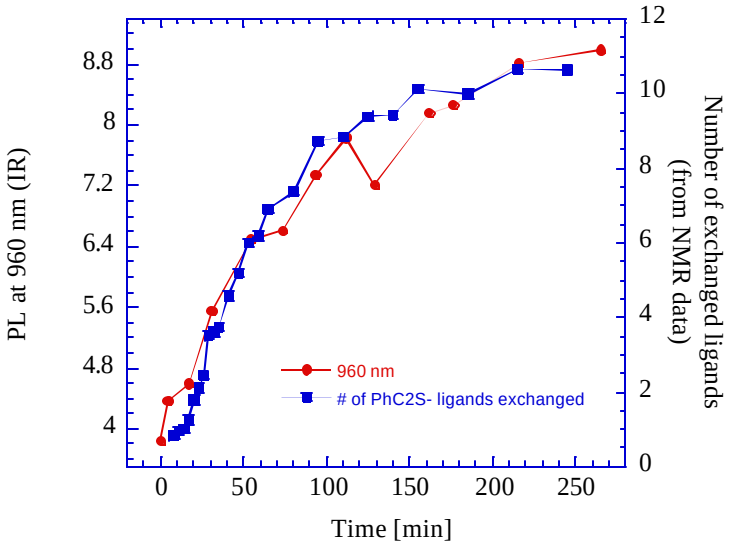
PL at 960 nm (IR)
Number of exchanged ligands (from NMR data)
Time [min]
960 nm
# of PhC2S- ligands exchanged
8.8
8
7.2
6.4
5.6
4.8
4
12
10
8
6
4
2
0
0
50
100
150
200
250

Figure 6.3 (a), Figure 6.4 (a). However, the intensity increase at maximum per ligand gain is smaller than that of 4-Cl-PhSH and 4-Br-PhSH. Changes of UV-vis spectra are also similar to 4-Cl-PhSH and 4-Br-PhSH case, shown in Figure 6.3 (b), Figure 6.4 (b). Good correlation between number of ligands exchanged and luminescence intensity are observed as well, see Figrue 6.3 (c) and Figure 6.4 (c).

Compared to other ligands used in this study, tiopronin and N-acetyl-L-cysteine are much more polar. They are soluble in water and have limited solubility in THF, in order for better comparison of ligand effects on the optical properties of $Au_{38}(SC2Ph)_{24}$ upon ligand exchange, all the study is done in THF. Shown in Figure 6.5 (a) is the luminescence spectra of Au_{38} $(SC2Ph)_{24}$ upon ligand exchange with tiopronin. An isospectic point indicating formation of two different species was observed at ~ 1040 nm with a decrease of luminescence intensity at higher wavelength and the growth of a new peak at ~ 780 nm (1.6 eV). The UV-vis spectra shown in Figure 6.5 (b) also changed a lot—the step like structure (400-470 nm) and the absorbance peak at 680 nm gradually became featureless with a new broad peak at ~ 600 nm growing in. Both luminescence and UV-vis spectra indicated strong ligand effects on the optical properties of $Au_{38}(SC2Ph)_{24}$ upon ligand exchange with tiopronin thiol, i.e., the electronic structure of the gold core is strongly perturbed by the ligand. Shown in Figure 6.5 (c) is the plot of number of exchanged tiopronin ligands and luminescence intensity at 780 nm versus time respectively, again pretty good overlap of two curves is observed. Pronounced changes of optical properties of $Au_{38}(SC2Ph)_{24}$ upon ligand exchange with N-acetyl-L-cysteine are also observed in Figure 6.6 and will be discussed later.

Figure 6.7 (a) shows the luminescence spectra of $Au_{38}(SC2Ph)_{24}$ upon ligand exchange with 2-mercaptoethanol. The peak maximum blue shifted to ~ 900 nm (1.38 eV) and

Figure 6.3 Luminescence spectra (excited at 450 nm) (a), and UV-vis spectra (b) of $Au_{38}(SC2Ph)_{24}$ upon ligand exchange with *p*-toluenethiol in THF. (c) Plot of number of exchanged *p*-toluenethiol ligands and luminescence intensity at 980 nm versus time respectively.

(a)

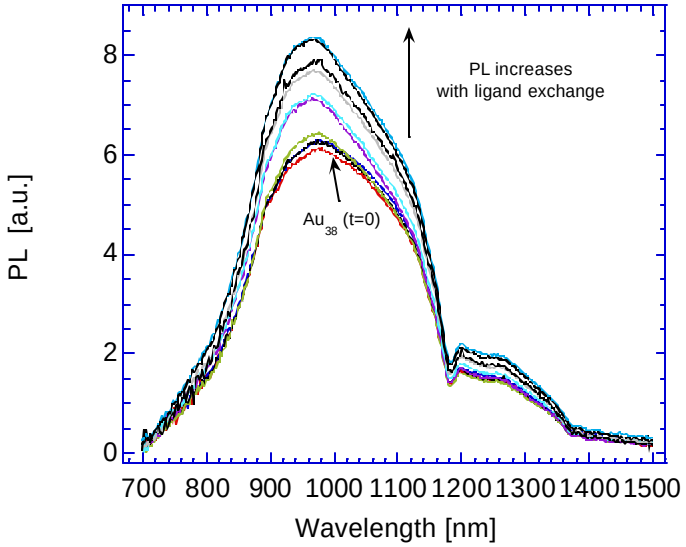
PL increases
with ligand exchange
Au38 (t=0)
PL [a.u.]
Wavelength [nm]
0
2
4
6
8
700 800 900 1000 1100 1200 1300 1400 1500

(b)

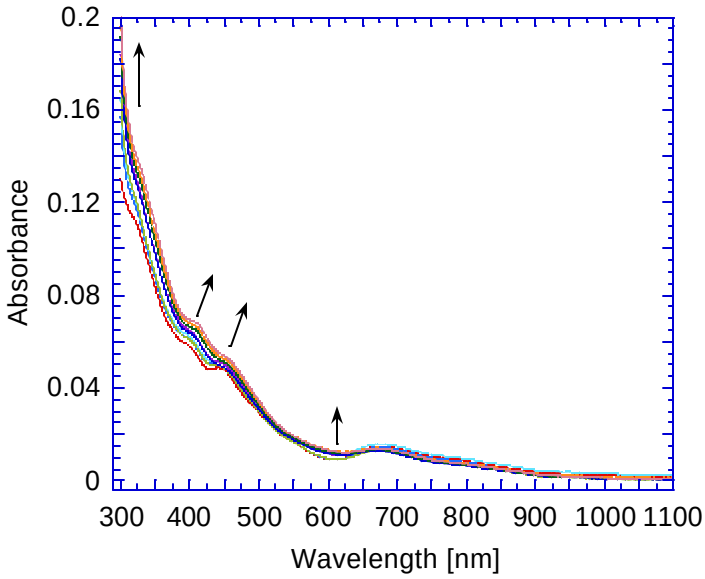
Absorbance
Wavelength [nm]
0
0.04
0.08
0.12
0.16
0.2
300 400 500 600 700 800 900 1000 1100

(c)

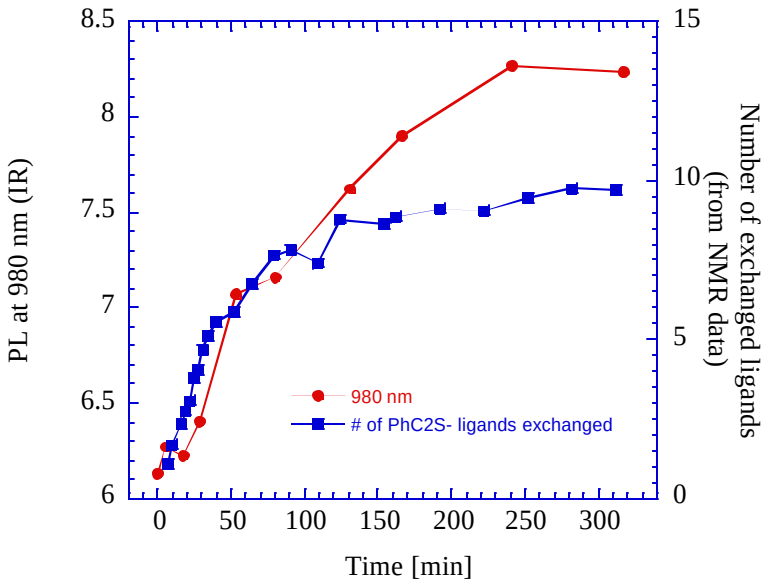
8.5
8
7.5
7
6.5
6
PL at 980 nm (IR)
15
10
5
0
Number of exchanged ligands (from NMR data)
0
50
100
150
200
250
300
Time [min]
980 nm
# of PhC2S- ligands exchanged

Figure 6.4 Luminescence spectra (excited at 450 nm) (a), and UV-vis spectra (b) of $Au_{38}(SC2Ph)_{24}$ upon ligand exchange with 4-methoxythiophenol in THF. (c) Plot of number of exchanged 4-methoxythiophenol ligands and luminescence intensity at 980 nm versus time respectively.

(a)

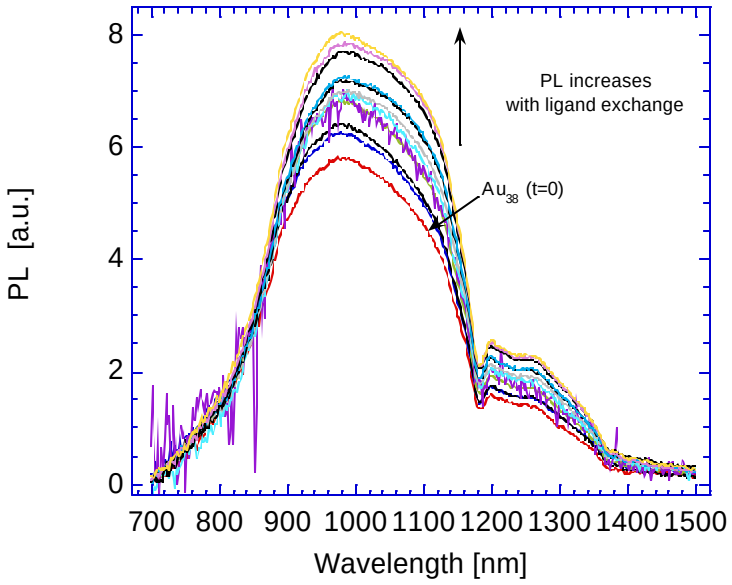
PL increases
with ligand exchange
Au38 (t=0)
PL [a.u.]
Wavelength [nm]
0
2
4
6
8
700
800
900
1000
1100
1200
1300
1400
1500

(b)

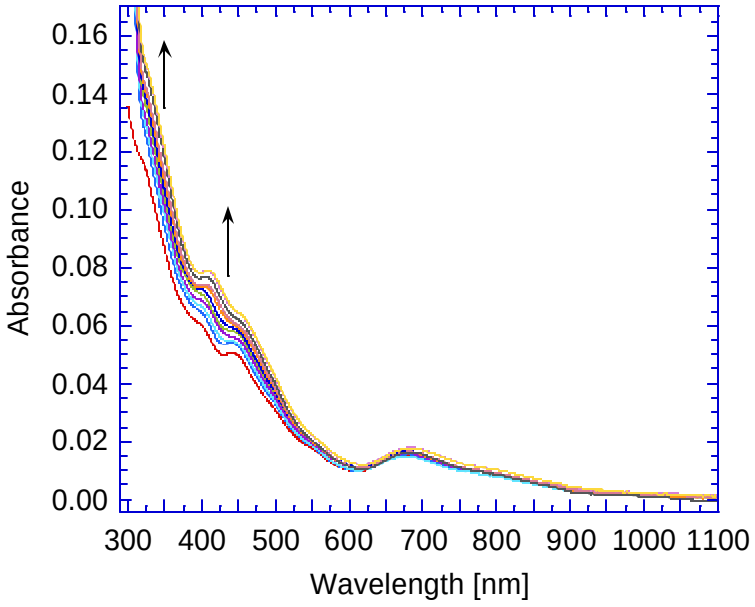
Absorbance
Wavelength [nm]
0.00
0.02
0.04
0.06
0.08
0.10
0.12
0.14
0.16
300
400
500
600
700
800
900
1000
1100

(c)

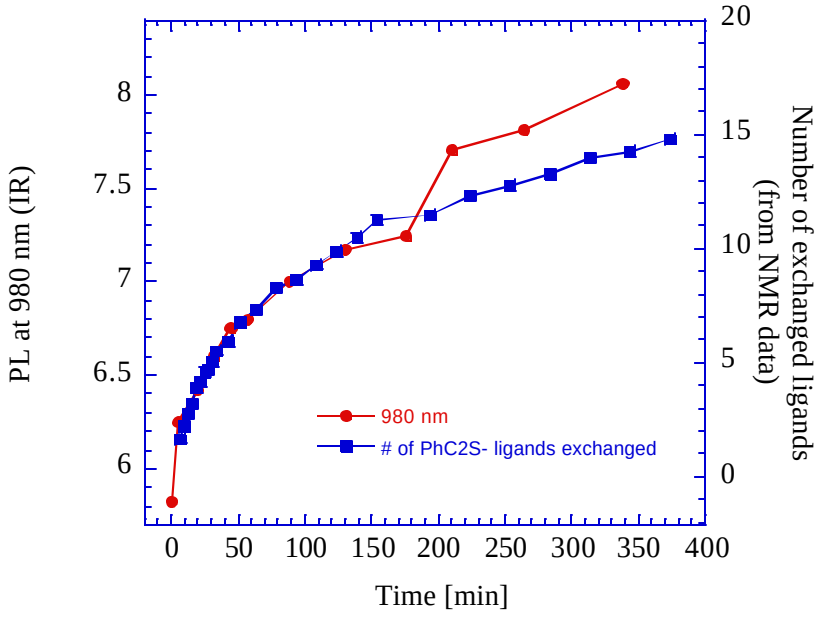
PL at 980 nm (IR)
Number of exchanged ligands (from NMR data)
Time [min]
980 nm
# of PhC2S- ligands exchanged
8
7.5
7
6.5
6
20
15
10
5
0
0
50
100
150
200
250
300
350
400

Figure 6.5 Luminescence spectra (excited at 450 nm) (a), and UV-vis spectra (b) of $Au_{38}(SC2Ph)_{24}$ upon ligand exchange with tiopronin in THF. (c) Plot of number of exchanged tiopronin ligands and luminescence intensity at 780 nm versus time respectively.

(a)

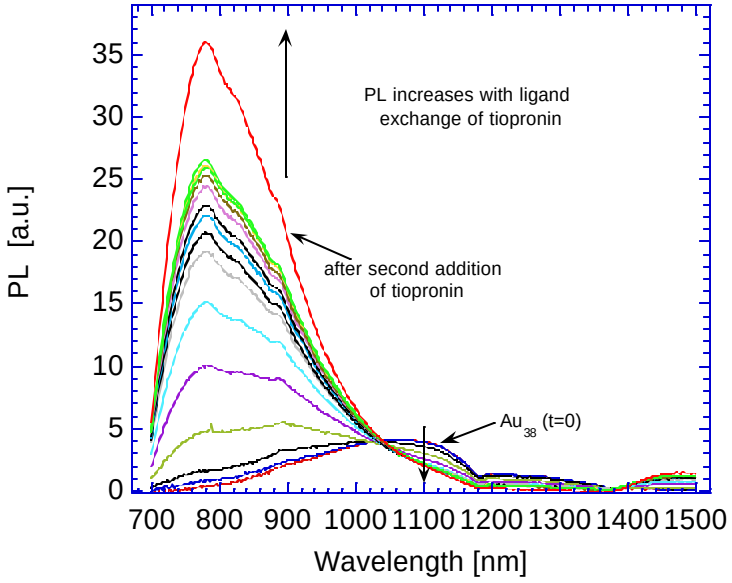
PL increases with ligand
exchange of tiopronin
after second addition
of tiopronin
Au38 (t=0)
PL [a.u.]
Wavelength [nm]
0
5
10
15
20
25
30
35
700
800
900
1000
1100
1200
1300
1400
1500

(b)

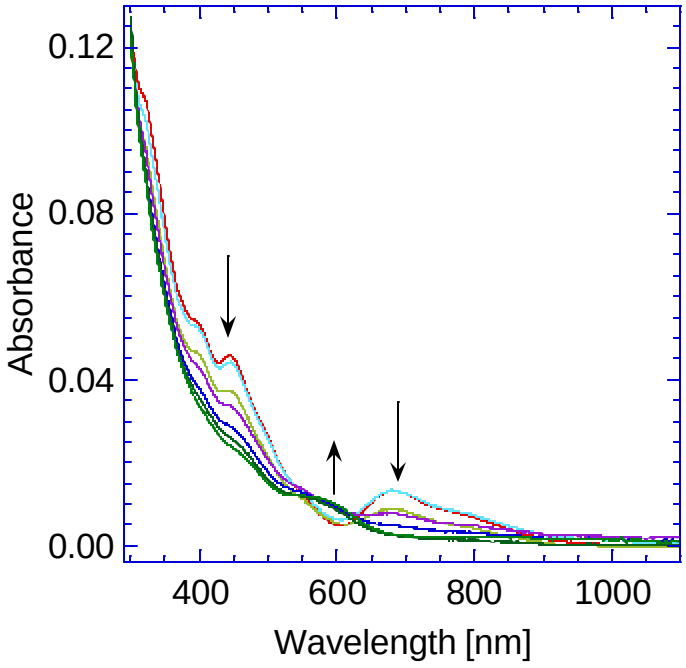
Absorbance
Wavelength [nm]
0.00
0.04
0.08
0.12
400
600
800
1000

(c)

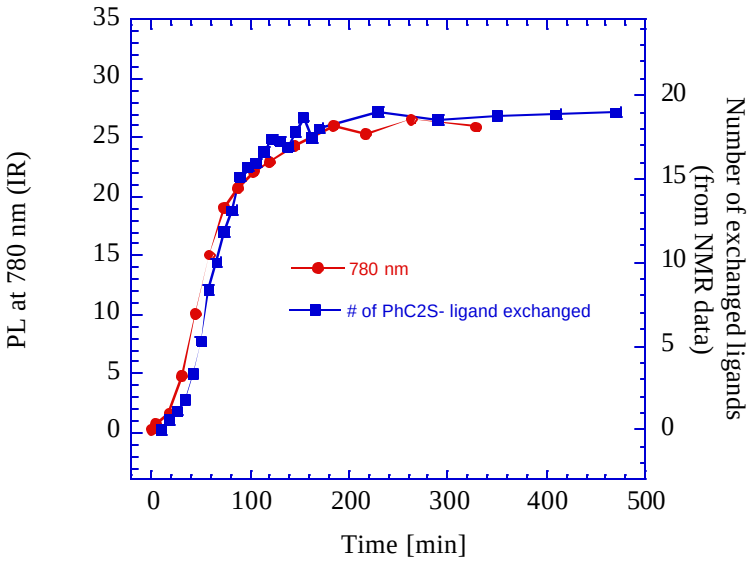
PL at 780 nm (IR)
Number of exchanged ligands (from NMR data)
Time [min]
780 nm
# of PhC2S- ligand exchanged
0
5
10
15
20
25
30
35
0
100
200
300
400
500

Figure 6.6 Luminescence spectra (excited at 450 nm) (a), and UV-vis spectra (b) of $Au_{38}(SC2Ph)_{24}$ upon ligand exchange with N-Acetyl-L-Cysteine in THF. (c) Plot of number of exchanged N-Acetyl-L-Cysteine ligands and luminescence intensity at 780 nm versus time respectively.

(a)

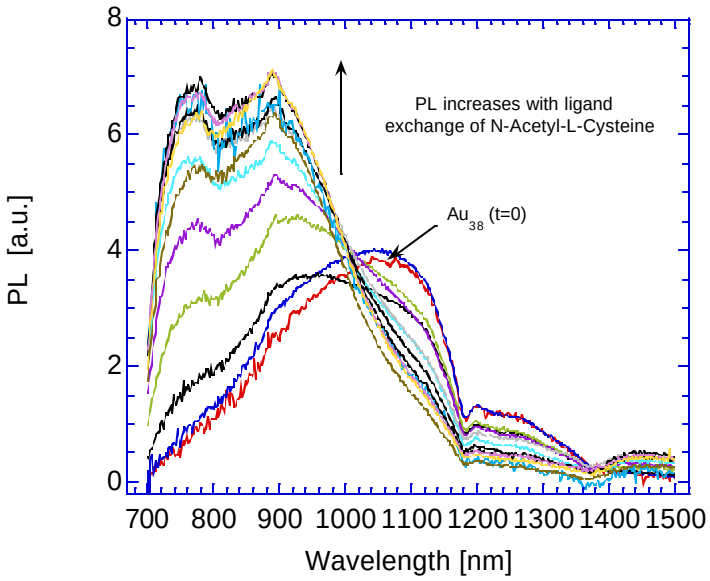
PL increases with ligand
exchange of N-Acetyl-L-Cysteine
Au38 (t=0)
PL [a.u.]
Wavelength [nm]
0
2
4
6
8
700 800 900 1000 1100 1200 1300 1400 1500

(b)

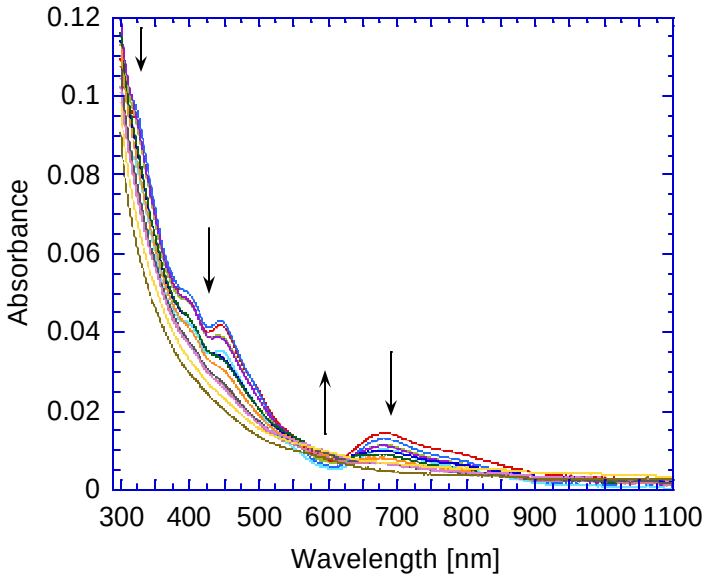
Absorbance
Wavelength [nm]
0
0.02
0.04
0.06
0.08
0.1
0.12
300 400 500 600 700 800 900 1000 1100

(c)

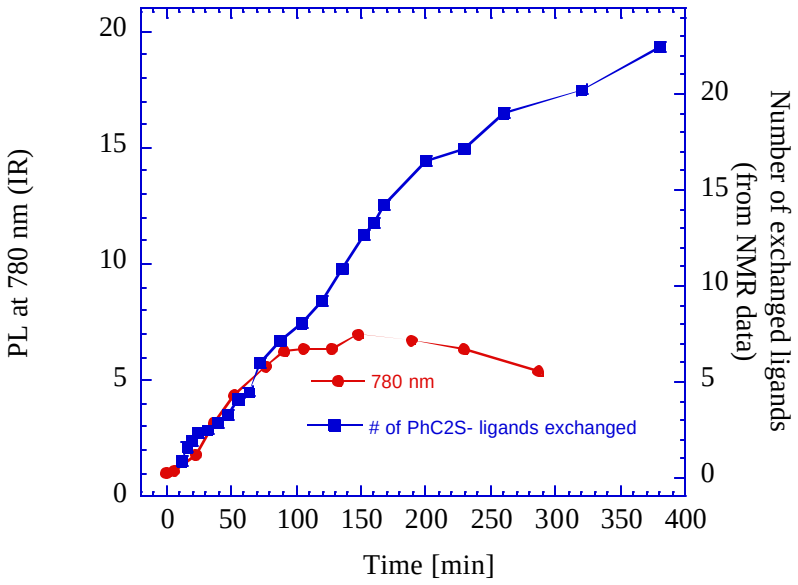
PL at 780 nm (IR)
Number of exchanged ligands (from NMR data)
Time [min]
780 nm
# of PhC2S- ligands exchanged
0
5
10
15
20
0
50
100
150
200
250
300
350
400

Figure 6.7 Luminescence spectra (excited at 450 nm) (a), and UV-vis spectra (b) of $Au_{38}(SC2Ph)_{24}$ upon ligand exchange with 2-mercaptoethanol in THF. (c) Plot of number of exchanged 2-mercaptoethanol ligands and luminescence intensity at 900 nm versus time respectively.

(a)

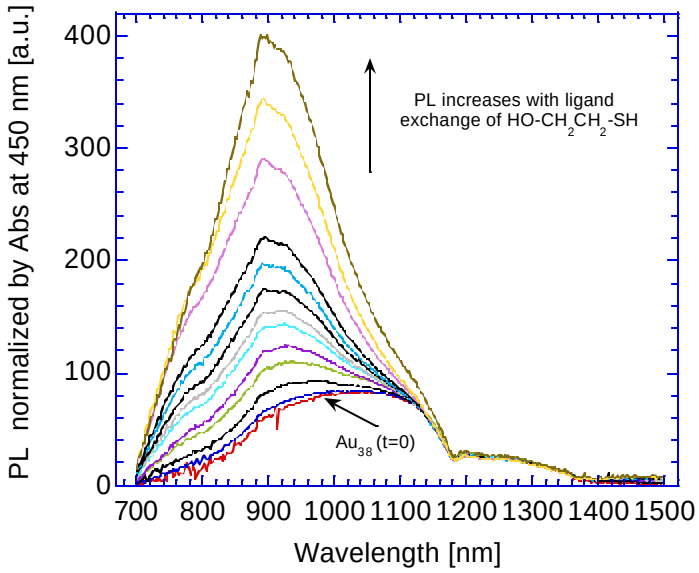
PL normalized by Abs at 450 nm [a.u.]
400
300
200
100
0
700 800 900 1000 1100 1200 1300 1400 1500
Wavelength [nm]
PL increases with ligand exchange of HO-CH2CH2-SH
Au38 (t=0)

(b)

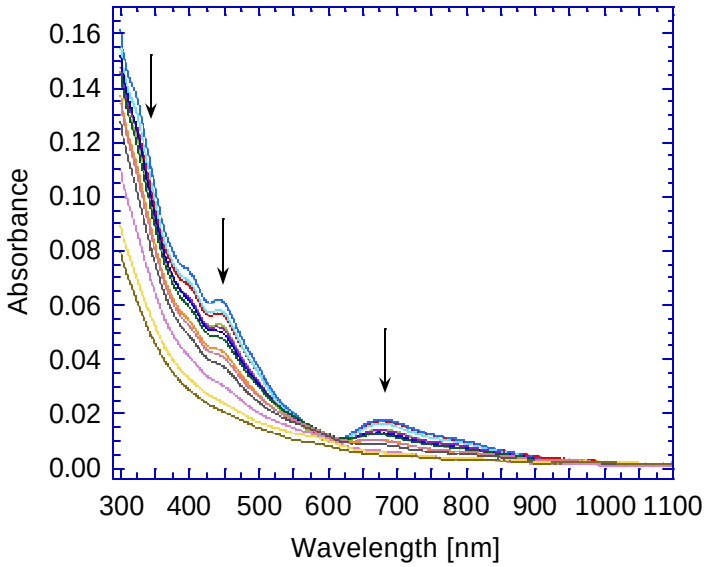
Absorbance
0.16
0.14
0.12
0.10
0.08
0.06
0.04
0.02
0.00
300 400 500 600 700 800 900 1000 1100
Wavelength [nm]

(c)

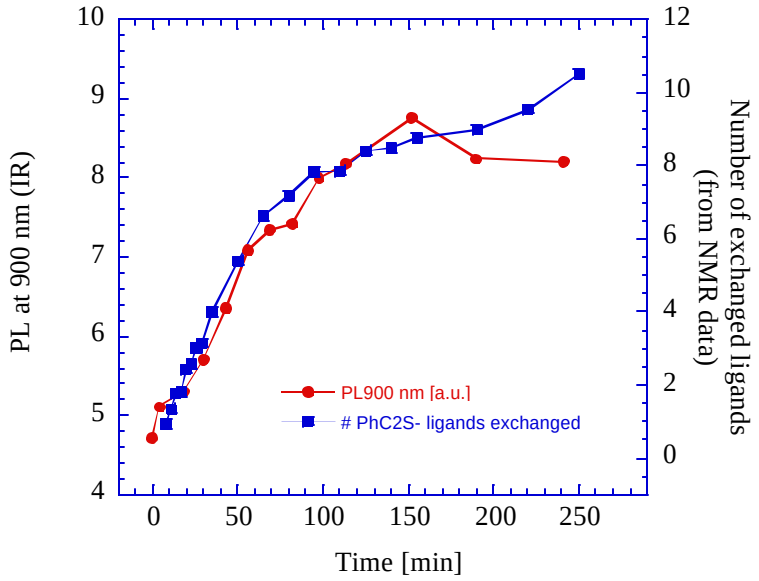
PL at 900 nm (IR)
Number of exchanged ligands (from NMR data)
Time [min]
PL900 nm [a.u.]
PhC2S- ligands exchanged
10
9
8
7
6
5
4
12
10
8
6
4
2
0
0
50
100
150
200
250

intensity increased ca. 4 times when eleven ligands are exchanged to the gold core. The step-like structure (400-470 nm) and the absorbance peak at 680 nm of UV-vis spectra became featureless gradually upon ligand exchange as was seen in Figure 6.7 (b). Curves of number of exchanged 2-mercaptoethanol ligands and luminescence intensity at 900 nm versus time again overlap very well, shown in Figure 6.7 (c). Results of 3-mercaptopropionic acid and 1-hexanethiol are similar and can be found in Figure 6.8 and 6.9.

Optical properties of gold nanoparticles are mainly determined by the electronic structure of the gold core while also affected by its ligands. Link *et al.*[35] proposed a solid-state model for the origin of two luminescence bands of a 28-atom gold cluster $Au_{28}(SG)_{16}$ where they attributed the high energy band to radiative interband transition between the sp and d-bands while the low energy band orginated from the radiative intraband transitions within the sp-band across the HOMO-LUMO gap. The HOMO-LUMO optical band edge is ca. 1.33 eV for $Au_{38}(SC2Ph)_{24}$ measured from UV-vis, and the absorption maximum at ca. 1050 nm (1.18 eV, smaller than the HOMO-LUMO gap energy) in the luminescence spectrum is an indication of surface state existence.

Now let us take a closer look at the optical spectra of $Au_{38}(SC2Ph)_{24}$ upon ligand exchange with different in-coming ligands. When the in-coming ligands are *p*-X-PhSH, the luminescence intensity maximum blue shifted and increased for all of them with larger extent observed for X= $-NO_2$ (see Figure 6.10 (a)), -Cl and –Br. In the case of 4-Cl-PhSH, the shape of luminescence spectra changed and blue shifted ca. 100 nm, see Figure 6.2 (a). The luminescence intensity has increased ca. twice when ca. eleven ligands are exchanged. Peak shifted from the original wavelength 1050 nm (1.16 eV) to 950 nm (1.31 eV, close to the HOMO-LUMO gap energy). This is clearly ligand effects on the electronic structure of

Figure 6.8 Luminescence spectra (excited at 450 nm) (a), and UV-vis spectra (b) of $Au_{38}(SC2Ph)_{24}$ upon ligand exchange with 3-mercaptopropionic acid in THF. (c) Plot of number of exchanged 3-mercaptopropionic acid ligands and luminescence intensity at 900 nm versus time respectively.

(a)

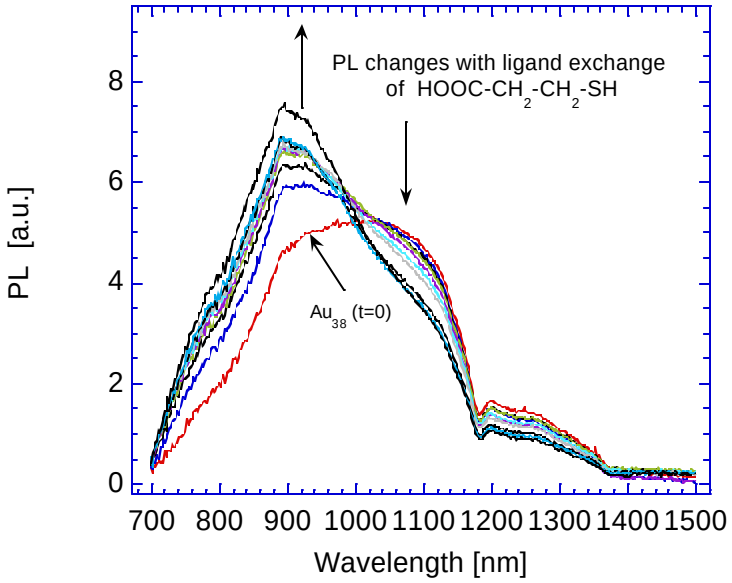
PL changes with ligand exchange
of HOOC-CH2-CH2-SH
Au38 (t=0)
PL [a.u.]
Wavelength [nm]
0
2
4
6
8
700 800 900 1000 1100 1200 1300 1400 1500

(b)

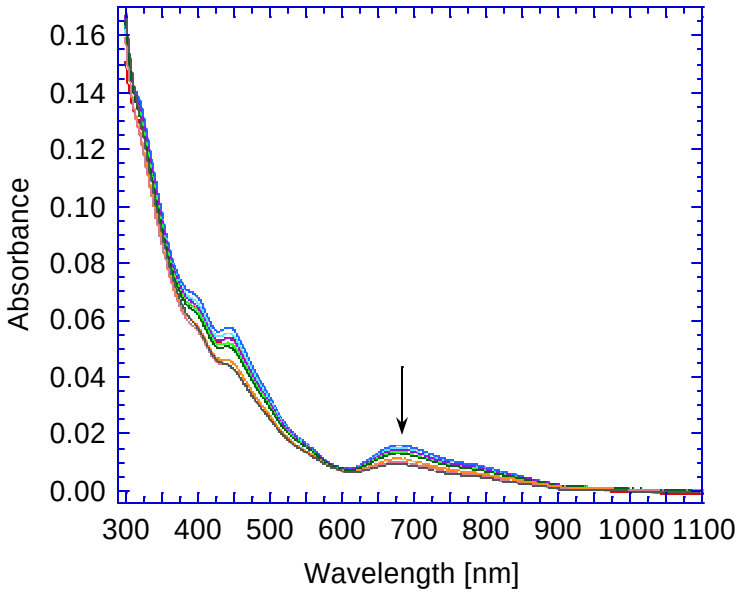
Absorbance
Wavelength [nm]
0.00
0.02
0.04
0.06
0.08
0.10
0.12
0.14
0.16
300 400 500 600 700 800 900 1000 1100

(c)

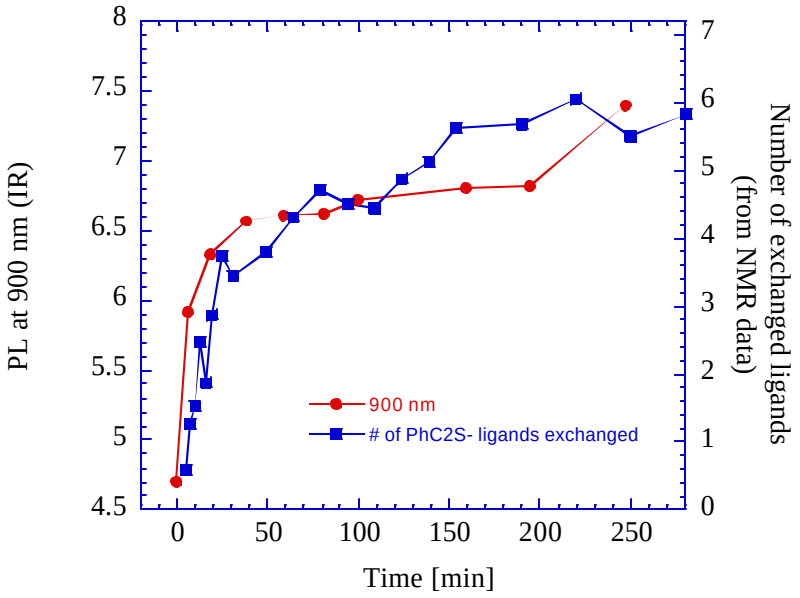
PL at 900 nm (IR)
Number of exchanged ligands (from NMR data)
Time [min]
900 nm
# of PhC2S- ligands exchanged
8
7.5
7
6.5
6
5.5
5
4.5
7
6
5
4
3
2
1
0
0
50
100
150
200
250

Figure 6.9 Luminescence spectra (excited at 450 nm) (a), and UV-vis spectra (b) of $Au_{38}(SC2Ph)_{24}$ upon ligand exchange with 1-hexanethiol in THF. (c) Plot of number of exchanged 1-hexanethiol ligands and luminescence intensity at 930 nm versus time respectively.

(a)

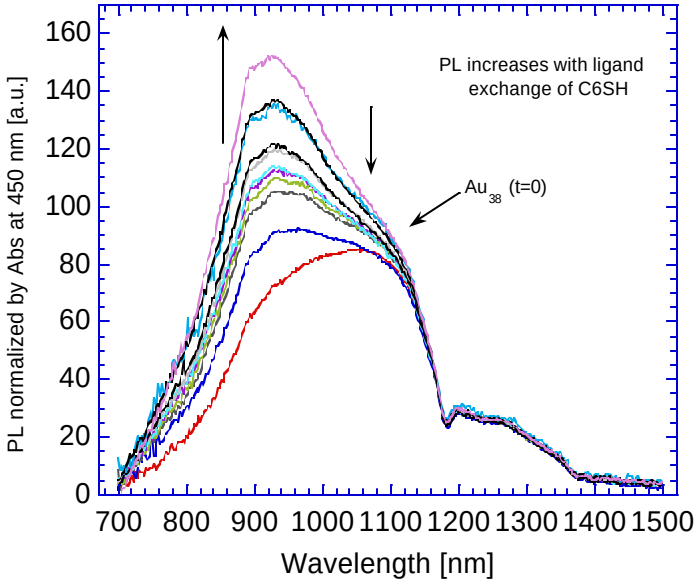
PL increases with ligand exchange of C6SH
Au38 (t=0)
PL normalized by Abs at 450 nm [a.u.]
Wavelength [nm]
0
20
40
60
80
100
120
140
160
700
800
900
1000
1100
1200
1300
1400
1500

(b)

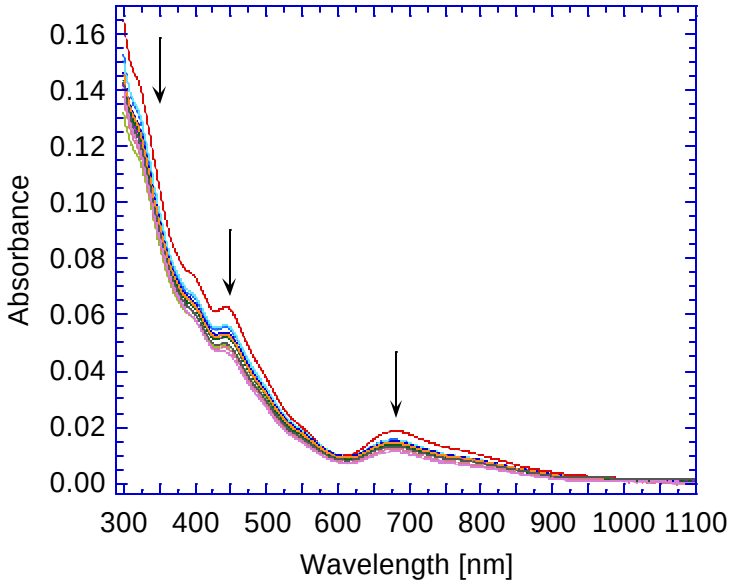
Absorbance
Wavelength [nm]
0.00
0.02
0.04
0.06
0.08
0.10
0.12
0.14
0.16
300
400
500
600
700
800
900
1000
1100

(c)

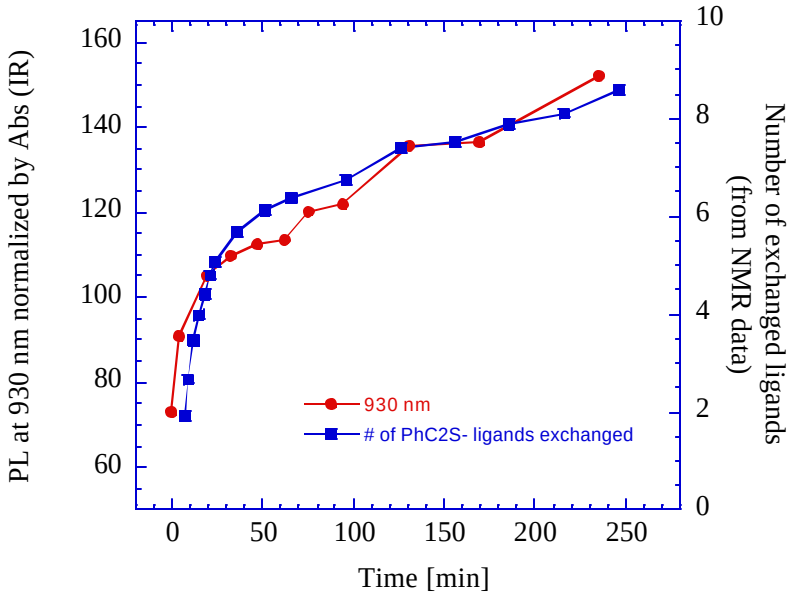
PL at 930 nm normalized by Abs (IR)
Number of exchanged ligands (from NMR data)
Time [min]
930 nm
# of PhC2S- ligands exchanged
160
140
120
100
80
60
10
8
6
4
2
0
0
50
100
150
200
250

Figure 6.10 Luminescence spectra (excited at 450 nm) (a), and UV-vis spectra (b) of $Au_{38}(SC2Ph)_{24}$ upon ligand exchange with 4-nitrothiophenol in THF. (c) Plot of number of exchanged 4-nitrothiophenol ligands and luminescence intensity at 930 nm versus time respectively.

(a)

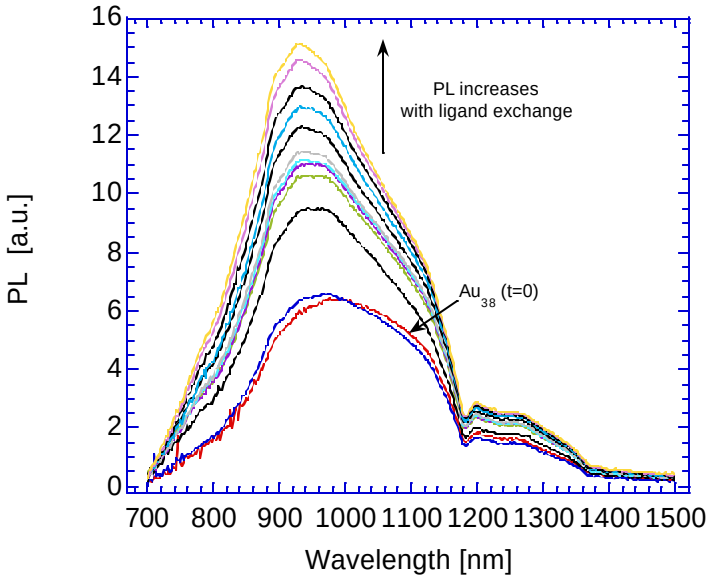
PL increases
with ligand exchange
Au38 (t=0)
PL [a.u.]
Wavelength [nm]
0
2
4
6
8
10
12
14
16
700
800
900
1000
1100
1200
1300
1400
1500

(b)

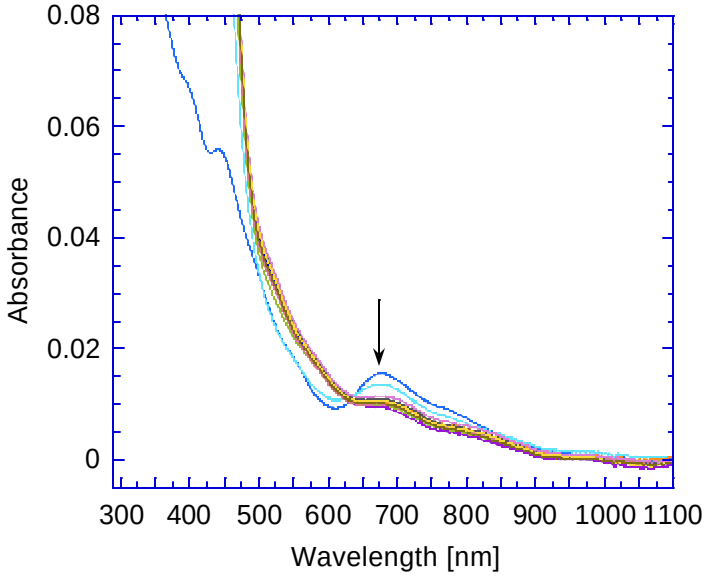
Absorbance
Wavelength [nm]
0
0.02
0.04
0.06
0.08
300
400
500
600
700
800
900
1000
1100

(c)

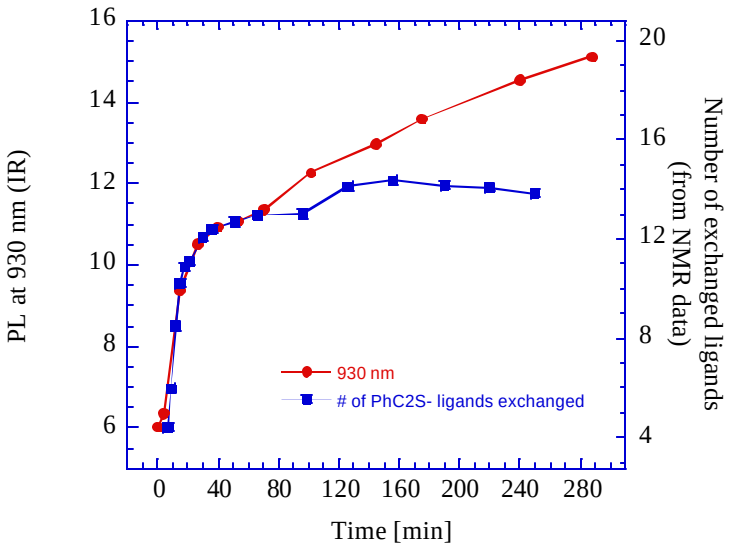
PL at 930 nm (IR)
Number of exchanged ligands (from NMR data)
Time [min]
930 nm
# of PhC2S- ligands exchanged
16
14
12
10
8
6
20
16
12
8
4
0
40
80
120
160
200
240
280

$Au_{38}(SC2Ph)_{24}$. Compared to the original phenylethylthiolate ligand of the Au_{38}, 4-chlorothiophenol ligand is much more polar and the electron withdrawing goup –Cl definetely withdraws electron density from the gold core thus makes the gold core more positive (electron deficient). The overall effect is luminescence from both LUMO-HOMO transition (~ 1.33 eV) and surface state emission (~ 1.16 eV) is enhanced. Similar effect is seen for 4-nitrothiophenol with an even stronger electron withdrawing group $–NO_2$. Since 4-nitrothiophenol has absorbance at 450 nm where the nanoparticle solution is excited, it is hard to normalized the luminescence intensity by the absorbance, although the mole number of the gold core is ca. the same for all UV-vis and luminescence measurements. But luminescence enhancement per exchanged 4-NO_2-PhSH is much greater than the rest *p*-X-PhSH, as can be seen from the slopes of Figure 6.1 (d) and Table 1. One thing worth mentioning is that similar luminescence spectrum is also observed for +1 charged $Au_{38}(SC2Ph)_{24}$. ---It is easy to understand that putting one positive charge and putting some ligands with very strong electron withdrawing groups to the gold core are identical in nature. Core charge effects on the luminescence properties of $Au_{38}(SC2Ph)_{24}$ are currently under study.

UV-vis spectra of $Au_{38}(SC2Ph)_{24}$ upon ligand exchange with 4-bromothiophenol changed a little bit, see Figure 6.1 (b). The absorbance at lower wavelength (less than 620 nm) increased a little bit while decreased at the ~ 680 nm peak. Peak **A** became less defined while peak **B** became better defined as the ligand exchange reaction went on--- similar UV-vis changes are also observed for *p*-X-PhSH where X= –Cl , -CH_3, OCH_3 (Figure 6.2 (b), Figure 6.3 (b), Figure 6.4 (b) respectively) indicating similar substituent effects on the Au_{38} core electronic structure based on their UV-vis spectra.

A more pronounced ligand effect on optical properties of $Au_{38}(SC2Ph)_{24}$ upon ligand exchange is seen for tiopronin thiol, shown in Figure 6.5. The isopectic point in the luminescence spectra, seen in Figure 6.5 (a) at ca. 1040 nm (1.19 eV) indicated the formation of two different species, possibly the unexchanged $Au_{38}(SC2Ph)_{24}$ as one species and exchanged $Au_{38}(SC2Ph)_x(tiopronin)_y$ as the other and it does not matter how many tiopronin ligands are exchanged. The intensity at wavelength greater than 1040 nm kept decreasing while increased at the higher energy (lower wavelength) side. The peak maximum at ca. 780 nm (1.59 eV) is likely due to the sp-band to d band interband transtion while the shoulder at ca. 890 nm (1.39 eV) corresponding to LUMO-HOMO transition, as indicated in Figure 6.11. Sp-band to d-band interband transition seem common in gold nanoparticles of different core size, from molecule-like $Au_{28}(SG)_{16}$ and the tiopronin exchanged $Au_{38}(SC2Ph)_x(tiopronin)_y$ to bulk metal like $Au_{201}tiopronin_{85}$.[33] Interestingly, all these gold nanoparticles are water soluble. The organic soluble $Au_{38}(SC2Ph)_{24}$ only shows very weak fluorescence at 780 nm. Besides, when $Au_{38}(SC2Ph)_{24}$ is exchanged by N-acetyl-L-cysteine leading to water soluble exchanged product, similar luminescence spectra are observed, see Figure 6.6 (a). The intensity at ca. 780 nm and 890 nm is greatly enhanced and a doublet grew in with a "pseudo" isospectic point observed as well. Based on these observations and previous luminescence study, we speculate that water soluble (very polar) ligands help stimulate the interband electronic transition and HOMO-LUMO intraband transition while suppress the surface state emission. One alternative explanation of the sp-d interband transition seen for nanoparticles with different core size is the emission is mainly determined by the surface composite (ligand effect) of the nanoparticles, say it is a *surface emission* instead of *volume emission.* [40]

Figure 6.11 Scheme for the origin of luminescence of $Au_{38}(SC2Ph)_{24}$.

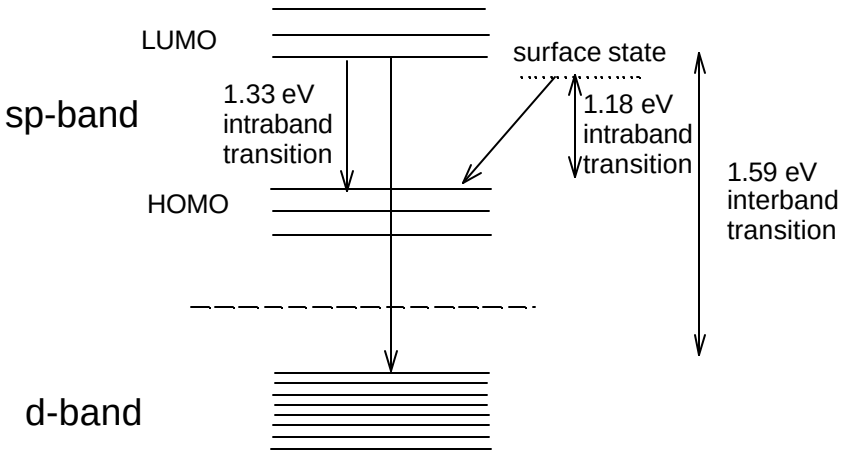
LUMO
surface state
sp-band
1.33 eV
intraband
transition
1.18 eV
intraband
transition
1.59 eV
interband
transition
HOMO
d-band

UV-vis spectra of $Au_{38}(SC2Ph)_{24}$ upon ligand exchange with tiopronin are also very interesting, see Figure 6.5 (b). The step-like structure and absorbance peak at 680 nm became less defined gradually and absorbance decreased upon ligand exchange while a broad peak at ca. 600 nm popped up. Two isospectic points can be seen, one at ca. 550 nm, the other at ca. 620 nm. All these changes clearly indicated ligand effects on the electronic structure of Au_{38} core, and perhaps core size also changed during ligand exchange--we assume no apparent core size change during ligand exchange reactions as long as the step-like structure and the absorbance peak at 680 nm still remained and this is the case if we only consider the first 5 to 10 ligands exchanged. Similar UV-vis spectra are also observed for N-acetyl-L-cysteine, see Figure 6.6 (b), although the isospectic points are not as obvious as those of tiopronin case.

When the in-coming ligand is 2-mercaptoethanol, a linear alkane thiol more polar than phenylethylthiol, luminescence enhancement is also observed, see Figure 6.7 (a). Again a peak at ca. 900 nm (1.38 eV) grew in and the intensity at the original wavelength 1050 nm (1.16 eV) increased as well. We also attributed this enhancement to the more polar ligand helping promote both the HOMO-LUMO and surface state electronic transitions. The step like fine structure and absorbance peak at 680 nm in the UV-vis spectra became less defined and the absorbance decreased gradually as seen in Figure 6.7 (b). Both luminescence and UV-vis spectra of $Au_{38}(SC2Ph)_{24}$ upon ligand exchange of 2-mercaptoethanol shows the ligand effect on the electronic strucure of Au_{38} core. Similar effects are also observed for 3-mercaptopropionic acid, see Figure 6.8

However, when 1-hexanethiol is the in-coming ligand, we still oberved the luminescence enhancement and peak blue shifted to ca. 930 nm (1.33 eV), see Figure 6.9

(a). Since 1-hexanethiol is as non-polar as phenylethylthiol, we can only speculate that this is due to the suppression of radiativeless decay from LUMO to surface state thus the LUMO-HOMO electronic transition is promoted. The mechanism is not clear at this point and need further study. Its UV-vis spectra change is similar to those of 2-mercaptoethanol and 3-mercaptopropionic acid but at an even slower rate. We also tried to exchange phenylethylthiol to $Au_{38}(SC2Ph)_{24}$, and saw almost no change in luminescence and UV-vis spectra.

6.3.3 Correlate Ligand Exchange Kinetics with Luminescence Properties. One really nice thing of this work is we monitored ligand exchange kinetics and luminescence properties of $Au_{38}(SC2Ph)_{24}$ upon ligand exchange simultaneously. Thus we can easily correlate number of in-coming ligands exchanged onto Au_{38} core with the corresponding luminescence properties. Figure 6.1 (d) shows the plot of number of various in-coming ligands exchanged onto Au_{38} core versus luminescence intensity at a certain wavelength (peak maximum of the final peak) respectively. We can see that all of them have pretty good linearity. And this is really amazing! Their slopes or the photoluminescence per exchanged ligand gain are summarized in Table 1. From the numbers in the table, we can easily tell that for para-substituted arylthiols, the more electron withdrawing the substituted group is, the more enhancement of photoluminescence is observed. This is probably due to the inductive effect of the substituted group on the electronic structure of gold core. Tiopronin gave the most luminescence enhancement while N-acetyl-L-cysteine and 2-mercaptoethanol also gave considerate extent of enhancement. Does this linear correlation indicate the existence of localized chemical state? Wang *et al.* [37] found that luminescence intensity of $Au_{140}(SC6)_{53}$ increased linearly with the number of TMA (N, N, N-trimethyl-(mercaptoundecyl)

ammonium) ligands exchanged to the Au_{140} core. Besides, the luminescence at 690 nm (due to gold atom luminesence) of products of core metal galvanic exchange reaction of Ag tiopronin MPCs with Au(I) [*p*- $SCH_2(C_6H_4)C(CH_3)_3$] increased linearly with the number of gold atoms incorporated to the silver core. All these results suggest the possible existence of localized surface sites / chemical states.

6.3.4 Ligand Exchange Kinetics in Tetrahydrofuran. ^{1}H NMR has been demonstrated to be a very powerful tool to study ligand exchange kinetics of both $Au_{140}(SC2Ph)_{53}$ and $Au_{38}(SC2Ph)_{24}$ with many in-coming thiol liands as long as the spectrum window between 2.70- 2.85 ppm is not interfered by other resonance signals.[24,41] Shown in Figure 6.12 is the ^{1}H NMR spectrum for the exchange of phenylethanethiolate (PhC2S-) by 4-bromothiophenol (4-Br-PhSH) onto $Au_{38}(SC2Ph)_{24}$ at 293 K in THF-d_8(not degassed) . The ca. 2.76 ppm quartet signal comes exclusively from α-proton of the liberated phenylethylthiol (HS-***CH_2***-CH_2-Ph) and is used to monitor the exchange process. Ferrocene was used as the internal standard and gave a resonance at ca. 4.15 ppm. Inset shows the quartet signal growth from (a) 7 min to (b) 73 min after ligand exchange occurred corresponding to on average ca. 0.5 and 5 bromothiophenol ligands exchanged respectively (See Figure 6.13 for ^{1}H NMR spectrum of $Au_{38}(SC2Ph)_{24}$ upon ligand exchange with tiopronin in THF-d_8). The ligand exchange of $Au_{38}(SC2Ph)_{24}$ with the rest ligands were all done in the same way and 2nd order rate constants K_{P-E} in THF-d_8 are summarized in Table 1. K_{P-E} values of $Au_{38}(SC2Ph)_{24}$ in CD_2Cl_2 upon ligand exchange with some para-substituted arylthiol from previous study are also included for better comparison. K_{P-E} increased for in-coming arylthiols with increase of electron withdrawing ability of para-substituted group, i.e., from 5.5×10^{-3} for –Br, 10.5×10^{-3} for –Cl, to 74.0×10^{-3} $M^{-1} \bullet S^{-1}$ for $-NO_2$ group. However, for

Figure 6.12 ^{1}H NMR spectrum for the exchange of phenylethanethiolate (PhC2S-) by 4-bromothiophenol (4-Br-PhSH) onto $Au_{38}(SC2Ph)_{24}$ at 293 K in THF-d_8 (not degassed). Inset: (a) at t = 7 min; (b) at t = 73 min. Ferrocene serves as internal standard. Quartet at *ca*. 2.8 ppm is α-CH_2 on liberated phenylethanethiol (HS-***CH_2***-CH_2-Ph) and is used for the kinetic measurement. The *ca*. 2.9 ppm peak is from β-CH_2 on bound phenylethanethiolate (-S-CH_2-***CH_2***-Ph) and on liberated phenylethanethiol (HS-CH_2-***CH_2***-Ph).

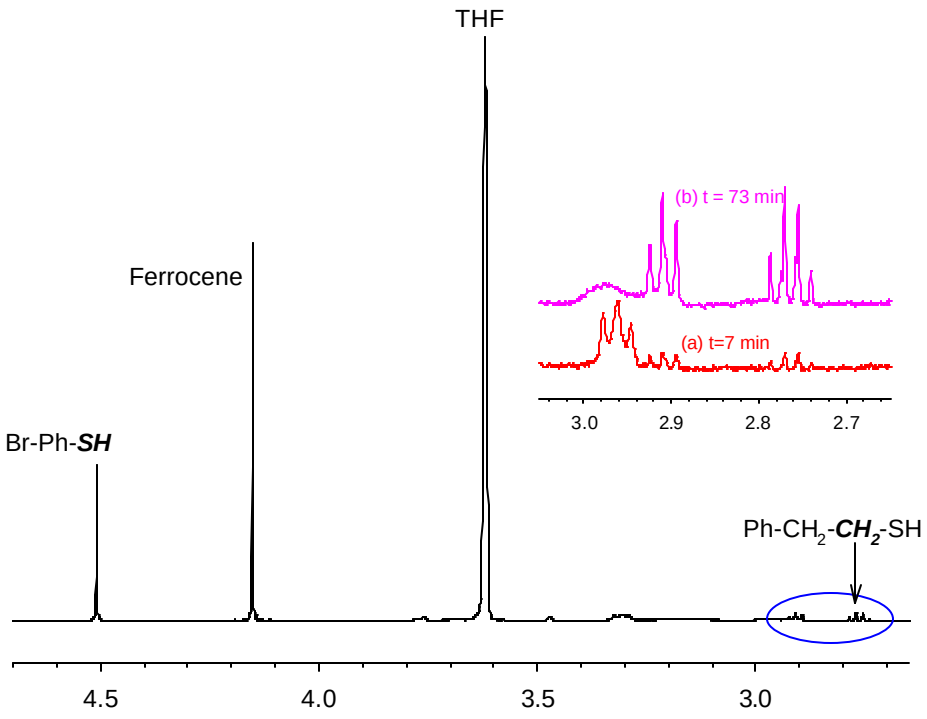
THF
Ferrocene
Br-Ph-SH
(b) t = 73 min
(a) t=7 min
3.0
2.9
2.8
2.7
Ph-CH2-CH2-SH
4.5
4.0
3.5
3.0

Figure 6.13 ^{1}H NMR spectrum for the exchange of phenylethanethiolate (PhC2S-) by tiopronin thiol onto $Au_{38}(SC2Ph)_{24}$ at 293 K in THF-d_8 (not degassed). Inset: (a) at t = 10 min; (b) at t = 50 min. Ferrocene serves as internal standard. Quartet at *ca*. 2.8 ppm is α-CH_2 on liberated phenylethanethiol (HS-***CH$_2$***-CH_2-Ph) and is used for the kinetic measurement. The *ca*. 2.9 ppm peak is from β-CH_2 on bound phenylethanethiolate (-S-CH_2-***CH$_2$***-Ph) and on liberated phenylethanethiol (HS-CH_2-***CH$_2$***-Ph). The broad peak at ca. 2.6 ppm comes from the hydrogen bonding of tiopronin in THF-d_8 and its peak area is found to be a constant within time scale of 10 tiopronin ligands exchanged. The rest resonance signals come from tiopronin.

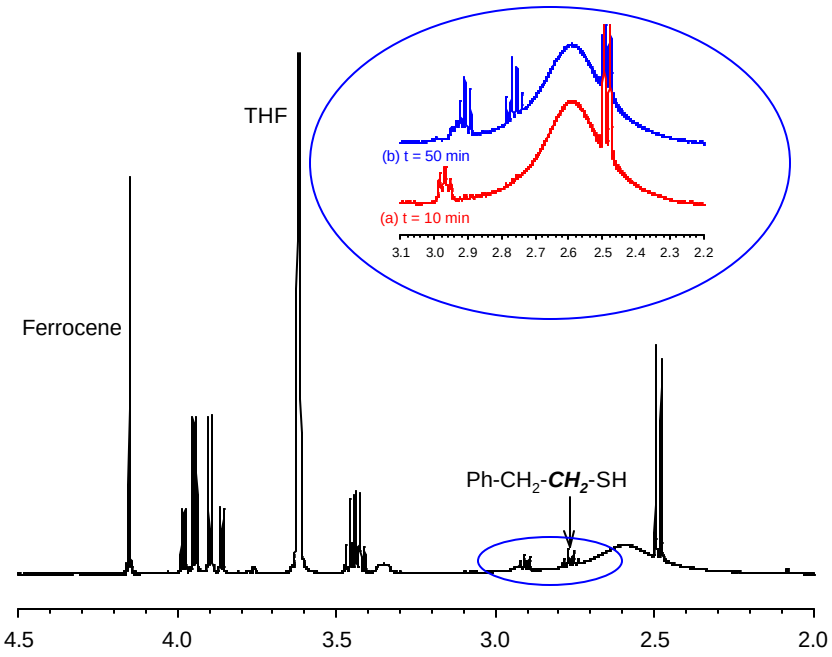
THF
Ferrocene
(b) t = 50 min
(a) t = 10 min
3.1 3.0 2.9 2.8 2.7 2.6 2.5 2.4 2.3 2.2
Ph-CH2-CH2-SH
4.5 4.0 3.5 3.0 2.5 2.0

para-substituted arylthiols with electrondonating groups, such as $-CH_3$ and $-OCH_3$, K_{P-E} did not follow the same trend. Similar substituent effects were seen in CD_2Cl_2 and interpreted as the electron withdrawing groups help stablize the build-up of negative charge in transition state thus accelarated the exchange rate. Most of the K_{P-E} values in THF-d_8 are in the order of 10^{-3} $M^{-1} \bullet S^{-1}$, 2 ~ 7 times larger than those in CD_2Cl_2,[41] with the most significant solvent effects on ligand exchange kinetics seen for 4-nitrothiophenol, an increase of ca. 7 times. Solvent effects on ligand exchange kinetics of $Au_{38}(SC2Ph)_{24}$ are not very clear and currently under study. Besides, an induction period in the exchange profile was observed for tiopronin (Figure 6.5 (c)) and 4-chlorothiophenol (Figure 6.2 (c)) — the exchange process is slow at the beginning (for the first one or two ligands exchanged) then became faster after that. It is likely when exchanging some very polar ligands to the non-polar environment of $Au_{38}(SC2Ph)_{24}$ monolayer, it is harder for the first one or two ligands to be exchanged onto the gold core, after that, it became easier. However, this induction period is not observed for N-acetyl-L-cysteine and 4-nitrothiophenol (k_{P-E} very large).

6.4 REFERENCES

1 Brust, M.; Walker, M.; Bethell, D.; Schiffrin, D. J.; Whyman, R. *J. Chem. Soc.-Chem. Commun.* **1994**, 801.

2 Scott, R. W. J.; Wilson, O. M.; Crooks, R. M. *J. Phys. Chem. B* **2005**, *109*, 692.

3 Zheng, J.; Zhang, C. W.; Dickson, R. M. *Phys. Rev. Lett.* **2004**, *93(7)*, 077402.

4 Devenish, R. W.; Goulding, T.; Heaton, B. T.; Whyman, R. *J. Chem. Soc.-Dalton Trans.* **1996**, 673.

5 Maye, M. M.; Zheng, W. X.; Leibowitz, F. L.; Ly, N. K.; Zhong, C. J. *Langmuir* **2000**, *16*, 490.

6 Zhong, C. J.; Zhang, W. X.; Leibowitz, F. L.; Eichelberger, H. H. *Chem. Commun.* **1999**, 1211.

7 Schaaff, T. G.; Whetten, R. L. *J. Phys. Chem. B* **1999**, *103*, 9394.

8 Wei, G. T.; Liu, F. K.; Wang, C. R. C. *Anal. Chem.* **1999**, *71*, 2085.

9 Wei, G. T.; Liu, F. K. *J. Chromatogr. A* **1999**, *836*, 253.

10 Wilcoxon, J. P.; Martin, J. E.; Provencio, P. *Langmuir* **2000**, *16*, 9912.

11 Wilcoxon, J. P.; Martin, J. E.; Provencio, P. *J. Chem. Phys.* **2001**, *115*, 998.

12 Bos, W.; Steggerda, J. J.; Yan, S. P.; Casalnuovo, J. A.; Mueting, A. M.; Pignolet, L. H. *Inorg. Chem.* **1988**, *27*, 948.

13 Whetten, R. L.; Khoury, J. T.; Alvarez, M. M.; Murthy, S.; Vezmar, I.; Wang, Z. L.; Stephens, P. W.; Cleveland, C. L.; Luedtke, W. D.; Landman, U. *Adv. Mater.* **1996**, *8*, 428.

14 Jimenez, V. L.; Leopold, M. C.; Mazzitelli, C.; Jorgenson, J. W.; Murray, R. W. *Anal. Chem.* **2003**, *75*, 199.

15 Schaaff, T. G.; Knight, G.; Shafigullin, M. N.; Borkman, R. F.; Whetten, R. L. *J. Phys. Chem. B* **1998**, *102*, 10643.

16 Templeton, A. C.; Cliffel, D. E.; Murray, R. W. *J. Am. Chem. Soc.* **1999**, *121*, 7081.

17 Brust, M.; Fink, J.; Bethell, D.; Schiffrin, D. J.; Kiely, C. *J. Chem. Soc.-Chem. Commun.* **1995**, 1655.

18 Templeton, A. C.; Hostetler, M. J.; Warmoth, E. K.; Chen, S. W.; Hartshorn, C. M.; Krishnamurthy, V. M.; Forbes, M. D. E.; Murray, R. W. *J. Am. Chem. Soc.* **1998**, *120*, 4845.

19 Ingram, R. S.; Hostetler, M. J.; Murray, R. W. *J. Am. Chem. Soc.* **1997**, *119*, 9175.

20 Hostetler, M. J.; Templeton, A. C.; Murray, R. W. *Langmuir* **1999**, *15*, 3782.

21 Song, Y.; Murray, R. W. *J. Am. Chem. Soc.* **2002**, *124*, 7096.

22 Song, Y.; Huang, T.; Murray, R. W. *J. Am. Chem. Soc.* **2003**, *125*, 11694.

23 Song, Y.; Harper, A. S.; Murray, R. W. *Langmuir* **2005**, *21*, 5492.

24 Donkers, R. L.; Song, Y.; Murray, R. W. *Langmuir* **2004**, *20*, 4703.

25 Guo, R.; Murray, R. W. *J. Am. Chem. Soc.* **2005**, *127*, 12140.

26 Lee, D.; Donkers, R. L.; Wang, G. L.; Harper, A. S.; Murray, R. W. *J. Am. Chem. Soc.* **2004**, *126*, 6193.

27 Hicks, J. F.; Miles, D. T.; Murray, R. W. *J. Am. Chem. Soc.* **2002**, *124*, 13322.

28 Quinn, B. M.; Liljeroth, P.; Ruiz, V.; Laaksonen, T.; Kontturi, K. *J. Am. Chem. Soc.* **2003**, *125*, 6644.

29 Chen, S. W.; Ingram, R. S.; Hostetler, M. J.; Pietron, J. J.; Murray, R. W.; Schaaff, T. G.; Khoury, J. T.; Alvarez, M. M.; Whetten, R. L. *Science* **1998**, *280*, 2098.

30 Balasubramanian, R; Guo, R; Mills, A.J.; Murray, R. W. *J. Am. Chem. Soc.* **2005,** *127(22)*, 8126.

31 Hercules, E. *Fluorescence and phosphorescence analysis*; Wiley & Sons, 1996.

32 Lakowicz, J. R. *Principles of fluorescence spectroscopy*; Plenum Press: New York, 1983.

33 Huang, T.; Murray, R. W. *J. Phys. Chem. B* **2001**, *105*, 12498.

34 Bigioni, T. P.; Whetten, R. L.; Dag, O. *J. Phys. Chem. B* **2000**, *104*, 6983.

35 Link, S.; Beeby, A.; FitzGerald, S.; El-Sayed, M. A.; Schaaff, T. G.; Whetten, R. L. *J. Phys. Chem. B* **2002**, *106*, 3410.

36 (a) Negishi, U.; Nobusada, K.; Tsukuda, T. *J. Am. Chem. Soc.* **2005,** *127*, 5261.

(b) Negishi, Y.; Takasugi, Y.; Sato, S.; Yao, H.; Kimura, K.; Tsukuda, T. *J. Am. Chem. Soc.* **2004**; *126*(21); 6518-6519.

37 Wang, G. L.; Huang, T.; Murray, R. W.; Menard, L.; Nuzzo, R. G. *J. Am. Chem. Soc.* **2005**, *127*, 812.

38 Donkers, R. L.; Lee, D.; Murray, R. W. *Langmuir* **2004**, *20(5)*, 1945.

39 *Handbook of Preparative Inorganic Chemistry*, Brauer, G., Ed.; Academic Press: New York, **1965**; p 1054.

40 Zhou, Z. Y.; Brus, L.; Friesner, R. *Nano Lett.* **2003**, *3*, 163.

41 Guo, R.; Song, Y.; Wang G.; Murray, R. W. *J. Amer. Chem. Soc.* **2005**, *127*, 2752-2757.

Chapter VII

SYNTHESIS AND CHARACTERIZATION OF FLUOROUS GOLD NANOPARTICLES

7.1 INTRODUCTION

Transition-metal nanoparticles[1] have recently attracted a lot of attention due to their potential applications in optical, electronic and magnetic devices and catalysts.[2] In general, metallic nanoparticles have diameters between 1 and 100 nm and are surrounded by a shell of adequate protecting agent or monolayer to prevent from aggregation. The protecting agents can be broadly divided into three categories: (i) those that provide electrostatic stabilization,[3] such as cationic and anionic surfactants, (ii) those that simply entrap nanoparticles, such as polymers,[4] cyclodextrins,[5] and dendrimers,[6] (iii) those that provide steric stabilization, such as organothiolates,[7] organoamines,[8] and organophosphines.[9] Among them, thiolate ligands are widely used for monolayer-protected clusters (MPCs) with gold cores.

Yonezawa *et al.*[10] first employed fluorinated thiols, 1*H*, 1*H*, 2*H*, 2*H*-perfluorodecanethiol and 1*H*, 1*H*, 2*H*, 2*H*-perfluorooctanethiol to directly synthesize fluorocarbon-stabilized gold nanoparticles in ethanol. The fluorinated nanoparticles obtained are ca. 3 nm in diameter and they are not soluble in common organic solvents but can be readily dispersed into fluorocarbon media. Cheetham *et al.*[11] synthesized ca. 4 nm size gold nanoparticles capped by 1*H*, 1*H*, 2*H*, 2*H*-perfluorooctanethiolate following a modified Brust

synthesis procedure[7(c)] and studied the structure with total scattering powder neutron diffraction. Esumi *et al.*[12] reported synthesis of gold nanoparticles from an organometallic compound triphenylphosphine gold (I) perfluorooctanoate in supercritical carbon dioxide and they obtained ca. 1 nm core size gold nanoparticles showing step-like fine UV-vis spectra in $ScCO_2$. Other metal nanoparticles, such as Ag,[13,14] Pt,[13] Pd,[14] Ir,[13] and Ag-Pd[14] nanoparticles have also been synthesized from their organo compounds in $ScCO_2$ as well. Moreno-Manas *et al.* obtained gold[15] and palladium[16] nanoparticles entrapped in heavily fluorinated compounds.

Ligand exchange reaction has been a powerful tool to manipulate MPC chemical properties, obtain mixed-monolayer[7(a),(d),8,17-25] or new monolayer-protected nanoparticles.[26] $Au_{55}(PPh_3)_{12}Cl_6$ synthesis was first reported by Schmid *et al.*[27] in the early 1980s and continued to draw attention as a template to prepare both organic and aqueous soluble 1-2 nm thiolate-protected gold nanoparticles using ligand exchange reactions.[28,29] Our lab[26(b)] has recently obtained $Au_{75}(SR)_{40}$ nanoparticles through ligand exchange reactions with $Au_{55}(PPh_3)_{12}Cl_6$ where RSH = $C_6H_{13}SH$, C_3H_7SH and PhC_2H_4SH. This Au_{75} nanoparticle was characterized by LDI-MS, electrochemistry, TGA, TEM, etc. This chapter describes the synthesis and characterization of fluorous Au_{75} nanoparticles by ligand exchange reactions of $Au_{55}(PPh_3)_{12}Cl_6$ with pentafluorobenzenethiol (1*H*, 1*H*, 2*H*, 2*H*- perfluorodecanethiol and 1*H*, 1*H*, 2*H*, 2*H*-perfluorooctanethiol).

7.2 EXPERIMENTAL SECTION

7.2.1 Chemicals. Pentafluorobenzenethiol (Aldrich, 97%), triphenylphosphine (Aldrich, 99%), boron trifluoride diethyletherate (Aldrich), Celite (Aldrich, high purity analytical grade), 1*H*, 1*H*, 2*H*, 2*H*- perfluorodecanethiol (Fluka, ≥ 99.0%), tetrabutylammonium

perchlorate (Bu_4NClO_4, Fluka, , ≥ 99%), 1*H*, 1*H*, 2*H*, 2*H*-perfluorooctanethiol (Fluka, ≥ 99.0 %), perfluoro (2-butyltetrahydrofuran) (Oakwood products), acetonitrile (Fisher, ≥ 99.9%), and dichloromethane (Fisher, 99.9%) were used as received. $HAuCl_4 \bullet 3H_2O$ was synthesized according to literature procedures[30] and Schmid's protocol[27] was used for the synthesis of $Au_{55}(PPh_3)_{12}Cl_6$.

7.2.2 Ligand Exchange of $Au_{55}(PPh_3)_{12}Cl_6$ with Fluorinated Thiols. In a typical reaction, 7 mg $Au_{55}(PPh_3)_{12}Cl_6$ was dissolved in 2 ml CH_2Cl_2, then 3.7 µl pentafluorobenzenethiol (3:1 thiol/ligand ratio) was added and the solution mixture reacted for ~ 22 h. The solvent CH_2Cl_2 was then evaporated and the exchange product was washed copiously with MeOH. The first exchange product (~ 4-5 mg) was redissolved in 2 ml CH_2Cl_2 and 5 µl pentafluorobenzenethiol was added again and reacted for another 22 h. CH_2Cl_2 was evaporated and the final exchange product (~ 2 mg) was obtained by precipitating and washing with MeOH. The final product was soluble in CH_2Cl_2, THF, DMF, etc, and insoluble in fluorous solvent Perfluoro (2-butyltetrahydrofuran). When the in-coming thiol is 1*H*, 1*H*, 2*H*, 2*H*- perfluorodecanethiol or 1*H*, 1*H*, 2*H*, 2*H*-perfluorooctanethiol, the exchange product precipitated out of CH_2Cl_2 by itself and was insoluble in regular organic solvents, but soluble in fluorous solvent perfluoro(2-butyltetrahydrofuran) and partially soluble in liquid CO_2 due to partially exchanged longer fluorinated alkanethiolates.

7.2.3 Electrochemical Measurement. Cyclic voltammetry and Osteryoung square wave voltammetry (OSWV) of Au MPCs were performed using a Bioanalytical Systems (BAS) Model 100B at 11°C in 0.1M Bu_4NClO_4/CH_2Cl_2. The 1.6 mm dia. Pt working electrode was polished, rinsed and sonicated in NANOpure water, rinsed with absolute ethanol and acetone,

and cleaned by potential-cycling in 0.5 M H_2SO_4 for 15 min. A Pt coil counter electrode and Ag wire quasi-reference electrode were used.

7.2.4 HPLC Experiment. HPLC separation was done with an instrument equipped with a Waters 600 controller pump, a photodiode array detector (Waters 996 PDA, detected at 400 nm), a Rheodyne 7725 injection valve with a 50 µl sample loop. A fluorophase WP stainless steel column (250 × 4.6 mm i.d. column, 5 µm particle size, 300 Å pore size, Thermo Electron Corp.) was used. The mobile phase was 90%CH_2Cl_2 (10 mM Bu_4NClO_4) /10% CH_3CN at a flow rate of 0.7 ml/min. The sample was filtered through a 0.45 µm Nalgene syringe filter with Teflon membrane prior to injection.

7.2.5 Other Measurements. ^1H NMR and ^{19}F NMR spectra of Au MPCs and free thiols in d_2-methylene chloride were collected with Bruker AC 400 and 500 MHz spectrometers. UV-vis spectra of Au MPCs in methylene chloride were taken using a Shimadzu UV-1601 UV-visible spectrophotometer. Thermogravimetric analysis (TGA) was carried out in a Perkin-Elmer Pyris 1 thermogravimetric analyzer with 2-3 mg of MPCs in an Al pan at a heating rate of 10 °C /min. Transmission electron microscopy phase contrast images were obtained with a side-entry Phillips CM 12 microscope operating at 120 KeV, of Au MPCs prepared by spreading a droplet of diluted MPC solution (~ 1mg/ 10 ml CH_2Cl_2), drying in air for 20 minutes on standard carbon-coated (20-30 nm) Formvar films on copper grids (400 mesh).

7.3 RESULTS AND DISCUSSION

7.3.1 Electrochemistry. Figure 7.1(a) shows the Osteryoung square wave voltammetry (OSWV) of 2 mg exchange product of $Au_{55}(PPh_3)_{12}Cl_6$ with

pentafluorobenzenethiol in 3 ml CH_2Cl_2 with 0.1 M Bu_4NClO_4 at 283 K. There are several observations here: (i) peaks in the negative-going scan (top) are better defined than those in positive-going scan; (ii) there is a "doublet" of ca. 255 mV spacing corresponding to first and second oxidation of exchange product and an ca. 737 mV electrochemical gap characteristic of electrochemistry of "molecule-like" nanoparticles;[26, 31] (iii) several reduction peaks can be observed in the negative-going scan although they are not clearly-defined in the positive-going scan; (iv) the exchange product is quite polydisperse, i.e., monodispersity is only about 10% based on the $(i_{peak+2/+1} - i_{valley+1})/i_{peak+2/+1}$ ratio. The oxidation and reduction peaks are not as well defined as those for $Au_{38}(SC2Ph)_{24}$,[31(a)] $Au_{38}(SC6)_{24}$[31(b)] and other $Au_{75}(SR)_{40}$[26(b)] nanoparticles where R= C_6H_{13}, C_3H_7 and PhC_2H_4. Au_{38} NPs' electrochemical gap and corrected electrochemical gap are ca. 1.6 and 1.3 eV respectively [26(a), 31(a)] while Au_{75} NPs' are ca. 0.74 and 0.47 eV respectively.[26(b)] Compared to electrochemistry of $Au_{75}(SR)_{40}$ nanoparticles synthesized previously in our lab, the exchange product gave a similar electrochemical gap and corrected electrochemical gap (0.74 and 0.48 eV respectively, based on better defined negative-going scan data) which is an indication that it is Au_{75} as well, but this needs to be further confirmed by mass spectrometry. Figure 7.1(b) is the corresponding cyclic voltammetry (CV) of the exchange product, due to the polydispersity of the sample, the peaks in CV are not well defined, and which is why we used OSWV in order to resolve peak position better.

7.3.2 Thermogravimetric Analysis (TGA). When MPCs are heated to a certain temperature, they will decompose by liberation of the thiolate ligands as volatile disulfides, leaving behind the aggregated gold cores.[32] Thus TGA is a convenient way to determine the weight fraction of the organic monolayer of the gold MPCs. Shown in Figure 7.2 is the TGA

Figure 7.1 (a) Osteryoung square wave voltammetry (OSWV), and (b) cyclic voltammetry (CV) of 2 mg exchange product of $Au_{55}(PPh_3)_{12}Cl_6$ with pentafluorobenzenethiol in 3 ml CH_2Cl_2 with 0.1 M Bu_4NClO_4 at 283 K.

(a)

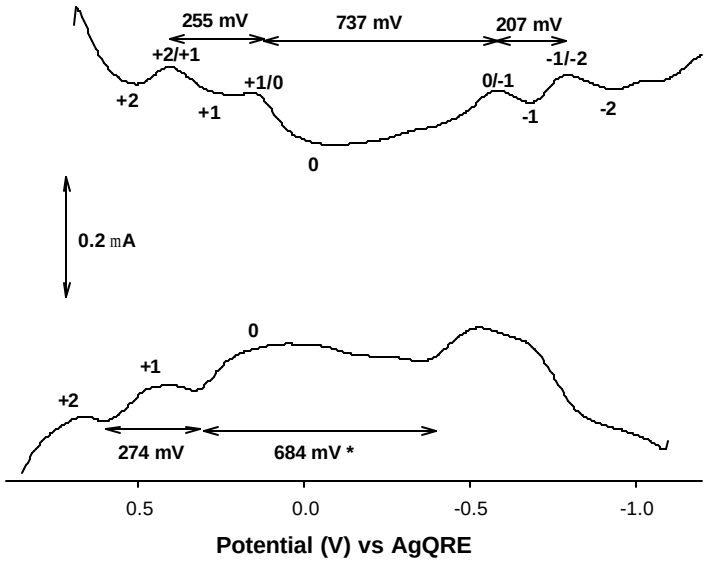
255 mV
737 mV
207 mV
+2/+1
+1/0
0/-1
-1/-2
+2
+1
0
-1
-2
0.2 mA
0
+1
+2
274 mV
684 mV *
0.5
0.0
-0.5
-1.0
Potential (V) vs AgQRE

(b)

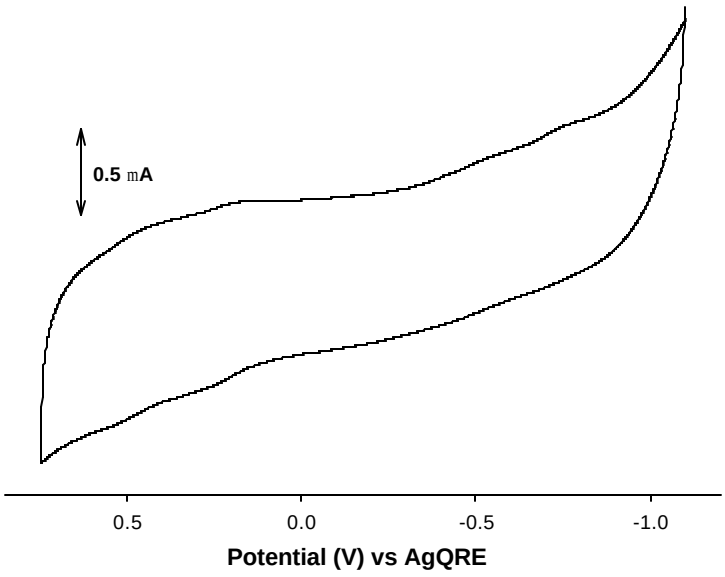
0.5 mA
0.5
0.0
-0.5
-1.0
Potential (V) vs AgQRE

Figure 7.2 Thermogravimetric decomposition of exchange product of $Au_{55}(PPh_3)_{12}Cl_6$ with pentafluorobenzenethiol.

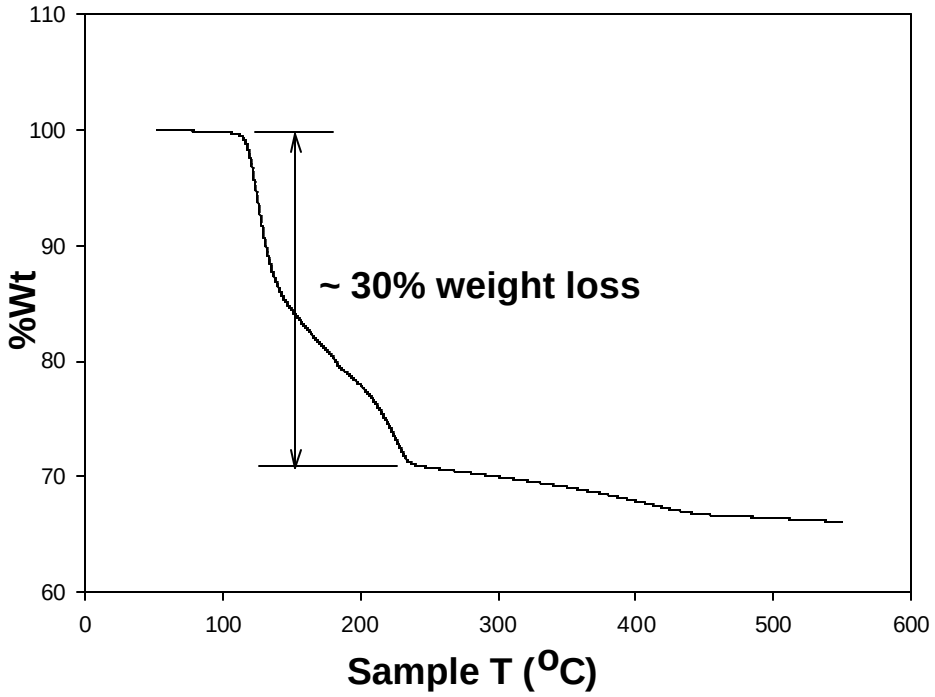
110
100
90
80
70
60
%Wt
~ 30% weight loss
0
100
200
300
400
500
600
Sample T (OC)

result of the exchange product. It shows a ~ 30% weight loss leading to the formula $Au_{75}(SC6F5)_{32}$ of the exchange product. Here we assumed it is a Au75 core based on electrochemistry. No triphenylphosphine or chloride was detected by XPS indicating close to 100% ligand exchange. The above calculation is quite crude since the sample is very polydisperse judging from the electrochemistry, and TEM images shown in Figure 7.3(a).

7.3.3 Optical Spectroscopy. Gold MPCs show size-dependent optical properties.[31(c), 33, 34] When the core diameter is greater than 2 nm, its UV-vis spectrum shows a surface plasmon resonance at ~ 520 nm.[32] When the gold core is 1.6 nm, such as $Au_{140}(SC6)_{53}$, the surface plasmon resonance is absent and UV-vis spectrum is almost featureless.[32] When the core diameter is even smaller, such as Au_{38}[26(a), 31(a), (b)] or Au_{11}[35], a step-like fine structure characteristic of molecule-like behavior is observed. Figure 7.4 (a) shows the UV-vis spectra of $Au_{55}(PPh_3)_{12}Cl_6$ and the exchange product $Au_{75}(SC6F5)_{32}$. $Au_{75}(SC6F5)_{32}$ is almost featureless and $Au_{55}(PPh_3)_{12}Cl_6$ has a very small bump at ~ 520 nm. $Au_{75}(SC6F5)_{32}$ shows an electrochemical gap in OSWV, and is considered as a molecule-like nanoparticle, but probably due to its polydispersity, its intrinsic spectral details might be buried by other size nanoparticles. Figure 7.4 (b) shows the luminescence spectrum of $Au_{75}(SC6F5)_{32}$ in CH_2Cl_2; the solution was excited at 400 nm where its absorbance is ca. 0.12. The luminescence intensity is very weak. Generally speaking, smaller core size nanoparticles with polar ligands or water soluble ligands have much stronger luminescence intensity than bigger ones with relatively non-polar organic soluble ligands.[31(a), 34(b), 35, 36, 37] The exchange product $Au_{75}(SC6F5)_{32}$ is very polydisperse and contains a lot of larger nanoparticles without a HOMO-LUMO gap, that probably is the reason why the luminescence of $Au_{75}(SC6F5)_{32}$ is so weak.

Figure 7.3 Transmission electron microscopy (TEM) images of $Au_{75}(SC6F5)_{32}$ (a) and $Au_{55}(PPh_3)_{12}Cl_6$ (b).

(a)

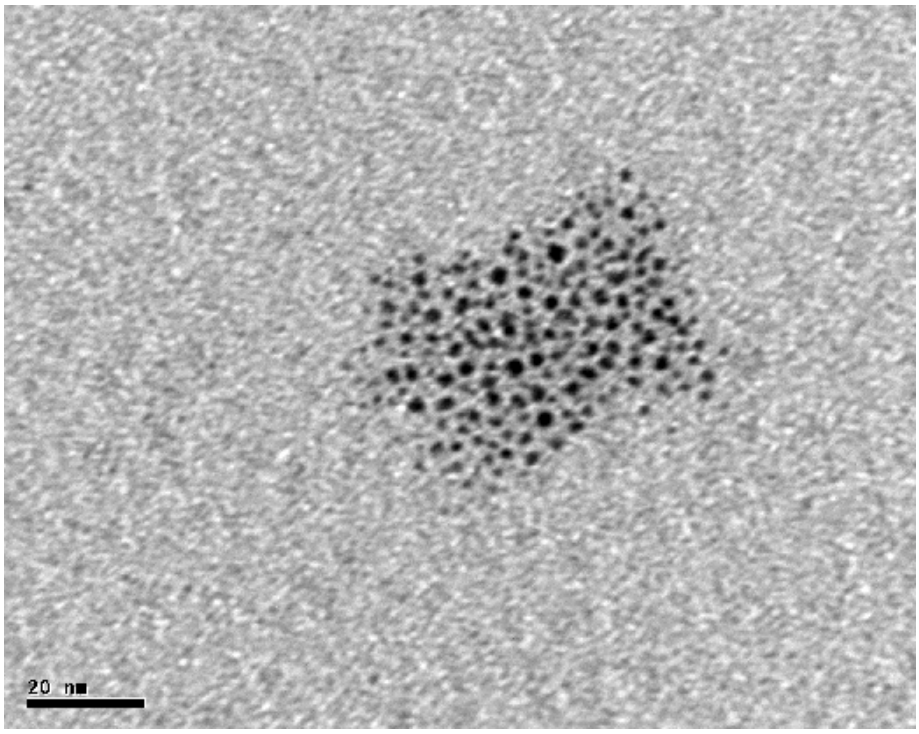

(b)

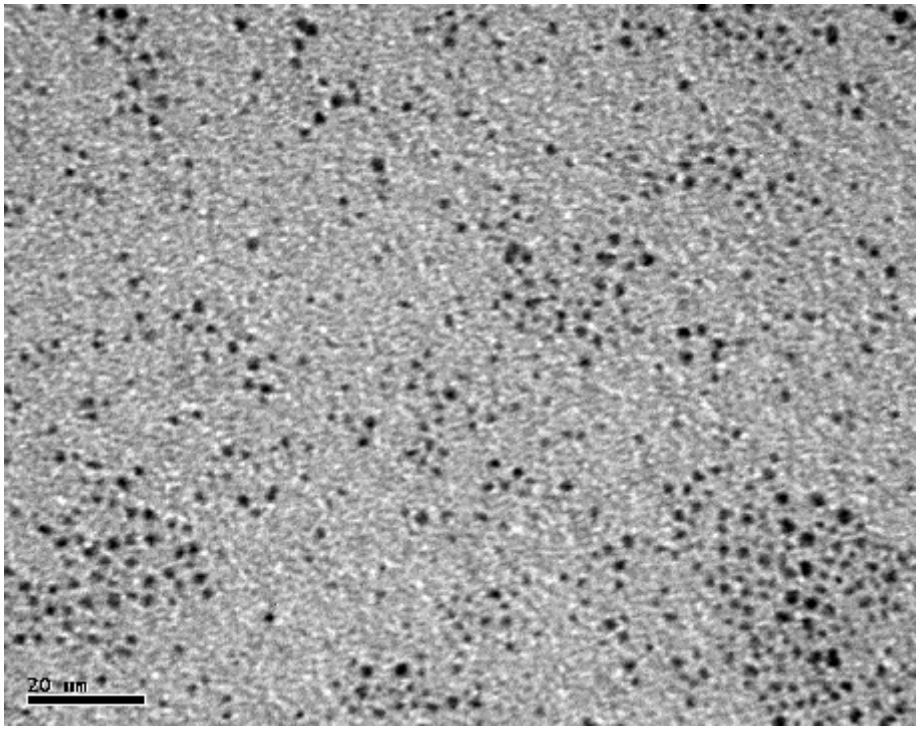

Figure 7.4 (a) UV-vis spectra of $Au_{55}(PPh_3)_{12}Cl_6$ and the exchange product $Au_{75}(SC6F5)_{32}$ in CH_2Cl_2. (b) Luminescence spectrum of $Au_{75}(SC6F5)_{32}$ in CH_2Cl_2; the solution was excited at 400 nm where the absorbance is 0.12.

(a)

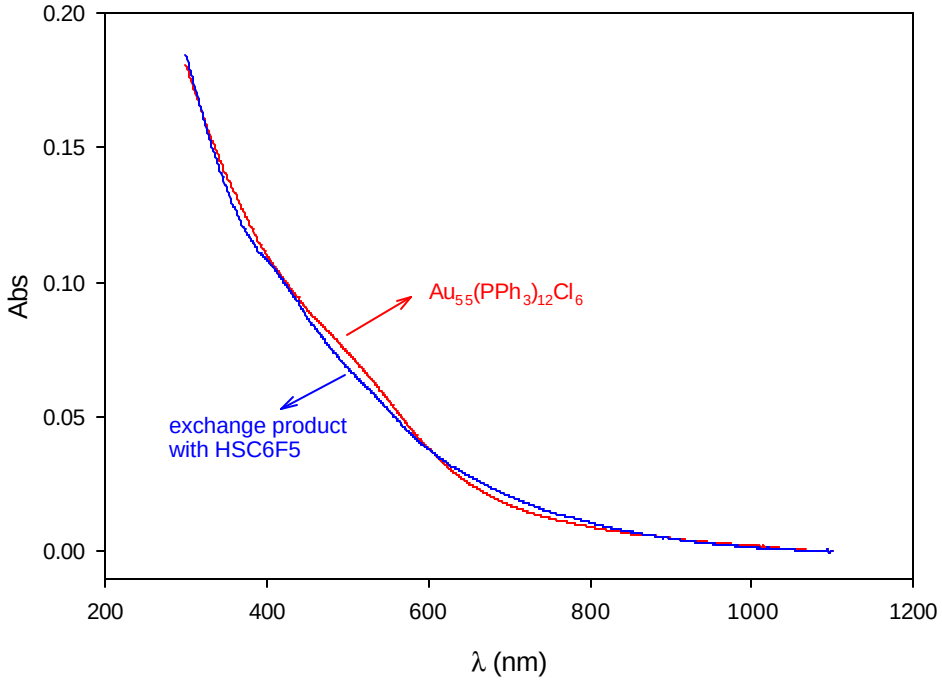
0.20
0.15
0.10
0.05
0.00
Abs
200
400
600
800
1000
1200
λ (nm)
Au55(PPh3)12Cl6
exchange product
with HSC6F5

(b)

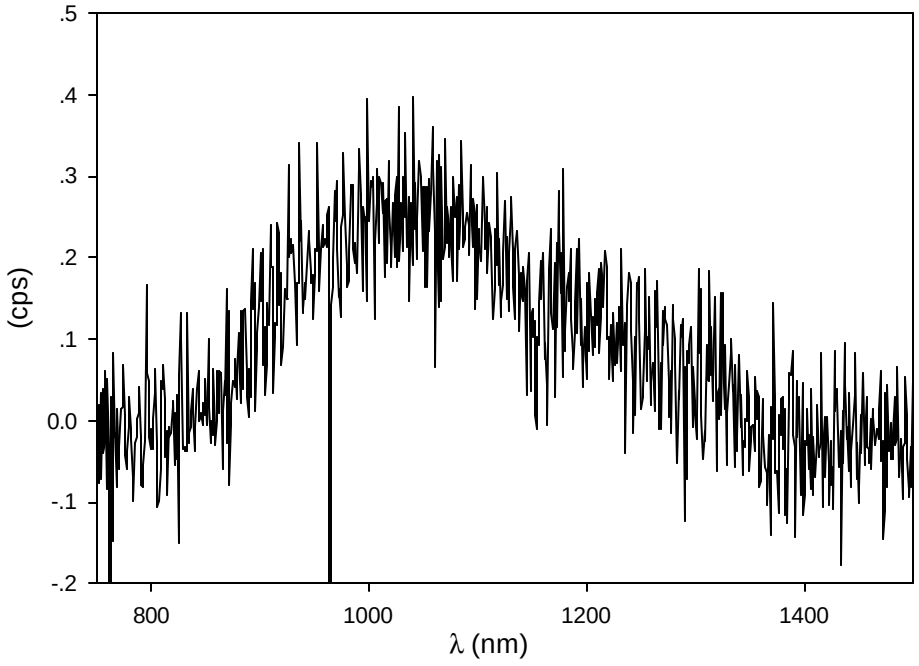
.5
.4
.3
.2
.1
0.0
-.1
-.2
(cps)
800
1000
1200
1400
λ (nm)

7.3.4 Reversed-Phase HPLC Separation. As-prepared nanoparticles are usually polydisperse and require further purification in order to characterize their size-dependent properties such as electrochemical and optical properties. Different chromatographic separations have been employed to separate polydisperse metal nanoparticles, such as size exclusion chromatography (SEC),[38] ion-exchange chromatography (IEC),[39] ion-pair[40] and reversed-phase chromatography.[41] There are many parameters that can affect the separation of the gold nanoparticles such as the core size, types of ligands, ligand heterogeneity, core charge state, stationary and mobile phase compositions, etc. Figure 7.5 shows the reversed-phase HPLC separation of ligand exchange product $Au_{75}(SC6F5)_{32}$ where the mobile phase was 90%CH_2Cl_2 (10 mM Bu_4NClO_4) /10% CH_3CN at a flow rate of 0.7 ml/min, the stationary phase was a fluorophase WP stainless steel column. There are five peaks eluted from the column---peaks **1-4** are comparable size and peak 5 is much smaller than the rest. UV-vis spectrum of peak **5** gave a step-like fine structure which is an indication of molecule-like nanoparticles, possibly Au_{38}. The UV-vis spectra of peaks **1-4** are very similar, and do not have many features. The surface plasmon resonance at 520 nm is not clearly defined indicating the nanoparticles are all less than 2 nm. However, if we take a closer look at the overlapped UV-vis spectra of peaks **1-4**, in Figure 7.6, we can see some differences. It is not clear at this time whether the minor difference is due to core size or core charge state difference, or ligand heterogeneity or sth else. But at least one conclusion can be drawn: the exchange product is quite polydisperse which is also supported by TEM image Figure 7.3 (a).

7.3.5 ^{1}H and ^{19}F NMR Spectroscopy. ^{1}H NMR has been successfully used to study the ligand exchange of MPCs.[7(a), 17(a),(b), 42] Significant peak broadening of proton signals of the

Figure 7.5 Reversed-phase HPLC of $Au_{75}(SC6F5)_{32}$. The mobile phase was 90%CH_2Cl_2 (10 mM Bu_4NClO_4) /10% CH_3CN at a flow rate of 0.7 ml/min, the stationary phase was a fluorophase WP stainless steel column. UV-vis spectra of peaks **1-5** obtained from PDA detector were shown on the top.

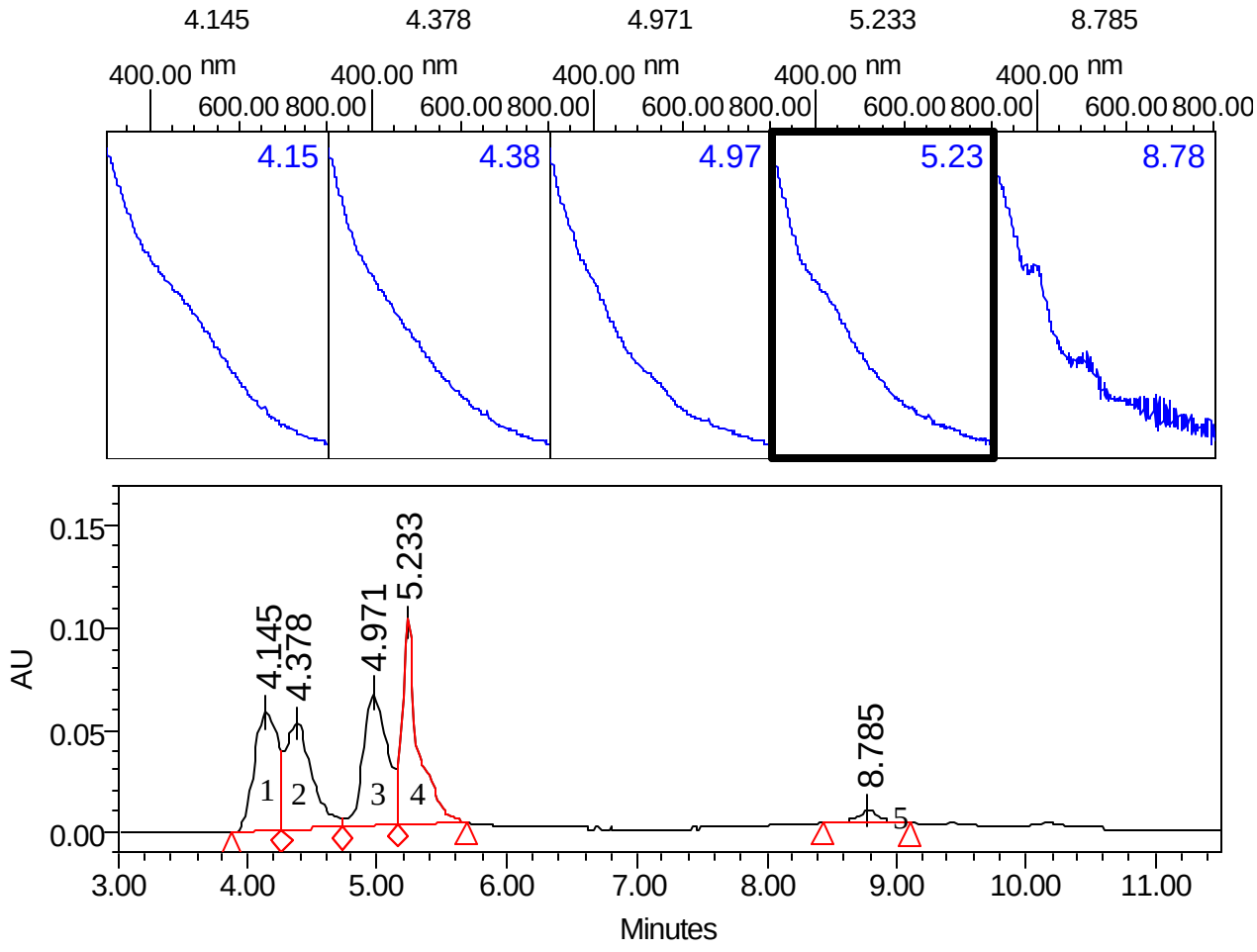
4.145
4.378
4.971
5.233
8.785
400.00 nm
600.00 800.00
4.15
4.38
4.97
5.23
8.78
AU
0.15
0.10
0.05
0.00
4.145
4.378
4.971
5.233
8.785
1
2
3
4
5
3.00
4.00
5.00
6.00
7.00
8.00
9.00
10.00
11.00
Minutes

Figure 7.6 Overlay of UV-vis spectra of peaks **1-5** from reversed-phase HPLC of $Au_{75}(SC6F5)_{32}$ in Figure 7.5. Absorbance is normalized at 300 nm.

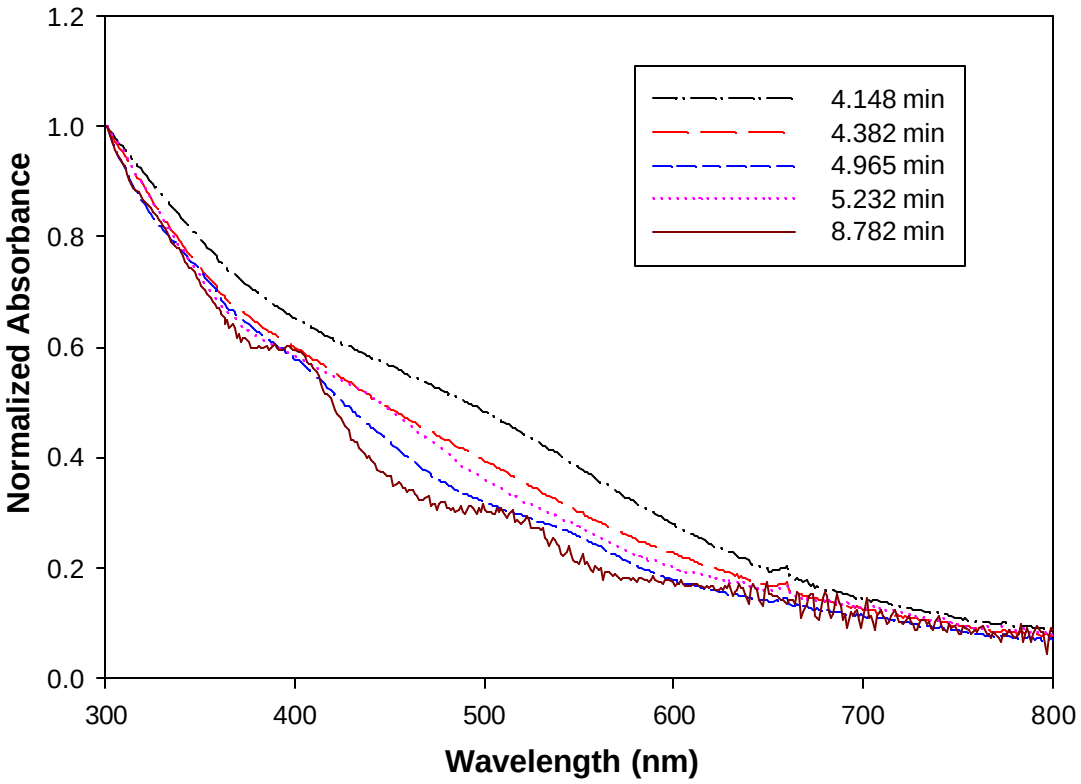
1.2
1.0
0.8
0.6
0.4
0.2
0.0
Normalized Absorbance
300
400
500
600
700
800
Wavelength (nm)
4.148 min
4.382 min
4.965 min
5.232 min
8.782 min

organic monolayer on the gold core compared to free ligands was observed probably due to[32]: (a) densely packed ligands lead to rapid spin-spin relaxation from dipolar interactions; (b) heterogeneous ligand binding sites (vertex, edge, terrace) on core surface lead to different chemical shifts even for the same type of protons; (c) polydispersity of the gold core leads to size-dependent spin-spin relaxation broadening. Figure 7.7 shows the ^{1}H NMR spectra of $Au_{55}(PPh_3)_{12}Cl_6$ (a); ligand exchange product $Au_{75}(SC6F5)_{32}$ (b); and free pentafluorobenzenethiol (c) in CD_2Cl_2. The broad bump at ca. 7 ppm in spectra (a) is due to the proton signal of triphenylphosphine. It is almost invisible in the exchange product $Au_{75}(SC6F5)_{32}$ indicating that most/all of the triphenylphosphine ligands have been replaced by the in-coming pentafluorobenzenethiolate. Since the exchange product is protected by pentafluorobenzenethiolate, we took ^{19}F NMR spectra of free pentafluorobenzenethiol and the exchange product $Au_{75}(SC6F5)_{32}$, as shown in Figure 7.8. The ortho-fluorine (Fo) signal of $Au_{75}(SC6F5)_{32}$ in Figure 7.8 (b) is invisible since it is very close to the gold core. There is a big bump at ca. -164 ppm probably corresponding to meta-fluorine (Fm). The para-fluorine (Fp) signal is not seen (supposed to be at around -159 ppm), which is not clear at this time. It is also possible that the big bump centered at -164 ppm originates from both Fp and Fm signals since the chemical shift of the bound pentafluorobenzenethiolate might be different from the free species.

Figure 7.7 ^{1}H NMR spectra of $Au_{55}(PPh_3)_{12}Cl_6$ (a); ligand exchange product $Au_{75}(SC6F5)_{32}$ (b); and free pentafluorobenzenethiol (c) in CD_2Cl_2.

(a)

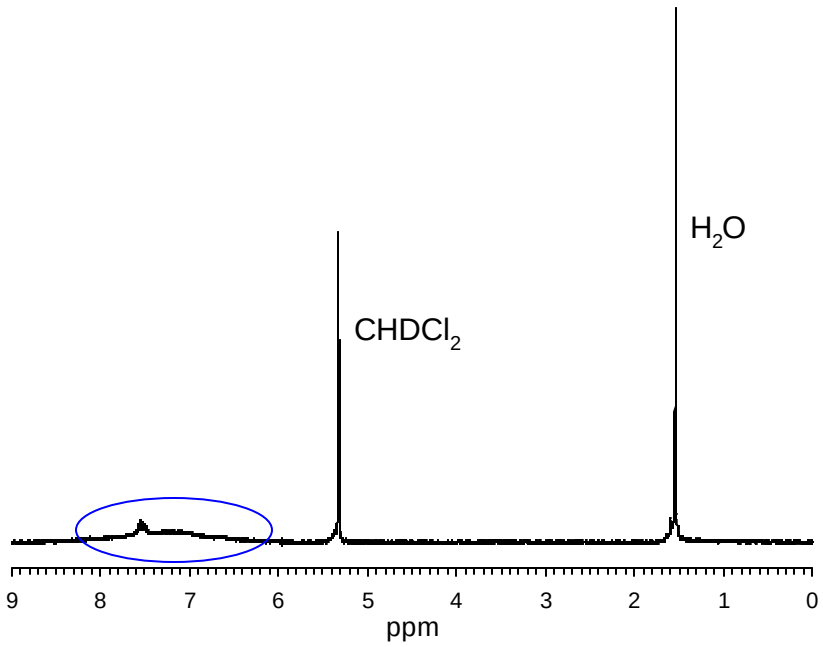
H2O
CHDCl2
9
8
7
6
5
4
3
2
1
0
ppm

(b)

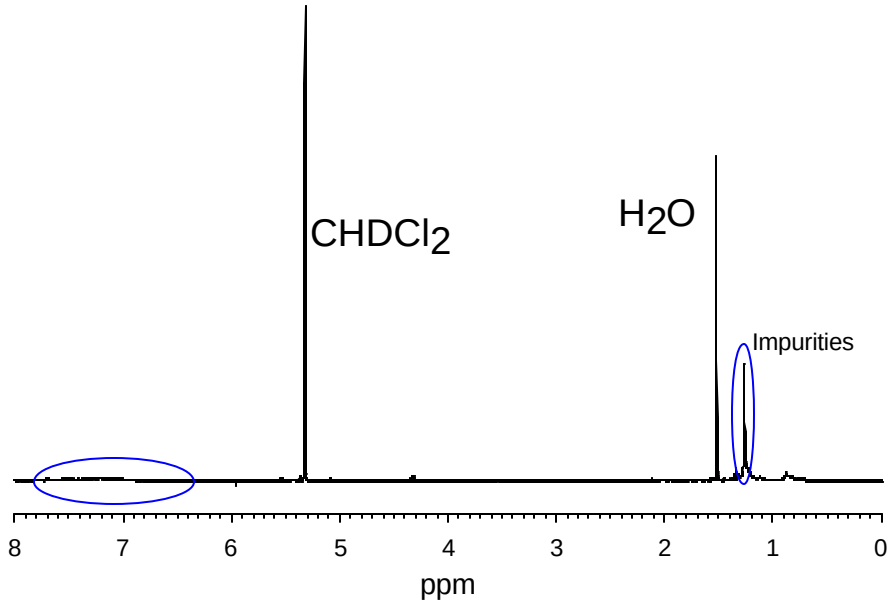
CHDCl2
H2O
Impurities
8
7
6
5
4
3
2
1
0
ppm

(c)

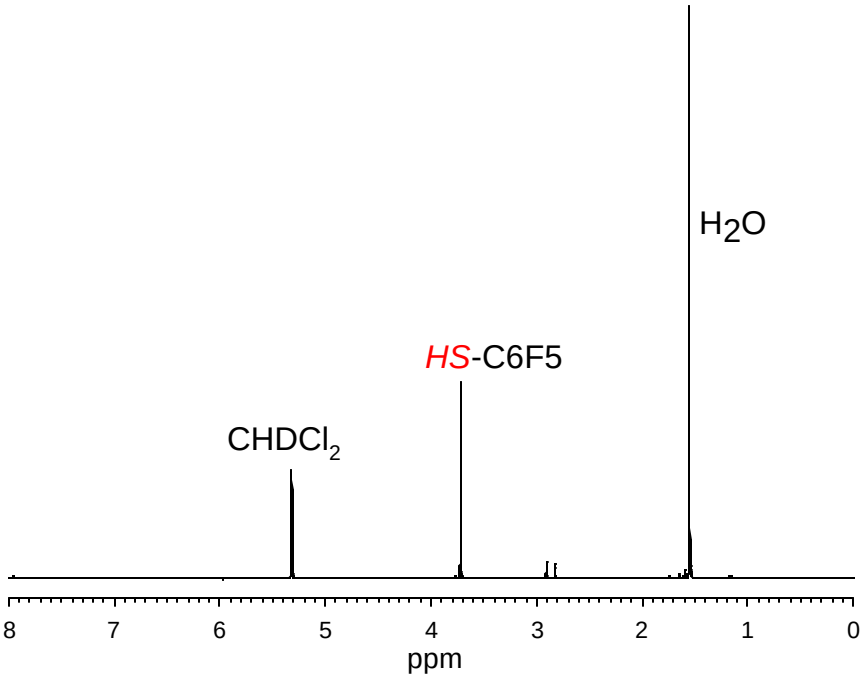

Figure 7.8 ^{19}F NMR spectra of free pentafluorobenzenethiol (a) and the exchange product $Au_{75}(SC6F5)_{32}$ (b) in CD_2Cl_2.

(a)

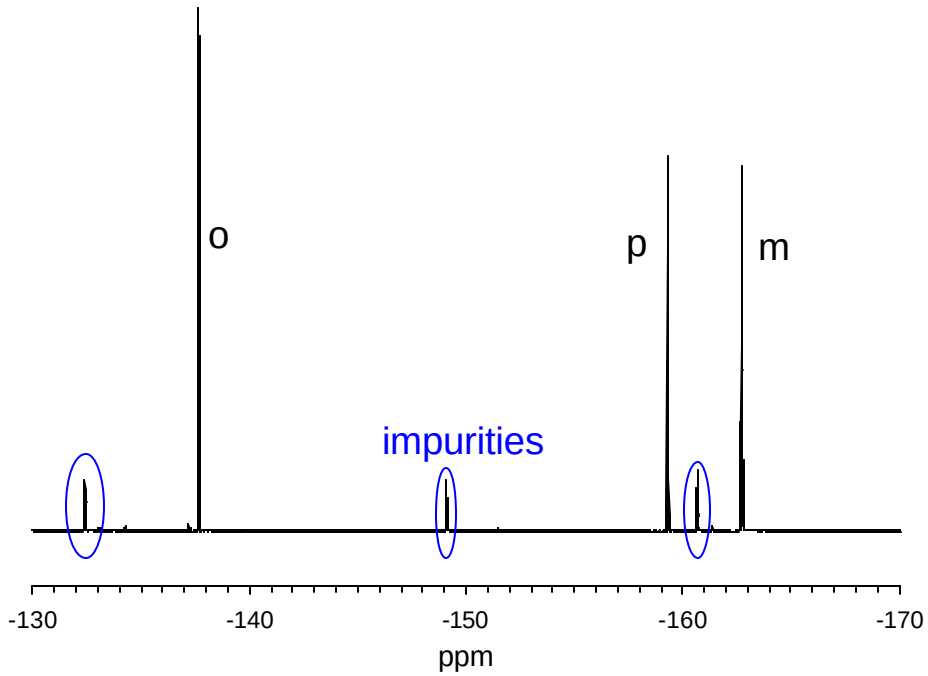
o
p
m
impurities
-130
-140
-150
-160
-170
ppm

(b)

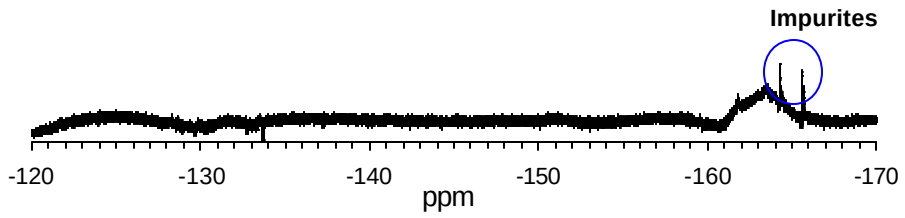
Impurites
-120
-130
-140
-150
-160
-170
ppm

7.4 References

1 (a) Schmid, G., Ed. *Clusters and Colloids*; VCH: Weinheim, Germany, **1994**. (b) Klabunde, K. J., Ed. *Nanoscale Materials in Chemistry*; John Wiley & Sons: New York, **2001**.

2 (a) Kamat, P. V. *J. Phys. Chem. B* **2002**, *106*, 7729. (b) Thomas, K. G.; Kamat, P. V. *Acc. Chem. Res.* **2003**, *36*, 888. (c) Shenhar, R.; Rotello, V. M. *Acc. Chem. Res.* **2003**, *36*, 549. (d) Schlögl, R.; Hamid, S. B. A. *Angew, Chem., Int, Ed.* **2004**, *43*, 1628. (e) Murphy, C. J. *Anal. Chem.* **2002**, *74*, 520A. (f) Feldheim, D. L.; Keating, C. D. *Chem. Soc. Rev.* **1998**, *27*, 1.

3 (a) Mafune, F.; Kohno, J.-y.; Takeda, Y.; Kondow, T.; Sawabe, H. *J. Phys. Chem. B.* **2001**; *105*(22); 5114. (b) Sau, T. K.; Murphy, C. J. *Langmuir* **2005**; *21*(7); 2923.

4 Yang, C-C.; Wang, Y-Y.; Wan, C-C. *J. Electrochem. Soc.* **2005,** *152(2),* C96.

5 Giuffrida, S.; Ventimiglia, G.; Petralia, S.; Conoci, S.; Sortino, S. *Inorg. Chem.* **2006**; *45*(2); 508.

6 (a) Scott, R. W. J.; Wilson, O. M.; Crooks, R. M. *J. Phys. Chem. B.* **2005**; *109*(2); 692. (b) Scott, R. W. J.; Ye, H.; Henriquez, R. R.; Crooks, R. M. *Chem. Mater.* **2003**; *15*(20); 3873.

7 (a) Templeton, A. C.; Wuelfing, W. P.; Murray, R. W. *Acc. Chem. Res.* **2000,** *33***, 27**. (b) Whetten, R. L.; Shafigullin, M. N.; Khoury, J. T.; Schaaff, T. G.; Vezmar, I.; Alvarez, M. M.; Wilkinson, A. *Acc. Chem. Res.* **1999**, *32*, 397. (c) Brust, M.; Walker, M.; Bethell, D.; Schiffrin, D. J.; Whyman, R. J.; *Chem. Soc. Chem. Commun.* **1994**, 801. (d) Brown, L. O.; Hutchison, J. E. *J. Am. Chem. Soc.* **1997**, *119*, 12384.

8 Brown, L. O.; Hutchison, J. E. *J. Am. Chem. Soc.* **1999**, *121*, 882.

9 (a) Schmid, G. *Chem. Rev.* **1992**, *92*, 1709. (b) Weare, W. W.; Reed, S. M.; Warner, M. G.; Hutchison, J.E. *J. Am. Chem. Soc.* **2000**, *122*, 12890. (c) Petroski, J.; Chou, M. H.; Creutz, C. *Inorg. Chem.* **2004**, *43*, 1597.

10 Yonezawa, T.; Onoue, S.; Kimizuka, N. *Langmuir* **2001**; *17*(8); 2291.

11 Page, K.; Proffen, T.; Terrones, H.; Terrones, M.; Lee, L.; Yang, Y.; Stemmer, S.; Seshadri, R.; Cheetham, A. K. *Chem. Phys. Lett.* **2004**, *393*, 385.

12 Esumi, K.; Sarashina, S.; Yoshimura, T. *Langmuir* **2004**, *20*, 5189.

13 Shah, P. S.; Husain, S.; Johnston, K. P.; Korgel, B. A. *J. Phys. Chem. B* **2001**, *105*, 9433.

14 Kameo, A.; Yoshimura, T.; Esumi, K. *Colloids Surf. A* **2003**, *215*, 181.

15 Moreno-Mañas, M.; Pleixats, R.; Tristany, M. *J. Fluorine. Chem.* **2005**, *126*, 1435.

16 **(a)** Tristany, M.; Courmarcel, J.; Dieudonne, P.; Moreno-Manas, M.; Pleixats, R.; Rimola, A.; Sodupe, M.; Villarroya, S. *Chem. Mater.* **2006**; *18*(3); 716. (b) Moreno-Manas, M.; Pleixats, R.; Villarroya, S. *Organometallics* **2001**, *20*, 4524. (c) Moreno-Manas, M.; Pleixats, R.; Villarroya, S. *Chem. Commun.* **2002**, 60.

17 (a) Song, Y.; Murray, R. W. *J. Am. Chem. Soc.* **2002**, *124*, 7096. (b) Hostetler, M. J.; Templeton, A. C.; Murray, R. W. *Langmuir* **1999**, *15*, 3782. (c) Wuelfing, W. P.; Zamborini, F. P.; Templeton, A. C.; Wen, W.; Yoon, H.; Murray, R. W. *Chem. Mater.* **2001**, *13*, 87. (d) Wuelfing, W. P.; Murray, R. W. *J. Phys. Chem. B.* **2002**, *106*, 3139. (e) Zamborini, F. P.; Leopold, M. C.; Hicks, J. F.; Kulesza, P. J.; Malik, M. A.; Murray, R. W. *J. Am. Chem. Soc.* **2002**, *124*, 8958. (f) Lee, D.; Donkers, R. L.; DeSimone, J. M.; Murray, R. W. *J. Am. Chem. Soc.* **2003**, *125*, 1182.

18 Kell, A. J.; Stringle, D. L. B.; Workentin, M. S. *Org. Lett.* **2000**, 3381.

19 Han, L.; Daniel, D. R.; Maye, M. M.; Zhong, C.-J. *Anal. Chem.* **2001**, *73*, 4441.

20 Kell, A. J.; Workentin, M. S. *Langmuir* **2001**, *17*, 7355.

21 Ionita, P.; Caragheorgheopol, A. *J. Am. Chem. Soc.* **2002**, *124*, 9048.

22 Lin, S.-Y.; Liu, S.-W.; Lin, C.-M.; Chen, C. *Anal. Chem.* **2002**, *74*, 330.

23 Li, D.; Li, J. *Surf. Sci.* **2003**, *522*, 105.

24 Pengo, P.; Broxterman, Q. B.; Kaptein, B.; Pasquato, L.; Scrimin, P. *Langmuir* **2003**, *19*, 2521.

25 Woehrle, G. H. ; Warner, M. G. ; Hutchison, J. E. *J. Phys. Chem. B* **2002**, *106*, 9979.

26 (a) Guo, R; Murray, R. W. *J. Am. Chem. Soc.* **2005**, *127(34)*, 12140. (b) Balasubramanian, R; Guo, R; Mills, A.J.; Murray, R. W. *J. Am. Chem. Soc.* **2005,** *127(22)*, 8126.

27 (a) Schmid, G.; Pfeil, F.; Boese, R.; Bandermann, F.; Meyer, S.; Calis, G. H. M.; van der Velden, J. W. A. *Chem. Ber.* **1981**, *114*, 3634. (b) Schmid, G. *Inorg. Synth.* **1990**, *27*, 214.

28 (a) Schmid, G.; Klein, N.; Korste, L.; Kreibig, U.; Schonauer, D. *Polyhedron* **1988**, *7*, 605. (b) Schmid, G.; Pugin, R.; Malm, J.-O.; Bovin, J.-O. *Eur. J. Inorg. Chem.* **1998**,

813. (c) Schmid, G.; Pugin, R.; Meyer-Zaika, W.; Simon, U. *Eur. J. Inorg. Chem.* **1999**, 2051.

29 (a) Warner, M. G.; Reed, S. M.; Hutchison, J. E. *Chem. Mater.* **2000**, *12*, 3316. (b) Woehrle, G. H.; Brown, L. O.; Hutchison, J. E. *J. Am. Chem. Soc.* **2005,** *127(7)*, 2172.

30 *Handbook of Preparative Inorganic Chemistry*, Brauer, G., Ed.; Academic Press: New York, **1965**; p 1054.

31 (a) Lee, D.; Donkers, R. L.; Wang, G.; Harper, A. S.; Murray, R. W. *J. Am. Chem. Soc.* **2004**, *126*, 6193. (b) Jimenez, V. L.; Georganopoulou, D. G.; White, R. J.; Harper, A. S.; Mills, A. J.; Lee, D.; Murray, R. W. *Langmuir*, **2004**, *20*, 6864. (c) Chen, S.; Ingram, R. S.; Hostetler, M. J.; Pietron, J. J.; Murray, R. W.; Schaaff, T. G.; Khoury, J. T.; Alvarez, M. M.; Whetten, R. L. *Science*, **1998**, *280*, 2098.

32 Hostetler, M. J.; Wingate, J. E.; Zhong, C. J.; Harris, J. E.; Vachet, R. W.; Clark, M. R.; Londono, J. D.; Green, S. J.; Stokes, J. J., Wignall, G. D.; Glish, G. L.; Murray, R. W. *Langmuir* **1998**, *14*, 17.

33 (a) Shichibu, Y.; Negishi, Y.; Tsukuda, T.; Teranishi, T. *J. Am. Chem. Soc.* **2005**; *127*(39); 13464-13465. (b) Negishi, Y.; Takasugi, Y.; Sato, S.; Yao, H.; Kimura, K.; Tsukuda, T. *J. Am. Chem. Soc.* **2004**; *126*(21); 6518-6519. (c) Negishi, U.; Nobusada, K.; Tsukuda, T. *J. Am. Chem. Soc.* **2005,** *127*, 5261. (d) Tsunoyama, H.; Negishi, Y.; Tsukuda, T. *J. Am. Chem. Soc.* **2006**; ASAP Article

34 (a) Schaaff, T.G.; Knight, G.; Shafigullin, M.N.; Borkman, R.F. and Whetten,R.L. *J. Phys. Chem.B* **1998,** *102*, 10643. (b) Link, S.; Beeby, A.; FitzGerald, S.; El-Sayed, M. A.; Schaaff, T. G.; Whetten, R. L. *J. Phys. Chem. B*, **2002**, *106*, 3410.

35 Yang, Y.; Chen, S. *Nano Lett*. **2003**, *3*, 75.

36 Huang, T.; Murray, R.W. *J. Phy. Chem.B* **2001,** *105(50)*, 1249.

37 Wang, G.; Huang, T.; Murray, R. W.; Menard, L.; Nuzzo, R. G. *J. Am. Chem. Soc.* **2005**; *127*(3); 812-813.

38 (a) Wei, G. T.; Liu, F. *J. Chromatogr., A* **1999**, *836*, 253. (b) Wei, G.; Liu, F.; Wang, C. R. C. *Anal. Chem.* **1999**, *71*, 2085. (c) Wilcoxon, J. P.; Martin, J. E.; Provencio, P. *Langmuir* **2000**, *16*, 9912. (d) Wilcoxon, J. P.; Martin, J. E.; Provencio, P. *J. Chem. Phys.* **2001**, *115*, 998. (e) Siebrands, T.; Giersig, M.; Mulvaney, P.; Fischer, C. –H. *Langmuir* **1993**, *9*, 2297. (f) Fischer, C.-H.; Weller, H.; Katsikas, L.; Henglein, A. *Langmuir* **1989**, *5*, 429.

39 Bos, W.; Steggerda, J. J.; Yan, S.; Casalnuovo, J. A.; Mueting, A. M.; Pignolet, L. H. *Inorg. Chem.* **1988**, *27*, 948.

40 Choi, M. M. F.; Douglas, A. D.; Murray, R. W. *Anal. Chem* .**2006** *ASAP article.*

41 (a) Jimenez, V. L.; Leopold, M. C.; Mazzitelli, C.; Jorgenson, J. W.; Murray, R. W. *Anal. Chem*. **2003**, *75*, 199. (b) Song, Y.; Jimenez, V. L.; Mckinney, C.; Donkers, R. L.; Murray, R. W. *Anal. Chem*. **2003**, *75*, 5088. (c) Song, Y.; Heien, M. LAV; Jimenez, V.; Wightman, R. M.; Murray, R. W. *Anal. Chem* .**2004,** *76*, 4911.

42 (a) Donkers, R. L.; Song Y.; Murray, R. W. *Langmuir* **2004,** *20*, 4703-4707. (b) Guo, R.; Song, Y.; Wang G.; Murray, R. W. *J. Amer. Chem. Soc.* **2005**, *127*, 2752-2757.